LBL--32136

DE92 016926

Structural Transformation of Nickel Hydorxide Films during Anodic Oxidation

Robert W. Crocker* and Rolf H. Muller
*(Ph.D. Thesis)

Department of Chemical Engineering
University of California

and

Materials Science Division
Lawrence Berkeley Laboratory
University of California
Berkeley, CA 94720

May 1992

This work was supported by the Assistant Secretary for Conservation and Renewable Energy, Office of Transportation Technologies, Electric and Hybrid Propulsion Division of the U.S. Department of Energy under Contract No. DE-AC03-76SF00098.

Structural Transformation of Nickel Hydroxide Films during Anodic Oxidation

Robert W. Crocker

Materials Science Division
Lawrence Berkeley Laboratory

and

Department of Chemical Engineering
University of California
Berkeley, California

Abstract

The transformation of anodically formed nickel hydroxide/oxy-hydroxide electrodes has been investigated. A mechanism is proposed for the anodic oxidation reaction, in which the reaction interface between the reduced and oxidized phases of the electrode evolves in a nodular topography that leads to inefficient utilization of the active electrode material.

In the proposed nodular transformation model for the anodic oxidation reaction, nickel hydroxide is oxidized to nickel oxy-hydroxide in the region near the metal substrate. Since the nickel oxy-hydroxide is considerably more conductive than the surrounding nickel hydroxide, as further oxidation occurs, nodular features grow rapidly to the film/electrolyte interface. Upon emerging at the electrolyte interface, the reaction boundary between the nickel hydroxide and oxy-hydroxide phases spreads laterally across the film/electrolyte interface, creating an overlayer of nickel oxy-hydroxide and trapping uncharged regions of nickel hydroxide within the film. The nickel oxy-hydroxide overlayer surface facilitates the oxygen evolution side reaction.

Scanning tunneling microscopy of the electrode in its charged state revealed evidence of 80 - 100 Angstrom nickel oxy-hydroxide nodules in the nickel hydroxide film. The number density of the nodules was 10^{12} per square centimeter.

In situ spectroscopic ellipsometer measurements of films held at various constant potentials agree quantitatively with optical models appropriate to the nodular growth and subsequent overgrowth of the nickel oxy-hydroxide phase. The ratio of the molar volumes of the beta nickel hydroxide and beta nickel oxy-hydroxide phases agrees quantitatively with unit cell volume calculations based on X-ray diffraction and EXAFS measurements in the literature.

A two-dimensional, numerical finite difference model was developed to simulate the current distribution along the phase boundary between the charged and uncharged material. The system was modeled as two film layers having different conductivities with an arbitrary single-valued boundary. The model was used to explore the effects of the physical parameters that govern the electrode behavior. The ratio of the conductivities of the nickel hydroxide and oxy-hydroxide phases was found to be the dominant parameter in the system.

Contents

Acknowlegements

During the course of my graduate study, I once heard Prof. John Prausnitz describe the engineer as a fusion of Apollo and Prometheus, describing the qualities that make up the engineering psyche. From the perspective of graduate school, another mythical figure comes to mind, and that would be Sisyphus. Constructing a theory about the nature of the physical world is much like rolling a stone up a hill and watching it fall as the flaws are discovered. However, unlike Sisyphus, who was condemned to this fate as punishment, engineers and scientists freely choose this lot.

> Sisyphus was condemned by the gods to forever roll a huge stone up a mountain, only to see it fall back to the bottom each time he reached the summit. Albert Camus has depicted this mythical figure as the archetypical existential hero. Sisyphus has no illusions to sustain him, no hope that some day his labors will end. But he has his pride and courage and the satisfaction that comes instinctively to a person undertaking a task. "The struggle itself toward the heights is enough to fill a man's heart," concludes Camus. "One must imagine Sisyphus happy."
>
> Samuel Florman, from *The Existential Pleasures of Engineering*

Some of the greatest sources of pleasure I have had while rolling my stone have been the associations with the people who have helped me. I would like to thank my advisor Rolf Muller, whose guidance and support have shaped my professional career, and Charles Tobias, whose insights have kept me on my toes. I owe a tremendous debt of thanks to the present and former members of the Muller and Tobias research groups as teachers and colleagues, particularly Rolfe Anderson, Mike Armstrong, Rick Gyory, Sholeh Hessami, Ken Jordan, Laura McVay, and Steve Mayer. Credit is also due to the wonderful technical staff at LBL, especially John

Jacobsen, Lee Johnston, Erlene Fong-Mah, Randy Michaelson, Jim Severns, Jerry Tunis, and Bob Ybarra.

Special thanks to my parents, Anne and Jim Crocker, for their patience, love, and support. Finally, I extend my greatest gratitude to my fiancée, Filiz Kinaci, for her technical assistance, a cornerstone of this work, and her constant companionship.

This work was supported by the Assistant Secretary for Conservation and Renewable Energy, Office of Transportation Technologies, Electric and Hybrid Propulsion Division of the U.S. Department of Energy under contract no. DE-AC03-76SF00098.

Chapter 1
Introduction

The nickel hydroxide/oxy-hydroxide electrode is a rechargeable, alkaline, positive electrode currently used in a great number of battery designs for a wide range of applications. Originally developed for use in electric vehicles in the early 1900's, the electrode is now found in applications ranging from children's toys to satellite power systems. Though the promise of widespread use of electric vehicles has, so far, gone largely unfulfilled, the electrode has been the subject of a tremendous body of research and development.

Many different negative electrodes are paired with the nickel hydroxide electrode to form cells, including cadmium/cadmium hydroxide, ferrous/ferric hydroxide, hydrogen, metal hydride, and zinc. The nickel-cadmium and nickel-iron systems were the first to employ nickel hydroxide positive electrodes. The most prevalent use of nickel hydroxide electrodes is in the nickel-cadmium (Ni-Cd) cell which is used for cordless appliances and other consumer products. Nickel-hydrogen batteries are used in satellite power systems because of the extremely long cycle life, which can

exceed 2000 charge-discharge cycles. Lightweight nickel-metal hydride batteries have been recently commercialized for pocket cellular telephones and portable computers. Compared to other alkaline positive electrodes such as mercury/mercuric oxide, silver/silver oxide, and oxygen(air), the nickel hydroxide electrode offers a good compromise between toxicity, cost, and energy density.

There have been several extensive reviews and symposia regarding the nickel hydroxide electrode. In 1967, Milner and Thomas[1] published a review of the nickel-cadmium battery, which included both fundamental and technical aspects of the nickel hydroxide and cadmium electrodes individually and together as a battery system including the roles of the electrolyte and separator. In 1973, Briggs[2] published an updated review of the nickel hydroxide electrode, drawing comparisons to the manganese hydroxide and cobalt hydroxide systems. Most recently in 1991, McBreen[3] published a thorough review encompassing the identities of the phases, the transformation between the phases, the relevant Faradaic reactions, as well as the updated nickel hydroxide electrode technologies.

Other collections of work on the nickel hydroxide system include of The Electrochemical Society [4,5] in 1981 and 1989 and a National Aeronautics and Space Agency (NASA) Symposium on Space Electrochemical Research and Technology.[6] The emphasis of the NASA symposium focused primarily on the role of the nickel hydroxide electrode in nickel-hydrogen batteries for unmanned space vehicles.

The half-cell reaction for the nickel hydroxide electrode is most commonly written as a transformation of divalent nickel hydroxide to trivalent nickel oxy-hydroxide. The reaction, as written in equation [1], is not rigorous with respect to the actual species or their valences. Many of the properties usually obtained from simple electrochemistry experiments on other electrode materials, such as the standard potential, valences, and molecular composition have been difficult to ascertain in the nickel hydroxide system.

$$Ni(OH)_2 \rightleftarrows NiOOH + H^+ + e^- \qquad [1]$$

We shall present evidence that the reaction interface between the reduced and oxidized phases of the electrode evolves during the anodic oxidation reaction in a nodular topography that affects the overall charge storage performance of the electrode. In the following sections of this chapter, the present understanding of the fundamental nature of the nickel hydroxide electrode will be reviewed. This review will serve as a foundation for the research presented in this dissertation. Before launching into the scientific underpinnings of the electrode behavior, it should be noted that the nickel hydroxide electrode has been applied in practical batteries for nearly a century. This long history of commercial, military, and scientific application underscores the motivation behind the research to understand how the electrode works and improve upon it.

1-1 History of Nickel Hydroxide Electrode Technology

The nickel hydroxide electrode has a rich history of research and development dating back to the turn of the century. The electrode was originally patented for electrical storage by Desmazures[7] in 1887 and developed by Thomas Edison[8] and Waldemar Jungner[9] for use in electric vehicles during the 1890's. The Edison battery employs a nickel hydroxide/oxy-hydroxide positive electrode and a ferrous/ferric hydroxide negative electrode in alkaline electrolyte. Jungner developed the nickel-cadmium battery using the cadmium/cadmium hydroxide negative electrode. Edison supposedly selected iron over cadmium believing that the anticipated market for electric vehicles would exceed the projected world cadmium reserves.[10]

The original nickel hydroxide electrode design was the pocket cell, in which nickel hydroxide and graphite or nickel flake were packed into tubular pockets. Pfleider[11] patented the sintered nickel plaque electrode in 1928. In this electrode

design, nickel carbonyl powders were molded into electrodes and sintered into porous nickel metal structures. The plaques were then chemically or electrochemically impregnated with nickel hydroxide material to form the storage electrode.

Edison obtained a patent in 1922 for an electrochemical process to form nickel hydroxide from a nitrate-containing nickel electrolyte[12]. Nickel hydroxide is precipitated in an alkaline surface layer formed by cathodically reducing nitrate anions. In 1962, Kandler[13] received a West German patent for a refined version of this process. Chemical impregnation techniques have been in use since World War II. Nickel hydroxide is precipitated in the porous electrode structure from nickel nitrate or sulfate using sodium or potassium hydroxide. Throughout the history of the electrode, there have been efforts to discover additives to enhance the performance of the electrode. Discussion of these additives will be deferred to section 1-5 of this chapter.

Development activities in the 1970's and 1980's focused on inventing lightweight substrates to replace nickel metal. Carbon fiber and foam substrates produced by pyrolysis of organic materials were created which had high specific surface area, comparable to that of the sintered metal substrates. In 1972, Williams[14] patented a substrate made from pyrolyzed non-woven cloth. Gutyahr[15] patented a carbon foam substrate in 1974. Graphite felt substrates were patented in 1980 by Ferrrando and Satula.[16]. In 1981, Joyce and Carlucci[17] patented the Fibrex electrode material, an extruded mixture of nickel hydroxide and binding materials.

Currently, the most advanced development work on the nickel hydroxide electrode is being conducted for its role as part of nickel-hydrogen and nickel-metal hydride batteries. The intended use for the nickel-hydrogen cell would be for space energy storage applications, whereas the nickel-metal hydride system is for terrestrial use in portable electronics such as cellular telephones and laptop

computers. The extremely long cycle-life of these systems makes them ideal candidates in maintenance-free situations.

1-2 Electrode Phase Identities

Much of the research on the electrode has been directed towards the identification of the molecular species involved in the storage reaction. Most researchers have agreed that there are at least two different phases for each of the reduced and oxidized species, depending on the preparation and electrochemical history of the electrode materials. The principal difference between the phases is the amount of water in the crystal structures. The relationship between the various phases of the oxidized and reduced species, illustrated in figure 1.1, was determined by Bode[18]. This work has been confirmed by extensive X-ray diffraction[19,20,21] and extended X-ray absorption fine structure spectroscopy(EXAFS). [22, 23, 24];

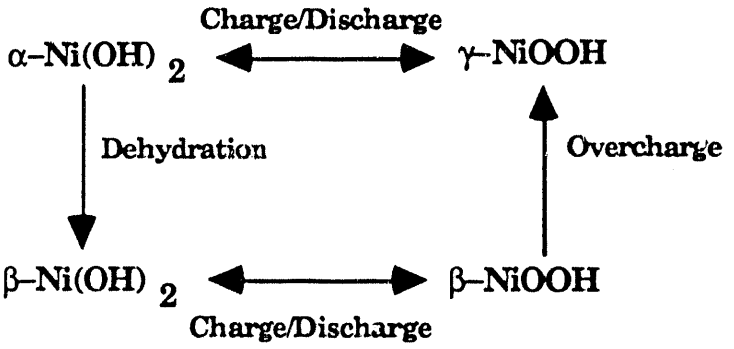

Figure 1.1: Bode reaction schematic illustrating the transformation reactions between the different phases of the uncharged nickel hydroxide and charged nickel oxy-hydroxide materials. (reference 18)

The reduced nickel hydroxide species has been identified in two different phases denoted alpha and beta. The beta form is the best characterized of all the species identified in the electrode system and is the active material in the storage electrode. It is a divalent nickel hydroxide which forms in a reasonably well ordered hexagonal crystalline structure of the C6 brucite form. This material contains no water in the

crystal lattice. However, the crystallites may include surface water. The unit cell dimensions, given in table 1.1, have been confirmed by X-ray[18,19,20,21,25] and neutron diffraction[26] techniques. This material is formed by precipitation in 100 °C potassium hydroxide, anodic oxidation of nickel, or dehydration of the alpha form of nickel hydroxide. The electrochemical activity is affected by the extent of disorder and hydration. Smaller crystallites increase the kinetic rates of the electrode reactions. Thermally formed anhydrous material exhibits the slowest reaction kinetics to oxidation.

The alpha form of nickel hydroxide is an extremely disordered material; X-ray diffraction patterns have been noted as nearly featureless.[27] Infrared spectroscopy[28] and EXAFS[22,23,24] have been used to determine the local environment around the nickel atoms. From these measurements, a turbostratic structure has been determined. This structure is similar to the hexagonal structure for the beta form, except that the c-axis has been expanded to accommodate a layer of semi-ordered water molecules. The basal planes, which contain the nickel atoms, are not oriented with respect to each other, explaining the weak X-ray diffraction patterns. The crystallite dimensions have been estimated to be 80 Å along the basal planes and 30 Å in the c-direction.[29] The alpha nickel hydroxide phase is formed by precipitation in dilute alkaline electrolyte, very mild anodic oxidation of nickel in 0.10 molar aqueous sodium hydroxide, or reduction of the gamma nickel oxy-hydroxide material[3,19]. This phase is considered to be unstable in alkaline solution, in which it readily dehydrates to the more ordered beta phase.

Phase	Structure	Unit Cell Dimensions		Unit Cell Volume	Reference
		a_0	c		
β-$Ni(OH)_2$	hexagonal	3.13 Å	4.6 Å	19. $Å^3$	25
α-$Ni(OH)_2$	turbostratic	3.09	8.0	33.	20
β-NiOOH	hexagonal	2.8	4.8	16.	19
γ-NiOOH	rhombohedral	2.8	20.6	~70.	19

Table 1.1: Structure and unit cell dimensions for nickel hydroxide electrode species.

Beta nickel oxy-hydroxide is formed by anodic oxidation of the beta nickel hydroxide phase and is the principal phase in the charged nickel hydroxide storage electrode. It has also been formed by chemical oxidation and precipitation by Glemser and Einerhand.[19] It maintains the hexagonal brucite structure of the beta nickel hydroxide phase with small changes to the unit cell dimensions, resulting in a 15% contraction in molecular volume. The dimensions are tabulated in table 1.1. This species is believed to contain only trivalent nickel.

The gamma nickel oxy-hydroxide phase is the anodic oxidation product of the alpha nickel hydroxide phase. It is also formed upon overcharge of the beta oxy-hydroxide phase. Structurally, it is related to the alkali metal nickelates, $MNiO_2$ (M = Na, K, Li). The structure contains water and potassium ions from the electrolyte. Glemser and Einerhand[19] assigned a rhombohedral structure to the material with a c-axis dimension of 20 Å. Problems with swelling of the electrode occur during formation of this phase. There is evidence suggesting that γ-NiOOH species may contain quadrivalent nickel based on coulometry and iodide titration. Analyses for active oxygen using iodide have determined an effective valence of 3.5 to 3.67 on the nickel ions.[30]

1-3 Electrode Material Properties

There are significant differences in the properties of the charged and discharged materials. The reduced form, nickel hydroxide is a poor electrical conductor. It is intrinsically a p-type semiconductor with a band gap of 3.7 electron Volts[33]. Conduction is predominantly ionic. Proton conductances have been reported for the material.[31,32] The oxidized, charged, oxy-hydroxide is an n-type semiconductor having a band gap of roughly 1.75 eV. It conducts primarily electronically. The band gap energies for both materials were estimated from absorbance spectra.[33]

One of the more dramatic differences, however, is in the optical properties of the materials. Absorbance spectra measured by Corrigan and Carpenter[33] are reproduced in figure 1.2. The hydroxide is weakly absorbing and nearly transparent in the visible spectrum. The oxy-hydroxide is strongly absorbing in the visible spectrum. This makes the electrode electrochromic. The difference is apparent even in films as thin as 100 Angstroms. Some interest has been shown in these materials for electrochromic windows.[34] The difference in the optical properties facilitates investigation via ellipsometry[35,36,37,38] and reflectance spectroscopy[33,39,40]

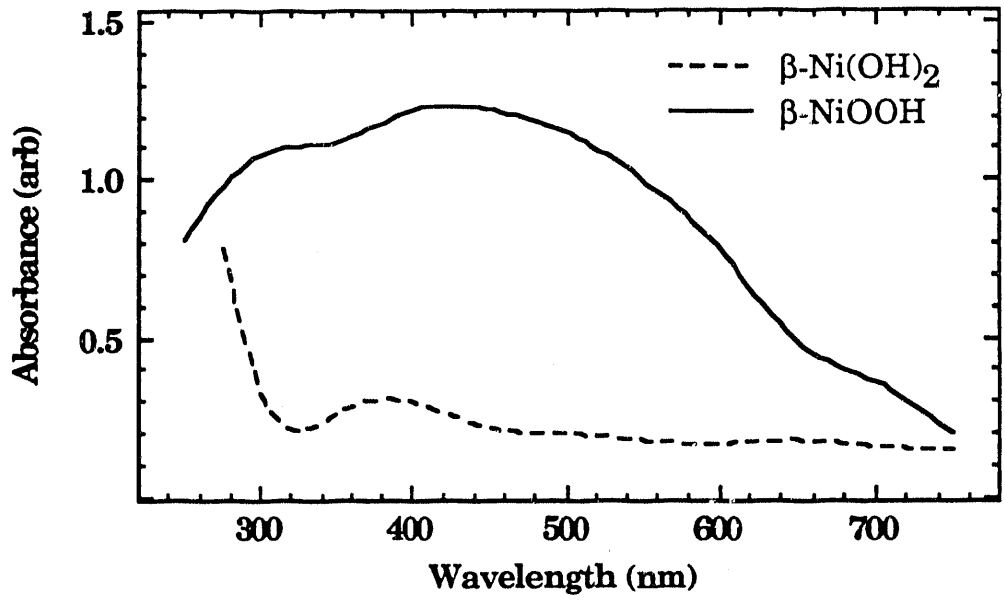

Figure 1.2: Absorbances of nickel hydroxide and oxy-hydroxide films measured by Corrigan, Carpenter (ref. 33) XBL 924-849

1-4 Electrode Reactions

The reactions occurring on the nickel hydroxide electrode and nickel metal substrate include oxidation of nickel metal, dehydration of the alpha form to the beta form of nickel hydroxide, oxidation of the nickel hydroxide phases to the oxy-hydroxide phases, and oxygen evolution. There were substantial research efforts during the 1980's to reconcile the experimental observations of the reactions with the identities of the various phases. Since the present research for this dissertation was conducted on nickel hydroxide films anodically formed on nickel metal substrates, we will describe the reactions for this system. These reactions are tabulated in table 1.2. The reactions for precipitated electrode films are similar and are described in the literature.[3]

Reaction	Potential vs. HgO/Hg
$Ni \longrightarrow \alpha\text{-}Ni(OH)_2 + 2\,e^-$	–0.800 Volts
$Ni \longrightarrow \beta\text{-}Ni(OH)_2 + 2\,e^-$	–0.500
$\alpha\text{-}Ni(OH)_2 \rightarrow \gamma\text{-}NiOOH + H^+ + e^-$	0.388
$\beta\text{-}Ni(OH)_2 \rightarrow \beta\text{-}NiOOH + H^+ + e^-$	0.424
$2\,OH^- \rightarrow 1/2\,O_2(g) + H_2O + 2\,e^-$	0.307

Table 1.2: Faradaic reactions occurring on nickel metal in alkaline electrolyte to form nickel hydroxide film electrodes.

Oxidation of the bare nickel metal substrate occurs rapidly in alkaline electrolyte. Weiniger and Breiter[41] demonstrated that nickel metal is unstable in alkaline electrolytes purged of dissolved oxygen with argon. At negative potentials cathodic of –0.80 Volts versus the mercury/mercuric oxide reference electrode, hydrogen gas is evolved from the nickel metal surface. Between –0.80 and –0.50 Volts, the alpha nickel hydroxide phase is formed, which may be reversibly reduced. However, at potentials more positive than –0.50 Volts, the film is dehydrated to form the beta nickel hydroxide phase. The beta phase, however, cannot be reduced to nickel metal. The substrate is oxidized to form the beta nickel hydroxide phase until the film thickness reaches approximately 50 Angstroms.

At potentials greater than 0.42 Volts versus the mercury/mercuric oxide reference electrode, the beta nickel hydroxide phase is oxidized to form the beta nickel oxy-hydroxide phase. This is the electrochemical storage reaction for the nickel hydroxide electrode. The standard potential for this reaction has been recognized as a mixed potential that is controlled by the alpha nickel hydroxide to gamma nickel oxy-hydroxide reaction and the reaction between the beta phases, as well as the oxygen reaction. Bourgalt and Conway[42] used a potential decay

technique to infer the open-circuit electrode potential for different states of charge. Barnard and coworkers[43] noticed that the potentials measured this way are independent of pH for the beta-beta oxidation (versus the mercury/mercuric oxide reference electrode), whereas the alpha-gamma reaction has a pH dependence. The open-circuit potential for the beta-beta couple is larger than that of the alpha-gamma pair, 0.424 versus 0.388 Volts.

Additional oxidation of the nickel metal substrate occurs after the film has been oxidized to the oxy-hydroxide phase. This results in film thickening up to approximately 110 Angstroms of the beta nickel oxy-hydroxide phase. Upon reduction, the beta nickel oxy-hydroxide phase is converted to the beta nickel hydroxide phase.

The oxygen evolution reaction occurs following the nickel oxy-hydroxide reaction. The nickel oxy-hydroxide electrode has been shown to catalyze the oxygen evolution reaction.[44] While this may be fortunate for designing water electrolyzers, it leads to poor charging efficiency and sealing problems for battery designs. Oxygen evolution is also the reaction occurring during self-discharge of the electrode at open-circuit.[45] One of the roles of additives used in practical nickel hydroxide electrodes is the poisoning of the oxygen evolution kinetics.

Beyond the storage reaction and obscured within the oxygen evolution reaction, the beta nickel oxy-hydroxide phase is oxidized and disordered into the gamma oxy-hydroxide phase. This phase contains considerably more water within the structure. The effective valence of the nickel species within this phase increases from 3.0 to 3.5 or 3.7, by oxidizing a fraction of the nickel species to quadrivalent nickel. Upon reduction, this phase is converted to the alpha nickel hydroxide phase according to the Bode reaction model, illustrated in figure 1.1.

1-5 Effects of Additives

Since the development work of Edison, it has been recognized that chemical additives to the electrode could enhance its performance. Edison used cobalt hydroxide to reduce swelling in the electrode during overcharge. He also included a small amount of lithium hydroxide in the electrolyte. Cobalt and lithium hydroxides remain as the most popular additives to the system despite controversy over their specific effects. The principal role of lithium hydroxide is to increase the oxygen evolution overpotential. Halpert[46] presented a table of claims made for the roles of cobalt and various common additives, underscoring the lack of consensus on the effects of cobalt hydroxide on the nickel hydroxide electrode. Other materials have been studied for their role as contaminants originating from the negative electrode including iron, cadmium, zinc, and silver. Casey and coworkers[47] examined a large number of ionic additives including twenty-five elements spanning the periodic table.

1-6 Structural Transformation during Anodic Oxidation

The nickel hydroxide/oxy-hydroxide electrochemical storage reaction proceeds as a solid-solid reaction with no dissolution of the active species. The mechanism of the transformation between nickel hydroxide to nickel oxy-hydroxide is not well known, but there have been studies of large-scale morphology at the micron scale as well as speculation in the literature to explain anomalous results. In this research, we have examined the microstructural aspects of the phase transformation of nickel hydroxide electrode films, specifically, how the evolution of the microstructure influences the performance characteristics of the electrode.

The differences in the optical properties of the hydroxide and oxy-hydroxide phases, referred to previously in figure 1.2, make the system quite accessible to optical techniques. There have been numerous studies of the nickel hydroxide films

using ellipsometry[35,36,37,38] and reflectance techniques.[33,39,40] Although, the reflectance measurements have identified spectroscopic differences between the phases, structural dimensions are difficult to determine using this technique. In contrast, monochromatic ellipsometer measurements are excellent for determining structural dimensions, if the optical constants are known.

Unfortunately, the optical constant spectra of the materials are difficult to fully determine from reflectance measurements, which determine the absorbance. The extinction coefficient, the imaginary component of the complex refractive index, can be determined from the absorbance; however, the real refractive index can only be indirectly calculated from the extinction coefficient spectra using the Kramer-Kroenig transformation. In practice, the Kramer-Kroenig transformation calculations require the extinction coefficient spectra for the entire electromagnetic spectrum to be known, or to be approximated by asymptotes.

In our research, we have approached the study of this electrode using spectroscopic ellipsometry to complement scanning tunneling electron microscopy and traditional electrochemical measurements. In spectroscopic ellipsometry, two parameters related to the phase and amplitude changes upon reflection of polarized light are measured at many wavelengths, spanning the visible portion of the electromagnetic spectrum. This technique can be used to determine either the complex optical constant spectrum or test structure hypotheses if the optical constant spectra of the materials are known.

In our preliminary investigations of the structural transformation, we compared monochromatic ellipsometer and electrochemical measurements to calculated transients for three prototype structures based on structural hypotheses proposed in the literature. The first structure, illustrated in figure 1.3a, is a laminar dual film structure in which a planar reaction interface propagates from the metal/film interface to the film/electrolyte interface. This one-dimensional structure can also

simulate the case of the reaction interface propagating from the electrolyte to the metal interface. It has been used in many ellipsometry investigations of the electrode reaction.[36,37,38] The optical properties of the films are modeled using classical electromagnetic theories, including Fresnel reflection coefficients and Drude equation for thin film interference. A more detailed discussion of optical modelling is presented in chapter four. Electrically, the ohmic resistance across the film can be modeled as two resistances in series weighted by the thicknesses of each layer of material.

The second structure, illustrated in figure 1.3b, is a two-dimensional island film model, in which islands of the oxy-hydroxide phase spread laterally across the film. This structure resembles the model proposed by Briggs and Fleischman[48] for nucleation and growth of cylindrical islands. The optical properties are calculated using a coherent superposition model. The ohmic resistance of this structure corresponds to two parallel resistances weighted by the relative areas of the phases.

The third structure hypothesis is a three-dimensional homogeneous transformation from the nickel hydroxide phase to the nickel oxy-hydroxide phase. This model, illustrated in figure 1.3c, uses effective medium approximation theories as a mixing rule for the optical and electrical properties of the electrode film. It tests the case in which the electrode acts as a solid solution of mixed valence oxides. In such a case, the mean oxidation state of the nickel atoms would continuously range from 2 to 3.7, including di-, tri-, and quadrivalent nickel cations.

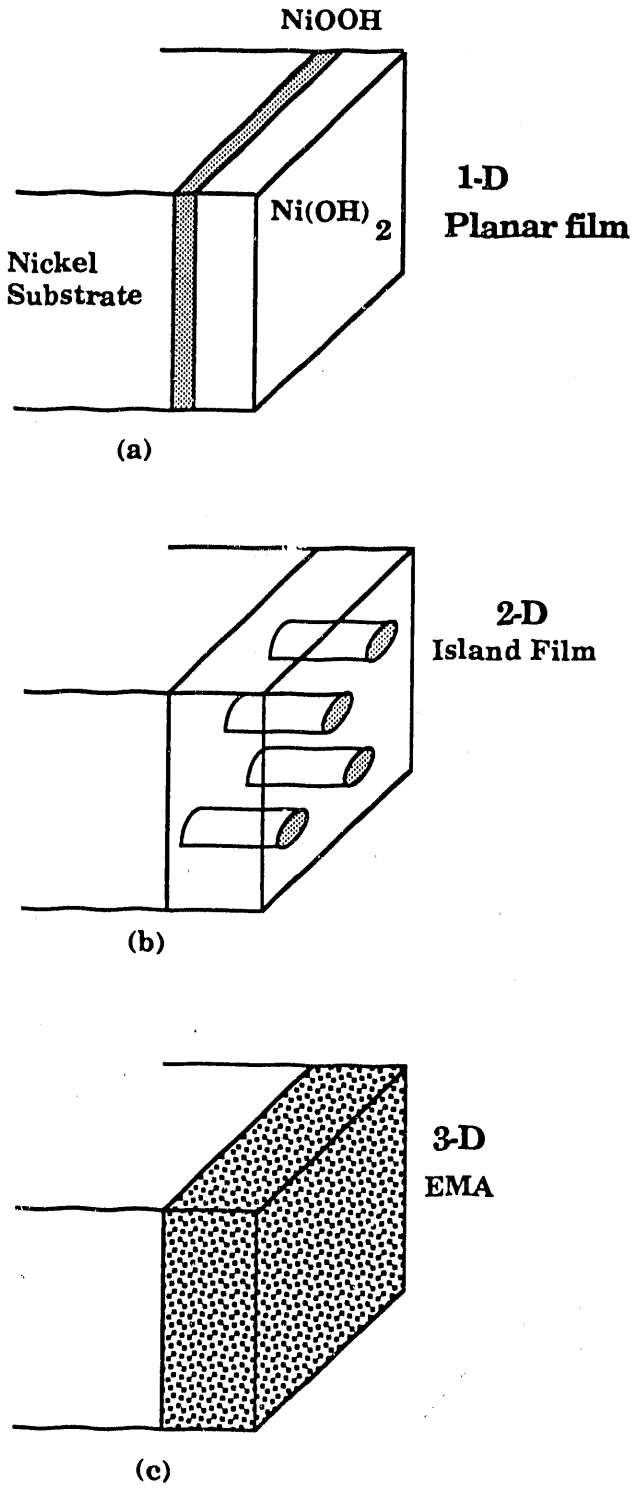

Figure 1.3: Prototype structures for the phase transformation between nickel hydroxide and nickel oxy-hydroxide during anodic oxidation reaction. (a) 1-D planar film structure, interface propagates through film parallel to surface. (b) 2-D island film structure, islands grow laterally through film, (c) 3-D homogeneous mixture representing solid solution using effective medium approximations for optical and electrical properties. XBL 924-850

The qualitative comparison between these models and galvanostatic measurements, illustrated in figures 1.4-1.7, indicates that none of these structures adequately describes the transformation process. Overpotentials of the anodic oxidation reaction from nickel hydroxide to nickel oxy-hydroxide are shown in figure 1.4. These overpotentials are calculated from the measured open-circuit potential of 0.480 Volts versus the mercury/mercuric oxide reference electrode. Comparing the overpotential transients in figure 1.4 to those in figure 1.5, one can clearly eliminate the planar structure since the expected transients are not linear with charge passed. To discriminate between the lateral and homogeneous models, one must compare the optical transients in figure 1.6 to the predictions in figure 1.7. None of the model structures predicted the complex shape of the optical transients. Based on the results of these preliminary experiments to characterize the phase transformation process, a more sophisticated theory, rooted in the physics of the process, was needed.

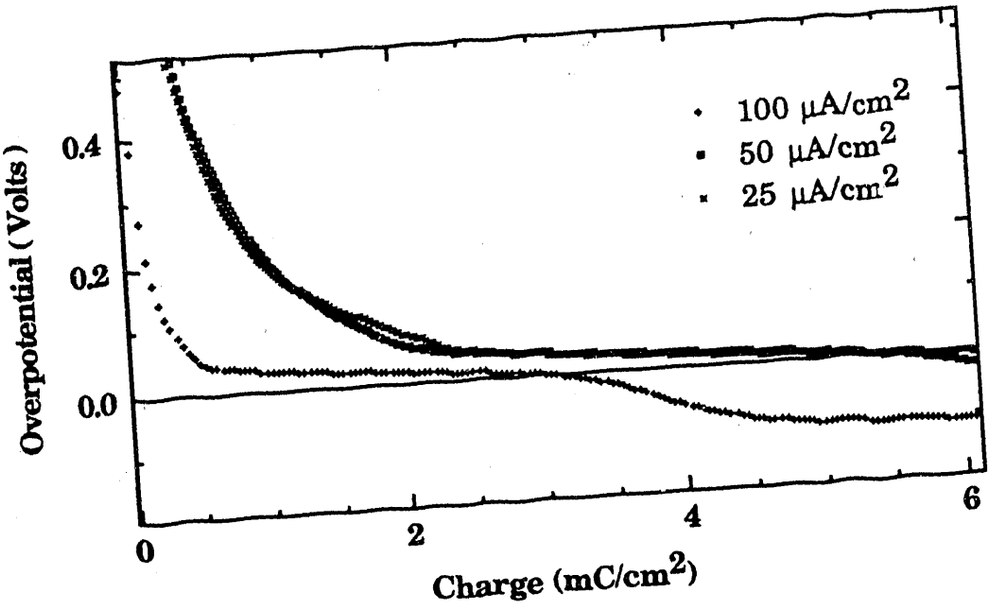

Figure 1.4: Measurements of overpotential for $Ni(OH)_2/NiOOH$ reaction during anodic oxidation. Overpotentials are referenced to open circuit potential 0.480 V. vs. Hg/HgO. Negative overpotentials denote transition to oxygen evolution. XBL 924-851

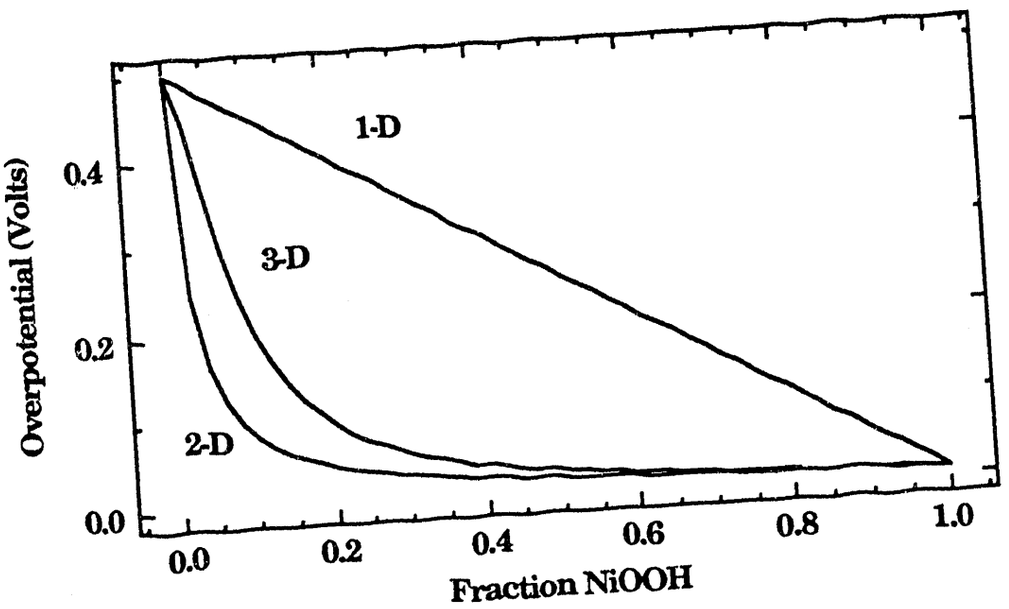

Figure 1.5: Predictions of overpotential for $Ni(OH)_2/NiOOH$ reaction during anodic oxidation based on the models in figure 1.3. XBL 924-852

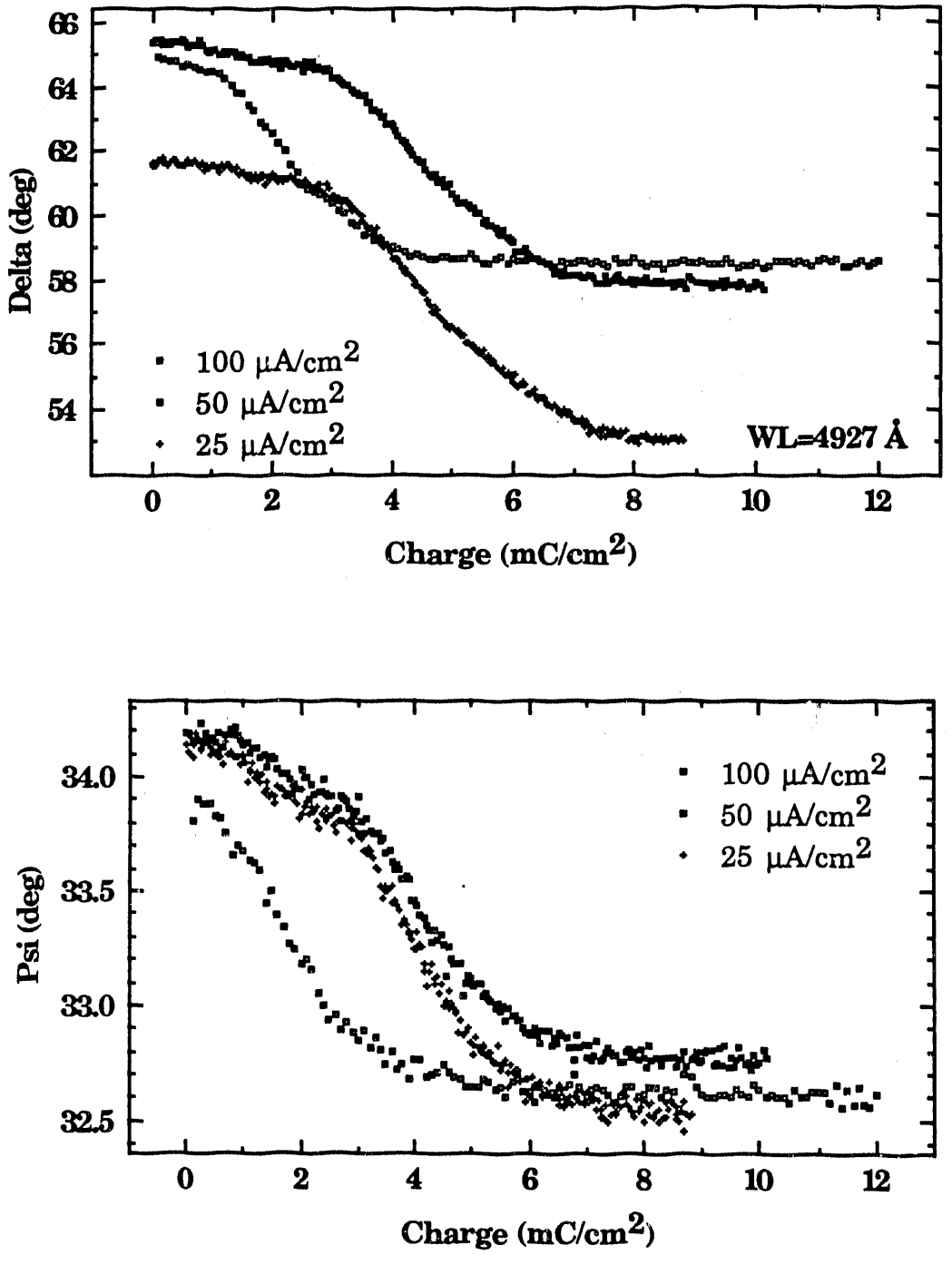

Figure 1.6: Measurements of ellipsometer parameters delta and psi for the conversion of $Ni(OH)_2$ to NiOOH reaction during anodic oxidation. XBL 924-853/4

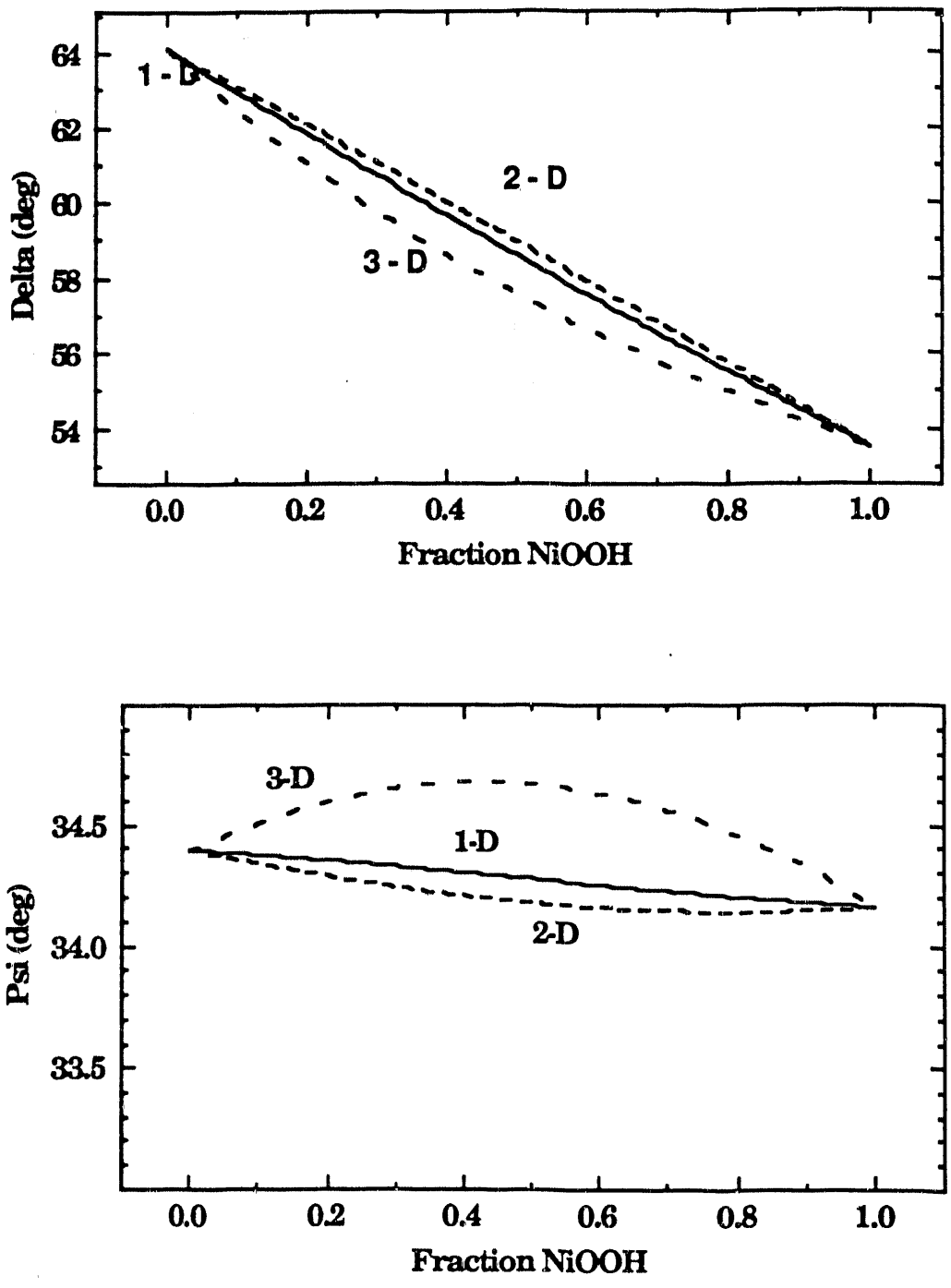

Figure 1.7: Predictions of ellipsometer parameters delta and psi for the conversion of $Ni(OH)_2$ to NiOOH reaction during anodic oxidation based on the models in figure 1.3. XBL 924-855/6

A fundamental approach to the problem, in light of the vastly different conductivities of the two phases, suggests that a nodular growth model is possible. Such a model is illustrated schematically in figure 1.8. For the anodic oxidation reaction, the initial condition for the system is a planar nickel hydroxide film on a nickel metal substrate, immersed in concentrated alkaline electrolyte. (figure 1.8a)

As the film is first anodized, nickel hydroxide is oxidized to nickel oxy-hydroxide in the region near the metal substrate. (figure 1.8b) The oxidation reaction should occur at the metal/film interface since this is the locus of holes for oxidation. Protons then migrate to the film./electrolyte interface where they quickly recombine with hydroxide ions to form water. Experiments by Kuchinskii and Erschler[49] on single grains of nickel hydroxide supported on a platinum pin confirm that the oxidation occurs near the metal current collector. Isotope tracer studies[3,50], indicate that hydrogen is exchanged with the electrolyte, but not oxygen.

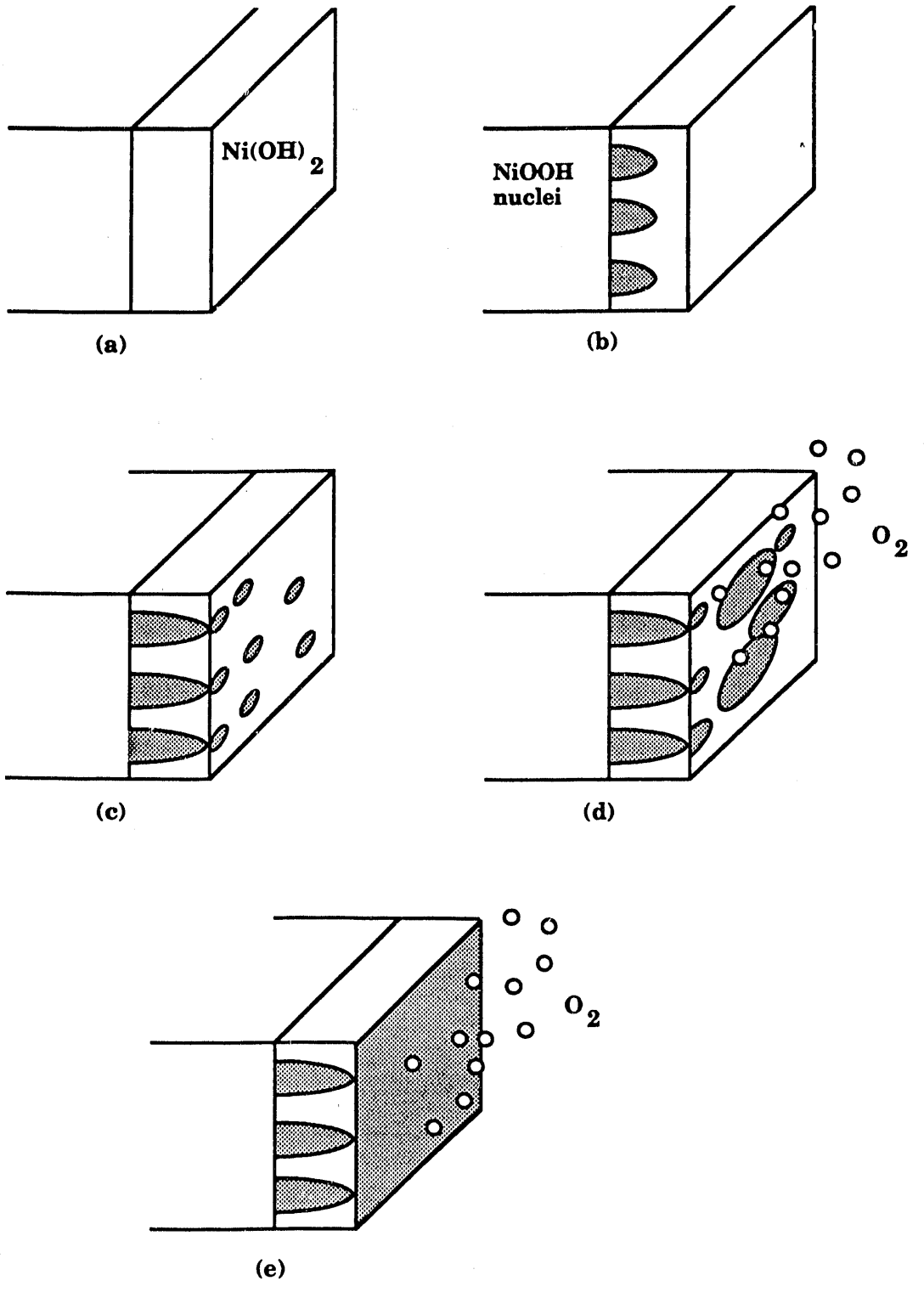

Figure 1.8: Nodular phase transformation schematic for anodic oxidation of nickel hydroxide to nickel oxy-hydroxide. (a) Initial uncharged nickel hydroxide film, (b) NiOOH nodule formation upon charging, (c) Nodules grow rapidly through film, (d) Overlayer forms across electrolyte interface, allowing oxygen evolution side reaction, (e) Overlayer traps unconverted material within film. XBL 924-857

As further oxidation occurs, since the nickel oxy-hydroxide is considerably more conductive than the surrounding nickel hydroxide, the current distribution favors points closest to the film/electrolyte interface. These nodular features grow rapidly to the film/electrolyte interface. Upon emerging at this interface, the nickel oxy-hydroxide surface facilitates the oxygen evolution reaction. The reaction boundary between the nickel hydroxide and oxy-hydroxide phases proceeds as a contact line on the film electrolyte interface, creating an overlayer of nickel oxy-hydroxide and trapping uncharged regions of nickel hydroxide within the film.

In this dissertation, we will demonstrate how the three-dimensional nodular growth of the phase boundary between the charged and uncharged material leads to inefficient utilization of the active electrode material. Experiments using scanning tunneling microscopy and spectroscopic ellipsometry provide evidence of this model. In addition, a numerical electrochemical model is presented to simulate the growth of the nodules through the film.

References

1 P.C. Milner, U.B. Thomas, "The Nickel-Cadmium Cell", *Advances in Electrochemistry and Electrochemical Engineering*, Vol. 5, P. Delahay, C.W. Tobias (ed.), Wiley, New York, 1967

2 G.W.D. Briggs, "The Nickel Hydroxide and Related Electrodes", *Electrochemistry*, Vol. 4, H.R. Thirsk (ed.), Ch. 3, The Chemical Society (of Britain), 1974

3 J. McBreen, "The Nickel Oxide Electrode", *Modern Aspects of Electrochemistry*, Vol. 21, R. E. White et al (ed), Plenum Press, NY, 1991

4 R.G. Gunther, *Proceedings of the Symposium on the Nickel Electrode*, Proc. Vol. 82-4, S. Gross (ed.), The Electrochem Soc., 1982

5 D.A. Corrigan, A.H. Zimmerman, (ed.), *Proceedings of the Symposium on Nickel Hydroxide Electrodes*, Proc. Vol. 90-4, The Electrochem Soc., 1990

6 P.M. O'Donnel, "Proceedings of the Second Space Electrochemical Research and Technology Conference", Journal of Power Sources, **29,** <3&4> (1990)

7 C. Desmazures, French Patent (1887), U.S. Patent 402,006 (1889)

8 T.A. Edison, U.S. 678,722 (1901)

9 W. Jungner, Swedish Patent 8,558 (1897)

10 B. Vanderbilt, "The Amazing Alkaline Storage Battery", *Thomas Edison, Chemist*, Ch. 7, ACS, 1971

11 G. Pfleider, F. Sploun, P. Gmelin, K. Ackerman, German Patent 491,498 (1928)

12 T.A. Edison, U.S. Patent 1,402,751 (1922)

13 L.W. Kandler, German Patent 1,133,442 (1962)

14 N.J. Williams, P.J. Bridges, D.S. Burr, Powder Metallurgy **15,** 29 (1972).

15 M.A. Gutyahr et al., W. German Patent DOS 24 27 422 (1974)

16 W.A. Ferrrando, R.A. Satula, U.S. Patent 4,215,190 (1980)

17 S.L. Carlucci, U.S. Patent 4,312,670 (1982)

18 H. Bode, K. Dehmelt, J. Witte, Electrochim. Acta **16,** 429 (1971)

19 O. Glemser, J. Einerhand, Z. anorgan. Chem. **261,** 26 (1950)

20 R.S. McEwen, J. Phys. Chem. **75,** <12>, 1782 (1971)

21 G.D.W. Briggs, M. Fleischman, Trans. Faraday Soc. **67,** 2397 (1971)

22 K.I. Pandya, .W.E. O'Grady, et al., J. Phys. Chem. **94,** 21 (1990)

23 J. McBreen, W.E. O'Grady, et al., Langmuir **3,** 428 (1987)

24 D. Guay, G. Tourillon, et al., J. Electroanal. Chem. **305,** 83 (1991)

25 G. Natta, Gazz. Chim. Ital. **58,** 344 (1928)

26 C. Greaves, M.A. Thomas, Acta Crystallogr., Sect. **B 42,** 51 (1986)

27 R.S. McEwen, J. Phys. Chem. **75,** <12>, 1784 (1971)

28 S. Le Bihan, M. Figlarz, J. Crystal Growth **13/14,** (1972)

29 S. Le Bihan, M. Figlarz, Electrochim. Acta **18,** 123 (1973)

30 D.A. Corrigan, S.L. Knight, J. Electrochem. Soc. **136,** 613 (1989)

31 B.B. Ezhov, O.G. Malandin, S.N. Kudryashov, Sov. Electrochem. **25,** 86 (1989)

32 D.M. MacArthur, J. Electrochem. **177,** 729 (1970)

33 M.K. Carpenter, D.A. Corrigan, J. Electrochem. Soc. **136,** 1022 (1989)

34 P.C. Yu, C.M. Lampert, Solar Energy Materials **19,** <2>, 1-16 (1989)

35 J.O'M. Bockris, A.K.N.Reddy, B. Rao, J. Electrochem. Soc. **113,** 1133 (1966)

36 J.L. Ord, J.C. Clayton, D.J. DeSmet, J. Electrochem. Soc. **124,** 1714 (1977)

37 W. Visscher, J. de Phys. Colloque C10, **44,** 213 (1983)

38 A.A. Wronskawa, Surf. Sci. **214,** 507 (1989)

39 C. Zhang, S. Park, J. Electrochem. Soc. **136,** 3333(1989)

40 F. Hahn, D. Floner, B. Beden, C. Lamy, Electrochim. Acta **32,** 1631 (1987)

41 J.L. Weiniger, M.W. Breiter, J. Electrochem. Soc. **110,** 484 (1963)

42 P.L. Bourgalt, B.E. Conway, Can. J. of Chem. **38,** 1557 (1960)

43 R. Barnard, C.F. Randell, F.L. Tye, J. App. Electrochem. **10,** 109(1980)

44 C.K. Dyer, J. Electrochem. Soc. **132,** 64 (1985)

45 B.E. Conway, P.L. Bourgalt, Can. J. of Chem. **40,** 1690 (1962)

46 G. Halpert, "The Nickel Hydroxide Electrode- An Overview" in *Proc. of the Symposium on Nickel Hydroxide Electrode,* D.A. Corrigan, A.H. Zimmerman (ed.), Proceedings Vol. 90-4, The Electrochemical Soc. (1990)

47 E.J. Casey, A.R. Dubois, P.E. Lake, W.Z. Moroz, J. Electrochem. Soc. **112,** 371 (1966)

48 G.W.D. Briggs, M. Fleischman, "Oxidation and Reduction of Nickel Hydroxide", Trans. Faraday Soc.., p. 2397 (1971)

49 E.M. Kuchinskii, B.V. Erschler, J. Phys Chem (USSR) **14,** 985 (1940)

50 S.A. Aleshkevich, L.N. Sagoyan, Khim.Tekhnol. Zhur. (Kharkov) **69,** (1968) [Chem Abs 72, 27, 675x (1970)]

Chapter 2

Experimental Methods

2-1 Electrochemical Equipment and Materials

Pure nickel (99.9+%) metal electrodes were embedded in epoxy mounts. A blend of Shell 736 and 826 epoxy resins was used for the mounts. The electrodes were 0.50 inch in diameter; the mounts, 1.50 inch. The electrodes were optically polished and anodically etched (1-2 millicoulombs/cm^2) in 1.0 molar aqueous sulfuric acid. Nickel hydroxide films were anodically grown on the electrodes in 1.0 molar aqueous sodium hydroxide by sweeping the potential at 10 -20 millivolts per second to anodic potentials typically 0.400 Volts versus a mercury/mercuric oxide reference electrode. The film thicknesses, determined by spectroscopic ellipsometry, were 40 - 60 Angstroms in the first cycle, and typically grew to 120 Angstroms as the electrodes were repeatedly oxidized and reduced from nickel hydroxide to nickel oxy-hydroxide and back.

A mercury/mercuric oxide reference electrode with no liquid junction was used for determining potentials in the alkaline electrolyte. A standard calomel electrode was used in sulfuric acid. In all cases, a platinum counter electrode was used. Electrolyte solutions were sparged with nitrogen prior to experiments to remove dissolved oxygen.

The electrochemical cell, made of Teflon™, contained 250 milliliters of electrolyte. Fused silica optical windows with 1.0 inch clear aperture were mounted on the cell to accommodate the optical beam path which reflects from the electrode at a 75° angle of incidence. This cell is pictured in figure 2.1. Electrochemical experiments were performed using an EG&G PAR 273 potentiostat controlled by an IBM PS/2™ model 50 computer running the data collection program, Headstart, provided by EG&G.

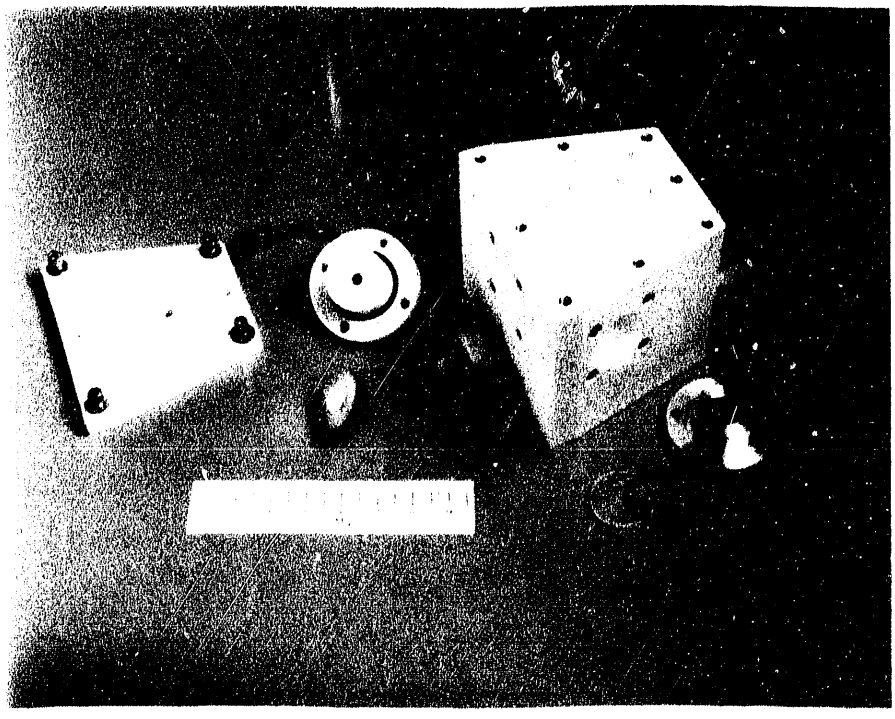

Figure 2.1: Electrochemical cell for ellipsometry experiments. The parts from left to right: lid with mounting screws, nickel electrode embedded in epoxy, Teflon electrode mount, Teflon cell with ports aligned for a 75° incident optical beam that reflects off the sample. Window parts (one set of two) fused silica window, Teflon O-ring, window mounting ring with screws. CBB 923-2183

2-2 Sample Preparation for Optical Measurements

The nickel metal samples, mounted in epoxy, were ground flat on 600 grit carbide abrasive paper prior to polishing. Polishing technique is, unfortunately, more of an art than a science. To wit, the procedure developed to produce a flat, specularly reflecting surface on the samples, depends as much on the skilled hand of the operator, as to the procedure and materials used. The following procedure was used for the samples in this study:

- After the grinding step, the samples were cleaned with a solution of liquid detergent in distilled water in an ultrasonic cleaning tank for 5 minutes.
- The samples were rinsed with distilled water in the ultrasonic tank for an additional minute.
- The samples were initially polished on Buehler nylon with 6 micron Metadi diamond paste and polishing oil to remove the grinding scratches. The final surface had a matte appearance with light polishing scratches. The nylon cloth was selected to preserve the flatness of the sample during the initial polishing steps.
- The samples were ultrasonically cleaned and rinsed as previous described.
- The samples were polished using 1 micron diamond paste on cotton broadcloth with polishing oil to remove the scratches left from the previous polishing step. Here also, a low nap cloth has been selected to preserve the flatness of the sample. This step was brief to avoid inducing large-scale surface waviness commonly referred to as "orange peel."
- The samples were ultrasonically cleaned as before.
- The samples were polished using 1 micron diamond paste on Buehler Microcloth™, a material with soft dense nap, with polishing oil. The surface was polished until it began to look bright.

- The samples were ultrasonically cleaned and rinsed.
- The final polishing step was performed with 0.25 micron diamond paste on Microcloth using distilled water as a lubricant. The final surface was extremely bright, flat, and nearly free of scratches and pits.
- The samples were ultrasonically cleaned as before and dried with warm air from a heat gun using the low setting.
- The samples were stored in a desiccator over Drierite™ absorbant until needed.

2-3 Ellipsometry Methods

Optical measurements were made using an automatic, self-nulling spectroscopic ellipsometer[1], illustrated pictorially in figure 2.2 and schematically in figure 2.3. The instrument measures the ellipsometer parameters, Δ and Ψ, at 400 wavelength points spanning the visible spectrum between 370 and 740 nanometers. The instrument is capable of acquiring a spectrum in less than 6 seconds. In the monochromatic mode, the instrument is capable of 100 measurements per second. Signal averaging was used to reduce noise in slowly varying samples. The angle of incidence for all of the measurements made in this study was 75°.

For highest precision, each final spectrum was derived from an average of four individual spectra in different measurement zones. The zones correspond to equivalent measurements at different prism azimuths arising from symmetries in the polarizing prisms. Four-zone averaging alleviates prism azimuth positioning errors.[2]

---

1 R.H. Muller, J.C. Farmer, "Fast, self-compensating, spectral-scanning ellipsometer", Rev. Sci. Instrum. **55**, <March>, 371 - 374 (1984)

2 R.H. Muller, "Principals of Ellipsometry", in *Adv. in Electrochemistry and Electrochem. Eng,* Volume 9, C.W. Tobias, and H. Gerischer (ed.), Wiley, 1973

The optical constant spectra of the nickel samples, both polycrystalline and (111) single crystal, were determined from spectroscopic ellipsometry spectra. The refractive index of the electrolyte was determined by refractometry to be independent of wavelength and equal to 1.34 for one molar sulfuric acid and sodium hydroxide. The nickel samples were measured in one molar sulfuric acid under cathodic polarization (10 microamp/cm^2) after a brief anodic etch (1-2 millicoulombs/cm^2). Measuring the samples in this way assured that the surface would be free from polishing stress, impurities, and native nickel oxides or hydroxides. The optical constant spectra derived from the ellipsometer measurements were compared to established spectra to maintain the consistency of the sample preparation method. The optical constant spectra of properly prepared samples were quite reproducible. Further details of the substrate optical properties are discussed in chapter 4 of this document.

Figure 2.2: Automatic, self-nulling, spectroscopic ellipsometer. The components, left to right: photomultiplier detector, analyser telescope/prism assembly, analyser Faraday cell, sample cell, achromatic compensator, polarizer Faraday cell, polarizer telescope/prism assembly, scanning monochromator, and xenon arc lamp. CBB 923-2187

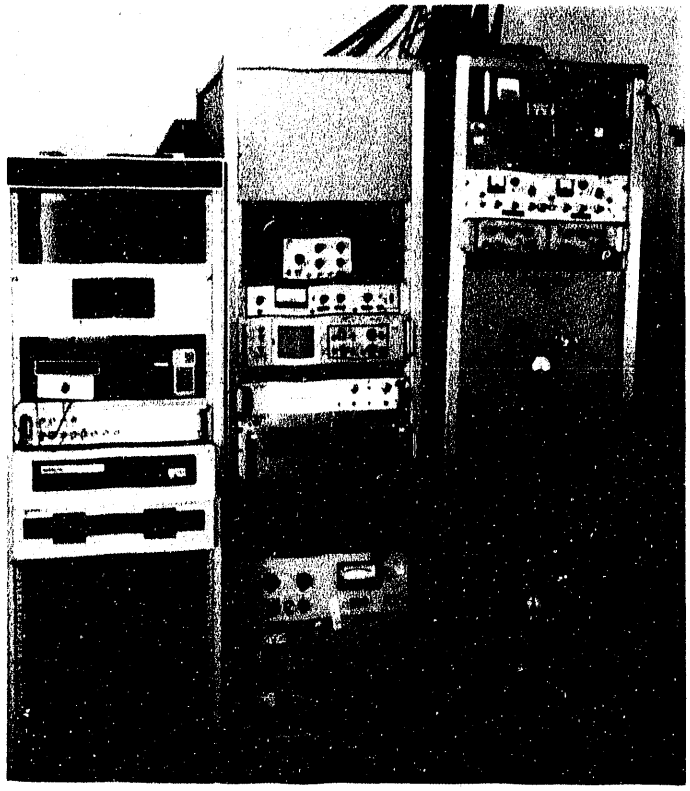

Figure 2.3: Electronic components for the automatic, self-nulling, spectroscopic ellipsometer. Leftmost rack: Prism azimuth encoder interface, LSI 11/73 computer. Middle rack: Ancillary equipment, stereo AC amplifier. Rightmost rack: High-voltage power supply, Faraday cell controller, Differential amplifier, Polarizer Faraday cell DC power supply, Stepper motor driver, Analyzer Faraday cell DC power supply. CBB 923-2185

Pure film samples of nickel hydroxide and nickel oxy-hydroxide were produced from anodic films on nickel metal samples. Nickel hydroxide films were grown by anodizing pure nickel substrates in 1.0 molar aqueous sodium hydroxide at potentials between –0.250 and 0.250 Volts versus the Hg/HgO reference electrode. This method produces films having thicknesses between 50 and 80 Angstroms. Care was taken to obtain measurements below the potential of conversion to nickel oxy-hydroxide (450 millivolts). Subsequently, we found that the films could be completely reduced from nickel oxy-hydroxide to nickel hydroxide. The film thickness increased to a limit of 130 Angstroms from repeated charge and discharge cycling. Nickel oxy-hydroxide films were formed by the anodic oxidation of nickel hydroxide films. This is accomplished by applying potentials greater than 600 millivolts for at least 30 seconds. The potential was reduced to 500 millivolts to stop oxygen gas evolution while maintaining the film in its oxidized form before making the ellipsometer measurements.

By maintaining the samples at a reducing potential (–0.250 Volts) for several minutes, the films were converted to nickel hydroxide. Applying a potential of 0.600 Volts, an oxidizing potential greater than the equilibrium potential of the nickel hydroxide/nickel oxy-hydroxide couple, for several minutes and waiting for the ellipsometer measurements to stabilize, the films were converted to nickel oxy-hydroxide. The charge required for reduction was measured to confirm that complete conversion had occurred. Films of varying thickness were made by cycling the films rapidly between charged and discharged states prior to fully converting them. The film thickness increases with cycling. Film samples having thicknesses between 50 and 120 Å were made.

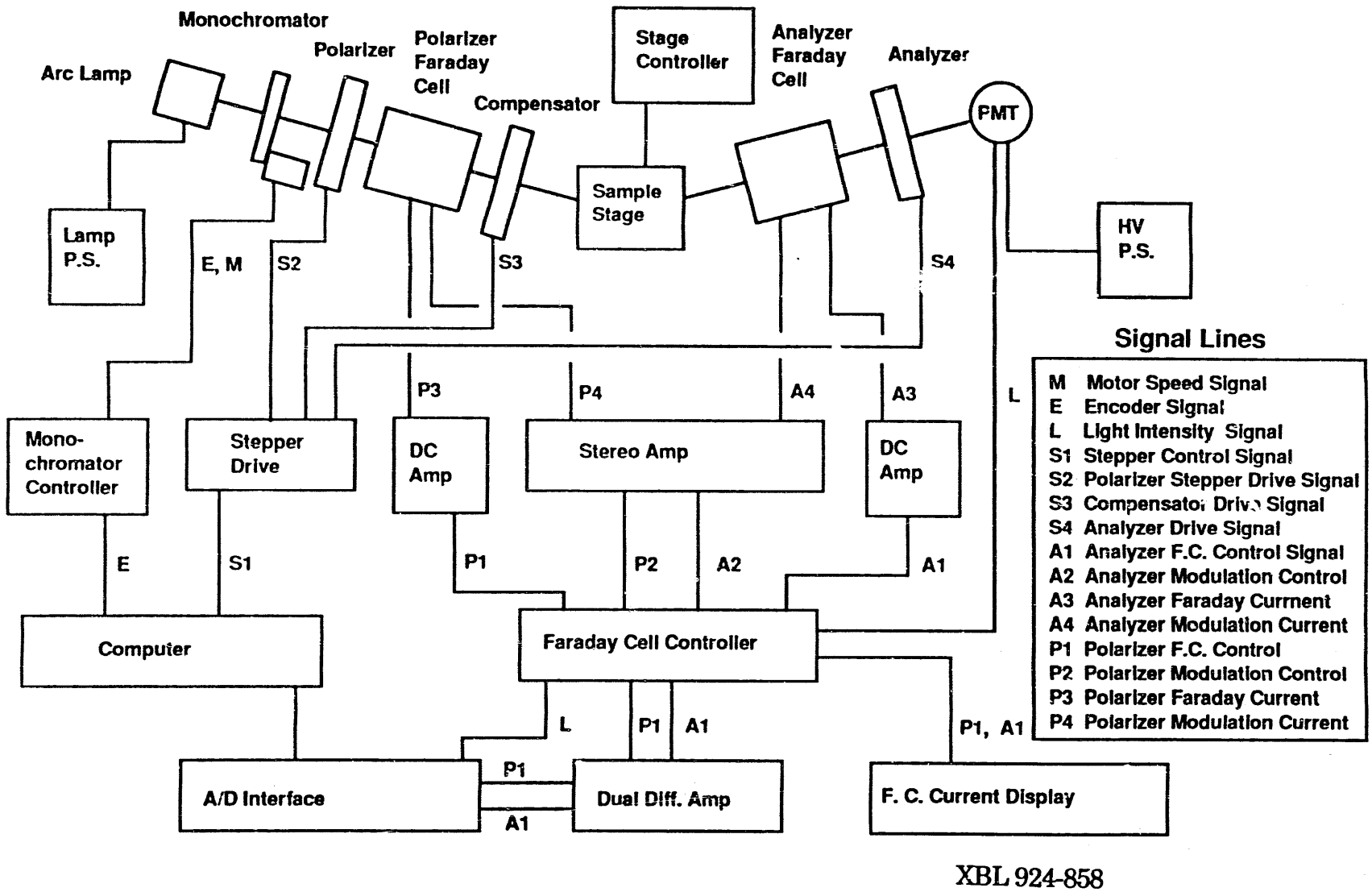

Figure 2.3: Automatic, Self-Nulling, Spectroscopic Ellipsomer system schematic.

2-4 Scanning Tunneling Microscopy (STM)

Scanning tunneling microscopy (STM) experiments were conducted on nickel hydroxide electrode films. The electrode films were formed on 99.9% pure polycrystalline nickel sheet samples. The electrode dimensions were approximately 1.5 centimeters square. The nickel substrates were etched in 1.0 molar aqueous sulfuric acid to remove the native oxide film. Nickel hydroxide films were formed *in-situ* in a 1 milliliter droplet of 1.0 molar potassium hydroxide electrolyte. The potentiostat controlled the potential on the nickel hydroxide working electrode versus a platinum wire counter electrode. A two-electrode cell arrangement was used, since precise potential measurements were unnecessary. The electrolyte was withdrawn prior to imaging the charged nickel oxy-hydroxide films in air. This step was an effort to prevent the possible reduction of the nickel oxy-hydroxide overlayer, if it was present, by the oxygen evolution self-discharge reaction. The electrolyte was withdrawn by pipette, with no effort to dehydrate the film.

A Digital Instruments Nanoscope™ I instrument was interfaced to an AST™ 286 computer for data collection. Data were collected in the constant tunneling current mode as a 200 x 320 array of height versus lateral position. The tunneling current setpoint was 2.5 nanoamperes. Tips were made from 0.010 inch platinum wire, sharpened by acute scission.

In our experiments, the STM measurements were made of the bare nickel metal substrate after the etch step using 90 millivolts of bias on the tip. Measurements were made at several points on the surface to ensure representation of aggregate behavior rather than local phenomena. A film of nickel hydroxide was formed on the electrode by cycling it between ± 1 Volt in 1.0 molar aqueous sodium hydroxide. This film could not be imaged using tip biases up to 10 Volts. The film was then oxidized to nickel oxy-hydroxide, evident by the

film coloration. The electrolyte was removed as the electrode was held at 800 millivolts versus the platinum counter electrode. This film was measured using a tip bias of 420 millivolts. The film was then reduced to nickel hydroxide and dissolved in distilled water. The substrate was measured again at 90 millivolts tip bias. These measurements were to check for substrate roughening.

Images were formed from the height data array. The images were produced using an algorithm that simulates diffuse reflectance from normal illumination. These images and other results of STM are presented in chapter 3 of this document.

Chapter 3

Scanning Tunneling Microscopy (STM)

3-1 Scanning Tunneling Microscopy (STM)

Scanning tunneling microscopy (STM) experiments were conducted on nickel hydroxide electrode films. The electrode films were formed on 99.9% pure polycrystalline nickel sheet samples. The nickel substrates were etched in 1.0 molar aqueous sulfuric acid to remove the native oxide film as determined by optical measurements. Nickel hydroxide films were formed *in-situ* in a 1 milliliter droplet of 1.0 molar potassium hydroxide electrolyte. The potentials were measured on the nickel hydroxide working electrode versus a platinum wire counter electrode. The electrolyte was withdrawn prior to imaging the charged nickel oxy-hydroxide films in air. This step was an effort to prevent the possible reduction of the nickel oxy-hydroxide overlayer, if it was present, by the oxygen evolution self discharge reaction. The electrolyte was withdrawn by pipette, with no effort to dehydrate the film.

In our experiments, the STM measurements were made of the bare nickel metal substrate after the etch step using 90 millivolts of bias on the tip in the constant tunneling current mode. The tunneling current setpoint was 2.5 nanoamperes for all of our experiments. Measurements were made at several points on the surface to ensure representation of aggregate behavior rather than local phenomena. A film of

nickel hydroxide was formed on the electrode by cycling the electrode between the nickel hydroxide and oxy-hydroxide states twice between ± 1.0 Volt in 1.0 molar aqueous sodium hydroxide. This film could not be imaged, because no significant tunneling currents could be achieved using tip biases up to 10 Volts.

The film was oxidized to nickel oxy-hydroxide, and the electrolyte removed as the electrode was held at 800 millivolts versus the platinum counter electrode. The presence of the nickel oxy-hydroxide phase was indicated by the observed film coloration. This film was measured using a tip bias of 420 millivolts to achieve the 2.5 nanoampere tunneling current setpoint. The film was then electrochemically reduced to nickel hydroxide by applying –1.0 volts and dissolved in distilled water. The substrate was measured again at 90 millivolts tip bias to check for substrate roughening.

Images were formed from the height data array, z_{ij}, using an algorithm that simulates diffuse reflectance from normal illumination.[1] In this algorithm, the simulated intensity, I, is proportional to the square of the cosine of the angle, θ, between the local surface normal and illumination direction, in our case, the global surface normal. Equation [1] is the kernel that was applied to the array of height data. The effect of the algorithm is to shade sloped areas and brighten flat areas. We have found these images to be more analogous to human vision than images based on coding grayscales directly to height data.

$$I_{i,j} = I_{max} \cos^2 \theta \cong \frac{4 I_{max}}{1 + (z_{i,j+1} - z_{i,j-1})^2 + (z_{i+1,j} - z_{i-1,j})^2} \qquad [1]$$

---

1 M.J. Armstrong, *The Role of Inhibitors During Electrodeposition of Thin Metallic Films*, Ph.D. Thesis, Univ. of California, .Berkeley, Lawrence Berkeley Lab, LBL-28972 (1990)

3-2 STM Images and Interpretation

Prior to growing the nickel hydroxide film, the nickel metal substrate was examined to characterize the topography underlying the film. These measurements are presented as simulated diffuse reflectance images in figures 3.1-3.4. These measurements were made at four different positions approximately 8000 Angstroms apart. Though the sample appeared optically bright, there is substantial topography at the 100 Angstrom scale. This topography takes the form of ranges of rounded mountain ridges.

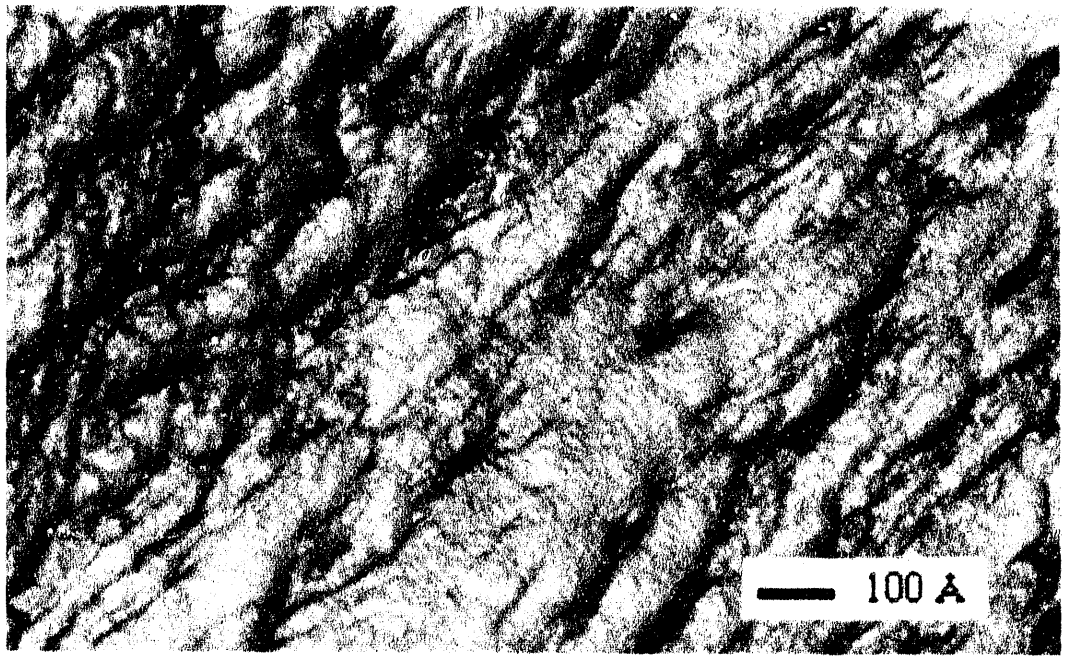

Figure 3.1: STM image of nickel metal substrate in air at one of several locations. Sample was prepared by polishing and etching. XBB 908-6847

Figure 3.2: STM image of nickel metal substrate in air. Same scale as figure 3.1, different location. XBB 908-6852

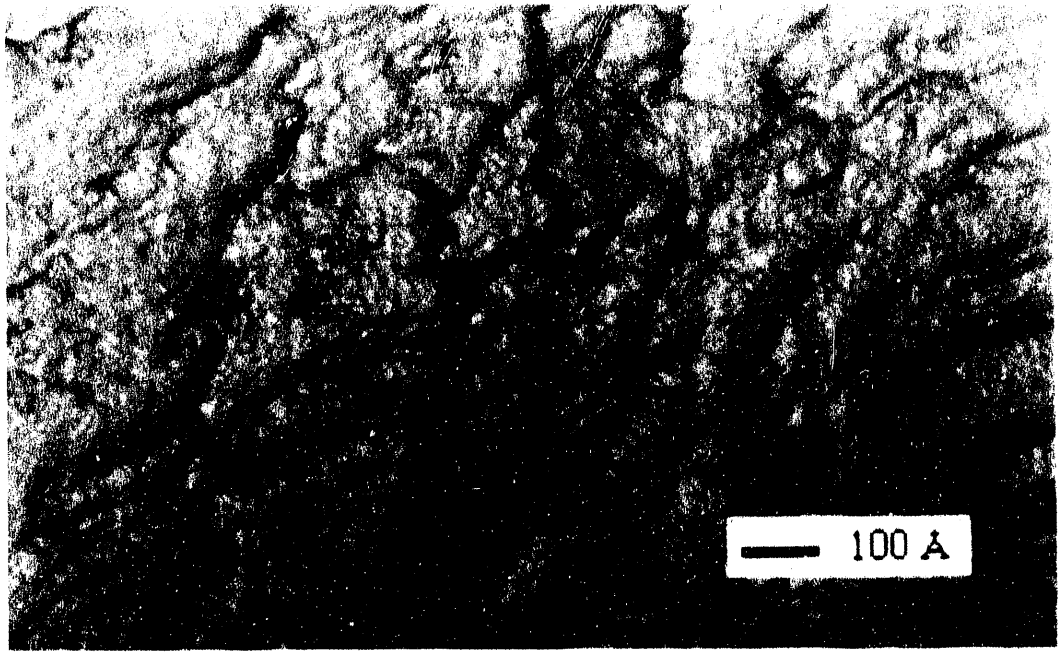

Figure 3.3: STM image of nickel metal substrate in air. Same as figure 3.1, different location. XBB 908-6850

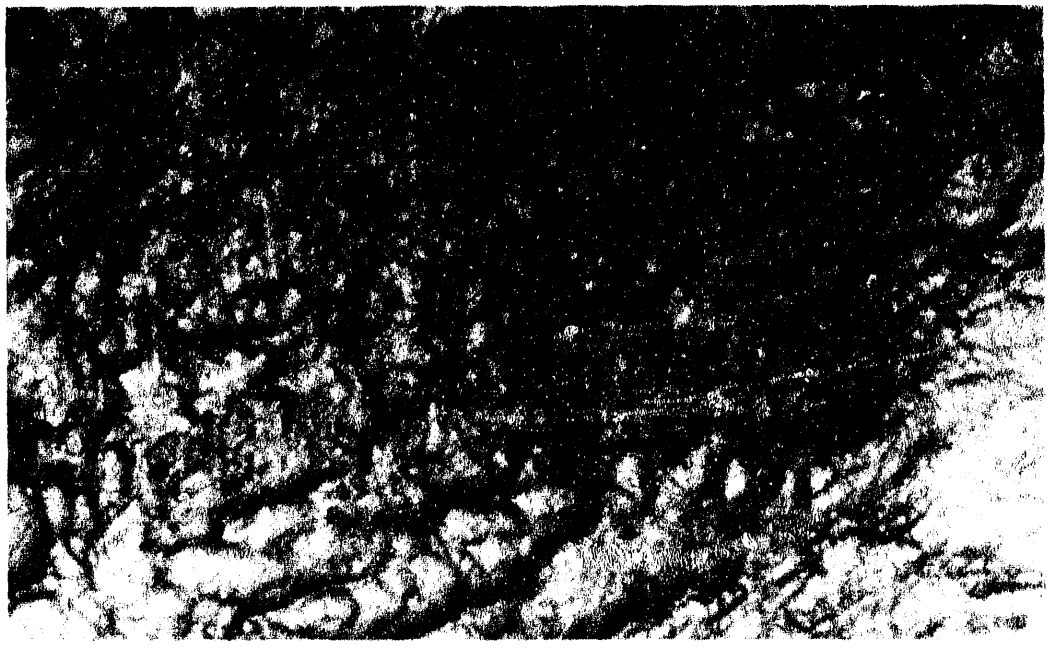

Figure 3.4: STM image of nickel metal substrate in air. Same as figure 3.1, different location. XBB 908-6851

The images of the oxidized electrode film were quite different, however. After forming a thick nickel hydroxide film, estimated to be 120 Angstroms in thickness, it was oxidized to convert the film to nickel oxy-hydroxide to the greatest extent possible by applying 1.0 Volts for one minute. The electrolyte was removed at 800 millivolts versus the platinum counter electrode. The electrode film were imaged wet, in the ambient air. Images of four different locations on the surface are presented in figures 3.5 through 3.9 .

The topography of the oxidized films is substantially different from that of the substrate. The surface appears to be strewn with round nodules 30 to 50 Angstroms in diameter with an average separation of 50 to 80 Angstroms. The number density of the nodules is of the order of 10^{12} per square centimeter.

It is important to note that the STM does not give an exact geometric measurement of the surface. The height measurement is the vertical displacement of the tip required to maintain the tunneling current between the surface and tip at the given current setpoint. The topography seen in the images is a convolution of the local work function and the geometry. It is only equivalent to the geometric surface in the limiting case of a homogeneous equipotential surface. This condition is probably met for the nickel metal substrates. However, in the film measurements, the images are affected by local variations in the work function and film resistance of the nickel hydroxide/nickel oxy-hydroxide/nickel metal film structure, in addition to local height differences. There is no reason, *a priori,* to assume that the film surfaces are equipotential.

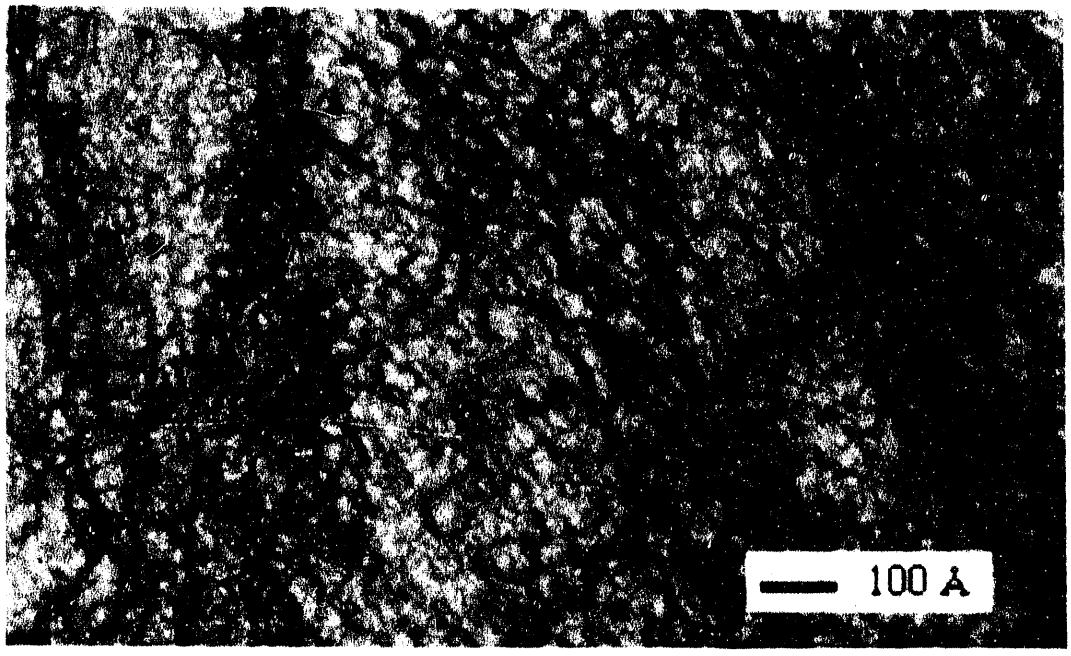

Figure 3.5: STM image of nickel oxy-hydroxide nodules within an oxidized nickel hydroxide film electrode on nickel metal substrate . The nodules are 30–50 Å in diameter. The number density is approximately 10^{12} nodules/cm^2. This image is one of several locations. XBB 908-6846

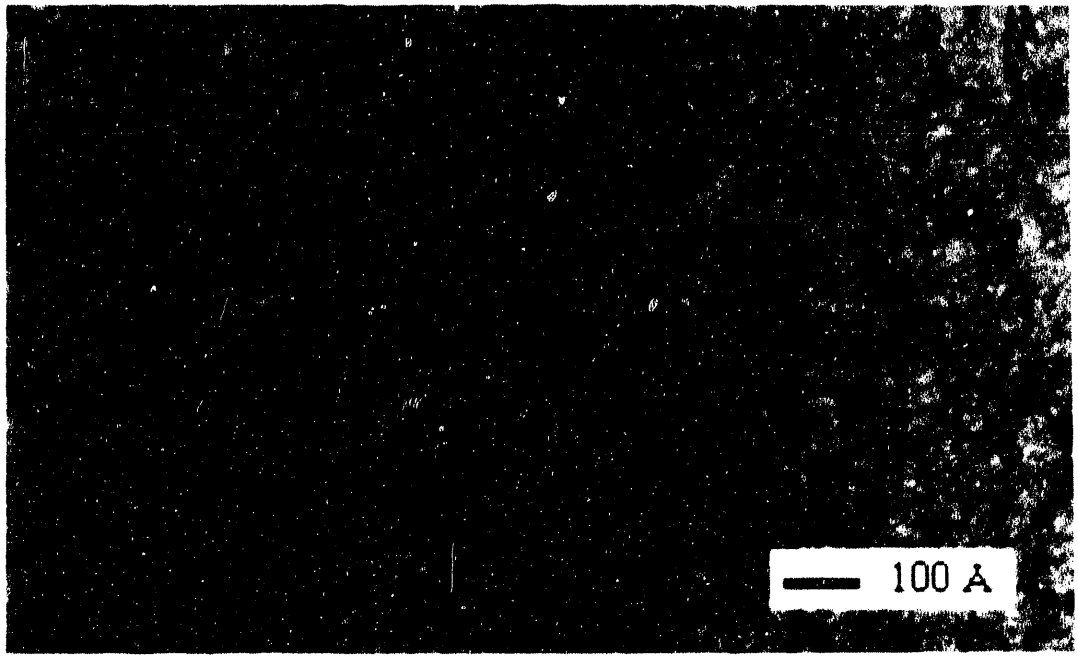

Figure 3.6: STM image of nickel oxy-hydroxide nodules within an oxidized nickel hydroxide film electrode on nickel metal substrate . Same as figure 3.5, different location. XBB 908-6853

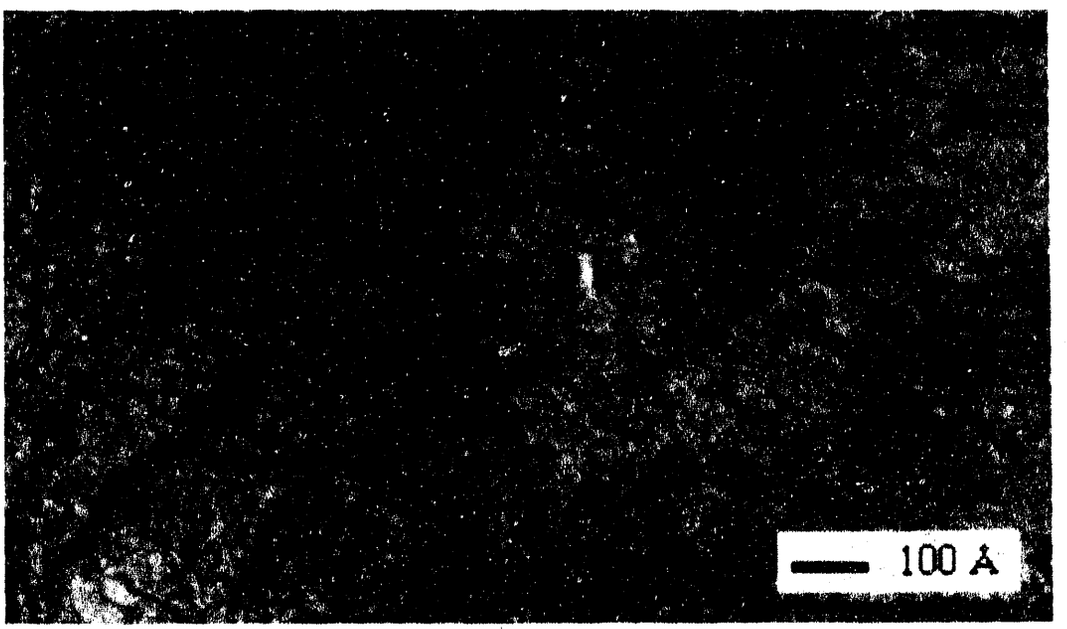

Figure 3.7: STM image of nickel oxy-hydroxide nodules within an oxidized nickel hydroxide film electrode on nickel metal substrate . Same as figure 3.5, different location. XBB 908-6849

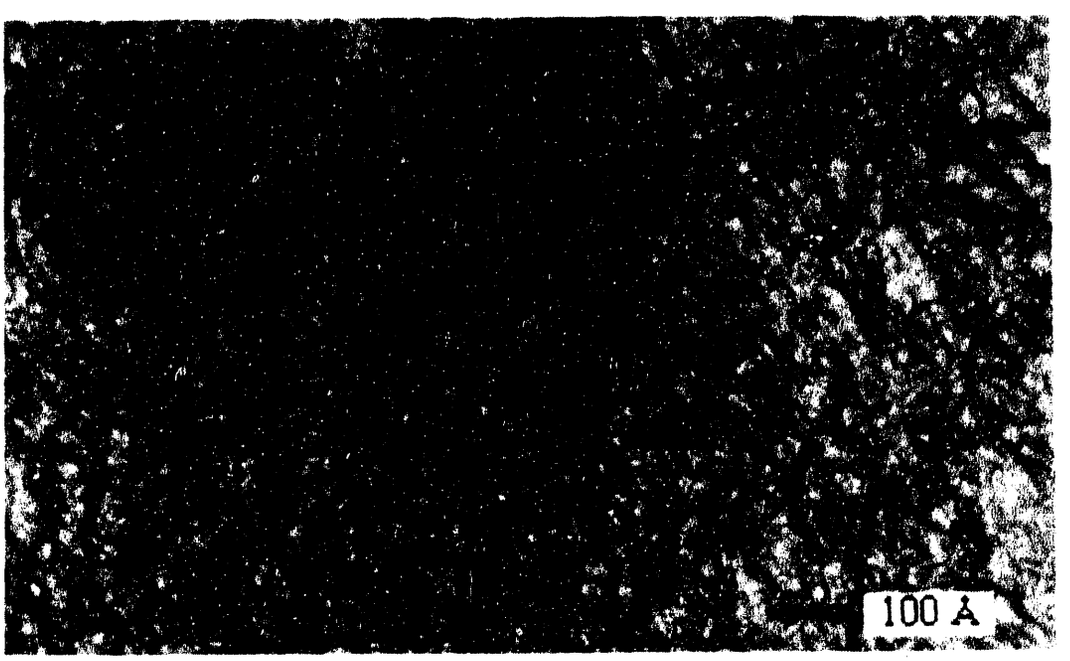

Figure 3.8: STM image of nickel oxy-hydroxide nodules within an oxidized nickel hydroxide film electrode on nickel metal substrate . Same as figure 3.5, different location. XBB 908-6848

In our interpretation of the STM images of the oxidized film electrode, we have considered several factors. One of the main factors affecting the tunneling currents is the electronic conductivity of the materials. Nickel metal has the highest electronic conductivity of the materials and was readily imaged. Nickel oxy-hydroxide, a semiconductor, has a substantial electronic conductivity which, however, is considerably lower than that of the metal. One would therefore reasonably expect to be able to image pure nickel oxy-hydroxide. Nickel hydroxide, however, is principally a dielectric material, having a large band-gap[2] (about 3.7eV). Its primary conduction mechanism is ionic migration. This ionic conductivity facilitates the electrochemical reaction between the two film species. However, electronic tunneling currents should be blocked.

STM has been used successfully in aqueous ambient environments because water molecules are not detected by the technique. The tunneling distances from tip to sample are approximately 10 to 30 Angstroms. In our experiments, we were not able to produce images in the presence of the nickel hydroxide films in the reduced form, despite application of substantial tip biases (±10 Volts). This problem is attributable to two causes. First, the surface of the film was not imaged because the dielectric nature of the films caused most of the bias to be applied across the 120 Angstrom film thickness, leaving the film/electrolyte interface at a potential near the tip potential. Secondly, though the tip bias was applied across the film, the film thicknesses were such that the electric field strength was too low to allow significant tunneling through the film. Thus, the metal substrate was not imaged through the film. The result of these two effects was tip crashes into the film.

There are two circumstances under which STM measurements would produce the observed images. The first is if the observed nodules were nickel oxy-hydroxide

---

2 M.K. Carpenter, D.A. Corrigan, J. Electrochem. Soc. **136**, 1022 (1989)

and the tunneling distances through the surrounding nickel hydroxide to the adjacent nodules were small enough to permit finite tunneling currents at every point on the surface. The second circumstance would be if there was a thin uniform overlayer across the film surface covering a layer of nickel oxy-hydroxide nodules. In this case, the variations in resistance between a given point on the film surface and the substrate would cause differences in the potential required to achieve the current setpoint. The resistance would be lowest directly over a nodule and highest between nodules. In the constant current STM mode, these resistance differences would be manifested as variations in the tip height. Both of these interpretations suggest the presence of a nodular structure for the nickel oxy-hydroxide in the electrode film in its charged state.

As a verification measure, after reducing the nickel oxy-hydroxide to nickel hydroxide, the films were dissolved in distilled water and the nickel metal substrates were examined once again. This experiment was conducted to determine whether the nodular structures that were observed were the result of roughening of the metal substrate. If the nodules were metallic nickel, they would not have been dissolved in distilled water. The images in figures 3.9-3.12, representing four locations on the substrate, show that the nodular structure is not present and that the metal substrate is comparable to the starting material. In fact, there seems to be a leveling effect from oxidizing the surface and dissolving the oxide away. Thus, the nodules are most likely composed of the nickel oxy-hydroxide species.

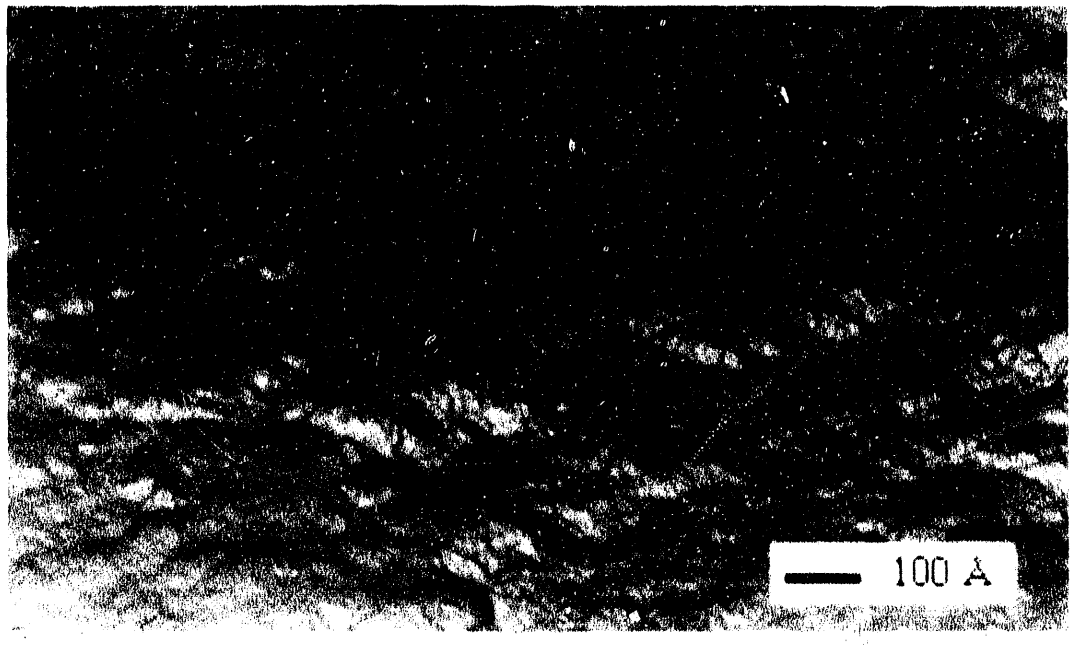

Figure 3.9: STM image of nickel metal substrate after dissolving nickel hydroxide film. One of several locations. XBB 908-6856

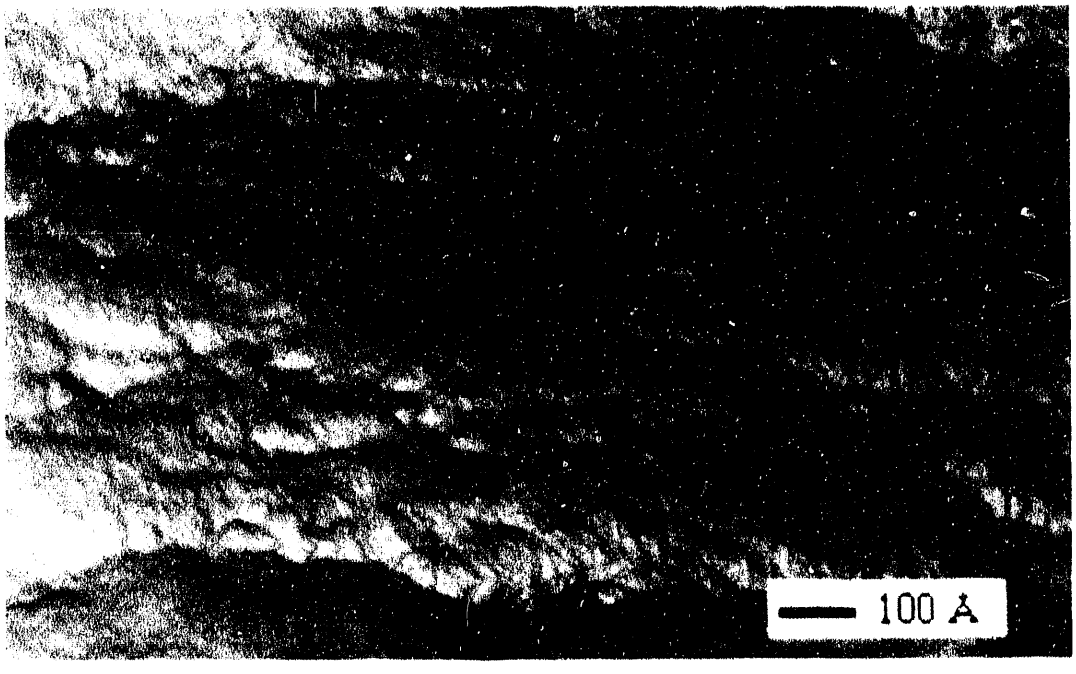

Figure 3.10: STM image of nickel metal substrate after dissolving nickel hydroxide film. Same as 3.9, different location. XBB 908-6845

Figure 3.11: STM image of nickel metal su
film. Same as 3.9, different location. XBB 9

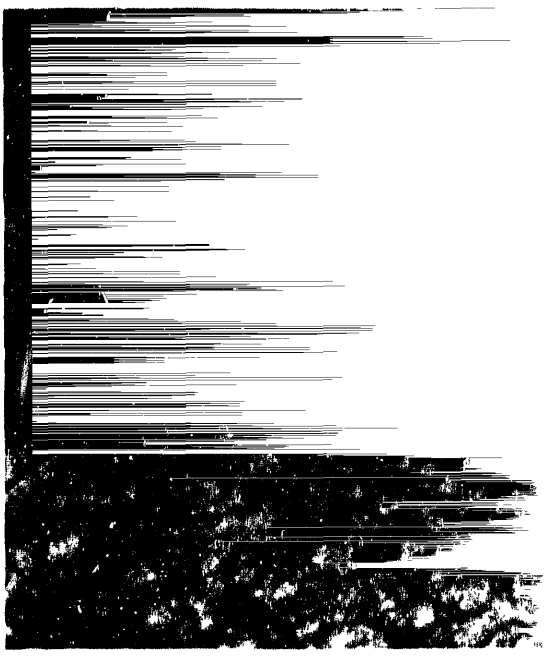

Figure 3.12: STM image of nickel metal s
film. Same as 3.9, different location. XBB

Chapter 4
Spectroscopic Ellipsometry

4-1 Introduction

The distinct difference in optical constants between the nickel hydroxide and the nickel oxy-hydroxide species facilitates the use of optical techniques in the study of the electrode structural transformation. Since the structures we are examining in this research exist in very thin films, spectroscopic ellipsometry is an appropriate tool to use. The ellipsometer is an instrument that measures the change in the state of polarization of a beam of light caused by the reflection from a sample surface. These polarization changes are extremely sensitive to the optical constants and structure of the sample surfaces. It is appropriate at this point to review the principles behind this technique. More complete references to ellipsometry and polarized light include the text by Azzam and Bashara[1] and the review articles by Muller[2,3]

The polarization of light refers to a specific orientation of the electric and magnetic fields. Most people are familiar with the polarization effects exhibited by dichroic polarizing sheets such as those used in sunglasses. The extinction of the beam through crossed polarizers is characteristic of linearly polarized light. Assigning coordinates to the plane normal to the propagation vector, linearly polarized light is characterized by a single azimuth parameter indicating the direction of the electric field vector. The electric field vector can then be decomposed into two orthogonal components. The ratio of the amplitudes of the two components is equal to the tangent of the azimuth angle.

Specular reflection from a surface provides a natural coordinate system for polarized light, defined by the plane of incidence. The plane of incidence is the plane that contains both the incident and the reflected beams. This paradigm is illustrated in figure 4.1a. The plane of incidence is used as a zero reference for measuring polarization azimuths.

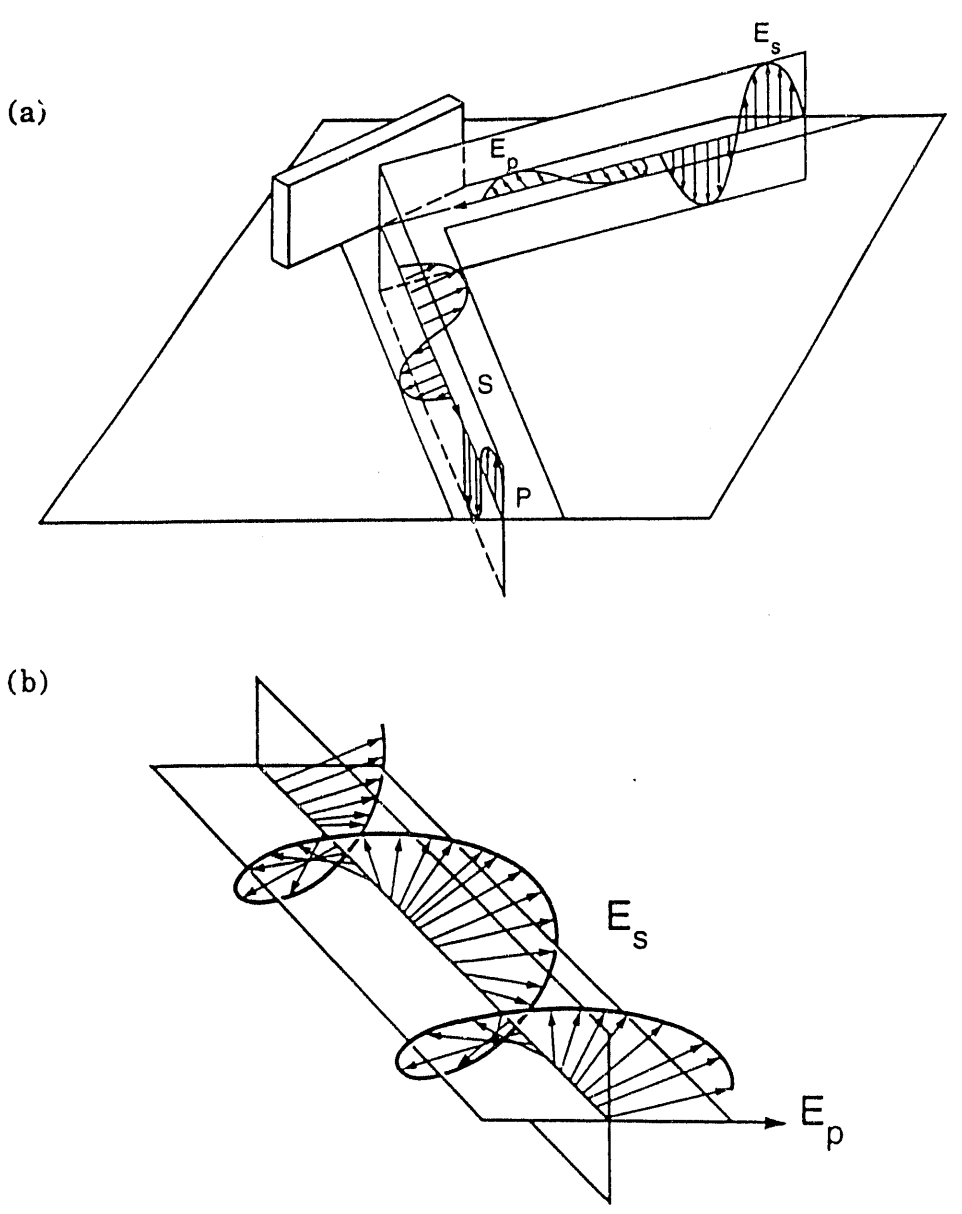

Figure 1: (a) Coordinates defined by plane of incidence. (b) Elliptically polarized light. Figures from Muller (ref.2) XBL 8511-11465, XBL 8511-11459

In general, polarized light is characterized by not one, but two parameters, the relative amplitude and the relative phase between the two components parallel and perpendicular to the plane of incidence. In ellipsometry, these two parameters are defined as psi, the arc tangent of the relative amplitude, and delta,

the relative phase angle, between the electric field components parallel(p) and perpendicular(s) to the plane of incidence. Linear polarization corresponds to the special case of delta equal to zero. Non-zero values of delta refer to elliptically polarized light. In this case, the tip of the electric field vector traces an ellipse as a function of time or an elliptic helix as a function of distance along the propagation direction illustrated in figure 4.1b, hence the name, ellipsometry.

4-2 Optical Modeling

The interpretation of ellipsometer measurements generally requires the construction of optical models and fitting them to experimental measurements. Optical models are constructed using classical electromagnetic theories including those of Fresnel, Drude, and Maxwell.[1-4] In monochromatic ellipsometry, the two parameters, delta, and psi, are measured at a single wavelength and angle of incidence. These may be used to determine at most two film parameters, such as thickness or complex refractive index. In general, measurements at different incident angles or wavelengths are required to determine more than two unknown film parameters. In addition, spectroscopic ellipsometry may be used to measure the optical constant spectrum of the sample material, if the film structure is known.

Since film structure is independent of the wavelength of the probe beam, spectroscopic ellipsometry is particularly useful for testing film structure hypotheses. To model the structure of the nickel hydroxide electrode in the present study, optical constant spectra were determined for the pure materials involved: metallic nickel, nickel hydroxide, nickel oxy-hydroxide, and the electrolyte solutions.

Optical model calculations are used to predict ellipsometer spectra. The ellipsometer parameters, delta and psi, are related to the ratio of the overall complex reflection coefficients, $r_{p,eff}$ and $r_{s,eff}$, for the p and s components of the

polarized light according to the ellipsometry equation [1].

$$\rho = \frac{r_{p.eff}}{r_{s.eff}} = \tan(\Psi)\exp(\hat{i}\Delta) \qquad [1]$$

The overall complex reflection coefficients of the film structure are calculated working from the substrate up to the ambient medium. The Fresnel reflection coefficients for each optical interface between media are calculated through equations [2] and [3]. Snell's law, equation [4], is used to calculate the angle of incidence in each medium. The Drude equation, [5]–[6], for thin film reflection, is used iteratively to calculate effective s and p reflection coefficients for each pair of optical interfaces.

$$r_{p12} = \frac{n_2 \cos(\hat{\theta}_1) - n_1 \cos(\hat{\theta}_2)}{n_2 \cos(\hat{\theta}_1) + n_1 \cos(\hat{\theta}_2)} \qquad [2]$$

$$r_{s12} = \frac{n_1 \cos(\hat{\theta}_1) - n_2 \cos(\hat{\theta}_2)}{n_1 \cos(\hat{\theta}_1) + n_2 \cos(\hat{\theta}_2)} \qquad [3]$$

$$n_0 \sin(\hat{\theta}_0) = n_1 \sin(\hat{\theta}_1) \qquad [4]$$

$$r_{v012} = \frac{r_{v01} + r_{v12} e^{\hat{i} D}}{1 + r_{v01} r_{v12} e^{\hat{i} D}}, \text{ where } (v = s, p) \qquad [5]$$

$$D = \frac{4\pi t}{\lambda} \hat{n}_1 \cos(\hat{\theta}_1) \qquad [6]$$

For absorbing media, the angle of refraction is represented by a complex number. Though the intuitive physical nature of such an angle is lost by adopting the complex representation, the extension of the modeling equations from the non-absorbing, real, case to the complex absorbing case is simplified. In this study, the

materials were assumed to be isotropic; anisotropic film modeling requires a tensor representation of the optical constants.

For example, in a dual film structure illustrated in figure 4.2, the Fresnel reflection coefficients of the substrate/film 2 (r_{23}) and film 1/film 2 (r_{12}) interfaces are used to calculate the Drude reflection coefficients, $r_{p,123}$, $r_{s,123}$. These results are combined with the Fresnel coefficients of the ambient/film 1 interface (r_{01}), in a second application of the Drude equation, to produce overall reflection coefficients, $r_{p,eff}$ and $r_{s,eff}$, for the structure. These overall complex reflection coefficients for p and s polarized light are then used in the ellipsometry equation, [1], to calculate predicted values of delta and psi.

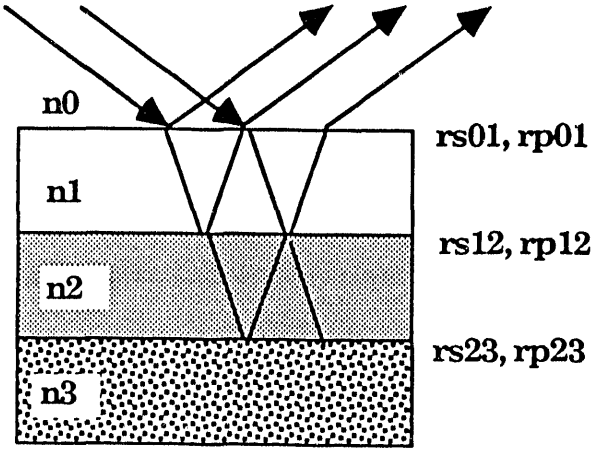

Figure 4.2: Dual film structure example with Fresnel reflection coefficients indicated for each interface, and complex refractive indices for each medium.

The unknown parameters in the model are fitted using a non-linear optimization routine to minimize the error between the measured, D_i^m and Ψ_i^m, and predicted values, D_i and Ψ_i. A chi-square error function, equation [7], is used to properly weight the errors by the measurement uncertainties, $\delta\Delta$ and $\delta\Psi$.

$$\chi^2 = \left[\frac{1}{2N} \sum_{i=1}^{N} \left[\left(\frac{\Delta_i^m - \Delta_i}{\delta\Delta} \right)^2 + \left(\frac{\Psi_i^m - \Psi_i}{\delta\Psi} \right)^2 \right] \right]^{1/2} \qquad [7]$$

4-2 Optical Constant Spectra of Bare Nickel Substrates

The nickel metal substrates, on which the nickel hydroxide electrode films were formed, were characterized to establish a consistent set of optical constants. To characterize the substrates, spectroscopic ellipsometer measurements were made of the samples in 1.0 molar aqueous sulfuric acid electrolyte while being held at a 5 microamperes per square centimeter cathodic current to protect the surface. These conditions ensured that the nickel was free from oxide surface layers. Typical ellipsometer spectra for delta and psi are shown in figure 4.3.

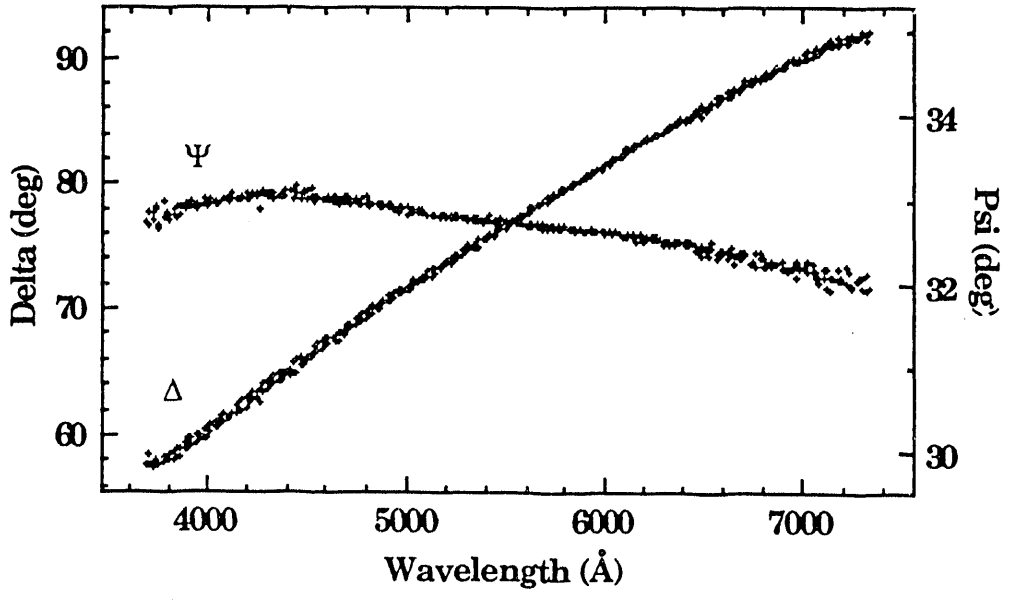

Figure 4.3: Ellipsometer spectra of bare nickel single crystal (111) surface in 1.0 M aqueous H_2SO_4. XBL 924-859

$$\hat{n}_s = \hat{n}_0 \sin\phi \left[1 + \left(\frac{\hat{\rho} - 1}{\hat{\rho} + 1} \right)^2 \tan^2 \phi \right]^{1/2} \qquad [8]$$

$$\hat{\rho} = \tan\Psi \exp^{\hat{i}\Delta} \qquad [9]$$

The complex refractive index spectra, $\hat{n}_s(\lambda)$, of the nickel substrate samples were derived from the ellipsometer spectra using equation [8] from Azzam[1]. The optical constant spectra determined by ellipsometry agree reasonably well with those found in the literature[5], as shown in figure 4.4. The spectra in figure 4.4 are averages of spectra from fifteen measured samples. The deviation in the blue region of the spectrum was quite consistent in our measurements and probably reflects differences between reflection and transmission measurement techniques. The uncertainties of the measured optical properties were 0.05 for the real refractive index and 0.08 for the extinction coefficient. Four-zone ellipsometer measurements were used to reduce instrumental inaccuracies caused by prism azimuth misalignment[2]. The optical constant spectra were used as an indicator of the quality of the sample preparation. Only samples having optical constant spectra consistent with the established values were used in the subsequent optical experiments.

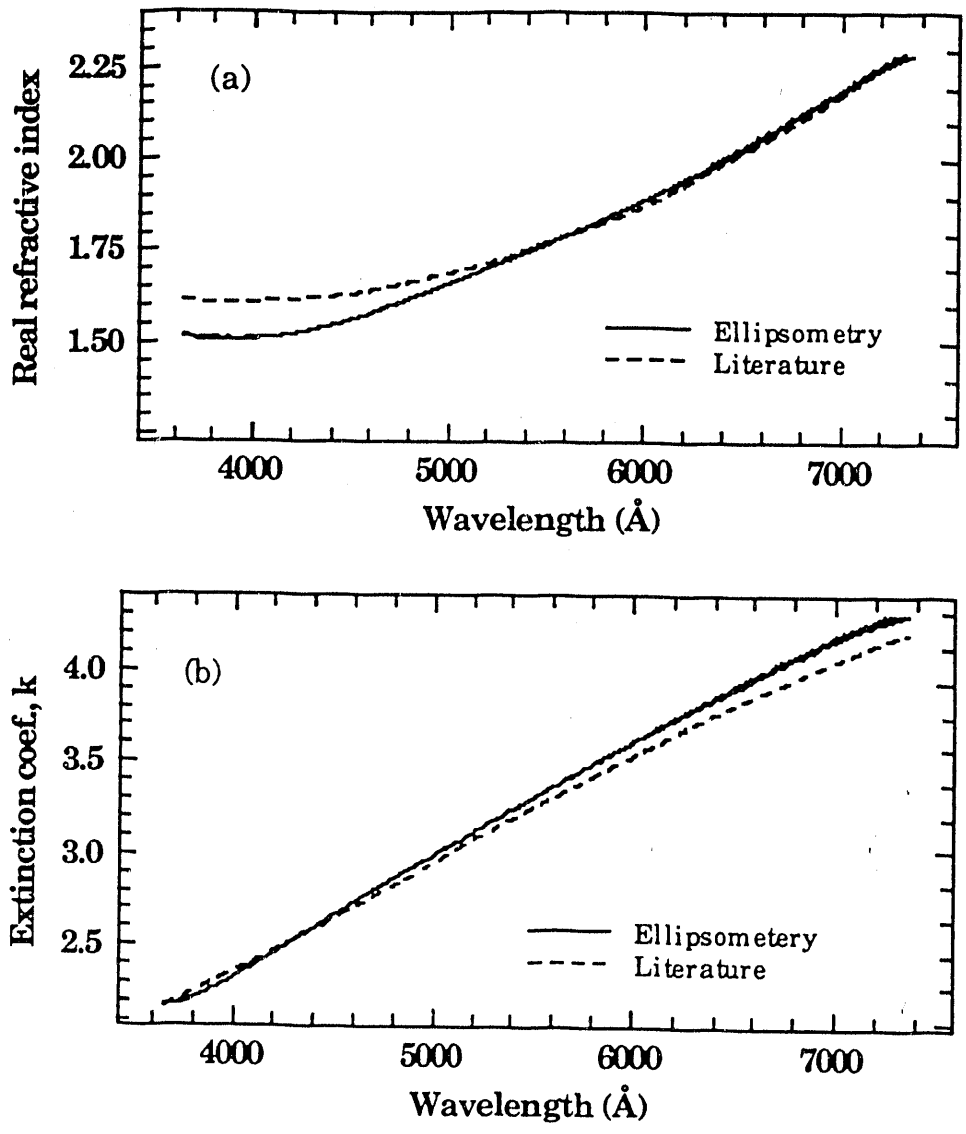

Figure 4.4: Optical constant spectra of nickel metal substrates determined by spectroscopic ellipsometry. The real index of refraction, (a), and the extinction coefficient, (b), are compared to values from the literature. (ref. 5) The uncertainties of the measured optical properties were 0.05 for n and 0.08 for k. XBL 924-860/1

4-3 Optical Properties of Nickel Hydroxide Film Materials

In order to develop optical models of the structures of the nickel hydroxide film electrode, we required the optical constant spectra of the pure film materials. These optical constant spectra were determined from *in-situ* spectroscopic

ellipsometry using film materials created electrochemically. Nickel hydroxide films were grown by anodizing pure nickel substrates in 1.0 molar aqueous sodium hydroxide. This method produces films having thicknesses between 50 and 150 Angstroms. Care was taken to obtain measurements below the potential of conversion to nickel oxy-hydroxide (480 millivolts versus the Hg/HgO reference electrode). Subsequently, we found that the films could be completely reduced from nickel oxy-hydroxide to nickel hydroxide. Nickel oxy-hydroxide films were formed by the anodic oxidation of nickel hydroxide films. This oxidation is accomplished by applying potentials greater than 600 millivolts for at least 30 seconds. The potential was reduced to 500 millivolts to stop oxygen gas evolution while maintaining the film in its oxidized form before making the ellipsometer measurements.

The derivation of optical constant spectra of films from spectroscopic ellipsometry is a difficult task. In theory, the task is straight forward. The unknown parameters are the real and imaginary components of the complex refractive index at each spectral point, and the thickness of each film. For this analysis, the films are assumed to be isotropic and to be of uniform thickness. The ellipsometer measures two parameters, the relative phase shift, delta, and amplitude, psi, between the components of the polarized light, parallel and normal to the plane of incidence. If the film thickness were independently known, the problem would be uniquely determined. Independently measuring the film thickness *in-situ* is difficult, as the best non-optical methods are ultra-high vacuum techniques such as depth profiling Auger electron spectroscopy. Ellipsometry, however, is one of the best methods of determining film thickness. Fortunately, there is a good solution for both the optical constants and the film thickness.

To determine the optical constant spectrum and the thickness of a thin film,

one must make measurements of more than one film of the material of interest. For the single film problem with N spectral points, there are 2N+1 unknowns and only 2N measurements. However, if one has M films, where M is greater than one, of the same material with unknown, but different thicknesses, then there are 2NM measurements and only 2N+M unknowns. The problem is then well over-determined and error estimates can be obtained for the fitted parameters, *at least in theory*.

The optical constant spectra of the pure film materials were determined numerically using the principle summarized in the preceding paragraphs. The optical constant spectrum of the nickel metal substrates determined in the previous section were used in the calculations of the film optical constant spectra. To circumvent the difficulty of fitting a large number of unknown spectral refractive index values for the film materials, the numerical algorithm uses a cubic spline approximation to the full complex optical constant spectrum. Since the optical constant spectra of the film materials are relatively smooth and slowly varying, it was well fitted by a small number of spline knots. Judicious positioning of the spline knots ensured that all of the broad spectral features were included. This algorithm is given as a FORTRAN program entitled MFITRI in appendix C.

The film thickness results and fitting errors from the determinations are summarized in tables 4.1 and 4.2 for the nickel hydroxide and oxy-hydroxide materials, respectively. The optical constant spectra for the film materials are presented in figure 4.12. Figures 4.5 through 4.11 show the ellipsometer spectra from which the optical constant spectra were determined and the spectra predicted by the fitting procedure.

The uncertainties of the results of the fitting process were determined by analyzing the sensitivity of the chi-square parameter to variations of the fitted parameters. The fits were most sensitive to variations of the film thickness. For

the nickel hydroxide film measurements, 5 angstrom variations in any one of the film thickness were enough to cause shifts in the global chi-square value of order unity, which represents shifts on the order of the precision of the measurements. Such sensitivity indicates that the uncertainties of film thickness parameters are small. This is because the film thickness affects each of the 400 predicted values of delta and psi for a single film. The roughness of the film is probably much greater than the uncertainty in thickness.

The fitting sensivity to the values of the optical constant spectrum spline points was not as great as that of the film thicknesses. To produce unit changes to the global chi-square parameter, defined in equation [7], a single real refractive index spline point would have to be shifted by 0.4; a single extinction coefficient point would have to be shifted 0.6. Each point, however, affects only one eighth of the spectrum. The uncertainties distributed over the entire optical constant spectrum are 0.05 for the real refractive index spectrum and 0.075 for the extinction coefficient spectrum.

Better estimates of the uncertainties can be determined by examining the model fits to the measured ellipsometer spectra at each wavelength. However, the uncertainties caused by measurement and fitting errors are considerably smaller than the limits of accuracy of the theories used to model the measurements.

Figure	Spectrum	Thickness	Errors (avg.) ± (rms)	
		[Å]	Delta [deg]	Psi [deg]
4.6	NM10	124. Å	.08° ± .16°	−.10° ± .13°
4.5	NM08	121.	−.05 ± .16	−.08 ± .20
4.8	NN10	85.	.01 ± .12	.09 ± .11
4.7	NN05	84.	−.06 ± .17	−.10 ± .13

Table 4.1: Optical property modeling of nickel hydroxide using the program MFITRI in appendix C. Errors are reported as the average and root-mean-square deviations between the measured and predicted spectra.

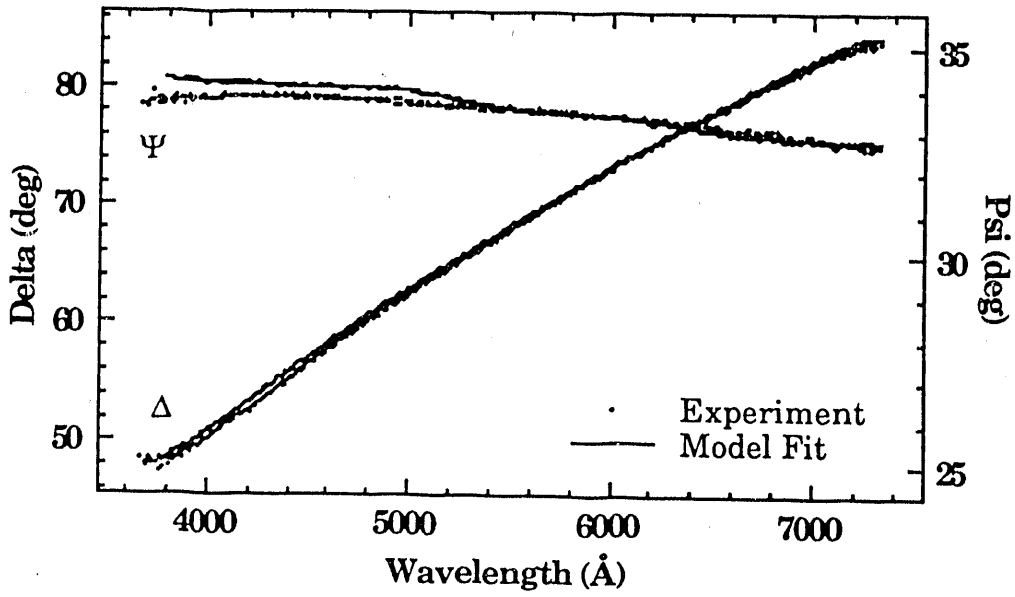

Figure 4.5: Measured and predicted ellipsometer spectra of a nickel hydroxide film. The film thickness was 121 Å. Spectrum NM08. XBL 924-863

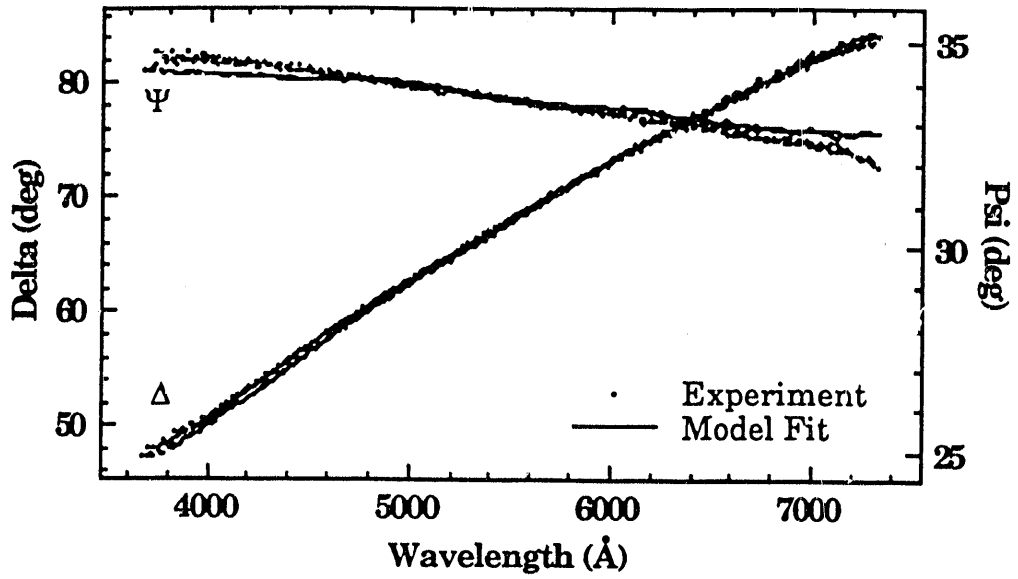

Figure 4.6: Measured and predicted ellipsometer spectra of a nickel hydroxide film. The film thickness was 124 Å. Spectrum NM10.XBL 924-864

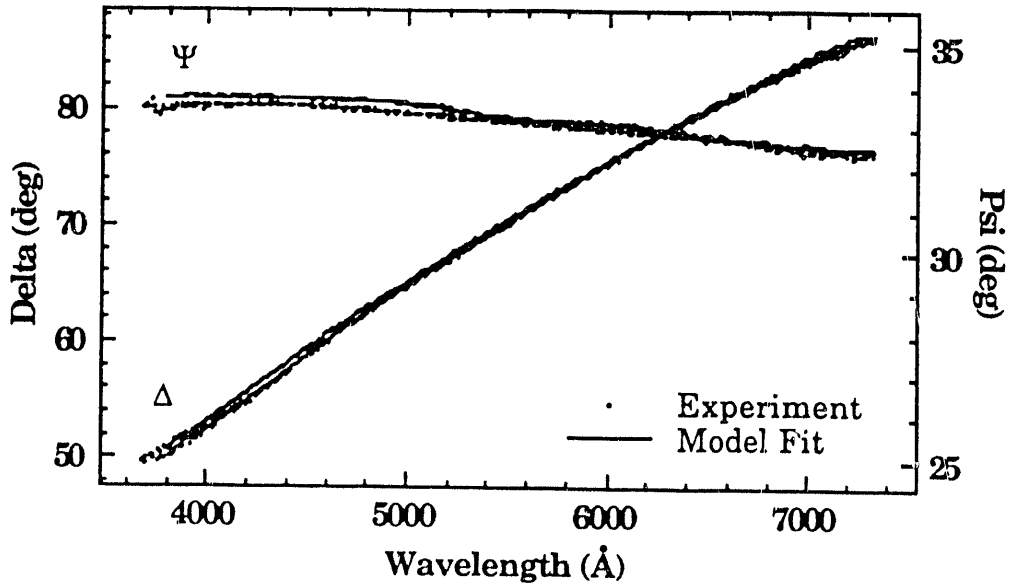

Figure 4.7: Measured and predicted ellipsometer spectra of a nickel hydroxide film. The film thickness was 84 Å. Spectrum NN05.XBL 924-865

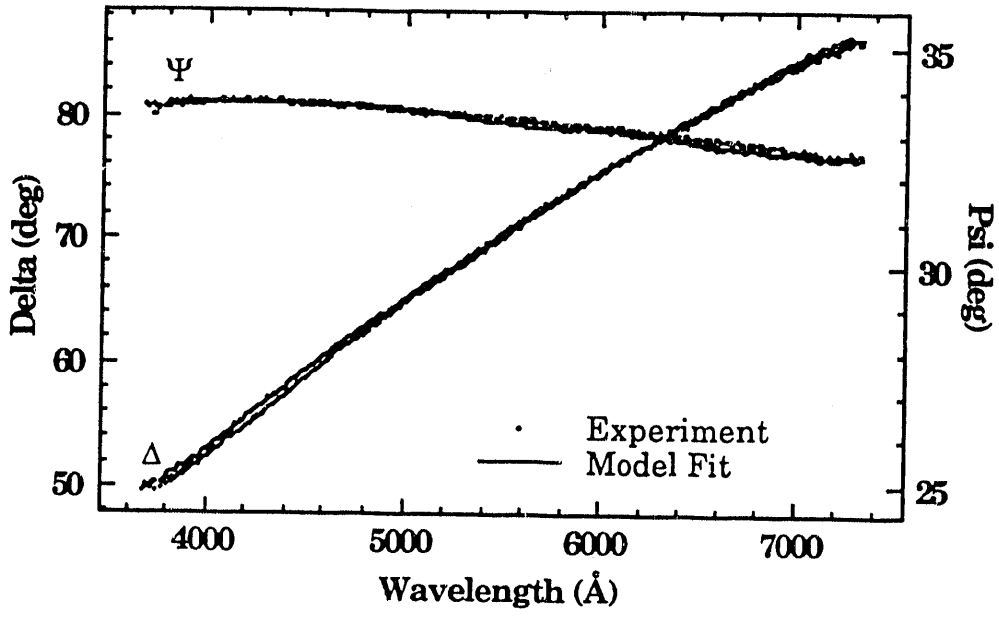

Figure 4.8: Measured and predicted ellipsometer spectra of a nickel hydroxide film. The film thickness was 85 Å. Spectrum NN10 XBL 924-866

Figure	Spectrum	Thickness	Errors (avg.) ± (rms)	
		[Å]	Delta [deg.]	Psi [deg.]
4.9	NM06	75. Å	−.04° ± .18°	.05° ± .08°
4.10	NM09	98.	.07 ± .17	−.02 ± .12
4.12	NN03	65.	−.08 ± .25	−.07 ± .13

Table 4.2: Optical property modeling of nickel oxy-hydroxide using the program MFITRI in appendix C. Errors are reported as the average and root-mean-square deviations between the measured and predicted spectra.

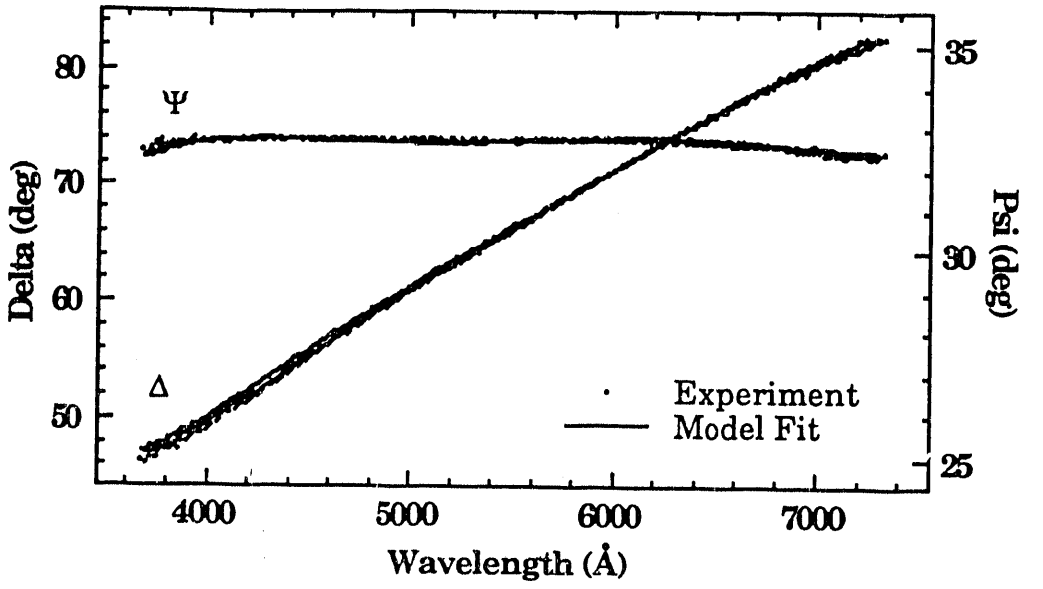

Figure 4.9: Measured and predicted ellipsometer spectra of a nickel oxy-hydroxide film. The film thickness was 75 Å. Spectrum NM06. XBL 924-867

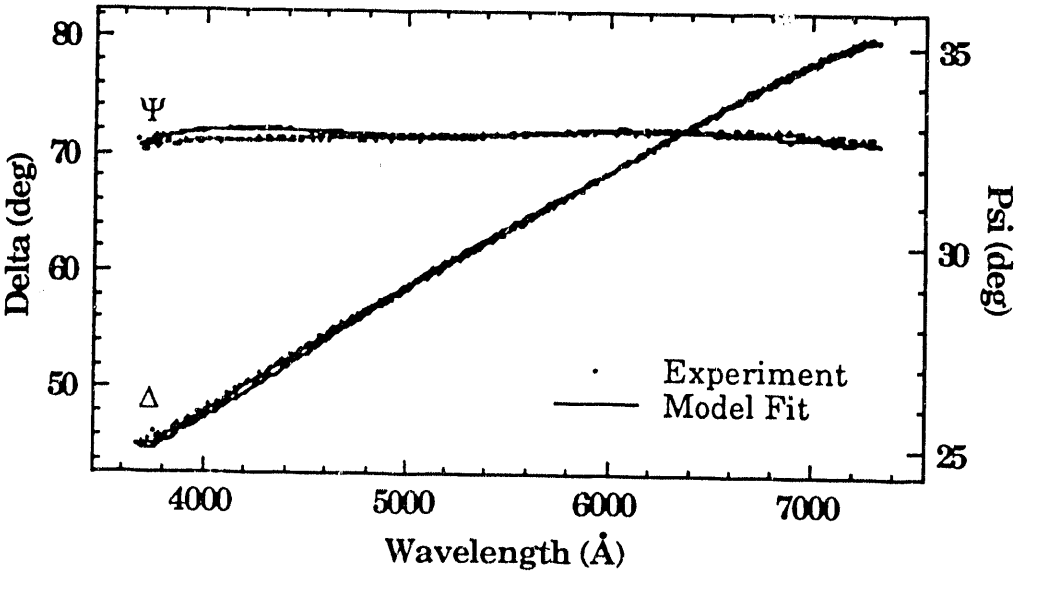

Figure 4.10: Measured and predicted ellipsometer spectra of a nickel oxy-hydroxide film. The film thickness was 98 Å. Spectrum NM09. XBL 924-868

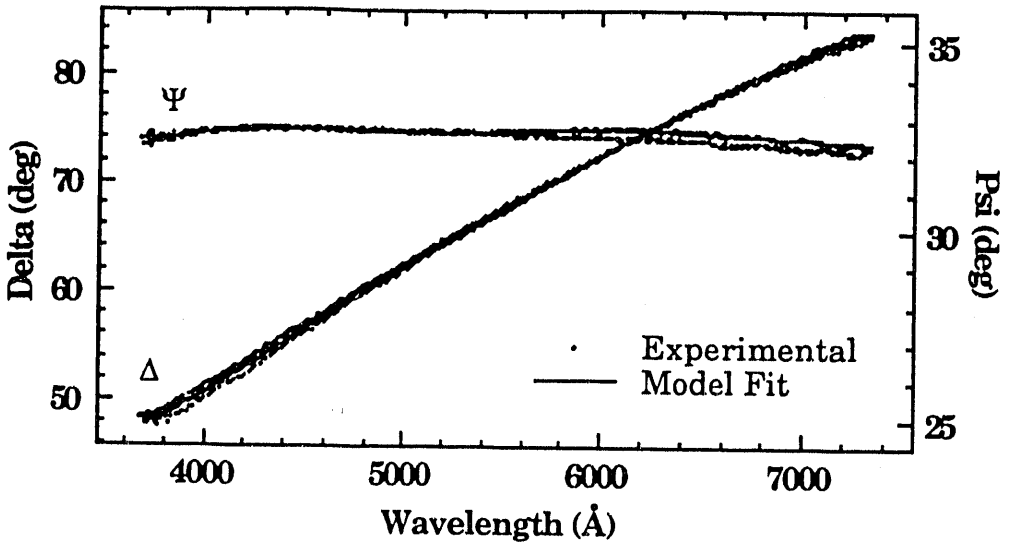

Figure 4.11: Measured and predicted ellipsometer spectra of a nickel oxy-hydroxide film. The film thickness was 65 Å. Spectrum NN03. XBL 924-869

The few refractive index data at single wavelengths reported in the literature are included in figure 4.12 and summarized in table 4.3. The inconsistency in the literature makes these data nearly irrelevant to our study. Unfortunately, no refractive index spectra were found in the literature to which to compare our measurements. This is perhaps the result of the relatively recent emergence of spectroscopic ellipsometry as an analytical tool. Monochromatic ellipsometry has been popular during most of the century. However, the amount of numerical computing required to fit spectroscopic models has impeded the popularity of spectroscopic ellipsometers. The recent availability and growing capability of desktop computers has lead to greater commercial development of these spectroscopic instruments.

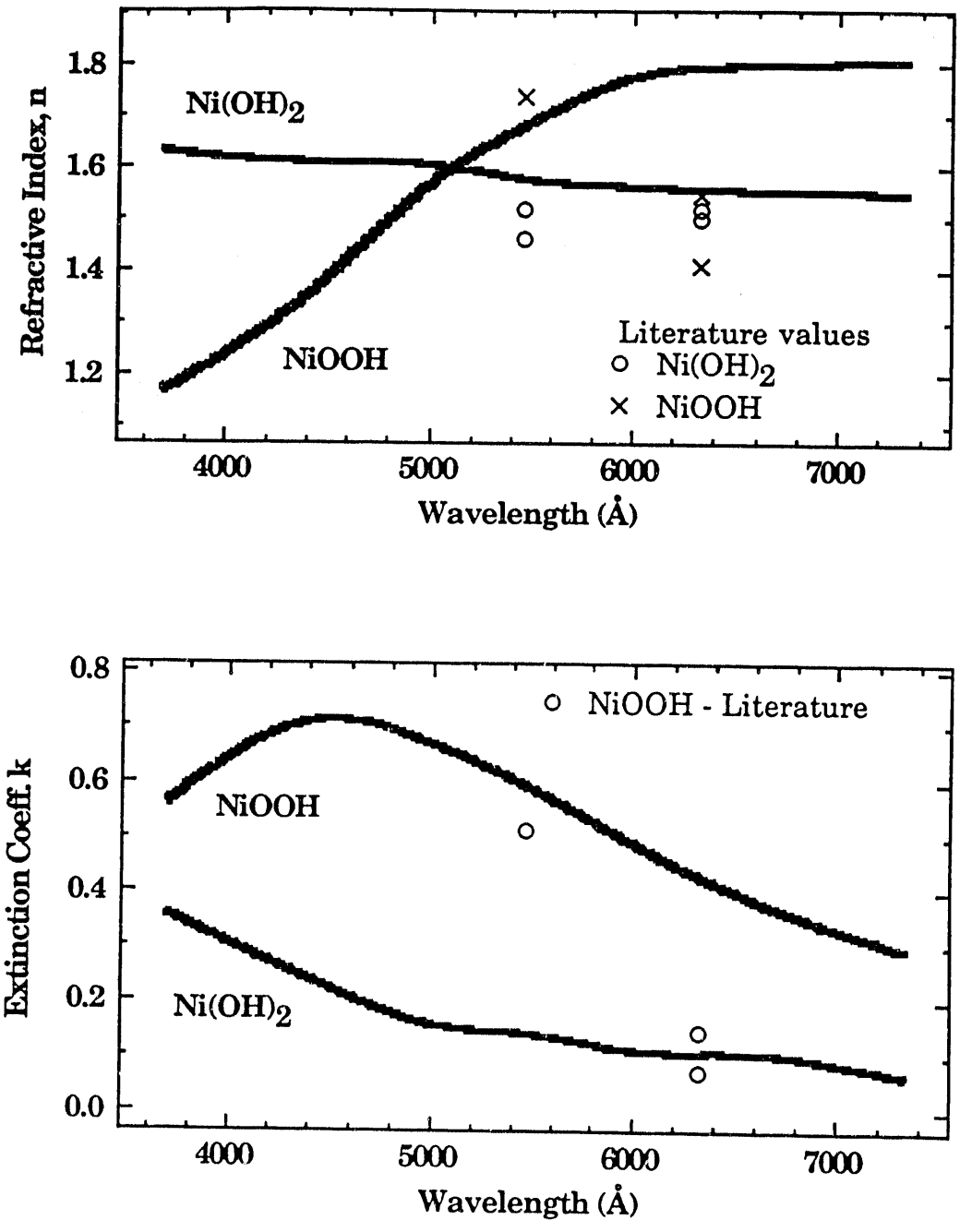

Figure 4.12: Refractive index spectra of pure nickel hydroxide and nickel oxyhydroxide formed by electrochemically oxidizing nickel metal in 1.0 M. NaOH. XBL 924-870/1

Wavelength	Species	Refractive Index	Reference
[Å]		(n, |k|)	
6328	ß-NiOOH	(1.41, .073)	6
5461	precip $Ni(OH)_2$	(1.46, 0*)	7
5461	precip NiOOH	(1.74, .51)	6
5461	anodic $Ni(OH)_2$	(1.52, 0*)	6
6328	anodic $Ni(OH)_2$	(1.52, 0*)	8
6328	anodic $Ni(OH)_2$	(1.50, 0*)	9
6328	anodic NiOOH	(1.55, .145)	8
		* k assumed equal to zero *a priori*	

Table 4.3: Refractive indices of nickel hydroxide and oxy-hydroxide at various wavelengths from the literature.

The optical constant spectra can be compared qualitatively to measurements of absorbances. The absorption coefficient is easily derived from the extinction coefficient data using equation [3]. The absorption coefficient spectra calculated from our optical constant spectra compare well with absorbance spectra found in the literature[10,11] as shown in figure 4.13. The nickel hydroxide material is mostly transparent in the visible spectrum, whereas nickel oxy-hydroxide has a broad absorption band. While the comparison to the literature values is not quantitative, the general spectral behavior is consistent.

$$\alpha = \frac{4\pi k}{\lambda} \qquad [10]$$

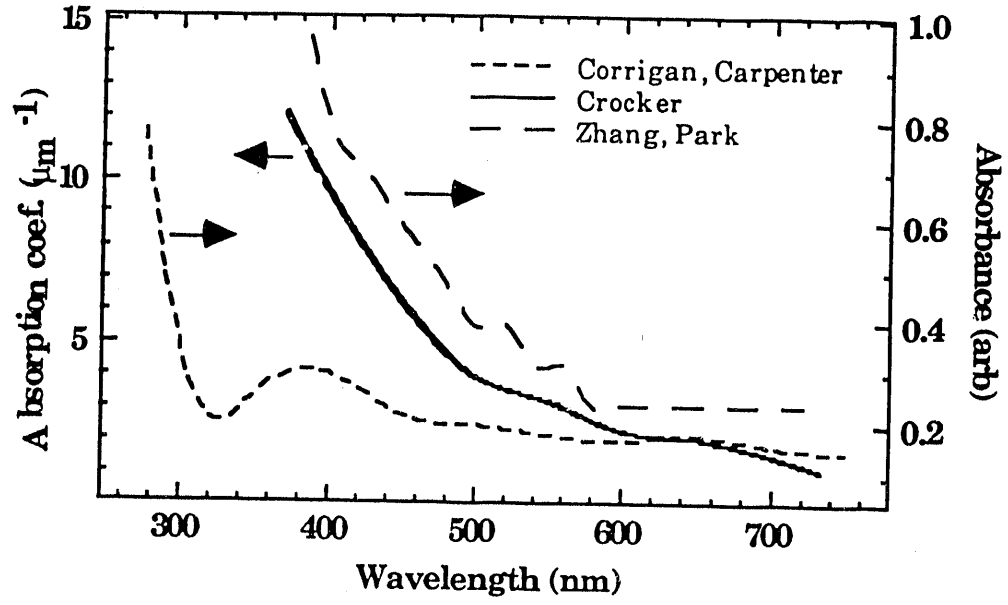

Figure 4.13: Absorbances of nickel hydroxide films calculated from refractive index spectra and compared to literature spectra measured by Corrigan, Carpenter (ref 11) and Zhang, Park.(ref 10) XBL 924-872

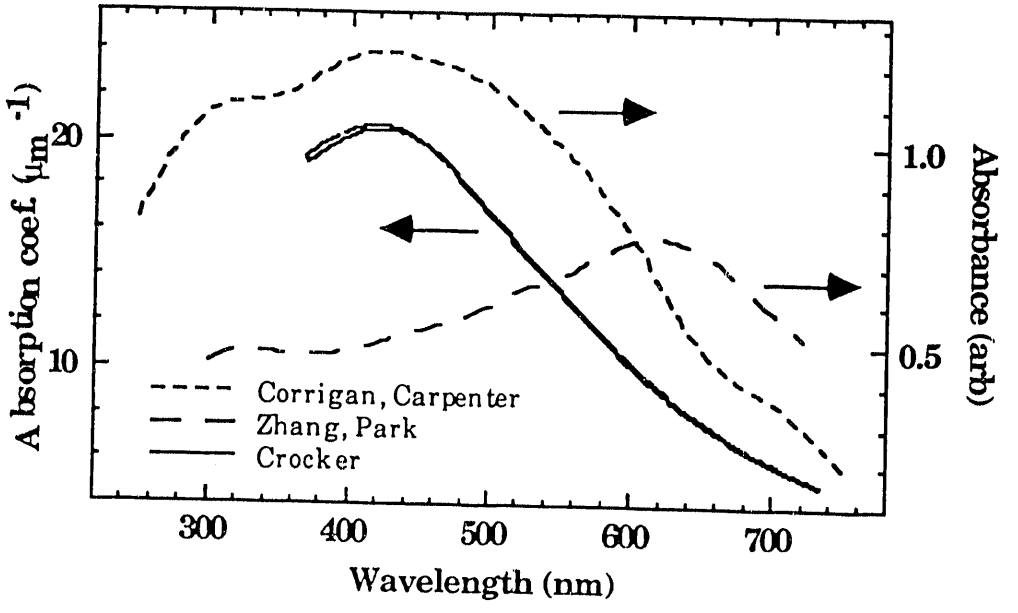

Figure 4.14: Absorbances of nickel oxy-hydroxide films calculated from refractive index spectra and compared to literature spectra measured by Corrigan, Carpenter (ref. 11) and Zhang, Park.(ref. 10) XBL 924-873

4-4 Optical Models for Nickel Hydroxide Electrode Structures

Using the optical constant spectra of the pure materials, we constructed optical film models to describe the structures that occur during the anodic charging reaction within the nickel hydroxide film electrode. The model structures were based on the hypothesis of nodular growth behavior and the observations of nickel oxy-hydroxide nodules in scanning tunneling microscopy experiments. These models were fitted to spectroscopic ellipsometer spectra collected *in-situ* during electrochemical experiments.

Four structural models were proposed, constructed of three archetypal layers representing the pure nickel hydroxide and oxy-hydroxide phases and the mixed nodule layer. These models are illustrated schematically in figure 4.15. For the nodule layer, the Bruggemann effective medium approximation (EMA)[12,13], equation [3], was used. The EMA is a mixing rule for the dielectric properties of non-homogeneous materials. The EMA is very suitable for the nodular layer since the theory was developed for electronically polarizable ellipsoids suspended in a continuous dielectric phase. The parameters required to define the EMA layer are the thickness of the layer, the volume fraction of the mixture, and the optical constants of the pure materials comprising the mixture.

$$\sum_{i=1}^{N} \phi_i \frac{\hat{\varepsilon}_i - \hat{\varepsilon}_h}{\hat{\varepsilon}_i + \gamma\hat{\varepsilon}_h} = 0. \qquad [11]$$

$$\hat{\varepsilon} = \hat{n}^2 \qquad [12]$$

Ellipsometer spectra of films held at various constant potentials were measured *in-situ* as the thin film electrodes were charged and discharged. The films were allowed to reach a steady-state before measuring them. They thickened from approximately 50 to 120 Angstroms as they were repeatedly charged and

discharged. The spectra were fitted to each of the optical structure models using the ellipsometric modeling application FlexiFit[14]. The only adjustable parameters in the models were the thicknesses of the layers and the volume fraction of nickel oxy-hydroxide in the nodule layer.

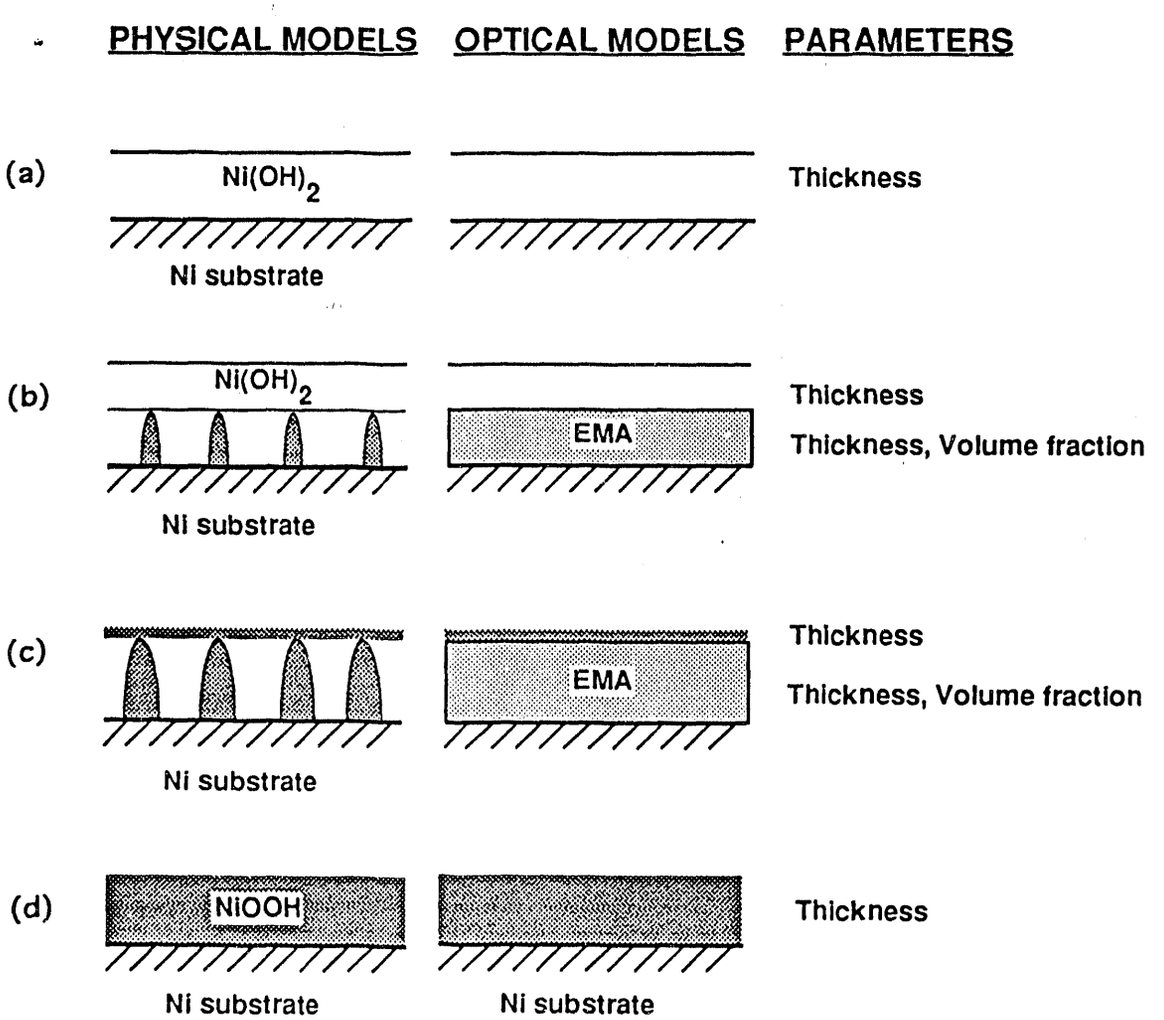

Figure 4.15: Schematic of physical and optical film models. The four archetypical models representing (a) uncharged film, (b) partially charged film with NiOOH nodules, (c) partially charged film with NiOOH overlayer, (d) fully charged film. An effective medium approximation is used to optically model the nodule layer. XBL 924-874

Each of the models was fitted to the measured ellipsometer spectra, chi-square values for each of the model fits are given in table 4.4. Fits returning non-physical

results for the parameters, such as negative film thicknesses, were disregarded. The model fit having the minimum chi-square statistic, defined in equation [7], was considered to represent the structure of the electrode film. Since the limiting cases of the individual models can give equivalent structures, the fitting process determined similar structures from different models. This is the case for the spectrum measured at 500 millivolts. The bilayer model indicated an 88% percent NiOOH nodule layer with a 4 Angstrom overlayer, while the single layer model approached that spectrum with 97 Angstroms of pure NiOOH. The bilayer model, however, produced closer fit to the experimental data. The fitted parameters and errors between the measured and predicted spectra for the best-fit models are summarized in table 4.5. Comparisons of fitted and measured spectra are presented in figures 4.16 through 4.21.

Potential	Model Fit χ^2 Errors				Spectrum
[mV]	$Ni(OH)_2$ (fig. 4.15a)	$Ni(OH)_2$/EMA (fig. 4.15b)	NiOOH/EMA (fig. 4.15c)	NiOOH (fig. 4.15d)	
–250	1.5	1.6	NP	NP	NM02
250	1.7	1.3	NP	NP	NM05
480*	NP	.4	.6	.5	NM06
–250	1.	1.6	NP	NP	NM08
500	7.5	NP	1.2	1.3	NM09
–250	1.0	NP	NP	NP	NM10
* Open circuit measurement.					

Table 4.4: Optical model fits to ellipsometer spectra of potentiostatic electrode films. The chi-square statistic is minimized in fitting process. Some fitting attempts give non-physical (NP) results (i.e., negative thicknesses).

			Nodule Layer		Overlayer	
Potential [mV]	Structure Figure	Spectrum Figure	Thickness [Å]	Fraction NiOOH	$Ni(OH)_2$ Thickness	NiOOH Thickness
–250	4.15 a	4.16			97 Å	
250	4.15 b	4.17	25 Å	.51	65.	
480*	4.15 b	4.18	72	.97	8.	
–250	4.15 a	4.19			122	
500	4.15 c	4.20	98	.88		4.4 Å
–250	4.15 a	4.21			123	
* Open circuit measurement.						

Table 4.5: Structures determined by optical model fits to ellipsometer spectra of potentiostatic electrode films. Structures correspond to schematics in figure 4.15.

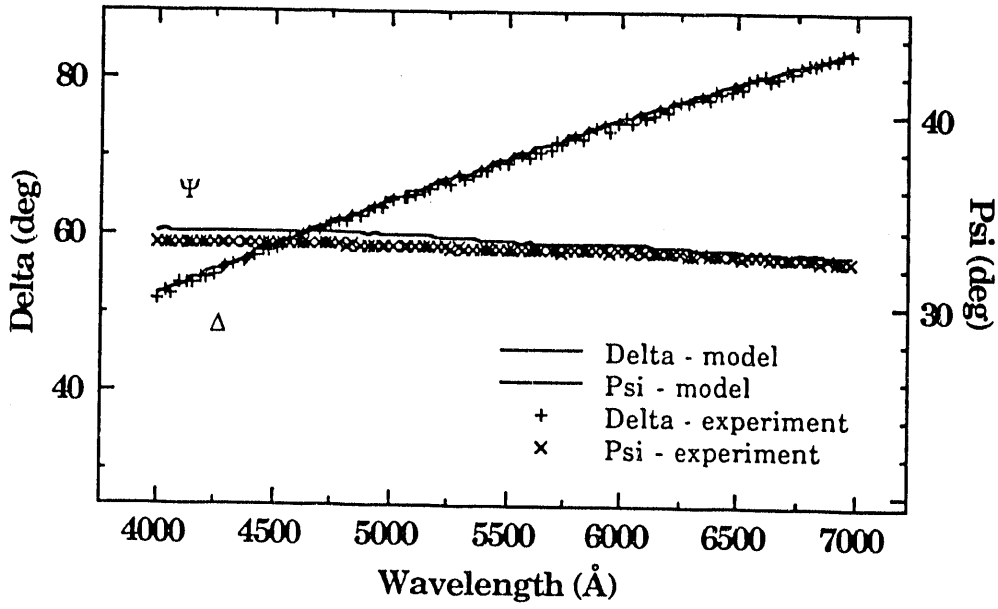

Figure 4.16: Comparison of best optical model fit to experimental ellipsometer spectra of electrode film held at –250 mV vs. HgO. The predicted film thickness was 97 Å of nickel hydroxide corresponding to the structure in fig. 4.15a. XBL 924-

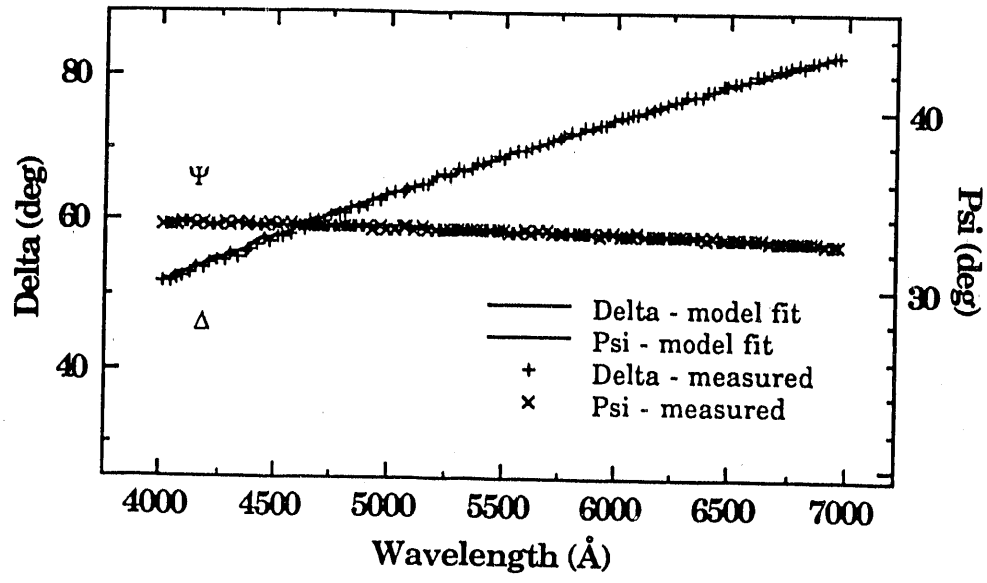

Figure 4.17: Comparison of best optical model fit to experimental ellipsometer spectra of electrode film held at 250 mV vs. HgO. The model corresponds to fig. 4.15b. The film consists of a 25 Å layer having 51%vol NiOOH beneath 65 Å of nickel hydroxide. XBL 924-876

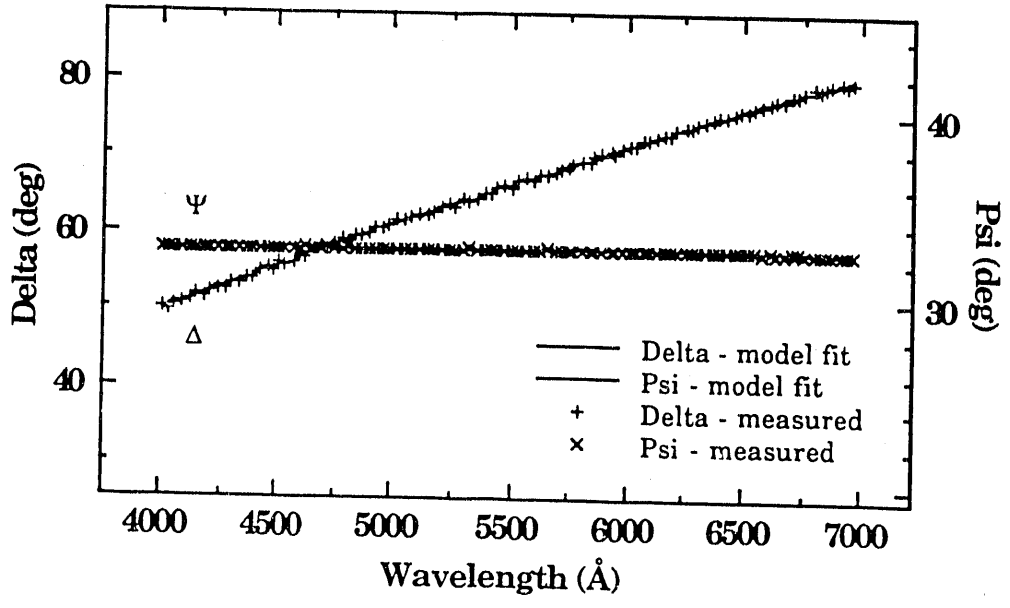

Figure 4.18: Comparison of best optical model fit to experimental ellipsometer spectra of electrode film charged at 550 mV vs. HgO and allowed to stand at open circuit (480 mV). The model corresponds to fig. 4.15b. The film consists of a 72 Å layer having 97%vol NiOOH with an overlayer of 8 Å of nickel hydroxide. XBL 924-877

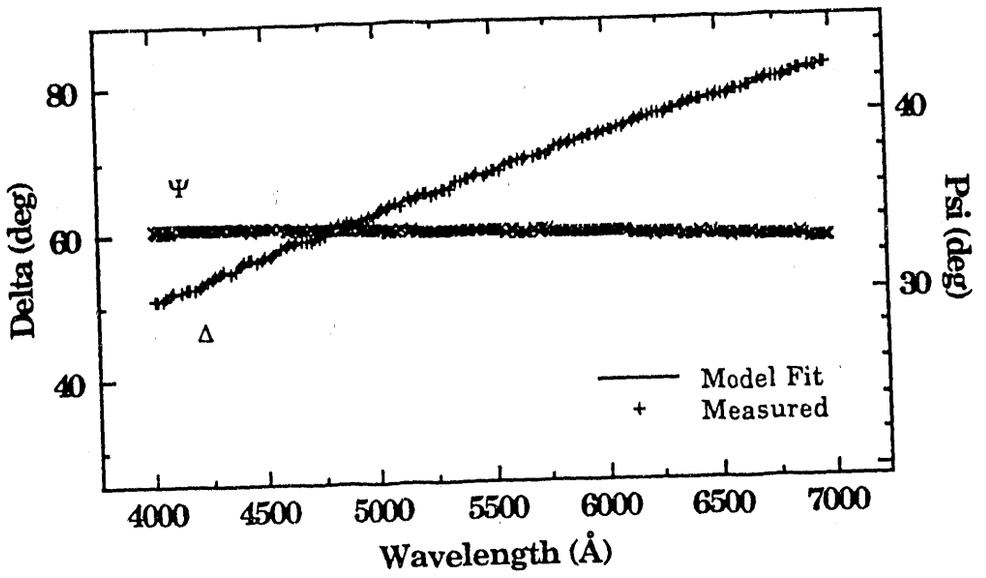

Figure 4.19: Comparison of best optical model fit to experimental ellipsometer spectra of electrode film held at –250 mV vs. HgO. The predicted film thickness was 122 Å of nickel hydroxide corresponding to the structure in fig. 4.15a. XBL 924-878

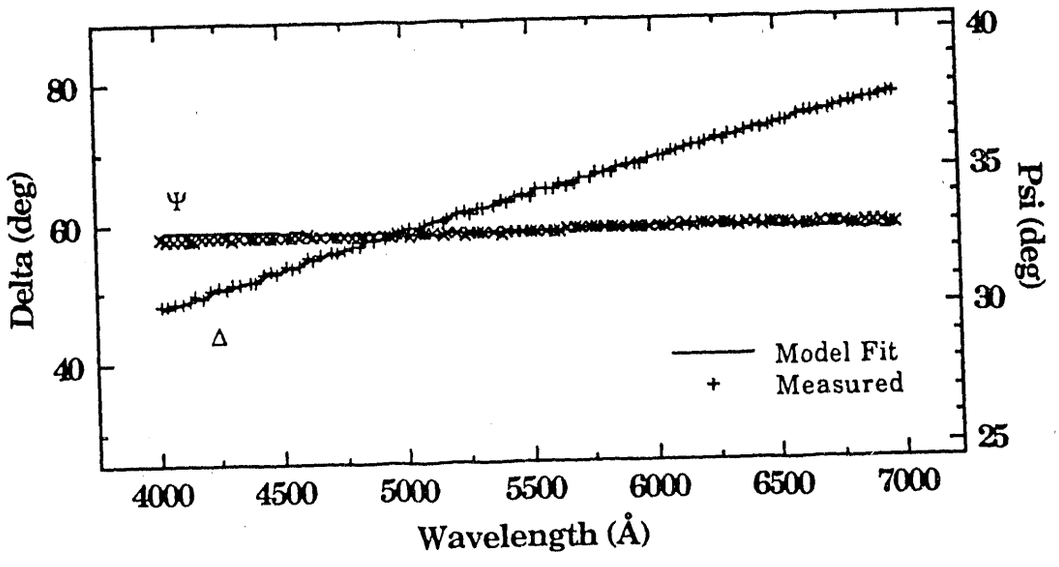

Figure 4.20: Comparison of best optical model fit to experimental ellipsometer spectra of electrode film charged at 500 mV vs. HgO. The model corresponds to fig. 4.15c. The film consists of a 98 Å layer having 88%vol NiOOH with an overlayer of 4 Å of NiOOH. XBL 924-879

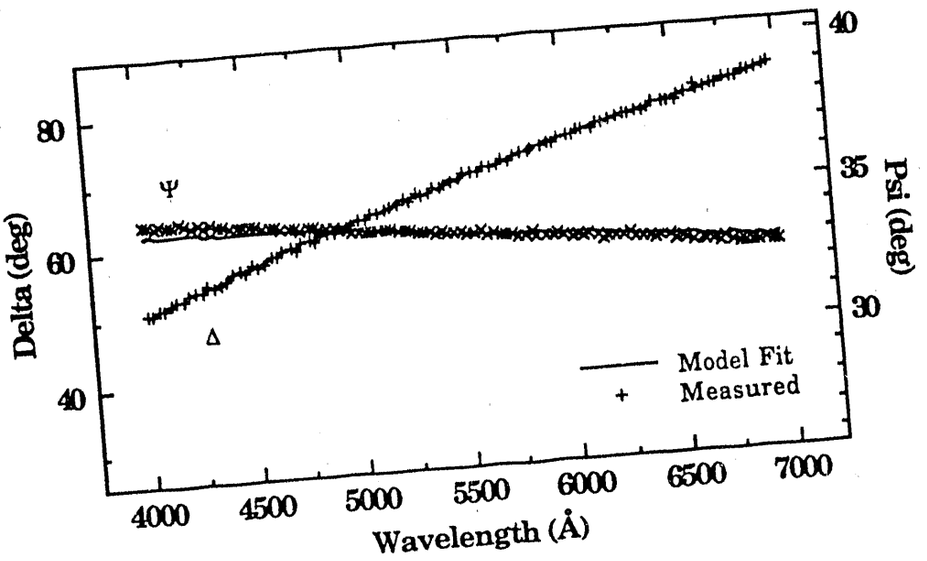

Figure 4.21: Comparison of best optical model fit to experimental ellipsometer spectra of electrode film held at –250 mV vs. HgO. The predicted film thickness was 123 Å of nickel hydroxide corresponding to the structure in fig. 4.15a. XBL 924-880

The results from the optical modeling of the electrode structures are summarized in table 4.5. The electrode films were completely reduced to nickel hydroxide at –250 millivolts versus Hg/HgO. If the film was incompletely reduced, held at +250 millivolts, a thin nodular layer persisted. Applying potentials greater than 500 millivolts converted more than 90% of the material to nickel oxy-hydroxide, even when the film was allowed to stand at open circuit.

An interesting result is the comparison between the charged nickel oxy-hydroxide film measured at open circuit and that held at 500 millivolts. In the open circuit case, the model indicates that there is a thin overlayer of nickel hydroxide; whereas at 500 millivolts, the overlayer appears to be nickel oxy-hydroxide. At sufficiently anodic applied potentials, the uppermost surface of the film is nickel oxy-hydroxide, whether the film is fully charged or an overlayer is formed. However, allowing the film to stand at open circuit allows the spontaneous

oxidation of hydroxide to form oxygen as the uppermost surface of the film is reduced to nickel hydroxide. This reaction is thermodynamically spontaneous by approximately 80 millivolts. The self-discharge reaction is hindered when the uppermost surface is converted to nickel hydroxide and reacting species would have to be transported though the layer.

It is evident from the optical model fits that the film contracts during charging; that is, the molecular volume of nickel oxy-hydroxide is smaller than that of nickel hydroxide. From our fits of the series of structures, the ratio of the molecular volume of the nickel oxy-hydroxide to that of the nickel hydroxide appears to be 0.80. This ratio agrees quantitatively with unit cell volume calculations based on X-ray measurements[15] in the literature that predict this ratio to be 0.84.

4-5 Optical Measurements during Galvanostatic Charge and Discharge

To examine the electrode performance under conditions similar to actual usage, spectroscopic ellipsometer measurements were performed during galvanostatic charge and discharge experiments. The optical measurements were used to analyze the state of charge of the electrode independent of the electrochemical measurements.

An electrode was initially charged potentiostatically to fully convert the film to nickel oxy-hydroxide. A spectroscopic ellipsometer measurement was made to determine the film thickness and state of charge. The electrode film was then discharged galvanostatically at 50 microamperes per square centimeter. Using the ellipsometer in a dynamic monochromatic mode, transient measurements were made to follow the change in the optical properties of the film. At the end of discharge, another spectroscopic ellipsometer measurement was made to determine the state of charge of the discharged film. The film was then charged and discharged at the same current density. Spectroscopic measurements were made between charge and discharge and after discharge.

The results of these experiments are presented in figures 4.22 through 4.28. Figures 4.22, 4.24, 4.26, and 4.28 are the spectroscopic ellipsometer measurements and the spectra predicted by the model fit used to determine the state of charge. Figures 4.23, 4.25, and 4.27 are the simultaneous transient monochromatic ellipsometer measurements and potential measurements.

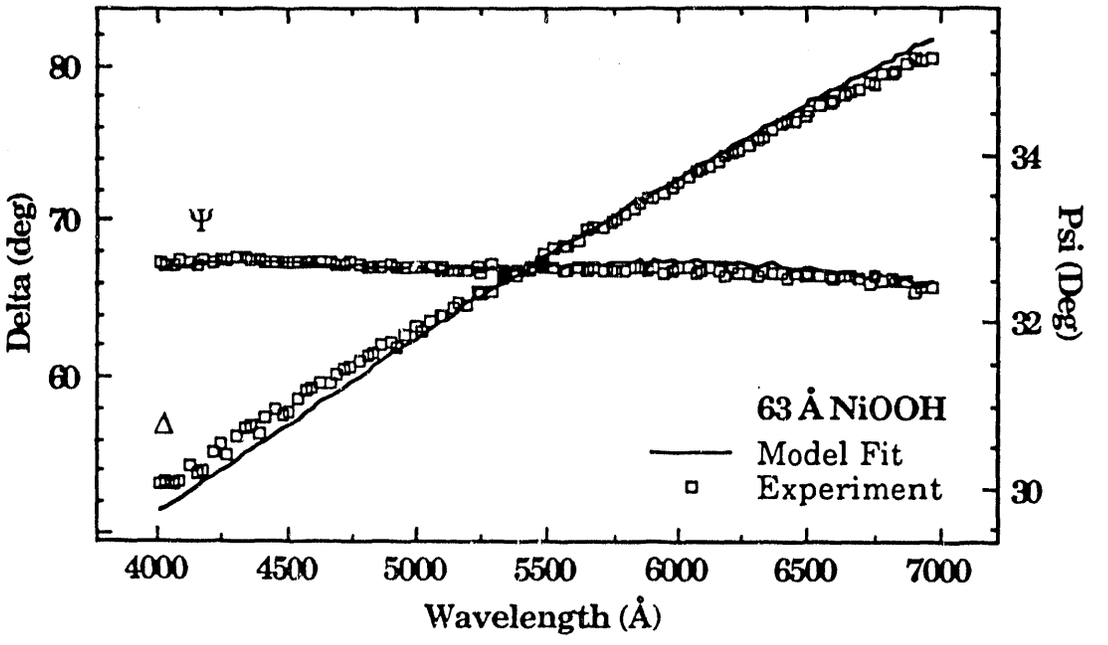

Figure 4.22: Comparison of measured and predicted ellipsometer spectra of the model fit of the initially charged electrode film. The film was 63 Å of NiOOH. The film was charged potentiostatically at .600 Volts vs. Hg/HgO. XBL 924-881

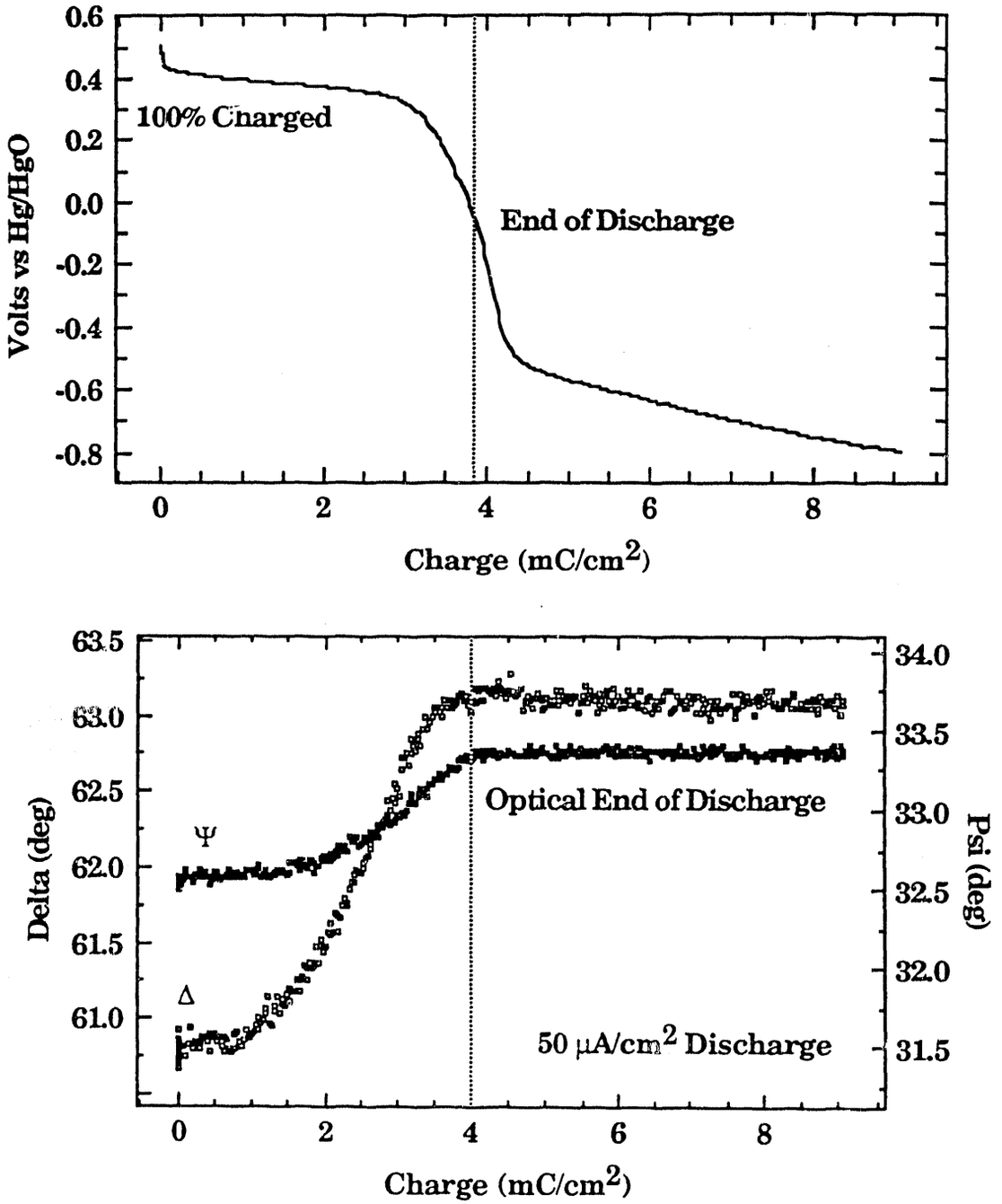

Figure 4.23: Galvanostatic discharge transients of the electrode film at 50 microamps/cm^2. Simultaneous monochromatic *in-situ* transient ellipsometry at 4760 Å. Reference lines indicate end-of-discharge as measured by electrochemical and optical means. XBL 924-881/2

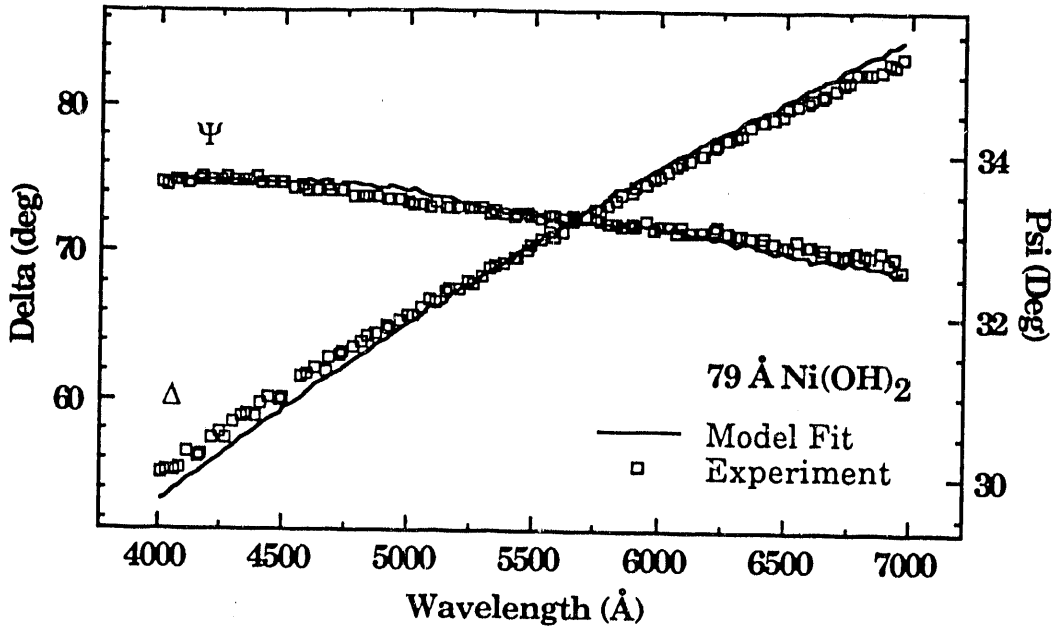

Figure 4.24: Comparison of measured and predicted ellipsometer spectra of the model fit of the discharged electrode film. The film was 79 Å of $Ni(OH)_2$. XBL 924-883

Table 4.6 presents the results of the spectroscopic ellipsometer measurements to determine the state of charge of the electrode films between the charge and discharge transients. The film, which was initially charged at 600 millivolts potentiostatically, began as 63 Angstroms of pure nickel oxy-hydroxide. After the first discharge transient, the film was found to be fully converted to 79 Angstroms of nickel hydroxide. The molecular volume ratio between the nickel oxy-hydroxide and nickel hydroxide films was 0.80 in agreement with the literature value. After the charging transient, the film was only 46% nickel oxy-hydroxide, indicating an incomplete charge. The model suggests the presence of a nickel oxy-hydroxide overlayer. After the final discharge transient, the film was completely converted to 84 Angstroms nickel hydroxide. The difference in film thicknesses between the two discharged states indicates that further oxidation of the nickel substrate had occurred.

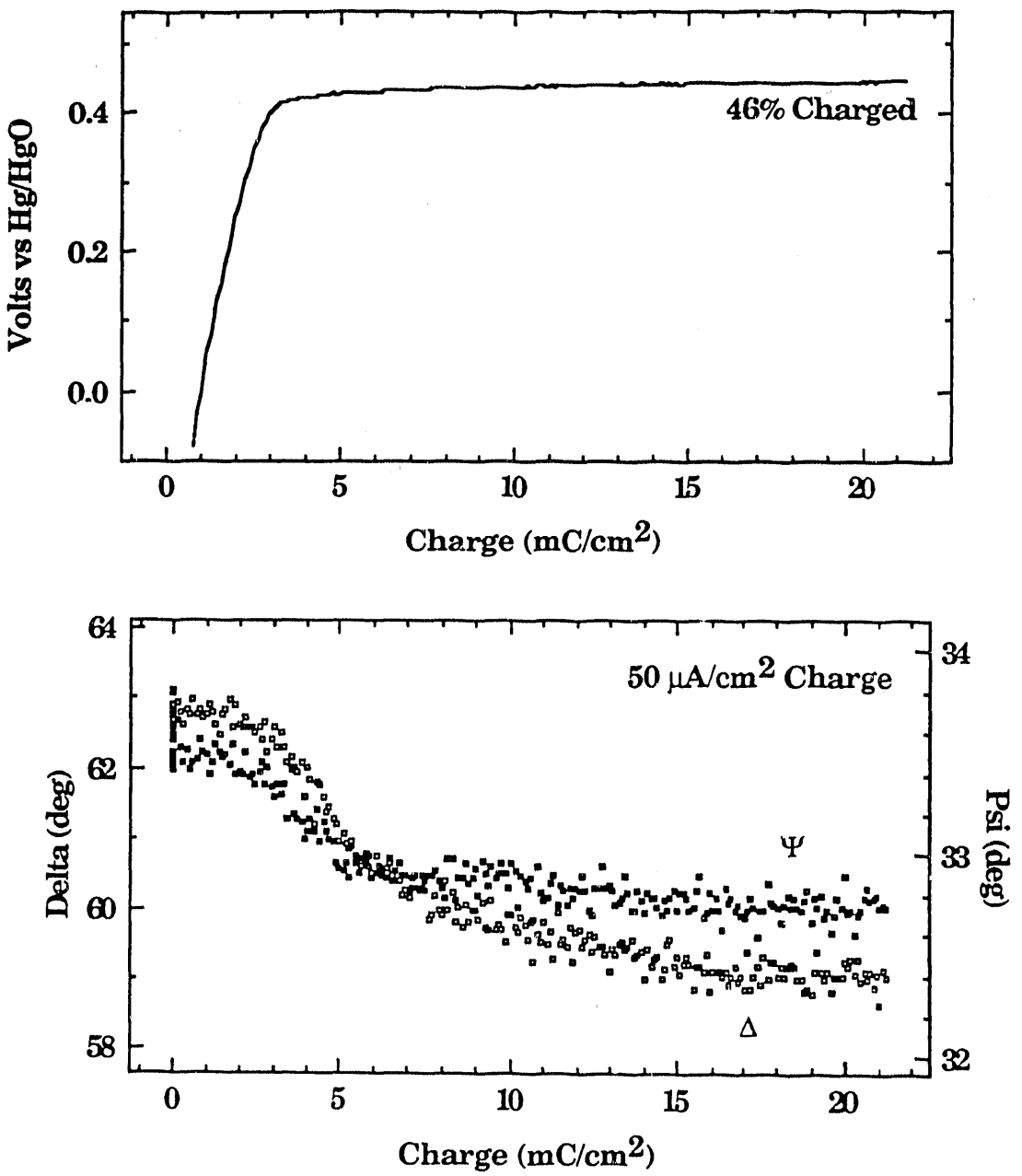

Figure 4.25: Galvanostatic charge transients of the electrode film at 50 microamps/cm^2. Simultaneous monochromatic *in-situ* transient ellipsometry at 4797 Å. XBL 924-884/5

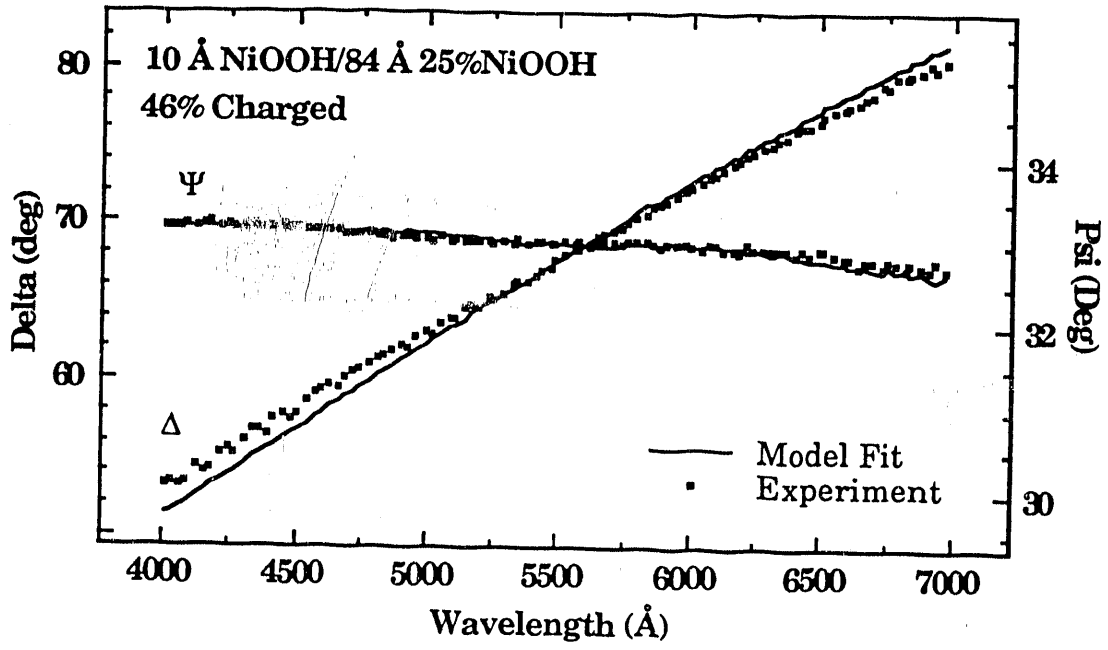

Figure 4.26: Comparison of measured and predicted ellipsometer spectra of the model fit of the charged electrode film. The film was 85 Å of 25% NiOOH with a 10 Å overlayer of NiOOH. XBL 924-886

Figure	Structure Model	Fraction NiOOH
4.22	63 Å NiOOH	1.0
4.24	79 Å $Ni(OH)_2$	0.
4.26	10 Å NiOOH 85 Å of 25% NiOOH	0.46
4.28	84 Å $Ni(OH)_2$	0.

Table 4.6: Results of spectroscopic ellipsometer measurements to measure the state of charge of the film electrodes between charge/discharge transients.

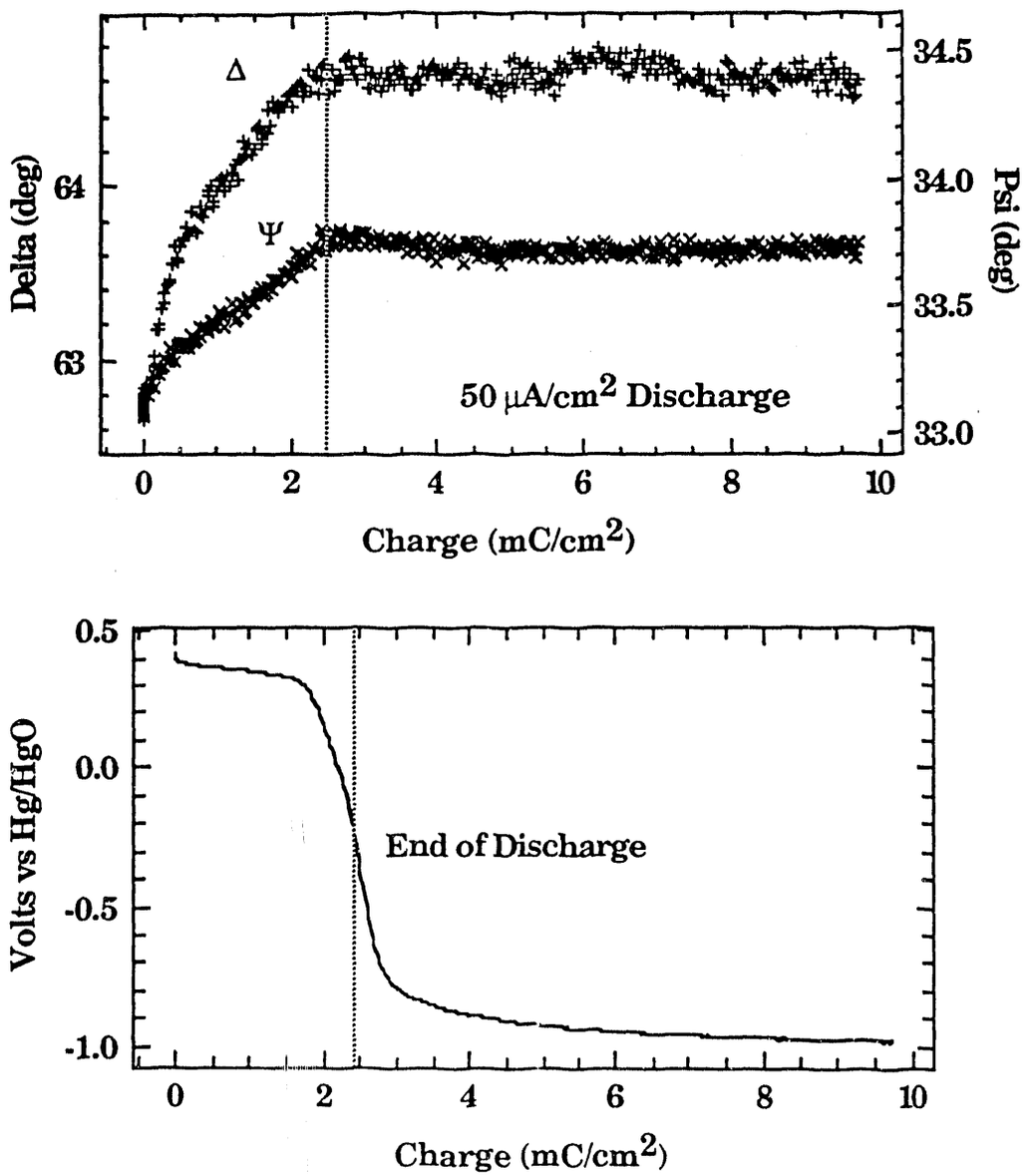

Figure 4.27: Galvanostatic discharge transients of the electrode film at 50 microamps/cm^2 and simultaneous monochromatic *in-situ* transient ellipsometry at 4924 Å. End of discharge measurement confirms optical measurement that film was incompletely charged. XBL 924-887/8

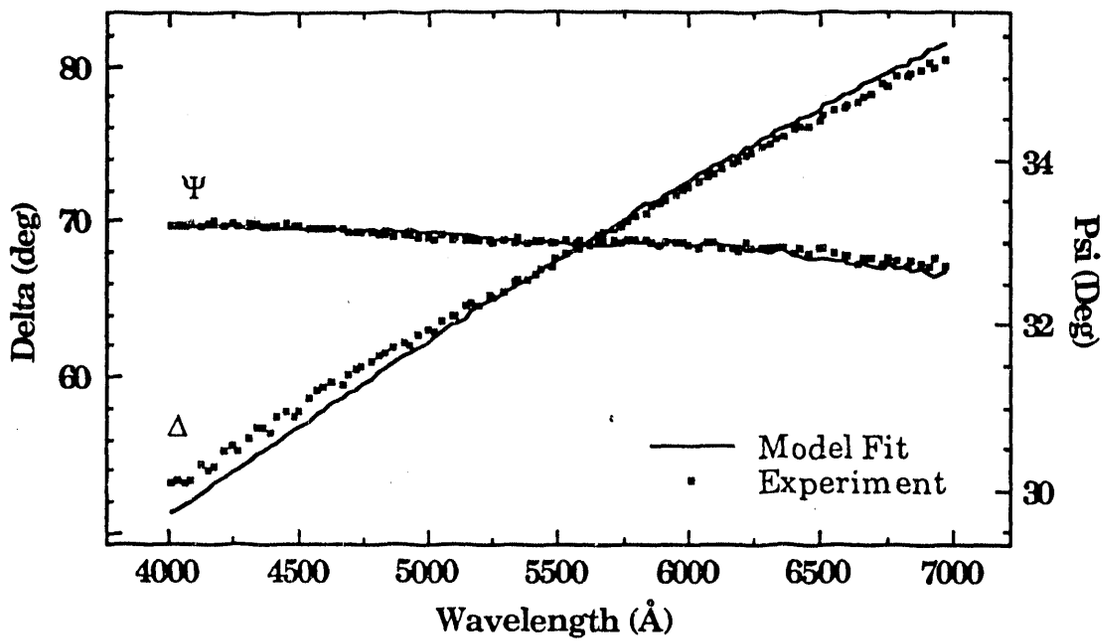

Figure 4.28: Comparison of measured and predicted ellipsometer spectra of the model fit of the discharged electrode film after 10 mC/cm^2. The film was 84 Å of $Ni(OH)_2$. XBL 924-889

In the discharge transients, figures 4.23 and 4.27, the point at which the optical properties stopped changing was defined as the "optical end-of-discharge." This point is compared to the traditional electrochemical end-of-discharge indicated by the inflection point in the potential transients. These measurements agree quite well, as presented in table 4.7.

The ellipsometry measurement of the charging transient in figure 4.25, indicates that the psi parameter reached a near steady-state before the delta parameter. Since model calculations indicate that the psi parameter is most sensitive to the uppermost surface of the film, this point could be interpreted as the formation of the nickel oxy-hydroxide overlayer that was found in the spectroscopic modeling of the endpoint.

Figure	Mode	Electrochem. End of (Dis)Charge	Optical End of (Dis)Charge	Changed Fraction NiOOH	Current Efficiency
4.23	Discharge	3.9 mC/cm^2	4.0 mC/cm^2	1.0	1.0
4.25	Charge	Not Observed	16	.46	.12
4.27	Discharge	2.4	2.5	.46	.96

Table 4.7: Results of galvanostatic charging and discharging experiments.

Further analysis of these transient experiments indicates that the charging reaction is very inefficient. The electrode required four times the theoretical charge capacity to reach a steady-state. Yet, only 46% of the electrode material were converted at that steady-state. The discharge transient of the film indicated that the film had 62% of the maximum charge stored in it. The discrepancy in the state of charge measurements between the optical model and the measured charge for reduction of the oxidized film is probably caused by a combination of two effects. The oxidation of the nickel metal substrate during the charging transient increased the film charge capacity 7% and the reduction of oxygen evolved during the overcharge period could account for the balance of the excess recovered charge.

These experiments demonstrated the reduction of usable charge capacity of the electrode caused by the shielding of the active material by the nickel oxy-hydroxide overlayer. This overlayer also facilitated parasitic oxygen evolution that resulted in dramatic loss of current efficiency between charge and discharge of the electrode.

4-6 Nomenclature

Subscripts:

- h host medium in Bruggeman EMA, defined in [11]
- o ambient
- p p-component, in the plane of incidence
- s substrate, or s-component, normal to plane of incidence
- 0,1,2 numerals refer to different media in reflection coefficients

Superscripts:

- m measured, as opposed to calculated in equation [7]
- ^ complex variable

Variables:

- D complex optical path length in Drude equation [5, 6]
- k extinction coefficient
- $\hat{i}$ imaginary unit, $\sqrt{-1}$
- n real refractive index in figures, complex refractive index $n - \hat{i}k$ in equations
- r complex reflection coefficient from Fresnel or Drude equations [2,3,5]
- t film thickness
- α absorption coefficient, defined in [10].
- γ screening factor in Bruggeman EMA, defined in [11]
- Δ Delta, relative phase shift ellipsometry parameter
- ε complex dielectric constant
- λ wavelength of light
- $\hat{\rho}$ complex relative reflectance ratio, equation [1]
- $\hat{\theta}$ complex angle of incidence, real in non-absorbing media
- ϕ_i volume fraction of species i in Bruggeman EMA, defined in [11]
- Ψ Psi, relative amplitude ellipsometry parameter
- χ^2 chi-square error statistic, defined in equation [7]

References

1 R.M.A. Azzam, N.M. Bashara,, *Ellipsometry and Polarized Light,* North Holland, Amsterdam, 1977

2 R.H. Muller, "Principals of Ellipsometry", in *Adv. in Electrochemistry and Electrochem. Eng,* Volume 9, C.W. Tobias, and H. Gerischer (ed.), Wiley, New York, 1973 (also issued as Lawrence Berkeley Laboratory report LBL-187)

3 R.H. Muller, "Ellipsometry as an In Situ Probe for the Study of Electrode Processes", in *Techniques for Characterization of Electrodes and Electrochemcial Processes*, p. 31-125, R. Varma, J.R. Selman (ed.) Wiley, New York, 1991

4 M. Born, E. Wolf, *Principles of Optics,* 6th edn., Pergamon, 1989

5 E. Palik, *Handbook of Optical Constants of Solids*, Academic Press, 1985

6 A.A. Wronskawa, Surf. Sci. **214,** 507 (1989)

7 W. Visscher, J. de Phys. Colloque C10, **44**, 213 (1983)

8 J. Hopper, J. Ord, J. Electrochem. Soc. **120**, 183 (1973)

9 J.L. Ord, J.C. Clayton, D.J. DeSmet, J. Electrochem. Soc. **124**, 1714 (1977)

10 C. Zhang, S. Park, J. Electrochem. Soc. **136**, 3333 (1989)

11 M.K. Carpenter, D.A. Corrigan, J. Electrochem. Soc. **136**, 1022 (1989)

12 D.A.G. Bruggeman, Ann. Physik (Leipzig) **24**, 636 (1935)

13 D.E. Aspnes, J.B. Theeten, "Investigation of EMA Models of Microscopic Roughness by Spectroscopic Ellipsometry", Phys. Rev. B **20**, 3292 (1979)

14 R.W. Crocker, R.H. Muller, "FlexiFit: Ellipsometric Modelling Application", Lawrence Berkeley Laboratory report LBL-32137, May 1992

15 R.S. McEwen, J. Phys. Chem. **75**, <12>, 1782 (1971)

Chapter 5

Numerical Simulation of the Phase Conversion of Nickel Hydroxide to Nickel Oxy-Hydroxide

It is useful to construct a picture of the morphological changes that occur during the electrode charging reaction. This is accomplished by assembling the relevant physical phenomena into a mathematical model. In the nickel hydroxide film electrode model, the potential and current distribution within the film are used to calculate the evolution of the phase boundary between the nickel hydroxide and nickel oxy-hydroxide phases. The important physical properties of the film include the overall conductivities of the phases, densities of the nickel species, and kinetic parameters. There are a number of assumptions that can be made about the valences of the nickel species, the kinetics, and the transport modes.

In the course of our study, we have incrementally developed our model from the simplest one-dimensional case in the limit of fast kinetics to the case of two dimensional axisymmetric nodules with a linear kinetic behaviour. There are interesting analogies to be found among the different cases; therefore, we shall develop the cases in the following sections.

In constructing a model that describes the transformation of nickel hydroxide to nickel oxy-hydroxide, we would like to describe the evolution of the reaction front through the film. From a purely electrochemical model, we should be able to simulate the potential and current distribution and the shape and position of the reaction front. Since the film is being transformed from a low conductivity material, nickel hydroxide, to a higher one, nickel oxy-hydroxide, there will be a characteristic transient behavior. If a constant potential is applied, the decreasing overall film resistance will cause the current to increase until the nickel hydroxide is exhausted, or under galvanostatic conditions, the overpotential should drop. We will examine this behavior starting with the one-dimensional ohmic and linear kinetic cases which can be treated analytically.

5-1 Special Cases of Nodule Growth: 1-D Ohmic

The system consists of a large planar metal substrate covered with a partially charged nickel hydroxide film immersed in concentrated electrolyte with a similar planar counter electrode facing the film. The partially charged film is treated as two phases, a nickel oxy-hydroxide film adjacent to the metal substrate, and an uncharged layer of nickel hydroxide between the nickel oxy-hydroxide and the electrolyte. This configuration is illustrated schematically in figure 5.1. Referring to figure 5.1, the potential is identically zero at the metal substrate, $y=0$, and equal to the applied potential, Φ_0, at the electrolyte interface, $y=L$. The potential is continuous across the phase boundary at $y=\lambda L$. The phases have different electrical conductivities, κ_1 and κ_2.

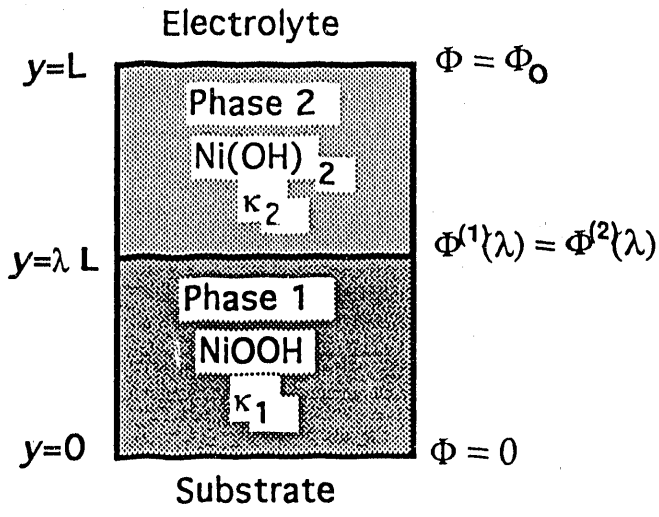

Figure 5.1: Schematic of one-dimensional electrochemical models of nickel electrode films. XBL 924-890

The potential and current distributions are described by the Laplace equation, which is shown converted to non-dimensional form in equation [1]. In this development, dimensional forms will be denoted by boldface variables.

Equation	Dimensionless Groups	Non-Dimensional Form	
$\frac{d^2\Phi}{dy^2} = 0$	$\Phi = \Phi/\Phi_0$, $y = y/L$	$\frac{d^2\Phi}{dy^2} = 0$	[1a-d]

The metal and electrolyte interfaces are assumed to be equipotential surfaces since the conductivities of the metal and electrolyte are both several orders of magnitude larger than either of the film materials. At the nickel hydroxide/nickel oxy-hydroxide reaction interface we assume, in this ohmic case, that the kinetics are very fast such that the potentials are equivalent on adjacent sides of the interface. In addition, we assume continuity of current across the interface, which prohibits accumulation of charge. These boundary conditions are summarized in equations [2]–[5]. The most important non-dimensional parameter in the problem is the ratio of the conductivity of the nickel hydroxide to the nickel oxy-hydroxide phase, the symbol, β, defined in [5b]

Equation	Dimensionless Groups	Non-Dimensional Form	
$\Phi(0) = 0$		$\Phi(0) = 0$	[2a,c]
$\Phi(L) = \Phi_0$		$\Phi(1) = 1$	[3a,c]
$\Phi^{(1)}(h) = \Phi^{(2)}(h)$	$\lambda = h/L$	$\Phi^{(1)}(\lambda) = \Phi^{(2)}(\lambda)$	[4a,b,c]
$\kappa_1\left[\frac{d\Phi^{(1)}}{dy}\right]_{x=h} = \kappa_2\left[\frac{d\Phi^{(2)}}{dy}\right]_{x=h}$	$\beta = \kappa_2/\kappa_1$	$\frac{d\Phi^{(1)}}{dy} = \beta\frac{d\Phi^{(2)}}{dy}$	[5a,b,c]

The solution of the Laplace equation, [1], which is an ordinary differential equation in this geometry, is found simply by integration. The solutions to the potentials in dimensionless form, for the respective nickel oxy-hydroxide (1) and nickel hydroxide (2) regions are given in equations [6] and [7]:

$$\Phi^{(1)}(y) = \frac{\beta}{1 + \lambda(\beta - 1)} y, \quad 0 \le y \le \lambda \qquad [6]$$

$$\Phi^{(2)}(y) = 1 - \frac{(1-y)}{1 + \lambda(\beta - 1)}, \quad \lambda \le y \le 1 \qquad [7]$$

The current density, *i*, is uniform though out the film and is given by equation [8]:

$$i = \frac{d\Phi^{(1)}}{dy} = \beta\frac{d\Phi^{(2)}}{dy} = \frac{\beta}{1 + \lambda(\beta - 1)}, \text{where } i = \frac{iL}{\kappa_1\Phi_o} \qquad [8a\text{-}d]$$

Using the analytical model result, we can simulate the response to charging the thin film electrode by applying an anodic potential step. The current and potential distribution are functions of the nickel hydroxide/oxy-hydroxide interface position. The position of the interface, λ, is differentially related to the current density as in equation [9] and [10]. The initial condition of the differential equation for the

potential step case is simply that the interface position is at the nickel substrate at zero time ($\lambda(0) = 0$). The result of integrating equation [9] using that initial condition gives equation [11]. The dimensionless time parameter defined in [10] contains the density, ρ, number of equivalents, n, and Faraday's constant, F.

$$\frac{d\lambda}{dt} = i(\lambda) = \frac{\beta}{1 + \lambda(\beta - 1)} \qquad [9a,b]$$

$$t = t\frac{\Phi_0 \kappa_2 M_w}{\rho n F L^2} = t\frac{(\text{Current})}{(\text{Charge})} \qquad [10a,b]$$

$$\lambda(t) = \frac{1 - \sqrt{1 + 2\beta(\beta - 1)t}}{(1 - \beta)} \qquad [11]$$

The completion time, t_f, the time at which the reaction front reaches the electrolyte interface, is determined by solving for $\lambda = 1$. We find:

$$t_f = \frac{(\beta + 1)}{2\beta} \qquad [12]$$

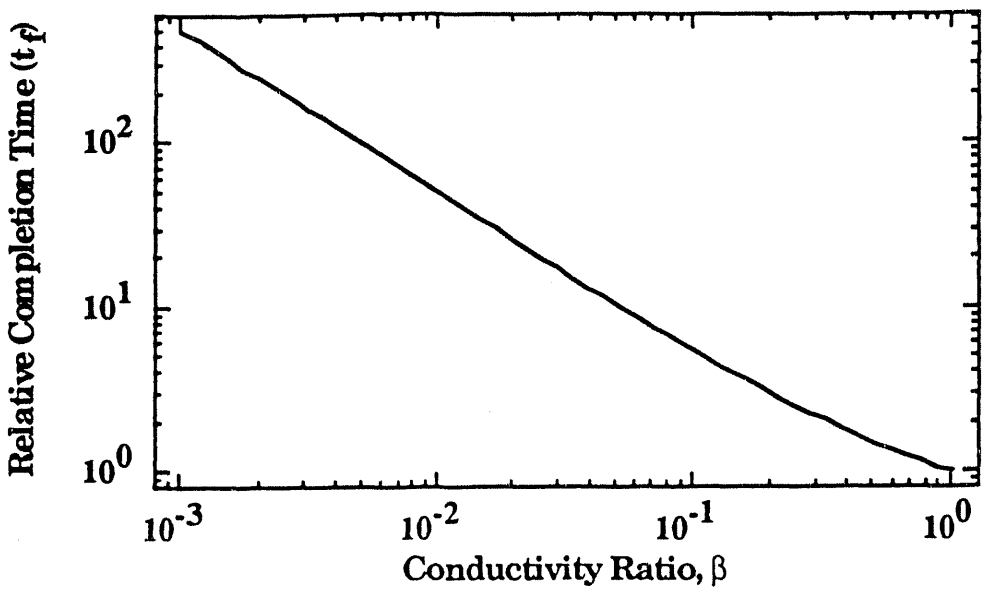

Figure 5.2: Non-dimensional completion time versus conductivity ratio. The completion time grows rapidly as the conductivity of the nickel hydroxide phase decreases. XBL 924-891

The results of this analysis are summarized in figures 5.2, 5.3, and 5.4, in which we present the relationships of the completion time, current transients, and boundary position transients as the conductivity ratio is varied. Lowering the conductivity ratio between the nickel hydroxide and nickel oxy-hydroxide phases dramatically increases the time required to charge the film, as the overall film resistance increases. The more interesting result is that the transients become more non-linear, tending to accelerate towards the end of charge as the ratio is lowered, as shown in figure 5.4. This acceleration effect is the result of the decreasing film resistance as the film is converted to nickel oxy-hydroxide. In the next case, we examine the effect of kinetics on this system.

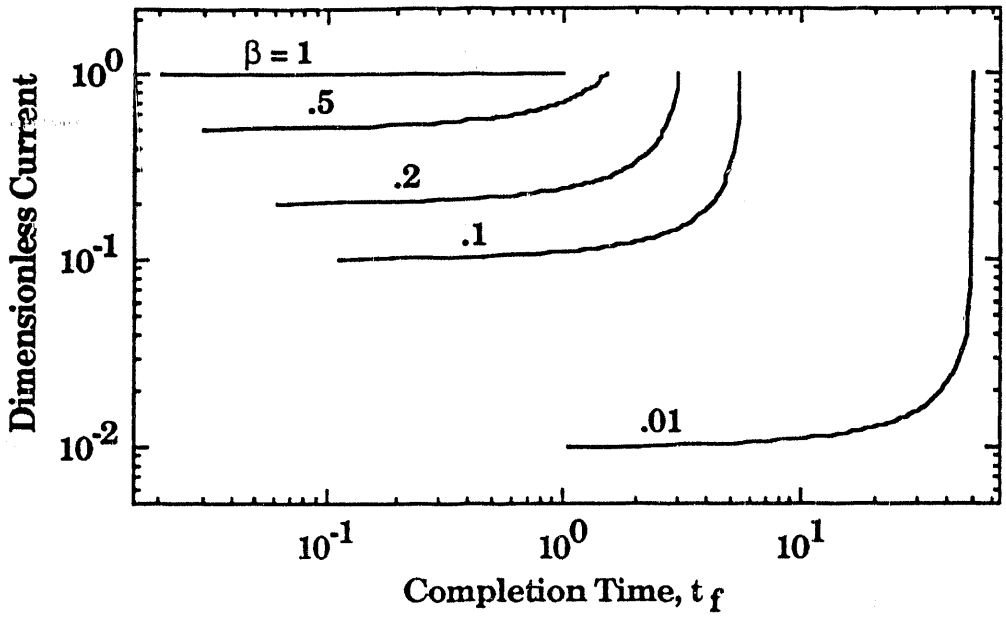

Figure 5.3: Current transients for various conductivity ratios for the 1-D case with fast kinetics. XBL 924-892

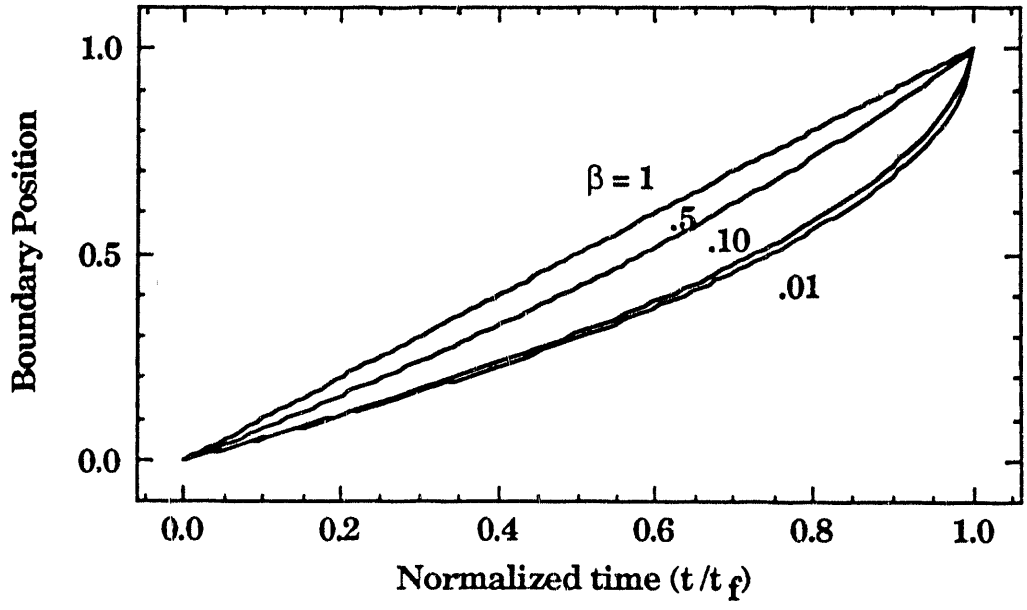

Figure 5.4: Boundary position transients for various conductivity ratios for the 1-D case with fast kinetics. The time values have been normalized by the completion times from equation [12] to facilitate comparison between the cases. XBL 924-893

5-2 Special Cases of Nodule Growth: 1-D Linear Kinetics

In this case, we replace the simple ohmic boundary between the nickel hydroxide and nickel oxy-hydroxide phases with a linear kinetic expression. The current continuity expression is still valid, but now there is a potential difference across the interface. This kinetic overpotential is proportional to the current across the interface. The modified boundary conditions on the kinetic interface are then:

Equation	Dimensionless Groups	Non-Dimensional Form	
$i = k(\Phi^{(2)}(h) - \Phi^{(1)}(h))$	$\lambda = h/L$	$i = \alpha(\Phi^{(2)}(\lambda) - \Phi^{(1)}(\lambda))$	[13a-e]
	$\alpha = k L/\kappa_1$		
$\kappa_1\left[\frac{\partial\Phi^{(1)}}{\partial y}\right]_{x=h} = \kappa_2\left[\frac{\partial\Phi^{(2)}}{\partial y}\right]_{x=h}$	$i = \frac{i L}{\kappa_2 \Phi_0}$	$\frac{\partial\Phi^{(1)}}{\partial y} = \beta\frac{\partial\Phi^{(2)}}{\partial y}$	[14a-d]
	$\beta = \kappa_2/\kappa_1$		

The solutions to the potentials in dimensionless form, for the respective nickel oxy-hydroxide and nickel hydroxide regions, are compared to the solutions for the ohmic case in equations [15] and [16]. As expected, the solutions are quite similar, the difference being a term in the denominator which represents the ratio of the conductivity ratio between the phases to the kinetics of the phase conversion reaction. This ratio increases the potential difference between the phases for slow kinetics. In the limit of very fast kinetics or very low conductivity in the nickel hydroxide phase ($\alpha >> \beta$), the linear kinetic expressions become identical to those for a simple ohmic junction.

Ohmic	Linear	
$\Phi^{(1)}(y) = \frac{\beta}{1 + \lambda(\beta - 1)} y$,	$\Phi^{(1)}(y) = \frac{\beta y}{\frac{\beta}{\alpha} + [1 + \lambda(\beta - 1)]}$, $0 \le y \le \lambda$	[15a,b]
$\Phi^{(2)}(y) = 1 - \frac{(1-y)}{1 + \lambda(\beta - 1)}$	$\Phi^{(2)}(y) = 1 - \frac{\alpha(1 - y)}{\frac{\beta}{\alpha} + [1 + \lambda(\beta - 1)]}$, $\lambda \le y \le 1$	[16a,b]

The current density is uniform throughout the film and is given by:

$$i(\lambda) = \frac{\alpha \beta}{\beta + \alpha[1 + \lambda(\beta - 1)]} \qquad [17]$$

The position of the interface, λ, is differentially related to the current density as in the ohmic case. The solution for λ, in equation [20], however is somewhat more complicated than the ohmic case (equation [11]):

$$\frac{\partial \lambda}{\partial t} = i(\lambda) \qquad [18]$$

$$t = t\frac{\Phi_0 \kappa_2 M_w}{\rho n F L^2} = t\frac{(\text{Current})}{(\text{Charge})} \qquad [19]$$

$$\lambda(t) = \frac{\alpha + \beta}{\alpha(\beta - 1)}\left[1 - \left[1 + \frac{2\,\alpha^2\beta(\beta - 1)t}{(\alpha + \beta)^2}\right]^{\frac{1}{2}}\right] \qquad [20]$$

The completion time, the time at which the reaction front reaches the electrolyte interface, is determined by solving for $\lambda = 1$. This result, shown in equation [21], shows the degree to which the completion is delayed by kinetic expressions. The effect is more easily seen in figure 5.5. Note that for low conductivity ratios, the effect of kinetic resistance is only slight.

$$t_f = \frac{\alpha + \alpha\beta + 2\beta}{2\,\alpha\beta} \qquad [21]$$

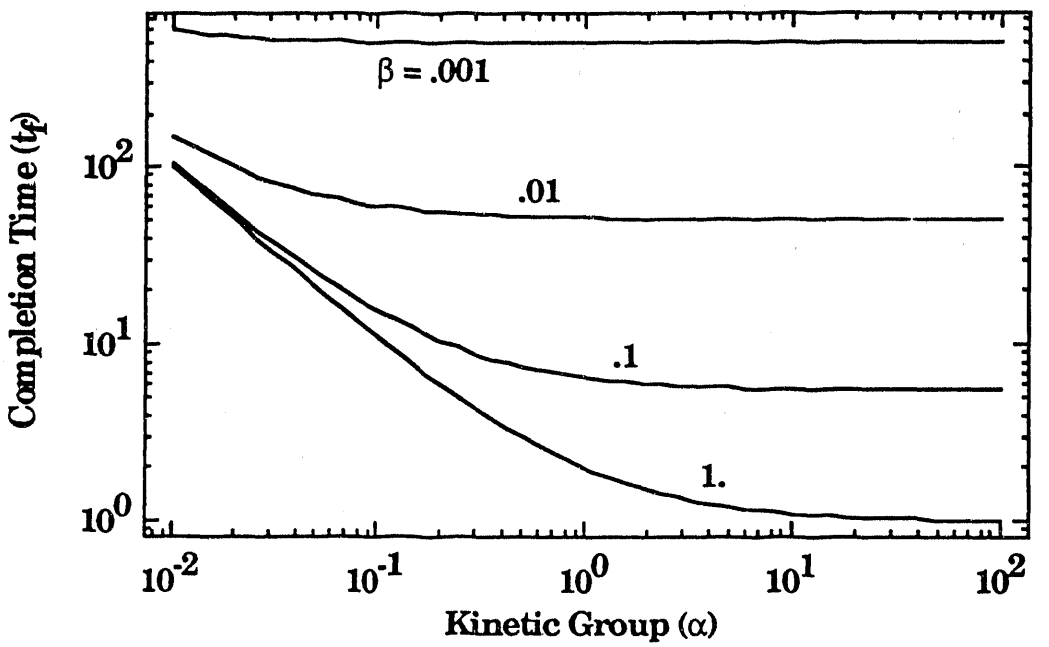

Figure 5.5: Reaction completion time versus the non-dimensional kinetic coefficient for various conductivity ratios, $\beta = \kappa_2/\kappa_1$, for the 1-D case. XBL 924-894

The kinetics also affect the shape of the current and phase boundary transients. For the ohmic case, the transients show an acceleration effect toward completion. The drag from slow kinetics not only extends the completion time as shown in figure 5.5, but tends to linearize the transient. This effect is shown in figure 5.6, where the completion time has been normalized in order to compare different cases. This flattening of the transient is the result of the interfacial kinetic resistance dominating the film resistances.

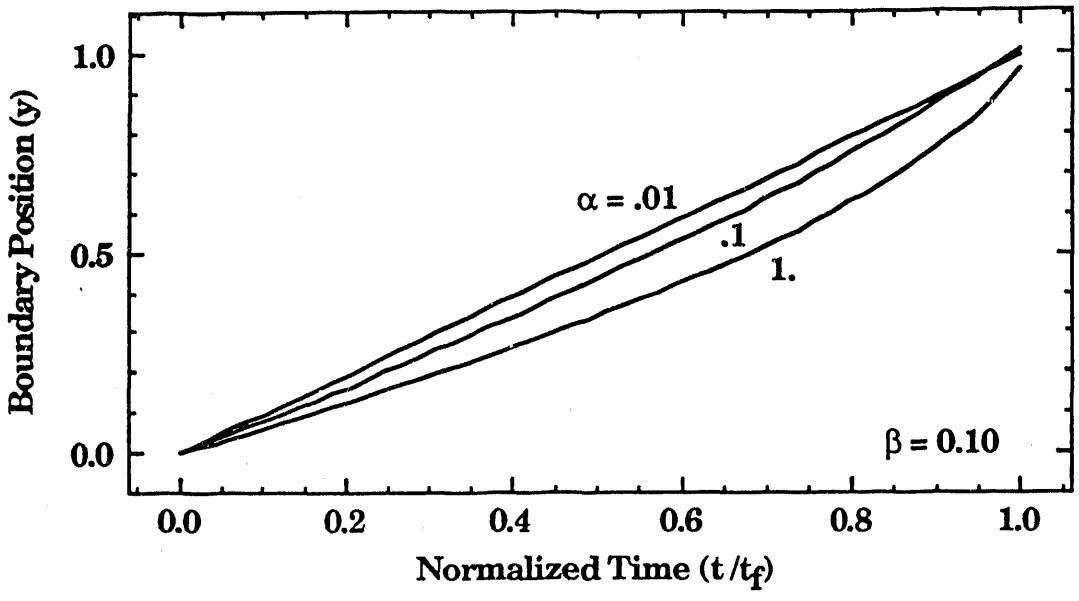

Figure 5.6: Boundary position transients for various kinetic values, α, for the 1-D case. XBL 924-895

5-3 Nomenclature for the 1-D Cases

Super- and Subscripts refer to film phase: 1, (1) nickel oxy-hydroxide; 2, (2) nickel hydroxide

F Faraday's Constant: 96,485 C/mol

h Position of nickel hydroxide/nickel oxy-hydroxide interface

i Current density

i Dimensionless current density, defined in [8d], [14b]

k Linear Kinetic Coefficient

L Overall Film Thickness

$\mathbf{M_w}$ Molecular weight

n Number of electrons per equivalent.

t Dimensionless time, defined in [10a,b]

t Time in seconds

y Dimensionless Position, defined in [1c]

y Position

α Dimensionless kinetic coefficient, defined in [13c]

β Relative conductivity, defined in [5b]

Φ Potential, Φ_0 potential at film/electrolyte interface.

κ Effective conductivity electronic and ionic.

λ Dimensionless Reaction interface position, defined in [4b]

ρ Density of nickel hydroxide materials

5-4 Two-Dimensional Model with Linear Kinetics

Intuition suggests that the fundamental nature of the charging transient in the nickel hydroxide electrode is one of nucleation and growth of nickel oxy-hydroxide nodules through the nickel hydroxide film. Therefore, the problem of modeling this phenomenon is inherently two or three dimensional. We have shown in the previous section that the current and phase boundary transients accelerate towards completion as the nickel hydroxide layer thins. This presents an opportunity for localized instability that would give rise to nodular growth of the nickel oxy-hydroxide phase. We have extended the simple one-dimensional model to a two-dimensional axisymmetric one in order to determine whether the simple physics embodied in our model will demonstrate complex growth behavior and verify our intuition about the nature of the transformation.

In constructing a model that describes the transformation of nickel hydroxide to nickel oxy-hydroxide, we would like to describe the evolution of the shape of the reaction front as the film is charged. To accomplish this, we will calculate the potential and current distribution from an electrostatic model. From the current distribution, we calculate the movement of the boundary using Faraday's Law.

In the electrostatics problem, the Laplace equation, [22], is solved in two adjacent regions having different conductivities and joined by a kinetic boundary that is single-valued in the y direction. This problem is illustrated schematically in figure 5.7. The external boundary conditions given in equations [23-24] are that the potential at the film/substrate interface is zero and some constant value at the film/electrolyte interface. These surfaces are treated as equipotential surfaces since the conductivities of the metal substrate and electrolyte phases are substantially larger than either of the two oxidized nickel phases. The lateral boundaries in equations [25a,b] have no-flux symmetry conditions representing the peak of the nodule and the mid-point between neighboring ones.

$$\frac{d^2\Phi}{dx^2} + \frac{d^2\Phi}{dy^2} = 0 \qquad [22]$$

$$\Phi(x,0) = 0 \qquad [23]$$

$$\Phi(x,H) = \Phi_0 \qquad [24]$$

$$\left.\frac{d\Phi}{dx}\right|_{x=0} = \left.\frac{d\Phi}{dx}\right|_{x=L} = 0 \qquad [25a,b]$$

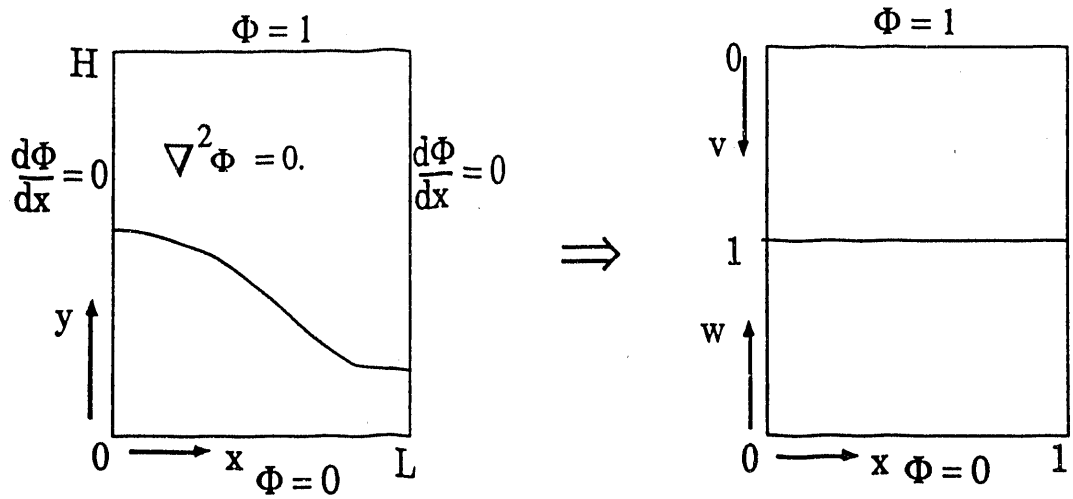

Figure 5.7: The domain and boundary conditions for the two-dimensional model for the nickel hydroxide electrode and the transformation of variables mapping the complicated, but single-valued, interface into a simple rectangular geometry. XBL 924-896

At the reaction interface, $y_B(x)$, the boundary conditions are continuity of current, [26a,b], and a linear kinetic expression, [27].

$$i(x,y_B) = -\kappa_1 \left.\frac{d\Phi^{(1)}}{dn}\right|_{y=y_B} = -\kappa_2 \left.\frac{d\Phi^{(2)}}{dn}\right|_{y=y_B} \qquad [26a,b]$$

$$i(x,y_B) = \alpha(\Phi^{(2)} - \Phi^{(1)}) \qquad [27]$$

The position of the phase boundary is differentially related to the current distribution along the boundary according to Faraday's Law, as shown in equation [28].

$$\left(\frac{\rho z F}{M_w}\right) \left.\frac{dy_B}{dn}\right|_{y=y_B} = -i(x,y_B) \qquad [28]$$

The problem is governed by three principal dimensionless groups representing the aspect ratio or spatial frequency of the initial nodule precursor, the kinetics relative to the conductivity of the nickel oxy-hydroxide phase, and the conductivity ratio of the two phases. The latter two parameters are carried over from the one-dimensional problem.

Aspect ratio: $$G_{asp} = \frac{H}{L} \qquad [29]$$

Kinetic group: $$G_{kin} = \frac{\alpha L}{\kappa_1} \qquad [30]$$

Relative Conductivity: $$G_{cond} = \frac{\kappa_1}{\kappa_2} \qquad [31]$$

5-5 Numerical Solution of the 2-D Case

The two-dimensional case is somewhat more difficult to solve than the one-dimensional cases. The manner of solution would be to find an expression for the potential distribution boundary value problem and apply this to the transient reaction interface initial value problem. As there are no analytical solutions available or readily proposed for even the potential distribution problem, a full numerical solution is therefore required. There are several ways to proceed in this manner.

The simplest method is perhaps to use a finite difference scheme[1] (FDM). A more advanced approach would be the use of finite element method[1] (FEM); and the most powerful solution technique would be the use of the boundary element method[2] (BEM). Because of the possible complexity of the evolving boundary between the nickel hydroxide and nickel oxy-hydroxide phases, the FEM would be the most difficult to implement effectively, requiring many nodes and a method to adjust the mesh as the boundary evolves.

The choice between FDM and BEM is one of simplicity versus robustness. The advantage of BEM is that it is well suited for solving the Laplace equation in arbitrary geometries. However, the implementation is somewhat involved for one domain, and rather difficult in two adjacent domains. Also, the solution is only found on the boundaries. This is not really a drawback, as one is generally interested only in the flux along the reaction front.

The implementation of the FDM is the most straight forward, replacing the differentials in the problem with difference equations and solving for the potentials at each point. Furthermore, if one restricts the boundary to being single-valued in one direction, one can make a transformation of variables into a simple orthogonal geometry having two adjacent rectangular domains. This transformation is illustrated in figure 5.7. This transforms the Laplace equation into a more general elliptic equation.

For the mapping, we define dimensionless coordinates for the lateral x-coordinate, [32]; and the vertical y-coordinate in the lower(w), [33]; and upper(v) domains, [34]. We also cast the position of the reaction interface in dimensionless

---

1 L. Lapidus, G. Pinder, *Numerical Soluton of Partial Differential Equations in Science and Engineering*, Wiley, 1982

2 C.A. Brebbia, *The Boundary Element Method for Engineers*, Wiley, 1978

form as in [35].

$$u = \frac{x}{L} \qquad [32]$$

$$w = \frac{y}{y_B(x)} \qquad [33]$$

$$v = \frac{H - y}{h - y_B(x)} \qquad [34]$$

$$\lambda = \frac{y_B(x)}{H} \qquad [35]$$

Transforming the Laplace equation for the upper nickel hydroxide domain into the (u,v) coordinate domain, the result, [36], is a fully elliptic differential equation. Casting [36] into a more tractable form and substituting for the partial derivatives gives [37], with the fully fleshed out coefficients {A...F} [38-42].

$$\left(\frac{\partial u}{\partial x}\right)^2 \frac{d^2\Phi}{du^2} + \left(\left(\frac{\partial v}{\partial x}\right)^2 + \left(\frac{\partial u}{\partial y}\right)^2\right)\frac{d^2\Phi}{dv^2}$$

$$+ 2\left(\frac{\partial u}{\partial x}\right)\left(\frac{\partial v}{\partial x}\right)\frac{d^2\Phi}{du\,dv} + 2\left(\frac{\partial^2 v}{\partial x^2}\right)\frac{d\Phi}{dv} = 0 \qquad [36]$$

$$A\frac{d^2\Phi}{du^2} + B\frac{d^2\Phi}{du\,dv} + C\frac{d^2\Phi}{dv^2} + D\frac{d\Phi}{dv} + E\frac{d\Phi}{du} + F = 0 \qquad [37]$$

$$A = 1 \qquad [38]$$

$$B = \frac{2v}{(1-\lambda)}\left(\frac{d\lambda}{du}\right) \qquad [39]$$

$$C = \left(\frac{v}{(1-\lambda)}\left(\frac{d\lambda}{du}\right)\right)^2 + \left(\frac{1}{G_{asp}(1-\lambda)}\right)^2 \qquad [40]$$

$$D = \frac{4v}{(1-\lambda)^2}\left(\frac{d\lambda}{du}\right)^2 + \frac{2v}{(1-\lambda)}\left(\frac{d^2\lambda}{du^2}\right) \qquad [41]$$

$$E = F = 0 \qquad [42]$$

Similarly for the lower nickel oxy-hydroxide (u,w) domain:

$$\left(\frac{\partial u}{\partial x}\right)^2\frac{d^2\Phi}{du^2} + \left(\left(\frac{\partial w}{\partial x}\right)^2 + \left(\frac{\partial u}{\partial y}\right)^2\right)\frac{d^2\Phi}{dw^2}$$

$$+ 2\left(\frac{\partial u}{\partial x}\right)\left(\frac{\partial w}{\partial x}\right)\frac{d^2\Phi}{du\,dw} + 2\left(\frac{\partial^2 w}{\partial x^2}\right)\frac{d\Phi}{dw} = 0 \qquad [43]$$

$$A\frac{d^2\Phi}{du^2} + B\frac{d^2\Phi}{du\,dw} + C\frac{d^2\Phi}{dw^2} + D\frac{d\Phi}{dw} + E\frac{d\Phi}{du} + F = 0 \qquad [44]$$

$$A = 1 \qquad [45]$$

$$B = \frac{-2\,w}{\lambda}\left(\frac{d\lambda}{du}\right) \qquad [46]$$

$$C = \left(\frac{w}{\lambda}\left(\frac{d\lambda}{du}\right)\right)^2 + \left(\frac{1}{G_{asp}\,\lambda}\right)^2 \qquad [47]$$

$$D = \frac{4\,w}{\lambda^2}\left(\frac{d\lambda}{du}\right)^2 - \frac{2\,w}{\lambda}\left(\frac{d^2\lambda}{du^2}\right) \qquad [48]$$

$$E = F = 0 \qquad [49]$$

In order to solve equations [37] and [44] numerically, they are discretized using central difference approximations to the derivatives. Equation [50] represents these equations in difference form. The coefficients, $\{a_{ij}...f_{ij}\}$, in the difference equation are related to those in the differential equations for each domain, {A...F}, through equations [51-56]. In our solution, we have chosen to construct the mesh with even node spacing in the vertical and lateral directions. The spacing constants are the variables m and n.

$$a_{ij}\,\Phi_{i,j+1} + b_{ij}\,\Phi_{i,j-1} + c_{ij}\,\Phi_{i+1,j} + d_{ij}\,\Phi_{i-1,j} + e_{ij}\,\Phi_{i,j} - f_{ij} = 0 \qquad [50]$$

$$a_{ij} = \frac{C}{n^2} - B\frac{mn}{(m^2+n^2)^2} + \frac{D}{2n} \qquad [51]$$

$$b_{ij} = \frac{C}{n^2} - B\frac{mn}{(m^2+n^2)^2} - \frac{D}{2n} \qquad [52]$$

$$c_{ij} = \frac{A}{m^2} + B\frac{mn}{(m^2+n^2)^2} + \frac{E}{2m} \qquad [53]$$

$$d_{ij} = \frac{A}{m^2} - B\frac{mn}{(m^2+n^2)^2} - \frac{E}{2m} \qquad [54]$$

$$e_{ij} = \frac{-2A}{m^2} - \frac{-2C}{n^2} \qquad [55]$$

$$f_{ij} = -F \qquad [56]$$

The kinetic boundary condition, equation [57], relates the current, which is proportional to the normal derivative of the potential, and the potentials at adjacent points on either side of the boundary.

$$\frac{d\Phi}{d\tilde{n}} = G_{kin}\,(\Phi^{(2)} - \Phi^{(1)}) \qquad [57]$$

Transforming the normal derivative into the new coordinates via trigonometric identities gives equation [58], which relates the normal derivative to each of the orthogonal components of the potential gradient.

$$\frac{d\Phi}{d\tilde{n}} = \frac{-G_{asp}\frac{d\lambda}{du}}{\left(1+\left(G_{asp}\frac{d\lambda}{du}\right)^2\right)^{1/2}}\frac{d\Phi}{du} + \frac{1+w\left(G_{asp}\frac{d\lambda}{du}\right)^2}{G_{asp}\,\lambda\left(1+\left(G_{asp}\frac{d\lambda}{du}\right)^2\right)^{1/2}}\frac{d\Phi}{dw} \qquad [58]$$

Substituting the normal derivative, [58], and difference equations into the boundary equation, [57], yields equation [59].

$$\Phi^{*}_{i,j+1} = Q\,\Phi_{i,j+1} + \Phi_{i,j-1} + R\,\Phi_{i+1,j} - R\,\Phi_{i-1,j} - Q\,\Phi_{i,j} \qquad [59]$$

$$Q = \frac{2\,n\,G_{kin}\,G_{asp}\,\lambda\left(1 + \left(G_{asp}\frac{d\lambda}{du}\right)^2\right)^{1/2}}{1 + w\left(G_{asp}\frac{d\lambda}{du}\right)^2} \qquad [60]$$

$$R = \frac{G_{asp}^2\,\lambda\left(\frac{n}{m}\right)\left(\frac{d\lambda}{du}\right)}{1 + w\left(G_{asp}\frac{d\lambda}{du}\right)^2} \qquad [61]$$

The point $\Phi^{*}_{i,j+1}$ is a virtual node, that is, a point spatially outside the domain but having the same properties as the domain. This virtual point comes from the central difference equations for the normal derivative of the potential. In contrast, $\Phi_{i,j+1}$, in equation [58], is a real point that belongs to the upper domain and is part of the expression for the kinetic overpotential. The expression for the virtual node is substituted into equation [50] for the nodes along the reaction interface.

For the upper domain, there are similar expressions. In this case, the virtual point is $\Phi^{*}_{i,j-1}$.

$$\Phi^{*}_{i,j-1} = \Phi_{i,j+1} - Q\,\Phi_{i,j-1} + R\,\Phi_{i+1,j} - R\,\Phi_{i-1,j} + Q\,\Phi_{i,j} \qquad [62]$$

$$Q = \frac{2\,n\,G_{cond}\,G_{kin}\,G_{asp}\,(1-\lambda)\left(1+\left(G_{asp}\frac{d\lambda}{du}\right)^2\right)^{1/2}}{1+v\left(G_{asp}\frac{d\lambda}{du}\right)^2} \qquad [63]$$

$$R = \frac{G_{asp}^2\,(1-\lambda)\left(\frac{n}{m}\right)\left(\frac{d\lambda}{du}\right)}{1+v\left(G_{asp}\frac{d\lambda}{du}\right)^2} \qquad [64]$$

The exterior boundary conditions are somewhat simpler to pose. For difference equations that refer to nodes across boundaries, the coefficients of the exterior nodes are set to reflect the proper boundary condition. For example, along the y=0 boundary (equation [65]), the potential is zero. In the difference equations for j=0, the $b_{0,i}$ coefficient is multiplied with a node whose potential is always zero. Therefore, that coefficient is set to zero. Similarly, along the upper boundary, the same thing occurs except the exterior node is always equal to unity.

Real Domain	Transformed Domain	Difference Equation	Difference Coefficients	
$\Phi(y=0) = 0$	$\Phi(v=0) = 0$	$\Phi_{i,-1} = 0$	$b_{0,i} = 0$	[65a-d]
$\Phi(y=H) = 1$	$\Phi(w=0) = 1$	$\Phi_{i,N+1} = 1$	Set $f_{in} = -a_{iN}$, Then set $a_{iN} = 0$.	[66a-e]
$\left.\frac{d\Phi}{dx}\right\|_{x=0} = 0$	$\left.\frac{d\Phi}{dx}\right\|_{u=0} = 0$	$\Phi_{-1,j} = \Phi_{0,j+1}$	First set $c_{0j} = c_{0j} + d_{0j}$, then set $d_{0j} = 0$.	[67a-e]
$\left.\frac{d\Phi}{dx}\right\|_{x=L} = 0$	$\left.\frac{d\Phi}{dx}\right\|_{u=1} = 0$	$\Phi_{M+1,j} = \Phi_{M,j}$	First set $d_{Mj} = d_{Mj} + c_{Mj}$, then set $c_{Mj} = 0$.	[68a-e]

The full set of difference equations forms an (MxN) by (MxN) sparse matrix equation. This is solved for the potentials, Φ_{ij}, using the method of simultaneous over-relaxation as developed by Press[3] and modified for adaptive step-size to optimize the convergence rate. The computer program for this numerical model is listed in Appendix B, coded in the C programming language.

3 W.H. Press, B.P. Flannery, S.A. Teukolsky, W.T. Vetterling, *Numerical Recipes, The Art of Scientific Computing,* Cambridge University Press, 1986

5-6 Nomenclature for the Two-Dimensional Model

Subscripts:

i	lateral node index
j	vertical node index
M	Number of lateral nodes
N	Number of vertical nodes

Roman Symbols

x	Lateral spatial coordinate in physical geometry
y	Vertical spatial coordinate in physical geometry
y_B	Vertical spatial coordinate of phase boundary in physical geometry
u	Dimensionless lateral spatial coordinate in transformed geometry, defined in [32]
v	Dimensionless vertical spatial coordinate in upper (nickel hydroxide) domain of transformed geometry, defined in [34]
w	Dimensionless vertical spatial coordinate in lower (nickel oxy-hydroxide) domain of transformed geometry, defined in [33]
i	Current density
L	Lateral dimension in physical geometry
H	Vertical dimension in physical geometry
{A...F}	Coefficients to diffentials in transformed the Laplace Eqn.
{a...f}	Coefficients to potential nodes in difference form of transformed the Laplace Eqn.
m	Vertical node spacing
n	Lateral node spacing
ñ	Coordinate normal to reaction interface
G_{asp}	Aspect ratio of film thickness to nodule spacing, defined in [29]
G_{cond}	Conductivity ratio between upper (nickel hydoxide) and lower phases (nickel oxy-hydoxide), defined in [31]

G_{kin} Dimensionless kinetic parameter, ratio of film resistance to kinetic resistance, defined in [30]

Q Coefficient for diffential equation of boundary condition

R Coefficient for diffential equation of boundary condition

Mw Molecular weight of film material

z Number of equivalents in reaction, one equiv/mol

F Faraday's constant: 96,485 Coulombs/mol

Greek symbols

α Linear kinetic coefficient

Φ Potential

κ Effective conductivity, ionic or electronic

λ Dimensionless vertical coordinate of interface position, defined in [35]

ρ Density of film materials

5-7 Results of Numerical Modeling

The first cases to which we applied the model were test cases to verify the accuracy of our model against previous results. The first and simplest cases were to verify the model against the analytical solutions of the one-dimensional cases from sections 5-1 and 5-2. In some respects, these tests present a difficult numerical challenge. Small numerical discrepancies between lateral nodes tend to become amplified just as small perturbations in the reaction interface would in reality. The comparisons to the one-dimensional ohmic and linear kinetic cases are presented in figures 5.8 and 5.9, respectively. The agreement is quite satisfactory. The slight discrepancy towards completion is most likely due to cumulative integration error in moving the boundary. Decreasing the integration step lessens this difference while increasing the number of times that the potential distribution must be solved.

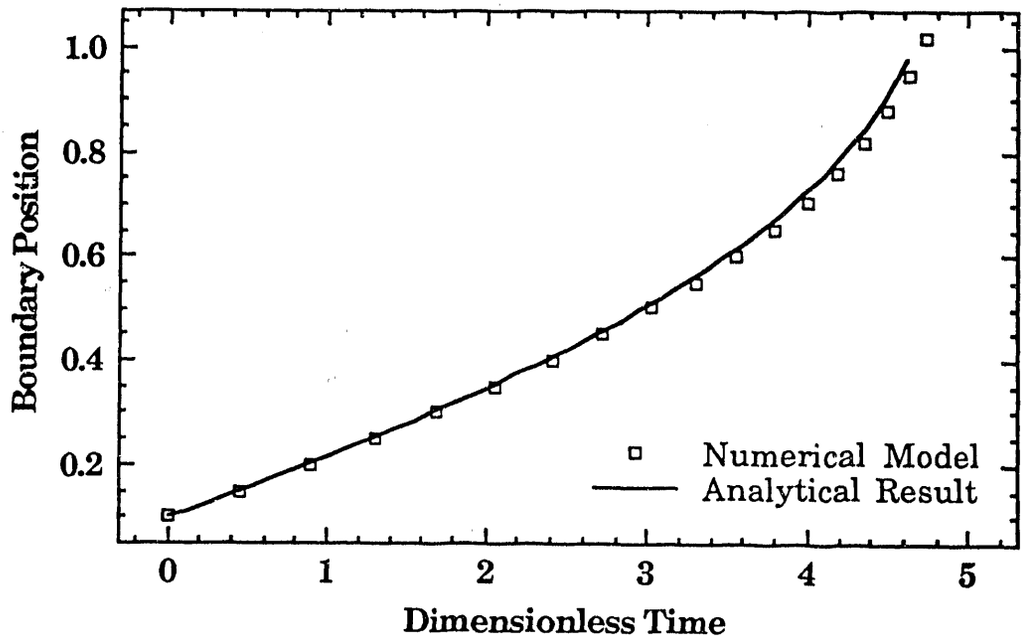

Figure 5.8: Comparison of the boundary position calculated by the numerical model to the analytical solution for a flat reaction interface with very fast kinetics. XBL 924-897

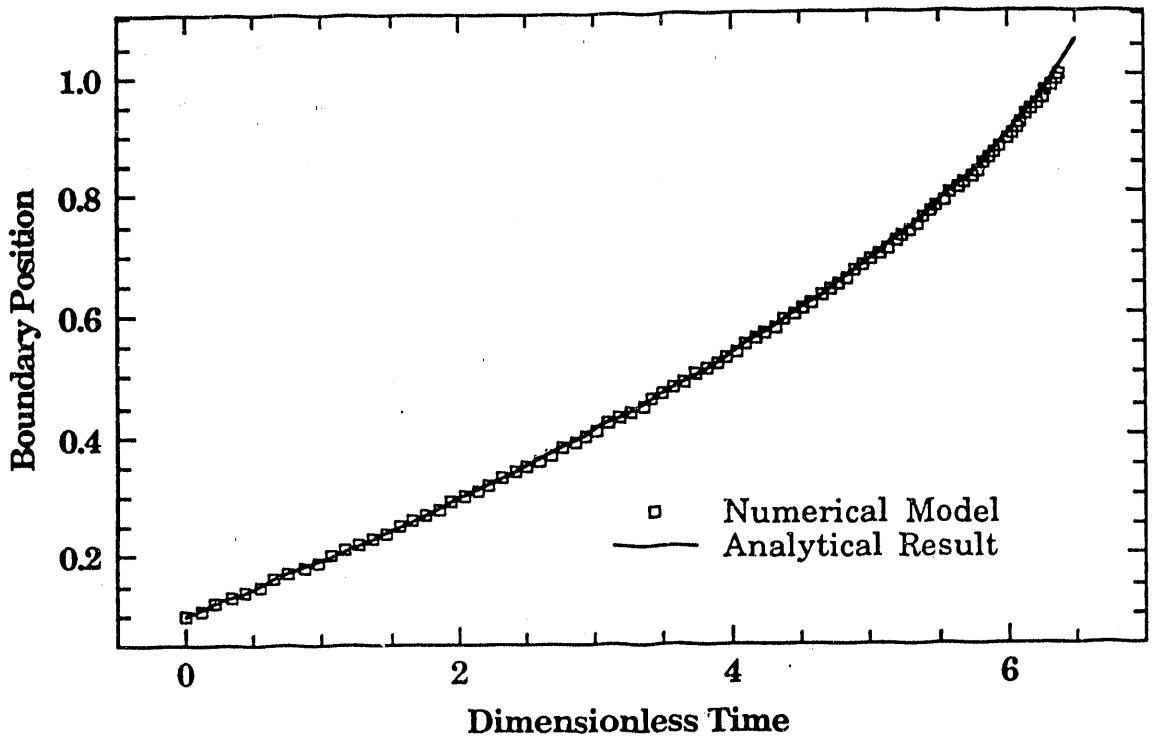

Figure 5.9: Comparison boundary position calculated by numerical model to the analytical solution for flat boundary with linear kinetics. XBL 924-898

Unfortunately, no analytical solutions could be produced or found in the literature for the two-dimensional case exactly as we have developed it. However, numerical and perturbation solutions do exist for the case of metal deposition from aqueous electrolyte to a sinusoidal profile. These solutions are the limiting case for our model as the conductivity of the lower, nickel oxy-hydroxide, phase becomes extremely large with respect to the upper phase and the aspec ratio becomes large. The comparison of the current distribution predicted by a perturbation solution by Fedkiw[4] and our model is presented in figure 5.10. Discrepancy in the valley of the profile is the result of the proximity of the

---

4 P. Fedkiw, J. Electrochem. Soc. **127**, 1304 (1980)

equipotential substrate surface. The perturbation solution does not seem particularly smooth, which may be the result of the truncating the solution at the fifth order terms.

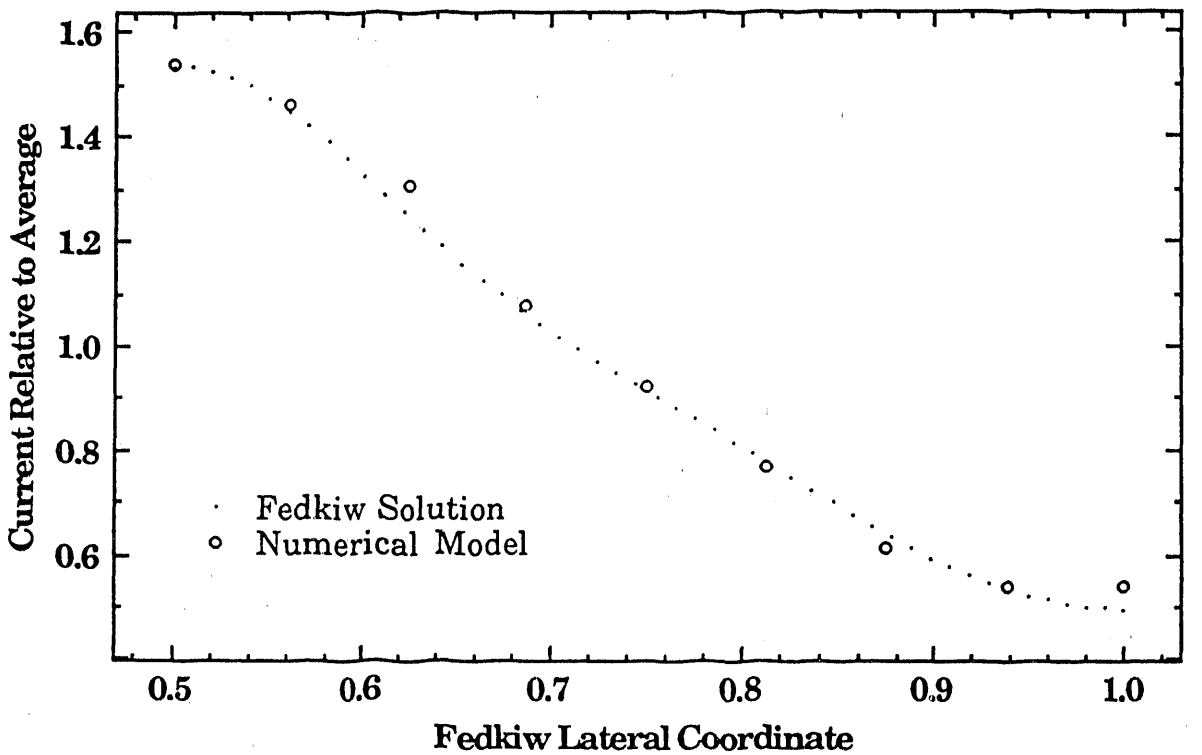

Figure 5.10: Comparison of the numerical model to an analytical perturbation solution by Fedkiw (ref. 4) for the current distribution to a sinusoidal profile. To approach this limit, the conductivity ratio and aspect ratios were both set to 1000. XBL 924-899

5-8 Simulated Nickel Oxy-hydroxide Nodule Growth

The results of our numerical simulation of the nickel hydroxide electrode charging process under conditions comparable to the physical experiments confirm our prediction of nodular growth within the thin films. We studied the simulated electrode behavior over a large parameter space spanning a wide range of conditions. Conductivity ratios between 1 and 1000 include conditions for pure and

doped materials. Aspect ratios between 0.10 and 10 span the range representing sparse and dense nodule area densities for a constant film thickness, or various total film thicknesses for fixed nodule size. Kinetic group values between 0.01 and 1000 range between behaviors governed by film resistance to those governed by interfacial kinetic resistance. Various shapes for the initial nodule configuration were also considered. Typical behavior is illustrated in the results for the phase boundary position and current transients in figures 5.11 and 5.12. For closer analysis, the boundary evolution and interfacial current distribution versus charge are presented in figures 5.13 and 5.14.

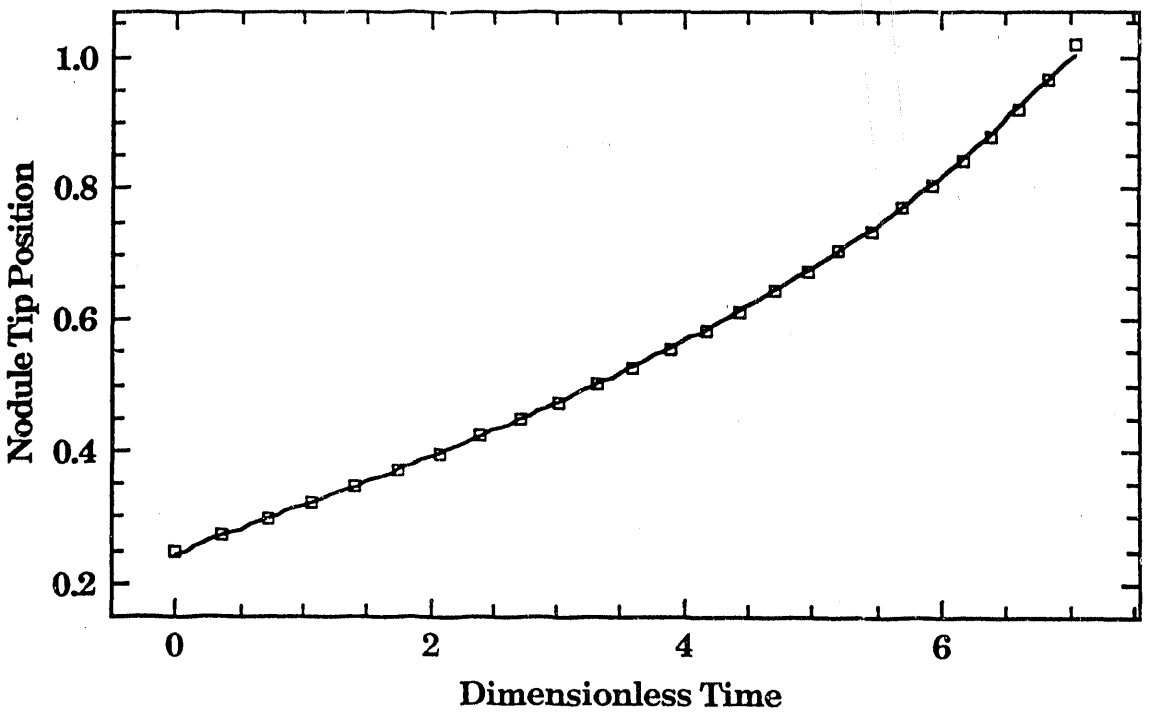

Figure 5.11: Nodule tip position transient as the electrode film is charged under typical conditions. Conductivity ratio: 20, Kinetic Group: 0.50, and Aspect ratio: 1. XBL 924-900

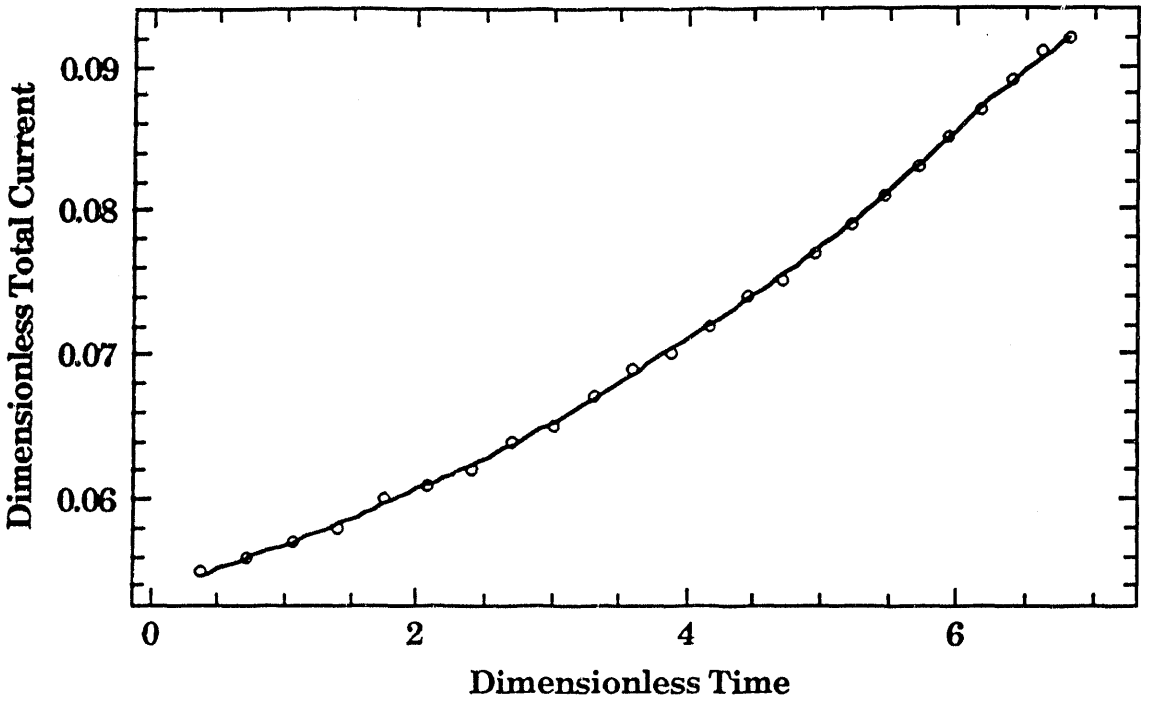

Figure 5.12: Current transient as the electrode film is charged under the typical conditions specified in figure 5.11. XBL 924-901

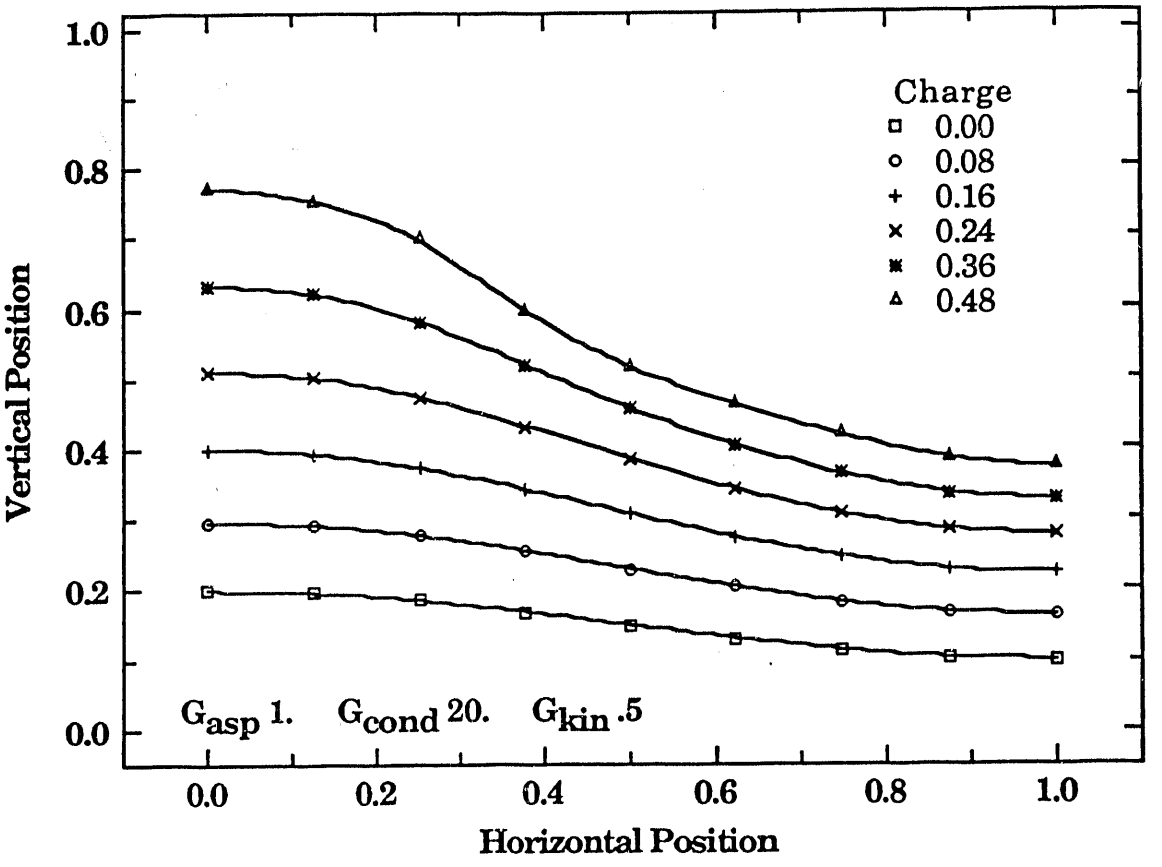

Figure 5.13: Reaction phase boundary evolution as the electrode film is charged under the conditions specified in figure 5.11. The initial nodule amplitude started at 5% of the overall film thickness and grew to more than 20% before the nodule emerged from the film. XBL 924-902

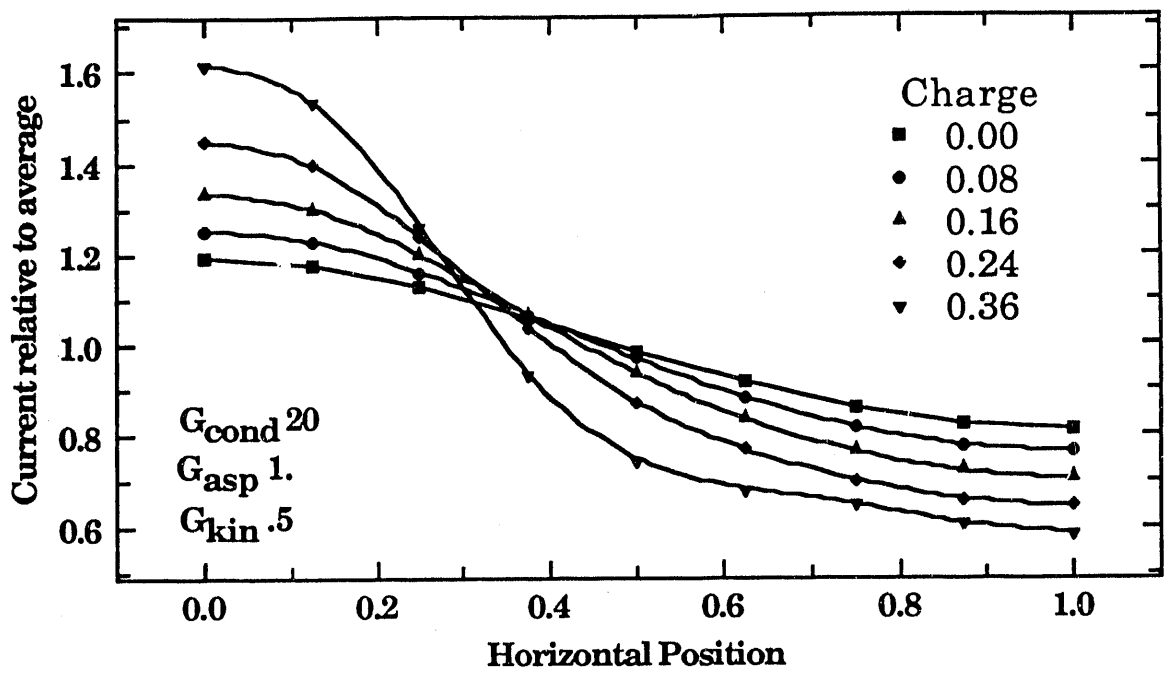

Figure 5.14: Interfacial current distribution on nodule profiles in figure 5.13 as the electrode film is charged under typical conditions.

5-9 Effect of Conductivity Ratio

The conductivity ratio between the nickel hydroxide and oxy-hydroxide phases is the dominant parameter in the model. The disparity in the conductivities is the proximate cause of the nodular growth behavior. In fact, if the conductivity ratio was less than unity (i.e., the nickel hydroxide phase was more conductive than the oxy-hydroxide phase), nodular growth would not occur at all; small perturbations on the nickel oxy-hydroxide interface would be leveled as the film was charged.

One measure of the charge utilization is the derivative of the tip position versus charge function; which, in most cases, seems to be linear. This derivative is related to the amount of charge necessary to advance the tip position a given amount. In the one-dimensional case, if the apparent volumetic charge density is small, the interface advances more quickly for a given amount of charge passed. In

the two-dimensional case, if the disparity between the peak and valley current density is large, the tip of the nodule advances quickly for a given amount of charge passed. Figure 5.16 shows that the material utilization efficiency decreases as the conductivity ratio increases.

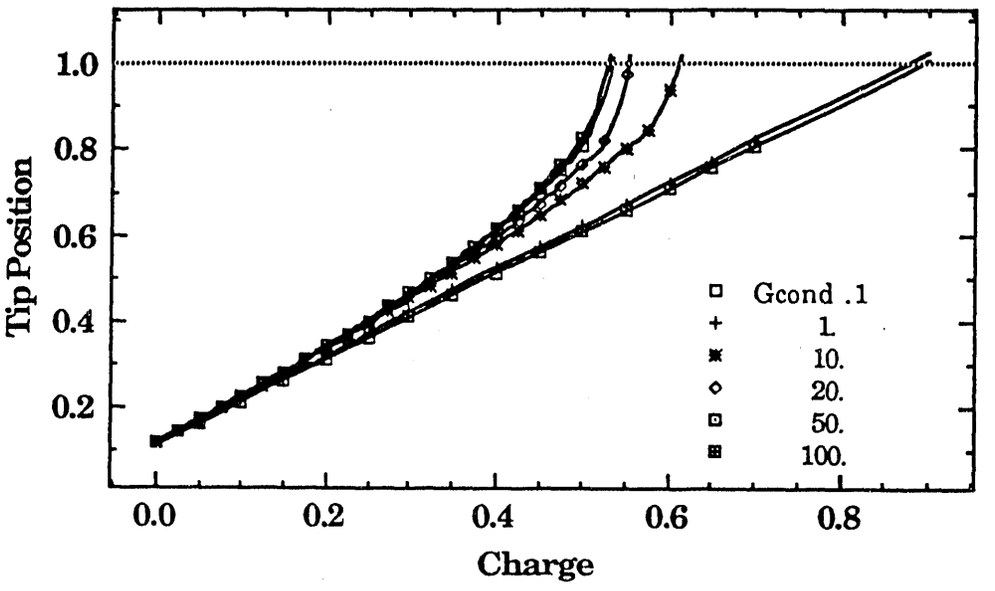

Figure 5.15: Tip position versus charge for various values of the conductivity ratio. The tip emerges at the electrolyte interface (dotted line) after smaller amounts of charge as the conductivity of the nickel oxy-hydroxide phase is increased. XBL 924-903

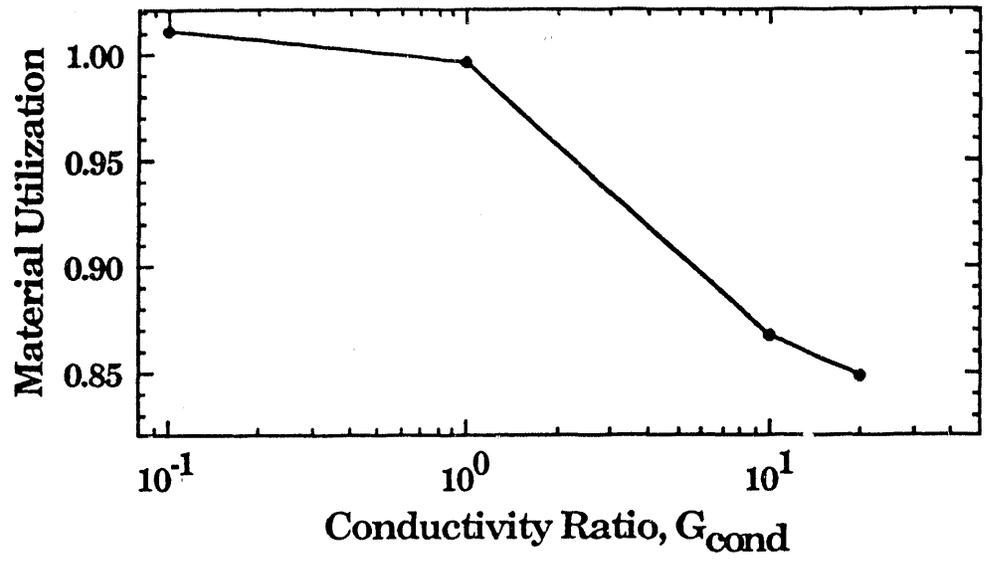

Figure 5.16: Fractional utilization of electrode material versus conductivity ratio for fast kinetic conditions. The values of the kinetic parameter and the aspect ratio are 100 and 1.0 respectively. At values greater than 50, numerical limitations of the model prevent accurate determination of the charging effieciency. XBL 924-904

5-10 Effect of Reaction Kinetics

The effect of the dimensionless kinetic parameter is significant, though less dramatic than the effect of the conductivity parameter. The kinetic parameter defined in equation [30], represents the ratio of the ohmic resistance in the film to the kinetic resistance across the reaction interface. The limiting values of this parameter range from a simple ohmic junction at high values to the case where the current is controlled by the kinetic resistance at the reaction interface. At high values, the potential is continuous across the reaction interface; whereas at low values, there is a significant kinetic overpotential between the phases across the interface. In all cases, the current is continuous across the interface.

The effect of the relative kinetic resistance on the performance of the electrode is largely beneficial. Figure 5.17 shows the transients of the tip position versus dimensionless charge passed for several values of the kinetic parameter. At low

values of the parameter where the kinetic resistance becomes significant, the transients are flattened. This indicates that the kinetic overpotential reduces the disparity in current density between the peak and valley of the growing nodule, inhibiting the tip-wise growth of the nodule. As illustrated in figure 5.18, this effect increases the material utilization as the kinetic resistance becomes significant.

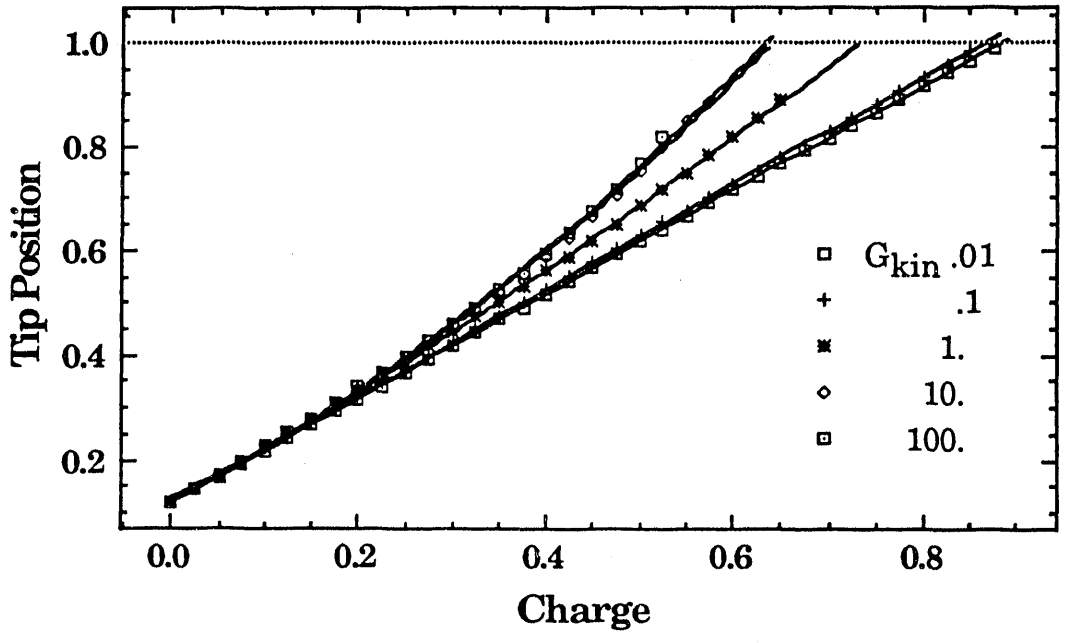

Figure 5.17: Tip position versus charge for various values of the dimensionless kinetic parameter. The parameter represents the ratio of the film resistance to the interfacial kinetic resistance. XBL 924-905

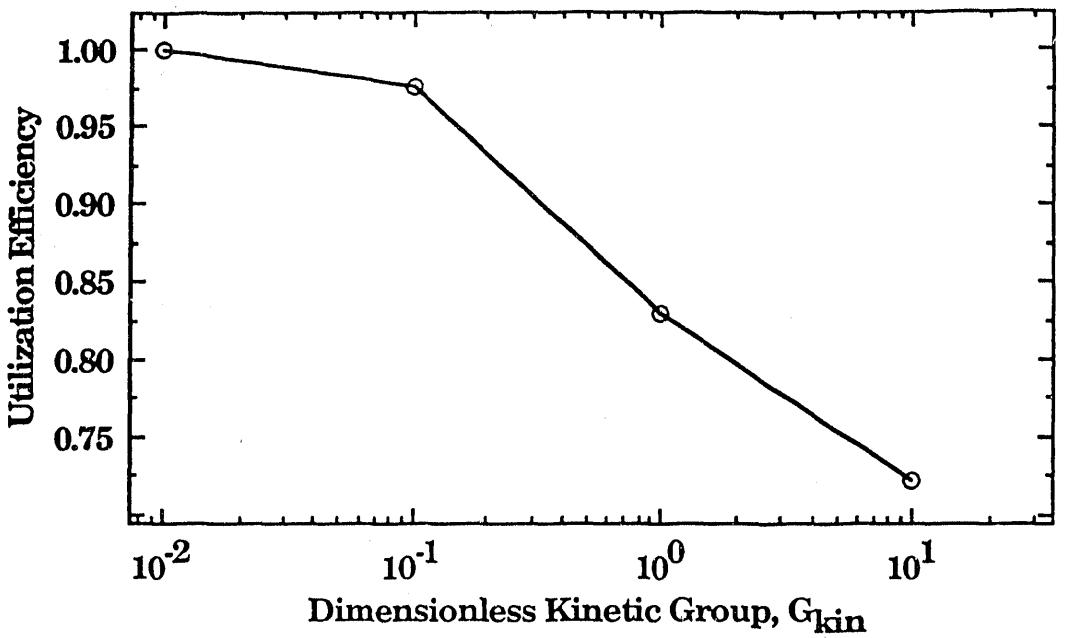

Figure 5.18: Charge utilization versus dimensionless kinetic parameter. At lower values of the parameter where the interfacial kinetic resistance becomes significant, charge utilization is increased. XBL 924-906

5-11 Effect of the Nodule Aspect Ratio

The aspect ratio, defined in equation [29], is proportional to the spatial period of the nodules, which is related to the number density of nodules on the surface. In this numerical experiment, to focus on the effect of the spatial period, we used a nodule amplitude that was a constant fraction of the film thickness, in this case 2%. The effect of this parameter is charted in figure 5.19, which shows the peak-to-valley current ratio versus the aspect ratio.

Since the numerical procedure is unstable at aspect ratios much greater than those found in the actual experiments, the nodule profiles cannot be calculated to the point of penetration of the film/electrolyte interface. Instead, the peak-to-valley current ratio is used here to characterize the nodule growth pattern. Larger initial current ratios lead to lower ultimate material utilization at penetration. For

reference, the material utilization for aspect ratio equal to unity is only 74% for the conductivity and kinetic parameter values used in this study.

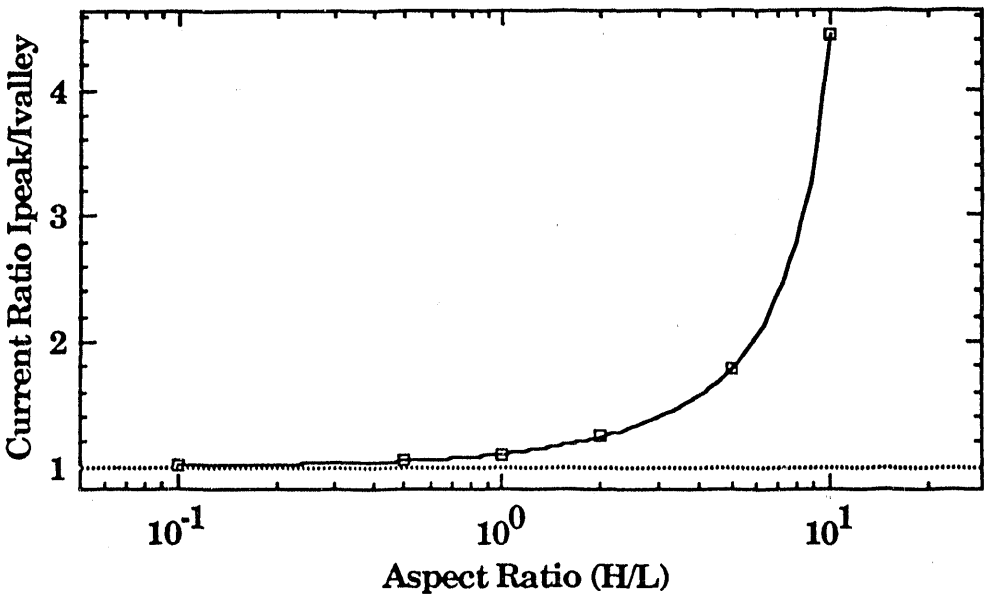

Figure 5.19: Peak-to-valley current ratio versus nodule aspect ratio. The nodule amplitude is 2% of the film thickness. The values of the kinetic and conductivity parameters are 100 and 20 respectively. XBL 924-907

5-12 Effect of Initial Nodule Shape

In this numerical experiment, we examined the effect of the initial nodule shape on the growth and material utilization pattern. One particular scenario of interest is that of renucleation; where a new nodule could grow from an existing one. For this experiment, we created a "renucleated" nodule using a superposition of two distinct Fourier cosine modes in the initial boundary shape. This shape and subsequent growth are illustrated in figure 5.20. Apparently, in this case, the current distribution along the nodule shape is governed principally by the thickness of the uncharged nickel hydroxide layer between the nickel oxy-hydroxide nodule and the film/electrolyte interface. Curvature effects do not affect

this system. The current distributions for the boundary positions in figure 5.20 are shown in figure 5.21.

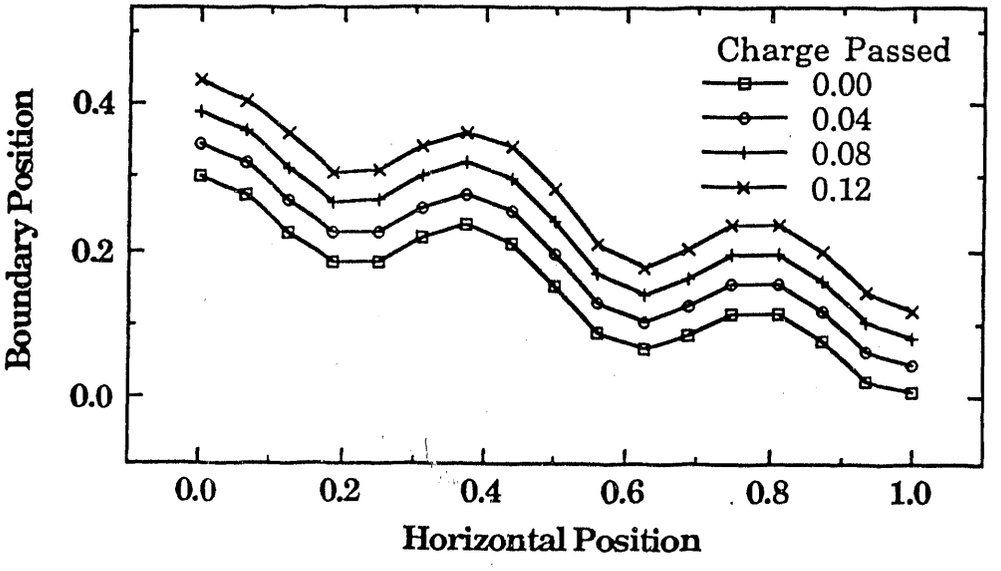

Figure 5.20: Boundary position evolution of a renucleated nodule. No preferential growth due to curvature was found. The values of the kinetic and conductivity parameters are 100 and 20 respectively. XBL 924-908

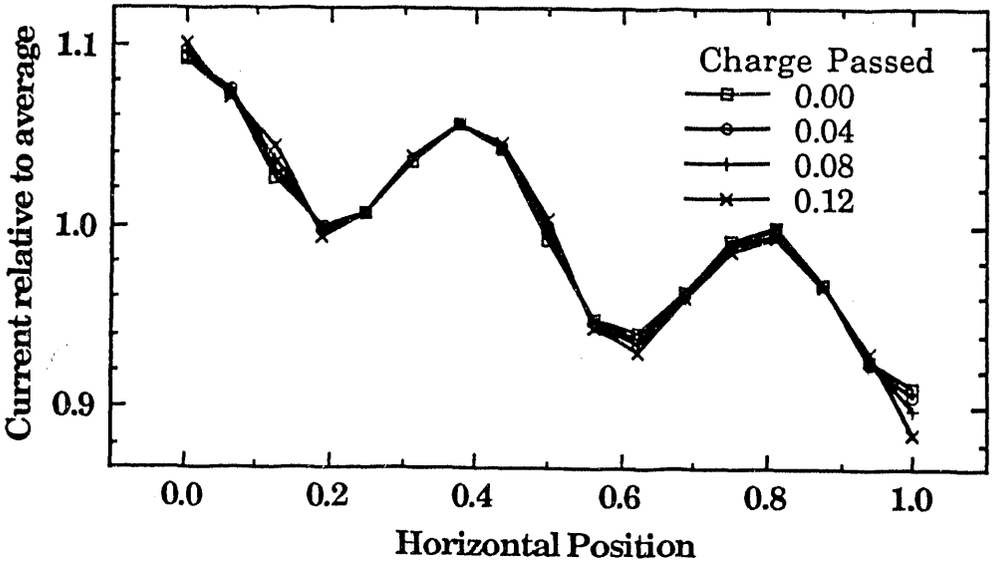

Figure 5.21: Current distributions for the boundary shapes in figure 5.20. The current distribution is principally governed by peak height as opposed to curvature. XBL 924-909

5-13 1-D/2-D Model Similarity

One of the more disconcerting revelations from the modeling is the similarity of the one and two-dimensional transients. The tip position and current density versus time functions from the two-dimensional model strongly resemble those generated from the one-dimensional model. By adjusting the apparent charge density, transient responses from the one and two-dimensional models can be made nearly identical as illustrated in figure 5.22.

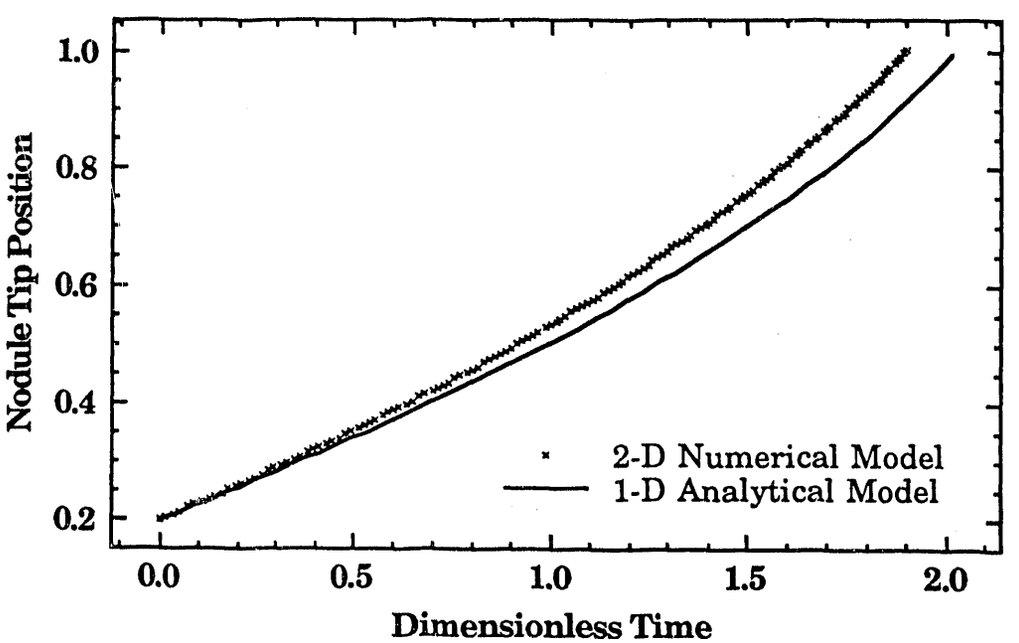

Figure 5.22: Comparison between tip transients between the one and two-dimensional models. The apparent charge density for the one-dimensional model is only 70% of that in the two-dimensional case. XBL 924-910

The root of this similarity lies in the fact that, initially the tip position is a linear function of the charge in almost all of the cases we have studied. As shown in figure 5.23, the principal difference between cases is the slope of the charge transients. This slope is related to the amount of charge necessary to advance the tip position a given amount. In the one-dimensional case, if the

apparent charge density is small, the interface advances quickly. In the two-dimensional case, if the disparity between the peak and valley current density is large, the tip advances quickly.

The main difference that distinguishes between the models, is the current versus charge behavior just before emergence of the nodules at the electrolyte interface, particularly when the kinetic resistance is relatively small compared to the film resistance. Figure 5.24 shows the increasing non-linearity of the current versus charge transients as the kinetic parameter is increased. The current versus charge transients for the one-dimensional models are always linear in the case of fast kinetics.

This similarity in the two models is unfortunate, as it only adds to the confusion in the literature regarding the discrepancies in the valence of the charged nickel oxy-hydroxide species.[5] Since pockets of uncharged material can be trapped in the film during charging, many measurements of the charge density or valence of the materials tend to underestimate the ultimate charge density of the molecular species. The similarity between the models disguises the structure that allows the material to go uncharged.

---

5 J. McBreen,"The Nickel Oxide Electrode", *Modern Aspects of Electrochemistry*, Vol. 21, R. E. White, et al (ed), Plenum Press, NY, 1991

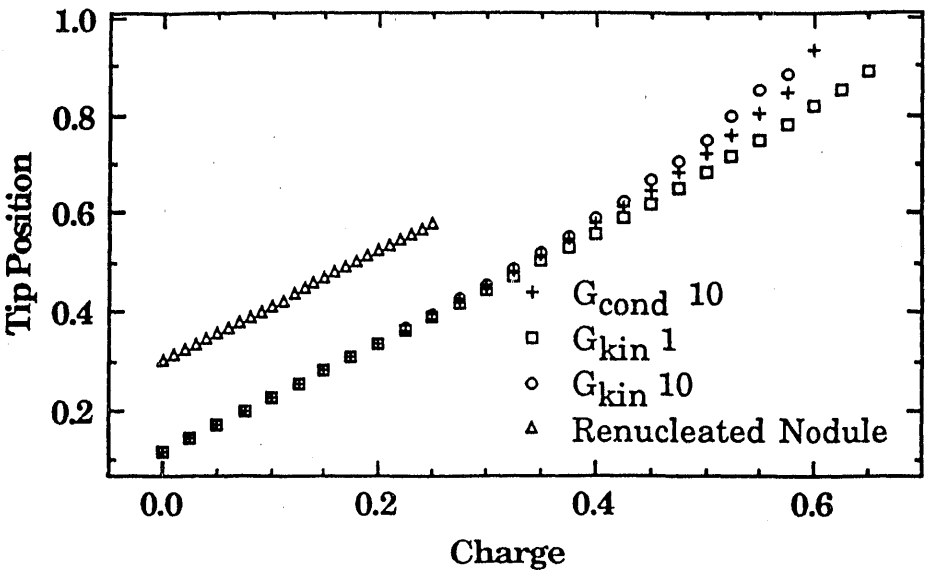

Figure 5.23: Comparison between tip transients for various conditions. Note that the functions are nearly linear as would be the case for the one-dimensional model. XBL 924-911

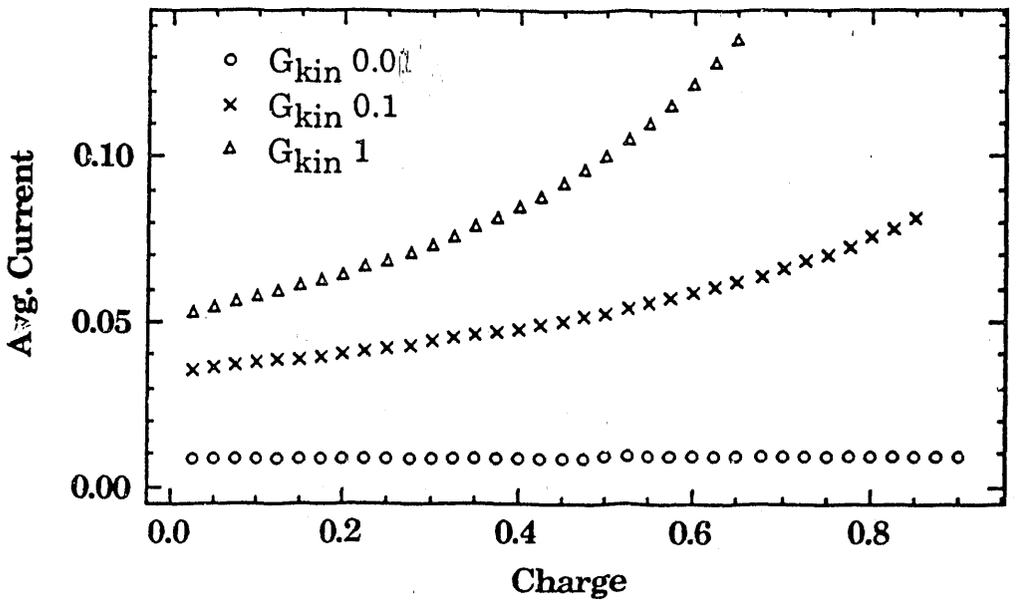

Figure 5.24: Comparison between current vs. charge transients as kinetic resistance is lowered. The functions become more non-linear as kinetics are increased. Corresponding current versus charge transients for the one-dimensional model are always linear. XBL 924-912

Chapter 6:

Summary and Analysis

6-1 Nodular Structure Evolution during Anodic Oxidation

The search for the structure evolution of the phase boundary between nickel hydroxide and nickel oxy-hydroxide during the anodic solid-solid oxidation reaction has lead to a nodular structure within the electrode film. This nodular growth mechanism is caused by the disparity in conductivity between the phases. Scanning tunneling microscopy and spectroscopic ellipsometry experiments provide evidence of this structure. A numerical model of the electrochemical transformation was developed to simulate the growth of the nodules through the film and analyze the effects of the various physical parameters that influence the reaction.

In our proposed structural mechanism of the anodic oxidation reaction, illustrated schematically in figure 6.1, the initial condition for the system is a planar nickel hydroxide film on a nickel metal substrate, immersed in concentrated alkaline electrolyte. (figure 6.1a) The structure represents the storage electrode in its discharged state. As the film is oxidized, small nodules of nickel oxy-hydroxide form

at the metal/film interface. (figure 6.1b) Images of the nickel oxy-hydroxide nodules were obtained by scanning tunneling microscopy of the oxidized electrode films.

Since the conductivity of nickel oxy-hydroxide is nearly one hundred times greater than that of nickel hydroxide, the current density to the tips of the nodules is much greater than to the base. The results of the numerical modeling of the nodule growth quantify the disparity in the current distribution between the peaks and valleys of small perturbations on the phase boundary. Calculations using typical values of the physical properties indicate that the current density to the peak of a small perturbation is at least twice as great as that to the valley. Under these conditions, the nodules grow rapidly to the film/electrolyte interface. (figure 6.1c)

The presence of the electronically conducting nickel oxy-hydroxide at the film/electrolyte interface facilitates a competing Faradaic reaction, oxygen evolution. Thermodynamically, oxygen evolution should occur at 308 millivolts, a lower potential than the nickel oxy-hydroxide formation, 424 millivolts versus the mercury/mercuric oxide reference. Sources in the literature have determined that the nickel hydroxide electrode is catalytic to the oxygen evolution reaction. Experiments by Kuchinskii and Erschler[1] using \ single grains of nickel hydroxide supported on a platinum pin confirm that oxygen evolution occurs preferentially on the nickel oxy-hydroxide grain rather than the platinum pin. Unfortunately, oxygen evolution is a parasitic reaction to the storage electrode charging process.

As further oxidation occurs, an overlayer of nickel oxy-hydroxide is created as the reaction boundary between the nickel hydroxide and oxy-hydroxide phases spreads laterally across the film/electrolyte interface. (figure 6.1d) Optical modeling of the spectroscopic ellipsometer measurements provides evidence of the nickel oxy-hydroxide overlayer. The presence of the overlayer inhibits further conversion of

---

1 E.M. Kuchinskii, B.V. Erschler, J. Phys Chem (USSR) 14, 985 (1940)

nickel hydroxide, leaving pockets of unconverted nickel hydroxide within the film.

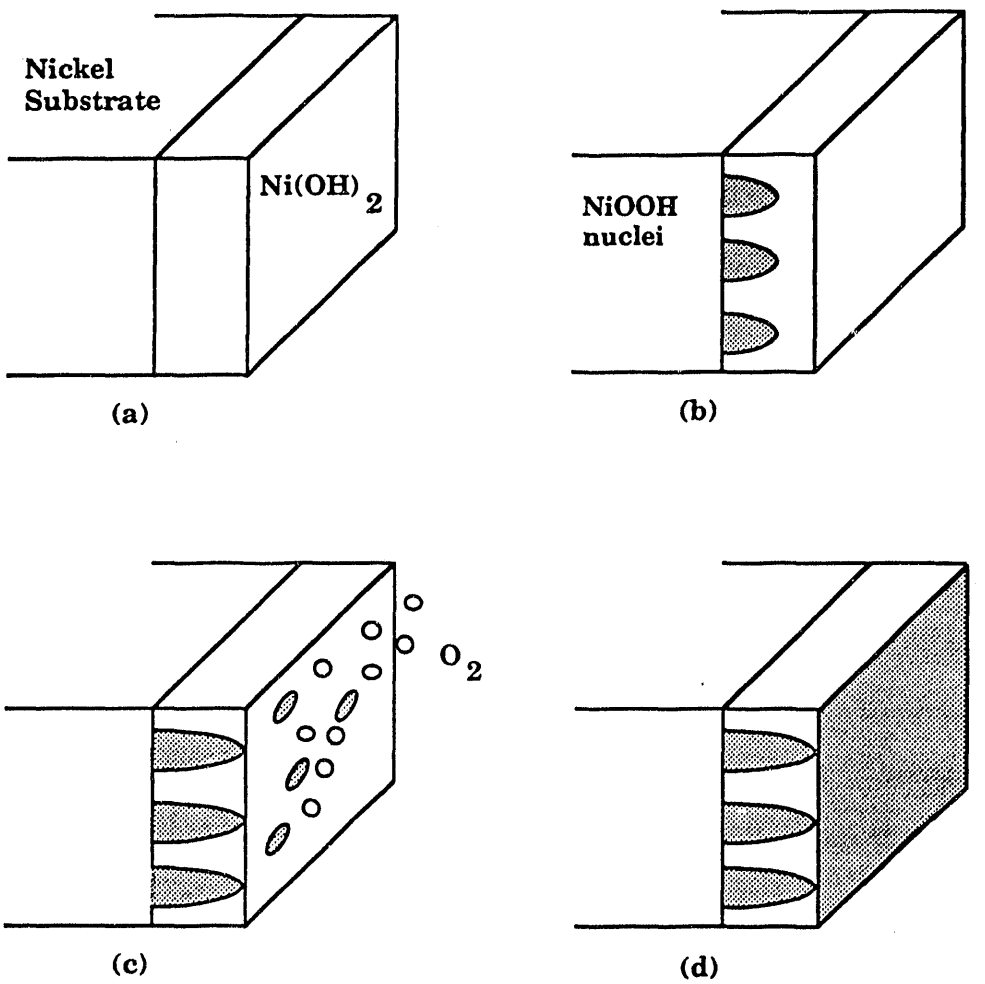

Figure 6.1: Nodular phase transformation schematic for anodic oxidation of nickel hydroxide to nickel oxy-hydroxide. (a) Uncharged nickel hydroxide film. (b) Formation of nickel oxy-hydroxide nodules. (c) Emergence of the nodules at the film/electrolyte interface with accompanying oxygen evolution. (d) Spreading of the nickel oxy-hydroxide overlayer across the interface, trapping nickel hydroxide within the film. XBL 924-857

6-2 STM Observations

Scanning tunneling microscopy of the electrode in its charged state reveals direct evidence of the presence of nickel oxy-hydroxide nuclei within the nickel hydroxide film. (figure 6.2) These nodules disappear upon removal of the film from the nickel metal substrate, and hence, are not merely roughness of the substrate. These

observations of the nodular structures indicate the proper choice of structure for the optical models that were developed to interpret the spectroscopic ellipsometer measurements.

The topography of the oxidized films is substantially different from that of the substrate: The surface appears to be strewn with round nodules 30 to 50 Angstroms in diameter with an average separation of 50 to 80 Angstroms. The number density of the nodules is of the order of 10^{12} per square centimeter. These observations of the nodules support the choice of optical models consisting of a partially oxidized layer and an unoxidized upper layer. These models were used to interpret the spectroscopic ellipsometer measurements.

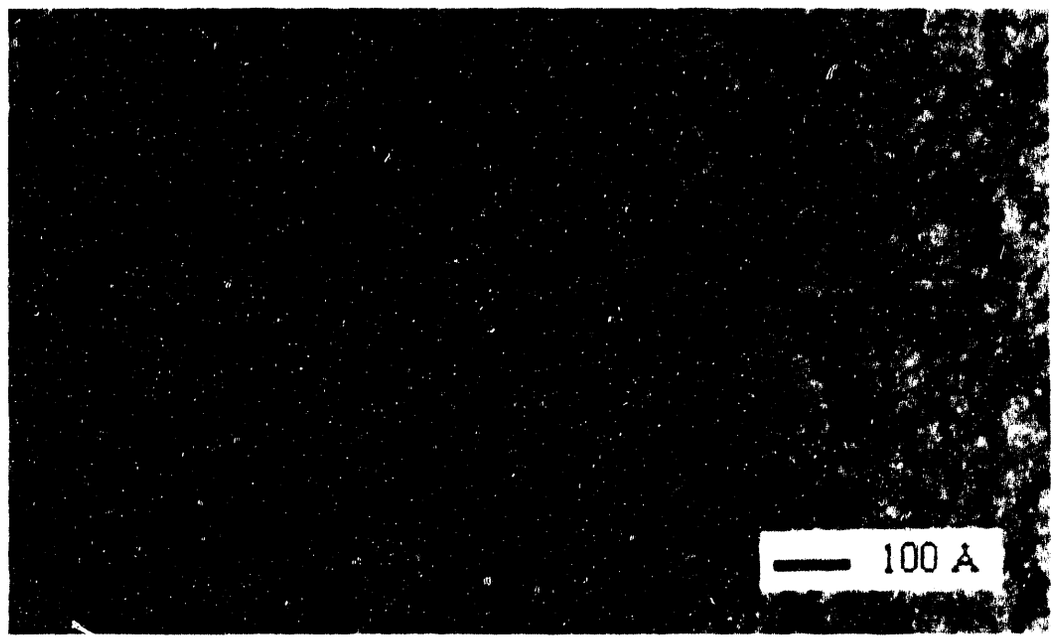

Figure 6.2: STM image of nickel oxy-hydroxide nodules within an oxidized nickel hydroxide film electrode on nickel metal substrate. The nodules are 30–50 Å in diameter. The number density is approximately 10^{12} nodules/cm^2. XBB 908-6853

It is important to note that the STM does not give an exact geometric measurement of the surface topography. The height measurement is the vertical displacement of the tip required to maintain the set tunneling current between the

surface and tip. The topography seen in the images is a convolution of the local work function and the geometry. Consideration of the work function and the film resistance of the nodular film is required to determine unambiguously the vertical dimensions of the nodules from the STM measurements.

6- 3 Spectroscopic Ellipsometry and Optical Modeling

Spectroscopic ellipsometry was employed to take advantage of the significant differences in the optical constant spectra of the nickel hydroxide and nickel oxy-hydroxide materials. Optical models of the film structures were fitted to the measured ellipsometer spectra to interpret the observed changes in the optical measurements.

Optical constant spectra of the pure film materials and nickel substrate were determined separately to limit the fitting process to structural parameters only. The optical absorbance spectra calculated from the refractive index spectra compare well with those found in the literature. The nickel hydroxide material is mostly transparent in the visible spectrum, whereas nickel oxy-hydroxide has a broad absorption band.

Optical models of the film transformation process were developed consisting of four film structure prototypes corresponding to the stages of the transformation: a pure nickel hydroxide film, pure nickel hydroxide over an effective medium representation of nickel oxy-hydroxide nodules in nickel hydroxide, pure nickel oxy-hydroxide over an effective medium of nickel oxy-hydroxide nodules in nickel hydroxide, and a pure nickel oxy-hydroxide film. These structures are illustrated schematically in figure 6.3.

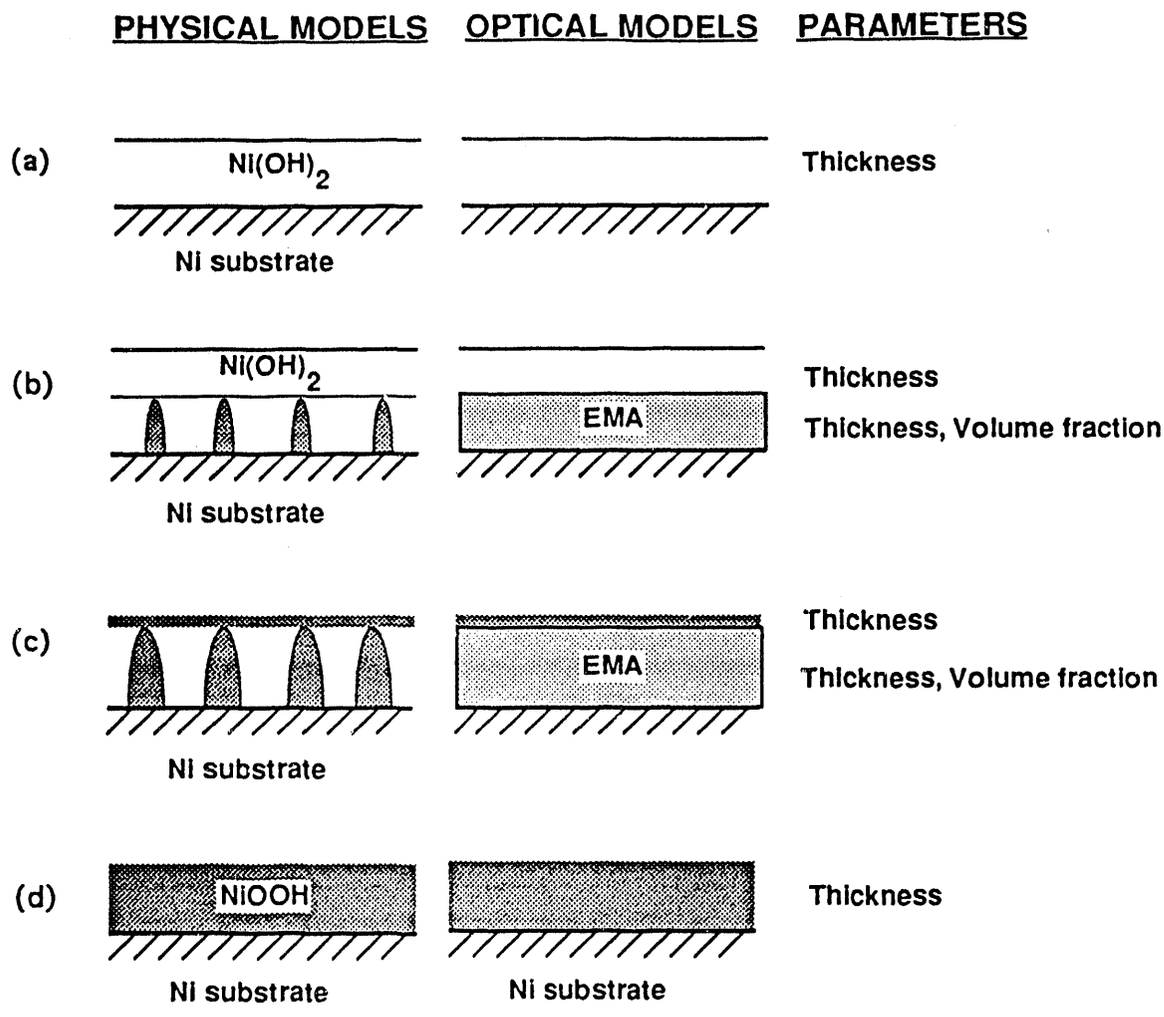

Figure 6.3: Schematic of physical and optical film models. The four archetypical models representing (a) uncharged film, (b) partially charged film with NiOOH nodules, (c) partially charged film with NiOOH overlayer, (d) fully charged film. An effective medium approximation is used to optically model the nodule layer.
XBL 924-874

The films were modeled using Fresnel reflectivities and Drude thin film interference equations. The self-consistent, Bruggemann effective medium approximation is an appropriate representation of the nodule layer since the theory was developed for small ellipsoidal inclusions in a continuous phase. The structural parameters in each model to be fitted were the thicknesses for each pure layer, and volume fraction and thickness for the nodule layer.

In-situ spectroscopic ellipsometer measurements of films held at various constant

potentials agree quantitatively with optical models appropriate to the nodular growth and subsequent overgrowth of the nickel oxy-hydroxide phase. The volumetric contraction of the films during oxidation is consistent with the unit cell measurements of the beta nickel hydroxide and beta nickel oxy-hydroxide phases determined from X-ray and neutron diffraction and EXAFS measurements in the literature.

In our optical measurements, the nickel hydroxide overlayer is found only while the potential is held above 500 millivolts versus the mercury/mercuric oxide reference electrode. The overlayer disappears when the oxidized film is allowed to stand at open circuit. However, holding the film at open circuit allows the spontaneous oxidation of hydroxide to form oxygen as the uppermost surface of the film is reduced to nickel hydroxide. This reaction is thermodynamically spontaneous by approximately 80 millivolts. The conversion of the uppermost surface to nickel hydroxide hinders transport and restricts the self-discharge reaction.

6-4 Electrode Performance Measurements

To examine the electrode performance under conditions similar to usage in practical battery systems, ellipsometer measurements were performed during galvanostatic charge and discharge experiments. *In-situ* spectroscopic ellipsometer measurements were used to analyze the state of charge of the electrode independent of the electrochemical measurements. In addition, transient monochromatic ellipsometer measurements were made to follow the transformation and indicate the endpoint of the nickel hydroxide reaction.

The results of these experiments were found to be consistent with our structural transformation model. Described in detail in chapter 4, they demonstrate that the current efficiency of the cathodic discharge reaction is nearly 100%, evidenced by the quantitative agreement of the endpoints measured electrochemically and optically. The current efficiency of the anodic charging reaction, however, is extremely poor.

Determination of the state of charge of the oxidized film indicated that, under the galvanostatic conditions of our experiment, nearly half of the nickel hydroxide material in the film was left uncharged. The nodular growth of the phase boundary, followed by the formation of the nickel oxy-hydroxide overlayer, electrically isolated uncharged material within the film. Only under potentiostatic conditions exceeding 550 millivolts, can the films be completely oxidized to nickel oxy-hydroxide, and then, with considerable oxygen evolution.

These experiments demonstrated the reduction of usable charge capacity of the electrode caused by the shielding of the active material by the nickel oxy-hydroxide overlayer. This overlayer also facilitated parasitic oxygen evolution that resulted in dramatic loss of current efficiency between charge and discharge of the electrode.

6-5 Numerical Modeling

In chapter five, we present a model that describes the evolution of the shape of the reaction front as the nickel hydroxide electrode film is charged. The problem is governed by three principal dimensionless groups representing the aspect ratio or spatial frequency of the initial nodule precursor, the kinetics relative to the conductivity of the nickel oxy-hydroxide phase, and the conductivity ratio of the two phases. The latter two parameters predominate over the electrode behavior.

We studied the simulated electrode behavior over a large parameter space spanning a wide range of conditions. The results of a numerical simulation of the nickel hydroxide electrode charging process under conditions comparable to the physical experiments confirm our prediction of nodular growth within the thin films. The evolution of the phase boundary for these conditions is reproduced in figure 6.4.

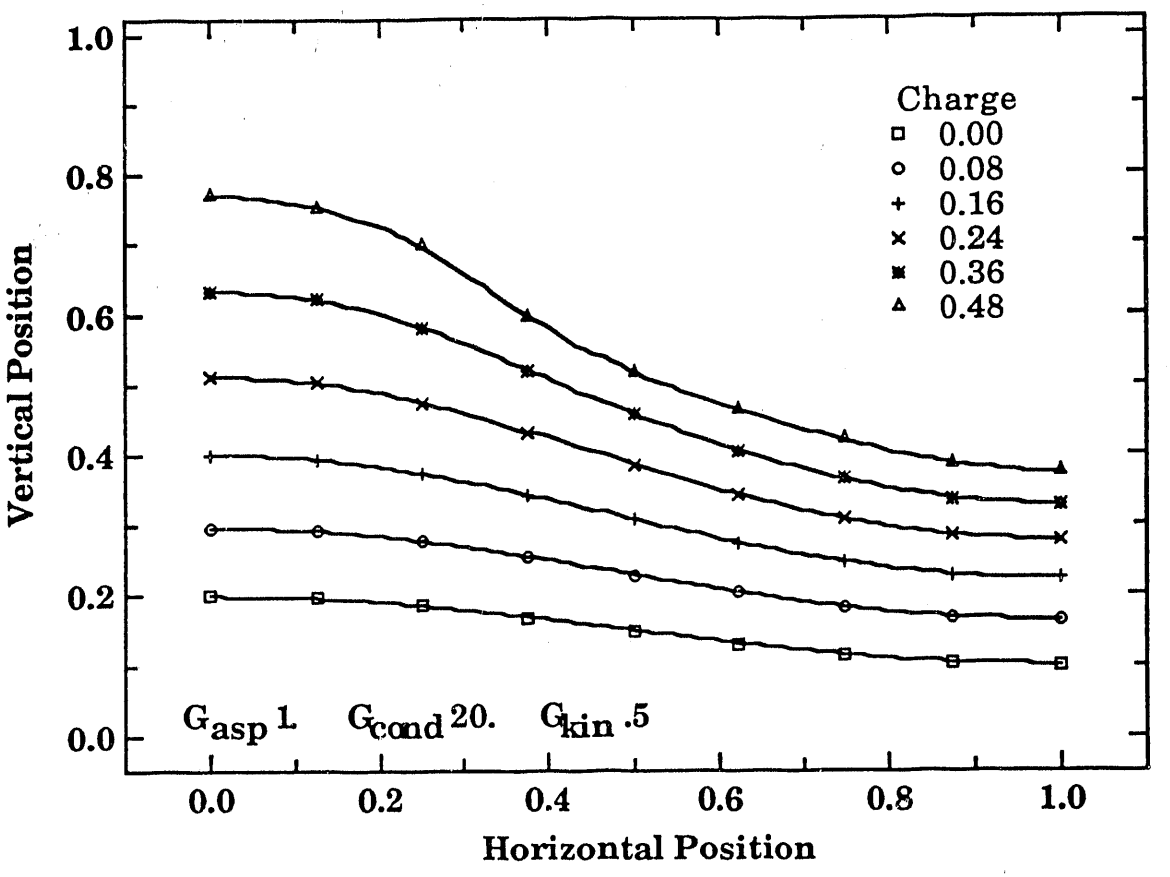

Figure 6.4: Model calculations of the dimensionless reaction phase boundary evolution as the electrode film is charged under nominal conditions. The initial nodule amplitude was 5% of the film thickness and grew to more than 20% before the nodule emerged from the film at the electrolyte interface. (y=1) XBL 924-902

The conductivity ratio between the nickel hydroxide and oxy-hydroxide phases is the dominant parameter in the model. The disparity in the conductivities is the proximate cause of the nodular growth behavior. In fact, if the conductivity ratio was less than unity (i.e., the nickel hydroxide phase was more conductive than the oxy-hydroxide phase), nodular growth would not occur at all; initial small perturbations would be leveled as the film was charged.

The effect of the dimensionless kinetic parameter is significant, though less dramatic than the effect of the conductivity parameter. The kinetic parameter represents the ratio of the ohmic resistance to the kinetic resistance in the film. The

limiting values of this parameter range from a simple ohmic junction at high values, where the potential is continuous across the reaction interface; to the case where the overall current is controlled by the kinetic resistance at the reaction interface.

The effect of the kinetic resistance on the performance of the electrode is largely beneficial. The tip-wise growth is inhibited by a kinetic overpotential that reduces the disparity in current density between the peak and valley of the growing nodule. This effect increases the material utilization as the kinetic resistance becomes significant.

One of the more disconcerting revelations from the modeling is the similarity of the transients for the simple one-dimensional laminar model without nodules and the two-dimensional nodule model. The tip position (or overall boundary position for the laminar model) and current density versus time functions from the two-dimensional model strongly resemble those generated from the one-dimensional model. By adjusting the apparent charge density, transient responses from the one and two-dimensional models can be made nearly identical as illustrated in figure 6.5.

This similarity in the two models is unfortunate, as it only adds to the confusion in the literature regarding the discrepancies in the valence of the charged nickel oxy-hydroxide species. Since pockets of uncharged material can be trapped in the film during charging, many measurements of the charge density or valence of the materials tend to underestimate the valence of the converted material. The similarity between the models disguises the structure that allows the material to remain uncharged.

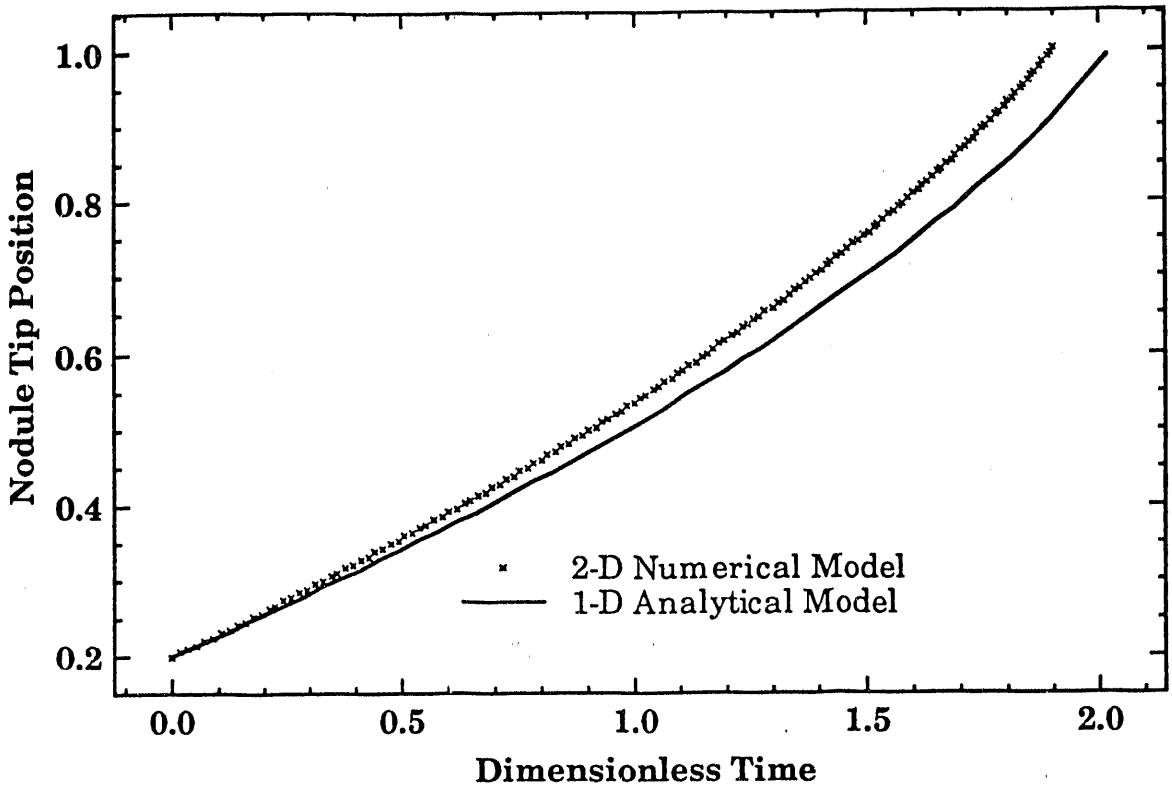

Figure 6.5: Comparison between tip transients between the one and two-dimensional models. The apparent charge density for the one-dimensional model is only 70% of that in the two-dimensional case. XBL 924-910

There are several limitations of the numerical model we have developed, related to simplified assumptions about ionic transport, reaction kinetics, and the boundary geometry. In our model, we made no distinction between electronic and ionic conductivity and treated the conductances in each phase as being uniform. While this assumption is reasonable for electronic conductors, it is restrictive with respect to ionic conductors, in which the mobile species can be greatly affected by space charge. Concentration gradients of mobile hydrogen ions in the nickel hydroxide phase, such as those produced by the nickel hydroxide oxidation reaction would create a space charge region within the film. The result of including space charge

effects would be to limit the oxidation reaction and reduce the disparity between the peak and valley current densities on the nodules.

The reaction kinetics in our model was linearized to simplify the numerical computation procedure. In addition, since the reaction kinetic parameters are not well known, linearizing reduced the number of unknown kinetic constants from two to one. However, a linear relationship between current and overpotential tends to reduce the disparity of the peak to valley current ratio. In the case of Tafel (or Butler-Volmer) kinetics the current increases exponentially with overpotential, accentuating the difference between peak and valley current densities.

The most restrictive assumption of our numerical model, however, is the limitations placed on the shape of the reaction interface between the nickel hydroxide and oxy-hydroxide phases. In our model, we transformed the vertical spatial coordinates (normal to the substrate) of the reaction interface from the physical geometry with a nodular boundary to one in which the boundary was flat. In doing so, we restricted the reaction interface position to a single-valued function, excluding the cases in which the slope of the interface is very large (vertical). This also prevents the model from simulating the formation of the overlayer. This restriction simplified the numerical procedure by allowing us to use a simple implementation of the finite difference method. To overcome this restriction, the boundary element method could be used.

This boundary element method is well suited for solving the Laplace equation in arbitrary geometries, particularly when the potentials and fluxes (currents) are only required on the boundaries of the phases. Implementation of this technique to simulate the overlayer formation would require kinetic expressions for the oxygen evolution reaction on the nickel oxy-hydroxide film/electrolyte interface.

6-6 Engineering Improvements for Nickel Hydroxide Electrodes

In the context of the structural transformation mechanism presented in this

dissertation, we can suggest some research directions for improving the energy storage performance of nickel hydroxide electrodes. The disparity between the peak and valley current densities on small perturbations on the phase boundary is the proximate cause for the nodular growth phenomenon that reduces the material utilization for conversion There are two approaches to restricting the nodule growth. The first is to reduce the difference between the conductivities of the nickel hydroxide and oxy-hydroxide materials. To do this one can either increase the ionic conductivity of the nickel hydroxide phase or reduce the conductivity of the oxy-hydroxide phase using additives. The latter method may be the one of the roles of cobalt hydroxide, an additive that has been used since the 1900's.

Cobalt hydroxide is reported by Corrigan and Capehart[2] to exist in the nickel hydroxide electrode as trivalent cations based on EXAFS measurements. Since nickel oxy-hydroxide is an intrinsically n-type semiconductor, cobalt ions may act as acceptors, reducing the electronic carrier density of the phase. In such a case, the conductivity would pass through a minimum as the amount of cobalt is increased.

Another approach to reducing the nodular growth phenomenon would be to employ an additive to decrease the kinetics of the nickel hydroxide oxidation reaction. By making the kinetics the controlling resistance in the film, the disparity between the current densities at the nodule peaks and valleys is reduced. This approach, however, reduces the energy storage efficiency of the electrode by increasing the charging overpotential and probably the discharge overpotential as well.

The formation of the nickel oxy-hydroxide overlayer in our model underscores the

---

2 D.A. Corrigan, T.W. Capehart, K.I. Pandya, R.W. Hoffman, "The Local Structures of Cobalt and Iron Ions Coprecipited in Nickel Hydroxide", *Proceedings of the Symposium on Nickel Hydroxide Electrodes*, D.A. Corrigan, A.H. Zimmerman (ed.), Vol. 90-4, The Electrochemical Society, (1990)

importance of the oxygen evolution reaction to the behavior of the nickel hydroxide electrode. The current efficiency of the oxidation reaction and the self-discharge rate are both negatively affected by the oxygen evolution reaction that occurs on the nickel oxy-hydroxide/electrolyte interface. An important role of additives to the electrode or the electrolyte is to poison this reaction. Several additives have been identified by electrochemical experiments that increase the overpotential for oxygen evolution. Lithium hydroxide is known to act in this manner.[3]

6-7 Conclusions and Outlook

The nodular growth mechanism for the phase transformation reaction presented in this research is based on a relatively limited aspect of the anodically-formed nickel hydroxide electrode. In this research, we have addressed the nature of the phase boundary evolution that occurs during the oxidation reaction of beta nickel hydroxide films to form beta nickel oxy-hydroxide. There are several directions indicated for future research to test our understanding of this electrode system further.

One future direction would be to extend the phase transformation model to include the discharge reaction from nickel oxy-hydroxide to nickel hydroxide. It is not clear from the present research whether the structure transformation is exactly the reverse of the charging reaction, particularly in light of the semiconductor properties of the phases. In the film reduction reaction, since the nickel oxy-hydroxide is intrinsically an n-type material, the nickel oxy-hydroxide/current collector junction is reverse biased. Also, the possibility exists to isolate charged material within the films by reducing the nickel oxy-hydroxide nearest the current

---

[3] Halpert, G, "The Nickel Hydroxide Electrode- An Overview" in *Proc. of the Symposium on Nickel Hydroxide Electrode,* D.A. Corrigan, A.H. Zimmerman (ed), Proceedings Vol. 90-4, The Electrochemical Soc. (1990)

collector. The techniques used in this research should be useful for this investigation.

The optical constant spectra for the beta phases of nickel hydroxide and nickel oxy-hydroxide were determined during the course of the present research. It would be interesting to compare these results to optical constant spectra for the other phases in the Bode model, alpha nickel hydroxide and gamma nickel oxy-hydroxide. Since this gamma phase may contain quadrivalent nickel in a rhombohedral nickelate structure rather than a hexagonal one, the optical constants should be significantly different. Unfortunately, this phase is formed in the oxygen evolution potential region, for this reason, back-side optical measurements may be required. In a similar vein, the optical constant spectra of the thicker precipitated films should be compared to those formed anodically in this study.

From the numerical model of the nodular growth mechanism, we have identified the conductivity ratio between the phases as the dominant parameter affecting the growth of the nodules and the utilization of the active electrode material. A test of our model and conclusions would be to conduct a study of the effect of additives on the conductivities of the phases and the effective charge capacity of the film electrodes. Electrochemical impedance spectroscopy would be a useful tool for measuring the conductivities of the film materials and determining the ionic transport conditions within the film.

APPENDIX A:

Details of Numerical Simulation of 2-D Nodule

The numerical model that describes the transformation of nickel hydroxide to nickel oxy-hydroxide is presented in chapter 5. In this appendix chapter, the model is presented in much greater detail to facilitate extensions and modifications. In addition, the modifications for the axisymmetric geometry are given here.

A-1 The Laplace Equation and Boundary Conditions

The numerical model of the electrochemical transformation is divided into two parts, an electrostatic part to determine the current distribution, and a mass adn charge balance to calculate the evolution of the phase boundary. In the electrostatics problem, the Laplace equation, [1], is solved in two adjacent regions having different conductivities and joined by a kinetic boundary that is single-valued in the y direction. This problem is illustrated schematically in figure A.1.

$$\frac{d^2\Phi}{dx^2} + \frac{d^2\Phi}{dy^2} = 0 \qquad [1]$$

$$\Phi(x,0) = 0 \qquad [2]$$

$$\Phi(x,H) = \Phi_0 \qquad [3]$$

$$\left.\frac{d\Phi}{dx}\right|_{x=0} = \left.\frac{d\Phi}{dx}\right|_{x=L} = 0 \qquad [4a,b]$$

The external boundary conditions given in equations [2-3] are that the potential at the film/substrate interface is zero and some constant value at the film/electrolyte interface. These surfaces are treated as equipotential surfaces since the conductivities of the metal substrate and electrolyte phases are substantially larger than either of the two oxidized nickel phases. The lateral boundaries in equations [4a,b] have no-flux symmetry conditions representing the peak of the nodule and the mid-point between neighboring ones.

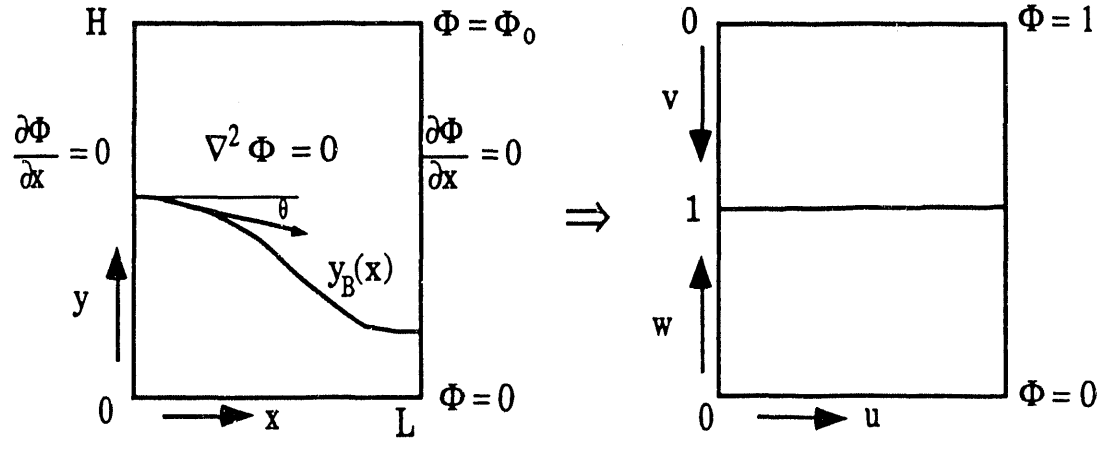

Figure A.1: The domain and boundary conditions for the two-dimensional model for the nickel hydroxide electrode and the transformation of variables mapping the complicated, but single-valued, interface into a simple rectangular geometry.

At the reaction interface, $y_B(x)$, the boundary conditions are continuity of current, [5a,b], and a linear kinetic expression, [6].

$$i(x,y_B) = -\kappa_1 \left.\frac{d\Phi^{(1)}}{dn}\right|_{y=y_B} = -\kappa_2 \left.\frac{d\Phi^{(2)}}{dn}\right|_{y=y_B} \qquad [5a,b]$$

$$i(x,y_B) = \alpha(\Phi^{(2)} - \Phi^{(1)}) \qquad [6]$$

The position of the phase boundary is differentially related to the local current density along the boundary according to equation [7], which is derived from the Faraday law.

$$\left(\frac{\rho z F}{M_w}\right) \left.\frac{dy_B}{dn}\right|_{y=y_B} = -i(x,y_B) \qquad [7]$$

A-2 Mapping into Dimensionless Form

The problem is governed by three principal dimensionless groups representing the aspect ratio or spatial frequency of the initial nodule precursor, the kinetics relative to the conductivity of the nickel oxy-hydroxide phase, and the relative conductivity of the two phases. The latter two parameters are carried over from the one-dimensional problem.

Aspect ratio: $$G_{asp} = \frac{H}{L} \qquad [8]$$

Kinetic group: $$G_{kin} = \frac{\alpha L}{\kappa_1} \qquad [9]$$

Relative Conductivity: $$G_{cond} = \frac{\kappa_1}{\kappa_2} \qquad [10]$$

The prblem is solved numerically using the finite difference method; replacing the differentials in the problem with difference equations and solving for the potentials at each point. Furthermore, if one restricts the boundary to being single-valued in one direction, one can make a transformation of variables into a simple orthogonal geometry having two adjacent rectangular domains. This

transformation is illustrated in figure A.1. This transforms the Laplace equation into a more general elliptic equation.

For the mapping, we define dimensionless coordinates for the lateral x-coordinate, [11]; and the vertical y-coordinate in the lower(w), [12]; and upper(v) domains, [13]. We also cast the position of the reaction interface, $y=y_B(x)$, in dimensionless form as in [14].

$$u = \frac{x}{L} \qquad [11]$$

$$w = \frac{y}{y_B(x)} \qquad [12]$$

$$v = \frac{H - y}{h - y_B(x)} \qquad [13]$$

$$\lambda = \frac{y_B(x)}{H} \qquad [14]$$

Transforming the Laplace equation for the upper nickel hydroxide domain into the (u,v) coordinates, the result, [15], is a fully elliptic differential equation. Casting [15] into a more tractable form and substituting for the partial derivatives in equations [16-23], gives [24], with the fully fleshed out coefficients {A...F} [25-29].

$$\left(\frac{\partial u}{\partial x}\right)^2 \frac{\partial^2 \Phi}{\partial u^2} + \left(\left(\frac{\partial v}{\partial x}\right)^2 + \left(\frac{\partial u}{\partial y}\right)^2\right)\frac{\partial^2 \Phi}{\partial v^2}$$

$$+ 2\left(\frac{\partial u}{\partial x}\right)\left(\frac{\partial v}{\partial x}\right)\frac{\partial^2 \Phi}{\partial u\, \partial v} + 2\left(\frac{\partial^2 v}{\partial x^2}\right)\frac{\partial \Phi}{\partial v} = 0 \qquad [15]$$

$$\frac{du}{dx} = \frac{1}{L} \qquad [16]$$

$$\frac{du}{dy} = 0 \qquad [17]$$

$$\frac{d2u}{dx2} = 0 \qquad [18]$$

$$\frac{dv}{dx} = \frac{H - y}{H(1-\lambda)^2}\left(\frac{du}{dx}\right)\left(\frac{d\lambda}{du}\right) = \frac{v}{L(1-\lambda)}\left(\frac{d\lambda}{du}\right) \qquad [19]$$

$$\frac{d^2v}{dx^2} = \frac{2(H-y)}{H(1-\lambda)^3}\left(\frac{du}{dx}\right)^2\left(\frac{d\lambda}{du}\right)^2 + \frac{(h-y)}{H(1-\lambda)^2}\left(\frac{du}{dx}\right)^2\left(\frac{d^2\lambda}{du^2}\right) \qquad [20]$$

$$\frac{d^2v}{dx^2} = \frac{2v}{L^2(1-\lambda)^2}\left(\frac{d\lambda}{du}\right)^2 + \frac{v}{L^2(1-\lambda)}\left(\frac{d^2\lambda}{du^2}\right) \qquad [21]$$

$$\frac{dv}{dy} = \frac{-1}{H(1-\lambda)} \qquad [22]$$

$$\frac{d^2v}{dy^2} = 0 \qquad [23]$$

$$A\frac{d^2\Phi}{du^2} + B\frac{d^2\Phi}{du\,dv} + C\frac{d^2\Phi}{dv^2} + D\frac{d\Phi}{dv} + E\frac{d\Phi}{du} + F = 0 \qquad [24]$$

$$A = 1 \qquad [25]$$

$$B = \frac{2v}{(1-\lambda)}\left(\frac{\partial\lambda}{\partial u}\right) \qquad [26]$$

$$C = \left(\frac{v}{(1-\lambda)\left(\frac{\partial\lambda}{\partial u}\right)}\right)^2 + \left(\frac{1}{G_{asp}(1-\lambda)}\right)^2 \qquad [27]$$

$$D = \frac{4v}{(1-\lambda)^2}\left(\frac{\partial\lambda}{\partial u}\right)^2 + \frac{2v}{(1-\lambda)}\left(\frac{\partial^2\lambda}{\partial u^2}\right) \qquad [28]$$

$$E = F = 0 \qquad [29]$$

Similarly, translating the lower nickel oxy-hydroxide region into the (u,w) domain:

$$\left(\frac{\partial u}{\partial x}\right)^2\frac{\partial^2\Phi}{\partial u^2} + \left(\left(\frac{\partial w}{\partial x}\right)^2 + \left(\frac{\partial u}{\partial y}\right)^2\right)\frac{\partial^2\Phi}{\partial w^2}$$

$$+ 2\left(\frac{\partial u}{\partial x}\right)\left(\frac{\partial w}{\partial x}\right)\frac{\partial^2\Phi}{\partial u\,\partial w} + 2\left(\frac{\partial^2 w}{\partial x^2}\right)\frac{\partial\Phi}{\partial w} = 0 \qquad [30]$$

$$\frac{dw}{dx} = \frac{-y}{H\lambda^2}\left(\frac{du}{dx}\right)\left(\frac{d\lambda}{du}\right) = \frac{-w}{L\lambda}\left(\frac{d\lambda}{du}\right) \qquad [31]$$

$$\frac{d^2w}{dx^2} = \frac{2y}{H\lambda^3}\left(\frac{du}{dx}\right)^2\left(\frac{d\lambda}{du}\right)^2 - \frac{y}{H\lambda^2}\left(\frac{du}{dx}\right)^2\left(\frac{d^2\lambda}{du^2}\right) \qquad [32]$$

$$= \frac{2w}{L^2\lambda^2}\left(\frac{d\lambda}{du}\right)^2 - \frac{w}{L^2\lambda}\left(\frac{d^2\lambda}{du^2}\right) \qquad [33]$$

$$\frac{dw}{dy} = \frac{1}{H\lambda} \qquad [34]$$

$$\frac{d^2w}{dy^2} = 0 \qquad [35]$$

$$A\frac{d^2\Phi}{du^2} + B\frac{d^2\Phi}{du\,dw} + C\frac{d^2\Phi}{dw^2} + D\frac{d\Phi}{dw} + E\frac{d\Phi}{du} + F = 0 \qquad [36]$$

$$A = 1 \qquad [37]$$

$$B = \frac{-2\,w}{\lambda}\left(\frac{\partial\lambda}{\partial u}\right) \qquad [38]$$

$$C = \left(\frac{w}{\lambda}\left(\frac{\partial\lambda}{\partial u}\right)\right)^2 + \left(\frac{1}{G_{asp}\,\lambda}\right)^2 \qquad [39]$$

$$D = \frac{4\,w}{\lambda^2}\left(\frac{\partial\lambda}{\partial u}\right)^2 - \frac{2\,w}{\lambda}\left(\frac{\partial^2\lambda}{\partial u^2}\right) \qquad [40]$$

$$E = F = 0 \qquad [41]$$

A-4 Difference Form of Elliptic Equation

In order to solve equations [24] and [36] numerically, they are discretized using central difference approximations to the derivatives. Equation [42] represents these equations in difference form. The coefficients, $\{a_{ij}...f_{ij}\}$, in the difference equation are related to those in the differential equations for each domain, {A...F}, through equations [43-48]. In our solution, we have chosen to construct the mesh with uniform node spacing in the vertical and lateral directions. The spacing constants are the variables m and n.

$$a_{ij}\,\Phi_{i,j+1} + b_{ij}\,\Phi_{i,j-1} + c_{ij}\,\Phi_{i+1,j} + d_{ij}\,\Phi_{i-1,j} + e_{ij}\,\Phi_{i,j} - f_{ij} = 0 \qquad [42]$$

$$a_{ij} = \frac{C}{n^2} - B\frac{mn}{(m^2+n^2)^2} + \frac{D}{2n} \qquad [43]$$

$$b_{ij} = \frac{C}{n^2} - B\frac{mn}{(m^2+n^2)^2} - \frac{D}{2n} \qquad [44]$$

$$c_{ij} = \frac{A}{m^2} + B\frac{mn}{(m^2+n^2)^2} + \frac{E}{2m} \qquad [45]$$

$$d_{ij} = \frac{A}{m^2} - B\frac{mn}{(m^2+n^2)^2} - \frac{E}{2m} \qquad [46]$$

$$e_{ij} = \frac{-2A}{m^2} - \frac{-2C}{n^2} \qquad [47]$$

$$f_{ij} = -F \qquad [48]$$

A-5 Kinetic Boundary Condition

The kinetic boundary condition, equation [49], relates the current, which is proportional to the normal derivative of the potential, and the potentials at adjacent points on either side of the boundary.

$$\frac{\partial \Phi}{\partial \tilde{n}} = G_{kin} (\Phi^{(2)} - \Phi^{(1)}) \qquad [49]$$

We have transformed the kinetic boundary condition by employing trigonometric identities to link the slope of the kinetic phase boundary with the normal derivatives of the potential. The derivative of the interface is expressed in [50] as the tangent of the slope of the interface.

$$\frac{dy_B}{dx} = \frac{H}{L}\left(\frac{d\lambda}{du}\right) = \tan\theta \qquad [50]$$

The normal derivatives of the potential along the boundary in the original coordinates are related to the angle, θ, in equation [51]. Transforming this equation into the new orthogonal coordinates, v and w, gives equation [52].

$$\frac{\delta \Phi}{\delta \tilde{n}} = -\sin(\theta)\frac{\delta \Phi}{\delta x} + \cos(\theta)\frac{\delta \Phi}{\delta y} \qquad [51]$$

$$\frac{\delta \Phi}{\delta \tilde{n}} = \left(-\sin(\theta)\frac{\delta \Phi}{\delta u} - \frac{1}{\lambda}\left(\frac{\cos(\theta)}{Gasp} + w\sin(\theta)\frac{d\lambda}{du}\right)\frac{\delta \Phi}{\delta w}\right) \qquad [52]$$

Substituting for the trigonometric functions:

$$\frac{\delta \Phi}{\delta \tilde{n}} = \frac{-G_{asp}\frac{d\lambda}{du}}{\left(1+\left(G_{asp}\frac{d\lambda}{du}\right)^2\right)^{1/2}}\frac{\delta \Phi}{\delta u} + \frac{1 + w\left(G_{asp}\frac{d\lambda}{du}\right)^2}{G_{asp}\lambda\left(1+\left(G_{asp}\frac{d\lambda}{du}\right)^2\right)^{1/2}}\frac{\delta \Phi}{\delta w} \qquad [53]$$

Substituting the difference equations for the differentials yields equation[54]. This equation contains a real and a virtual node for the potential $\Phi_{i,j+1}$. The point $\Phi^{*}_{i,j+1}$ is a virtual node, that is, a point spatially outside the domain but having the

same properties as the domain. This virtual point comes from the central difference equations for the normal derivative of the potential. In contrast, $\Phi_{i,j+1}$, in equation [58], is a real point that belongs to the upper domain and is part of the expression for the kinetic overpotential.

$$\frac{-G_{asp}\frac{d\lambda}{du}}{\left(1+\left(G_{asp}\frac{d\lambda}{du}\right)^2\right)^{1/2}}\left(\frac{\Phi_{i+1,j}-\Phi_{i-1,j}}{2m}\right) + \frac{1+w\left(G_{asp}\frac{d\lambda}{du}\right)^2}{l\,G_{asp}\,\lambda\left(1+\left(G_{asp}\frac{d\lambda}{du}\right)^2\right)^{1/2}}\left(\frac{\overset{*}{\Phi}_{i,j+1}-\Phi_{i,j-1}}{2n}\right) = G_{kin}\left(\Phi_{i,j+1}-\Phi_{i,j-1}\right) \quad [54]$$

In this boundary condition expression, we will solve for the virtual node and substitute the expression, [55], into the system of equations for the Laplace equation.

$$\overset{*}{\Phi}_{i,j+1} = Q\,\Phi_{i,j+1} + \Phi_{i,j-1} + R\,\Phi_{i+1,j} - R\,\Phi_{i-1,j} - Q\,\Phi_{i,j} \quad [55]$$

$$Q = \frac{2\,n\,G_{kin}\,G_{asp}\,\lambda\left(1+\left(G_{asp}\frac{d\lambda}{du}\right)^2\right)^{1/2}}{1+w\left(G_{asp}\frac{d\lambda}{du}\right)^2} \quad [56]$$

$$R = \frac{G_{asp}^2\,\lambda\left(\frac{n}{m}\right)\left(\frac{d\lambda}{du}\right)}{1+w\left(G_{asp}\frac{d\lambda}{du}\right)^2} \quad [57]$$

For the upper domain, there are similar expressions. In this case, the virtual point is $\overset{*}{\Phi}_{i,j-1}$.

$$\Phi^{*}_{i,j-1} = \Phi_{i,j+1} - Q\,\Phi_{i,j-1} + R\,\Phi_{i+1,j} - R\,\Phi_{i-1,j} + Q\,\Phi_{i,j} \qquad [58]$$

$$Q = \frac{2\,n\,G_{cond}\,G_{kin}\,G_{asp}\,(1-\lambda)\left(1+\left(G_{asp}\frac{d\lambda}{du}\right)^2\right)^{1/2}}{1+v\left(G_{asp}\frac{d\lambda}{du}\right)^2} \qquad [59]$$

$$R = \frac{G_{asp}^2\,(1-\lambda)\left(\frac{n}{m}\right)\left(\frac{d\lambda}{du}\right)}{1+v\left(G_{asp}\frac{d\lambda}{du}\right)^2} \qquad [60]$$

A-6 Exterior Boudary Conditions

The exterior boundary conditions are somewhat simpler to pose. For difference equations that refer to nodes across boundaries, the coefficients of the exterior nodes are set to reflect the proper boundary condition. For example, along the y=0 boundary (equation [61]), the potential is zero. In the difference equations for j=0, the $b_{0,i}$ coefficient is multiplied with a node whose potential is always zero. Therefore, that coefficient is set to zero. Similarly, along the upper boundary, the same thing occurs except the exterior node is always equal to unity.

The no-flux boundaries are satisfied by imposing reflection nodes. In this case, the node outside the boundary is set equal to the node just inside the boundary [63c]. The result is is that the difference forms of the derivatives are identically zero.

Real Domain	Transformed Domain	Difference Equation	Difference Coefficients	
$\Phi(y=0) = 0$	$\Phi(v=0) = 0$	$\Phi_{i,-1} = 0$	$b_{0,i} = 0$	[61a-d]
$\Phi(y=H) = 1$	$\Phi(w=0) = 1$	$\Phi_{i,N+1} = 1$	Set $f_{in} = -a_{iN}$, Then set $a_{iN} = 0$.	[62a-e]
$\left.\frac{d\Phi}{dx}\right\|_{x=0} = 0$	$\left.\frac{d\Phi}{dx}\right\|_{u=0} = 0$	$\Phi_{-1,j} = \Phi_{0,j+1}$	First set $c_{0j} = c_{0j} + d_{0j}$, then set $d_{0j} = 0$.	[63a-e]
$\left.\frac{d\Phi}{dx}\right\|_{x=L} = 0$	$\left.\frac{d\Phi}{dv}\right\|_{u=1} = 0$	$\Phi_{M+1,j} = \Phi_{M,j}$	First set $d_{Mj} = d_{Mj} + c_{Mj}$, then set $c_{Mj} = 0$.	[64a-e]

The full set of difference equations forms an (MxN) by (MxN) sparse matrix equation. This is solved for the potentials, Φ_{ij}, using the method of simultaneous over-relaxation as developed by Press[1] and modified for adaptive step-size to optimize the convergence rate. The computer program for this numerical model is listed in Appendix B, coded in the C programming language.

A-7 Special Case: 2-D Axisymmetric

In this case, we simply rotate the x-axis around the origin and call the new rotated axis the r-axis. the Laplace equation in this cylindrical coordinate system is:

$$\frac{d^2\Phi}{dr^2} + \frac{1}{r}\frac{d\Phi}{dr} + \frac{d^2\Phi}{dz^2} = 0 \qquad [65]$$

The problem is only slightly changed, adding the 1/r term. Transforming into

1 W.H. Press, et al., Numerical Recipes, The Art of Scientific Computing, Cambridge University Press, 1986

the (u,w) domain:

$$\frac{d\Phi}{dr} = \frac{1}{l}\frac{d\Phi}{du} - \frac{w}{l\lambda}\left(\frac{d\lambda}{du}\right)\frac{d\Phi}{dw} \qquad [66]$$

$$D = \frac{4w}{\lambda^2}\left(\frac{d\lambda}{du}\right)^2 - \frac{2w}{\lambda}\left(\frac{d^2\lambda}{du^2}\right) - \frac{w}{u\lambda}\left(\frac{d\lambda}{du}\right) \qquad [67]$$

$$E = \frac{1}{u} \qquad [68]$$

Transforming into the (u,v) domain:

$$\frac{d\Phi}{dr} = \frac{1}{l}\frac{d\Phi}{du} + \frac{v}{l(1-\lambda)}\left(\frac{d\lambda}{du}\right)\frac{d\Phi}{dv} \qquad [69]$$

$$D = \frac{4v}{(1-\lambda)^2}\left(\frac{d\lambda}{du}\right)^2 + \frac{2v}{(1-\lambda)}\left(\frac{d^2\lambda}{du^2}\right) + \frac{v}{u(1-\lambda)}\left(\frac{d\lambda}{du}\right) \qquad [70]$$

$$E = \frac{1}{u} \qquad [71]$$

These expressions replace the coefficients {D, E} in equations [28-29] and [40-41] for each of the respective domains. No other adjustments are necessary.

A-8 Nomenclature for the Two-Dimensional Model

Subscripts:

i	lateral node index
j	vertical node index
M	Number of lateral nodes
N	Number of vertical nodes

Roman Symbols

x	Lateral spatial coordinate in physical geometry
y	Vertical spatial coordinate in physical geometry
y_B	Vertical spatial coordinate of phase boundary in physical geometry
u	Dimensionless lateral spatial coordinate in transformed geometry, defined in [11]
v	Dimensionless vertical spatial coordinate in upper (nickel hydroxide) domain of transformed geometry, defined in [13]
w	Dimensionless vertical spatial coordinate in lower (nickel oxy-hydroxide) domain of transformed geometry, defined in [14]
i	Current density
L	Lateral dimension in physical geometry
H	Vertical dimension in physical geometry
{A...F}	Coefficients to diffentials in transformed the Laplace Eqn.
{a...f}	Coefficients to potential nodes in difference form of transformed the Laplace Eqn.
m	Vertical node spacing
n	Lateral node spacing
ñ	Coordinate normal to reaction interface
G_{asp}	Aspect ratio of film thickness to nodule spacing, defined in [8]
G_{cond}	Conductivity ratio between upper (nickel hydoxide) and lower phases (nickel oxy-hydoxide), defined in [10]

G_{kin} Dimensionless kinetic parameter, ratio of film resistance to kinetic resistance, defined in [9]

Q Coefficient for diffential equation of boundary condition

R Coefficient for diffential equation of boundary condition

Mw Molecular weight of film material

z Number of equivalents in reaction, one equiv/mol

F Faraday's constant: 96,485 Coulombs/mol

Greek symbols

α Linear kinetic coefficient

Φ Potential

κ Effective conductivity, ionic or electronic

λ Dimensionless vertical coordinate of interface position, defined in [14]

ρ Density of film materials

θ Tangent angle of reaction interface, defined in [50]

APPENDIX B:
Nickel Hydroxide Nodule Growth Model Software

B-1 Description, purpose, numerical techniques

The program described in this appendix is a numerical simulation of the nodule phase boundary evolution within the nickel hydroxide electrode. In its most basic form, it solves the Laplace equation in two dimensions for two stacked domains having different conductivities, between two equipotential surfaces. The domains are separated by a linear kinetic boundary, which is single valued in the y-direction. The flux distribution along the kinetic boundary is used to evolve the boundary. A full description of the model in the context of the nickel hydroxide electrode is given in chapter 5 and appendix A of this document.

The solution of this partial differential equation is found by transforming the geometry into a simple orthogonal one using a substitution of variables. This substitution transforms the Laplace equation into a more general elliptic equation. This equation is discretized and solved numerically using the finite difference method. The differentials are approximated by central difference equations. The resulting system of linear equations is solved for the potential nodes using the

simultaneous over-relaxation technique as developed by Press[1].

The program is written in ANSI compatible C. The program was developed on an Apple Macintosh IIcx computer using the Symantec Think C, version 5.0.1.

B-2 Sample input/output

The program requires input data in the form of definitions in the source code, user prompts, and a data file for the initial boundary configuration. The program generates four series of output files at each time step describing the potential solution, the current distribution, a Fourier spectral growth rate for the boundary, and a single transient data file summarizing the nodule tip position and current density versus time and charge passed.

The definitions in the source code define the mesh dimensions for each of the domains, the charge step size, the number of time steps between output files, and the tuning parameters of the matrix solving algorithm. The option of rectangular or axisymmetric solutions is also in the definitions section.

The user is prompted for the three dimensionless groups governing the problem, the conductivity ratio between the two domains, the dimensionless kinetic parameter, and the aspect ratio of the domain. The program also prompts for the name of a text file containing the initial nodule configuration.

The initial nodule description file contains a list of Fourier cosine series coefficients, a_n in equation [1]. The symmetry of the problem makes the Fourier cosine series an excellent choice for specifying the boundary. The zeroeth order term is the average boundary height, a constant.

$$\lambda(u) = \sum_n a_n \cos(n\pi u) \qquad [1]$$

---

[1] W.H. Press, et al., Numerical Recipes, The Art of Scientific Computing, Cambridge University Press, 1986

An example is given below of the file format. The first line is a comment line; the subsequent lines contain the order of the term and the amplitude of the mode. This examples is for a gaussian nodule shape.

```
*Gaussian Boundary Coefficient File
 0      0.1083
 1      0.0097
 2      0.0019
 3      0.0001
 4      0.0000
 5      0.0000
 6      0.0000
 7      0.0000
 8      0.0000
 9      0.0000
10      0.0000
11      0.0000
12      0.0000
13      0.0000
14      0.0000
15      0.0000
```

The transient file format is shown below. The time, date, and experiment identifier label are listed, as well as the values of the key dimensionless groups. At each charge step, the elapsed time, average current density, nodule tip position, and number of iterations required to solve the potential problem are reported. Since the transient is based on constant charge steps, the elapsed time is calculated from the charge divided by the average current density. The experiment concludes when the tip position reaches the film/electrolyte interface, yBmax equals unity.

```
*Transient File: md6a    Wed Mar 4 23:16:59 1992
*kinGrp:  100.000, conGrp: 20.000, aspectRatio:  1.000
*Iteration      Time      Charge    Itot      yBmax    SOR passes
 0     0.000    0.000     0.0000    0.1514     0
 1     0.175    0.010     0.0572    0.1669    520
 2     0.346    0.020     0.0583    0.1819    436
 3     0.514    0.030     0.0596    0.1976    303
 4     0.678    0.040     0.0612    0.2145    659
 5     0.837    0.050     0.0629    0.2326    333
 6     0.991    0.060     0.0647    0.2524    375
 7     1.144    0.070     0.0654    0.2738    596
```

The form of the current distribution output file, which is generated at a given charge step interval, includes a header of information about the experiment including the step, time, and charge passed, and the average current density. The boundary position and current distribution are listed for each node in the x direction.

```
*Current Distribution     Curmd6a.1     Wed Mar 4 23:17:25 1992
 *Step  0, Time: 0.0000, Charge: 0.0000,Average Current 0.05717
*x, yBound, current/avg
0.0000      0.1400      0.9179
0.0625      0.1435      1.0402
0.1250      0.1500      1.3419
0.1875      0.1514      1.5480
0.2500      0.1424      1.3806
0.3125      0.1258      1.0258
0.3750      0.1099      0.7963
0.4375      0.1014      0.7779
0.5000      0.1000      0.9542
0.5625      0.0986      1.1679
0.6250      0.0901      1.1463
0.6875      0.0742      0.8871
0.7500      0.0576      0.6538
0.8125      0.0486      0.5665
0.8750      0.0500      0.6666
0.9375      0.0565      0.8799
1.0000      0.0600      0.9993
```

The potential map is reported at specified intervals. The potential map is a text file listing the potentials and positions of each node in the mesh. These can be used to generate contour maps, or other charts. The format is x<tab>y<tab>potential<cr>.

B-3 Main program code: NiNod.c

```
/*          2 Dimensional Nodule Growth module for NiOOH/Ni(OH)2
 *               Bob Crocker 14 Dec 90
 *
 *   This program calculates the growth of an arbitrary boundary between
 *   two phases of different conductivity with linear kinetics. the Laplace
 *   equation in the complicated geometry is mapped into a simple
 *    rectangular
 *   domain. The resulting elliptic PDE for the potential is then solved
```

```
 *    for
 *    each time step by finite differences.  The current distribution on
 *    the
 *    boundary is then used to move it.
 *
 *    This program was written in Symantec Lightspeed C 5.0/ANSI
 *
 *         Robert Crocker, Lawrence Berkeley Lab, 1991
 *
 *         Flat Boundary ± Axisym   OK  7 FEb 91 RWC
 */
#include      <stdio.h>
#include      <stdlib.h>
#include      <stddef.h>
#include      <math.h>
#include      <time.h>

#include      "subs.h"
#include      "FFT.h"

#define       ONE             1.
#define       TWO             2.
#define       ZERO        0.
#define       TIME_TO_FREQ    -1
#define       FREQ_TO_TIME    1
/*
 *    MPTS is the mesh size in the x-direction, and is common to both
 *     domains, NPTS is the mesh size in the y-direction.
 *    L is position of the interface between the domains.
 *
 *         MPTS must be 2**n + 1
 */
#define       MPTS            17
#define       NPTS            32
#define       L               7
#define       MMAX            (MPTS-1)
#define       NMAX            (NPTS-1)

#define       AXISYM          0
#define       DELTA_CHARGE    .01

#define       PHI_MAP_INT         10
#define       SP_GROWTH_INT       10
#define       I_DISTR_INT         4

#define       MAXIT           10000
#define       EPS                 1.e-8
#define       J_RADIUS        .95


void PolInt( double *xa, double *ya, int n, double x, double *y,
                    double *dy);
```

```
int SOR( double **a, double **b, double **c, double **d, double **e,          double **f,
double **u, int mMax, int nMax, double rJac,
        double epsilon, int maxIt);

main()
{
    double    kinGrp, condGrp, aspectRatio;
    double    avgCurrent, current[MPTS], charge, dCharge, myTime, dTime;
    double    temp, temp2, du, dv, dw, dwOdu, dvOdu;
    double    newX[MMAX+2], newY[MMAX+2], dy;
    double    u, v, w, x, y, yBCoef[MPTS], yBmax, yBmin;
    double    *phi[MPTS], yBound[MPTS], dYBdu[MPTS]
    double    d2YBdu2[MPTS], oldYBC[MPTS];
    double    *a[MPTS], *b[MPTS], *c[MPTS], *d[MPTS], *e[MPTS], *f[MPTS];
    double    A, B, C, D, E, F, Q, R;
    char      boundaryFileName[255], expPrefix[5], filename[255];
    char      label[255];
    int   i, j, n, numPts, itCount, countSOR;
    int       mapFileCount, spGrFileCount, iDistrFileCount;
    FILE      *SpGrowthFile, *iDistrFile, *PhiMapFile, *TransientFile;
    time_t    tp;
/*
 *   Allocate Memory for Coefficient Matrices
 */
    for(i=0; i<=MMAX; i++)
        {     phi[i] = calloc(NPTS, sizeof(double));
              a[i] = calloc(NPTS, sizeof(double));
              b[i] = calloc(NPTS, sizeof(double));
              c[i] = calloc(NPTS, sizeof(double));
              d[i] = calloc(NPTS, sizeof(double));
              e[i] = calloc(NPTS, sizeof(double));
              f[i] = calloc(NPTS, sizeof(double));
        }

/*   Get Model Parameters: Conductivities, Lengths, kinetic par,
 *   Boundary coeff, numerical pars.
 *   Dimensionless Pars:  Kinetic              (alpha*length/kappa1)
 *                        Conductivity         (kappa1/kappa2)
 *                        Aspect ratio  (H/L)
 *                        Boundary coef.   d[i]/L
 */
    GetModelParams(&kinGrp, &condGrp, &aspectRatio, expPrefix);

/*
 *   Read in Boundary Fourier coefficients, d[i]
 */
    GetBounds(yBCoef, MMAX);

/*
 *   Calculate Boundary from coefficients and make sure it's proper.
 */
    CalcBounds( yBCoef, yBound, &yBmin, &yBmax, aspectRatio, MPTS);
/*
 *   Open Time/Charge Transient File
```

```
*/
    time(&tp);
    sprintf( filename, "Trans%s", expPrefix);
    if ( (TransientFile = fopen( filename, "w")) == NULL)
        {   printf( "Can't open %s\n", filename);
            exit;
        }
        fprintf(TransientFile, "*Transient File: %s \t %s", expPrefix,
        ctime(&tp));
        fprintf(TransientFile, "*kinGrp:  %6.3f, conGrp: %6.3f,
    aspectRatio: %6.3f \n",kinGrp, condGrp, aspectRatio);

        fprintf(TransientFile,
            "*Iteration \t Time \t  Charge \t Itot \t\t yBmax\t SOR
    passes\n");
        printf( "*Iteration \t Time \t  Charge \t Itot \t\t yBmax\t SOR
    passes\n");

/*
*   Initialize Potential Map with linear profile
*/
    for(j=0; j<=NMAX; j++)
    {   temp = (double)(j+1)/(NMAX+1);
        for(i=0; i<=MMAX; i++) phi[i][j] = temp;
    }
/*
*   Initialize counters and sums
*/
        charge = ZERO;
        myTime = ZERO;;
        avgCurrent = ZERO;
        iDistrFileCount = 0;
        spGrFileCount  = 0;
        mapFileCount = 0;
        countSOR      = 0;

/*  Define increment constants
*/
                    du = (double)ONE/MMAX;
                    dw = (double)ONE/(L+1);
                    dv = (double)ONE/(L-NMAX);  /* Negative ! */
                    dwOdu = (double)MMAX/(L+1);
                    dvOdu = (double)MMAX/(L-NMAX);  /* Negative ! */

/*
*   Enter incremental charge loop - exit when boundary hits top of film
*/
    for ( itCount=0; yBmax <= 1.; itCount++ )
{
/*
*       Report iteration, time, charge, avgCurrent, peak position,
*           solution steps
*/
        fprintf(TransientFile,
```

```
                "%4i \t %6.3f \t %6.3f \t %6.4f \t %6.4f \t %6i \n",
                itCount, myTime, charge, avgCurrent, yBmax, countSOR);

        printf( "%4i \t %6.4f \t %6.4f \t %6.4f \t %6.4f \t %6i \n",
                itCount, myTime, charge, avgCurrent, yBmax, countSOR);

/*
 *   Calculate derivatives of boundary (from coefficients)
 */
    for(i=0, d2YBdu2[MMAX]=0.; i<=MMAX-1; i++)
     { dYBdu[i] = -yBCoef[i]*i*PI;
       d2YBdu2[i] = dYBdu[i]*i*PI;
       d2YBdu2[MMAX] += d2YBdu2[i]*(1-2*(i%2));
     }
    SinFT(&(dYBdu[-1]), MPTS-1, FREQ_TO_TIME);
      dYBdu[MMAX] = ZERO;
    CosFT(&(d2YBdu2[-1]), MPTS-1, FREQ_TO_TIME);

/*  for(i=1; i<=MMAX-1; i++)
 *  {
 *       dYBdu[i] = (yBound[i+1] - yBound[i-1])/(2.*du);
 *       d2YBdu2[i] = (yBound[i+1] - 2.*yBound[i] + yBound[i-1])/(du*du);
 *  }
 *       dYBdu[0] = 0;
 *       dYBdu[MMAX] = 0;
 *       d2YBdu2[0] = (2.*yBound[1] - 2.*yBound[0])/(du*du);
 *       d2YBdu2[MMAX] = (2.*yBound[MMAX-1] - 2.*yBound[0])/(du*du);
 */
/*
 *   Calculate coef. Matrix
 *       A Puu + B Puv + C Pvv + D Pv + E Pu + F = 0.
 *                 (Puu : sec. deriv. of P wrt u)
 */
        for( i=0; i<=MMAX; i++)
        {
            u = (double)i/MMAX;
            for(j=0; j<=L; j++)
            {
/* Lower */         w = (double)(j+1)/(L+1);
                    temp = dYBdu[i]/yBound[i];
                    A = ONE;
/*                  B = ZERO;                   */
                    B = -2.*w*temp;
                    C = ONE/sq(aspectRatio*yBound[i]) + sq(w*temp);
                    D = 4.*w*sq(temp) - TWO*w*d2YBdu2[i]/yBound[i];
                    E = 0.;
                    F = 0.;
/*
 *   Allow for axisymmetric case
 */
                    if( AXISYM && (u != 0) )
                    {   E = 1/u;
                        D += -w*temp/u;
                    }
```

```
/*
 *    Calculate discretized coeff. matrix.
 *         a P[i,j+1] + b P[i,j-1] + c P[i+1,j]
 *                    + d P[i-1,j] + e P[i,j] - f = 0.
 */
                    a[i][j] = C/sq(dwOdu) + B*dwOdu/sq(ONE + sq(dwOdu))
                                          +  D*du/(TWO*dwOdu);
                    b[i][j] = C/sq(dwOdu) + B*dwOdu/sq(ONE + sq(dwOdu))
                                          -  D*du/(TWO*dwOdu);
                    c[i][j] = A - B*dwOdu/sq(ONE + sq(dwOdu)) + E*du/TWO;
                    d[i][j] = A - B*dwOdu/sq(ONE + sq(dwOdu)) - E*du/TWO;
                    e[i][j] = -TWO*A - TWO*C/sq(dwOdu);
                    f[i][j] = -F;
               }    /* next j */

               for(j=L+1; j<=NMAX; j++)
               {
/* Upper */            v = ((double)(NMAX +1 - j))/(NMAX - L);
                    temp = dYBdu[i]/(ONE- yBound[i]);
                    A = ONE;
/*                  B = ZERO;                   */
                    B = TWO* v *temp;
                    C = sq(v *temp)
                              + ONE/sq(aspectRatio*(ONE- yBound[i]));
                    D = TWO*v*(d2YBdu2[i]/(ONE- yBound[i]) + TWO*sq(temp) );
                    E = 0.;
                    F = 0.;
/* Axis Symmetry */
                         if( AXISYM && (u != 0) )
                         {    E = 1/u;
                              D += v*temp/u;
                         }

                    a[i][j] = C/sq(dvOdu) + B*dvOdu/sq(ONE + sq(dvOdu))
                                          +  D*du/(TWO*dvOdu);
                    b[i][j] = C/sq(dvOdu) + B*dvOdu/sq(ONE + sq(dvOdu))
                                          -  D*du/(TWO*dvOdu);
                    c[i][j] = A - B*dvOdu/sq(ONE + sq(dvOdu)) + E*du/TWO;
                    d[i][j] = A - B*dvOdu/sq(ONE + sq(dvOdu)) - E*du/TWO;
                    e[i][j] = -TWO*A - TWO*C/sq(dvOdu);
                    f[i][j] = -F;
               }    /* next j */
          }    /* next i */
/*
 *    Kinetic Boundary Conditions
 */
/*    (i,L) and (i,L+1) Edges
 */
          v = ONE;
          w = ONE;

     for(i=0; i<=MMAX; i++)
     {
```

```
                u = (double)i/MMAX;
                temp = aspectRatio*dYBdu[i];
            /*
             *    Lower Kinetic Expression (i,L)
             */
                    Q = TWO*dw*kinGrp*aspectRatio*yBound[i]
                                        /sqrt(ONE + temp*temp);
                    R = aspectRatio*temp*dwOdu*yBound[i]/(ONE + temp*temp);
                    temp2 = a[i][L];
                    b[i][L] += temp2;
                    c[i][L] += temp2*R;
                    d[i][L] -= temp2*R;
                    e[i][L] -= temp2*Q;
                    a[i][L] *= Q;
            /*
             * Upper Kinetic Expression (i,L+1)
             */
                    Q = TWO*dv*kinGrp*condGrp*aspectRatio*(ONE - yBound[i])
                            /sqrt(ONE + temp*temp);
                    R = aspectRatio*temp*dvOdu*(ONE - yBound[i])
                            /(temp*temp + ONE);
                    temp2 = b[i][L+1];
                    a[i][L+1] += temp2;
                    c[i][L+1] += temp2*R;
                    d[i][L+1] -= temp2*R;
                    e[i][L+1] += temp2*Q;
                    b[i][L+1] *= -Q;
        }
/*
 *    Make corrections for Edge Boundary Conditions
 */
/*
 *    (i,0) Edge:       phi[i][j-1] = 0., thus b[i][j] = 0.
 */
            for(i=0; i<=MMAX; i++)        b[i][0]=ZERO;
/*
 *    (0,j) and (M,j) Edges:
 *          phi[i-1][j] = phi[i+1][j] and d[i][j] = 0.  along i=0.
 *          phi[i+1][j] = phi[i-1][j] and c[i][j] = 0.  along i=M.
 */
            for(j=0; j<=NMAX; j++)
            {
                    c[0][j] += d[0][j];
                    d[0][j] = ZERO;
                    d[MMAX][j] += c[MMAX][j];
                    c[MMAX][j] = ZERO;
            }
/*
 *    (i,N) Edge:   phi[i][j+1] = 1. and f[i][j] = -a[i][j]*ONE,
 *                                and a[i][j] = 0.
 */
            for(i=0; i<=MMAX; i++)
            {     f[i][NMAX] = -a[i][NMAX];
                  a[i][NMAX] = ZERO;
```

```
        }

/*
 *      Solve for Potential Distribution
 *              using Simultaneous Over-Relaxation
 */
        countSOR = SOR(a, b, c, d, e, f, phi, MMAX,
                                NMAX, J_RADIUS, EPS, MAXIT);

/*
 *  Output Potential Map
 */
        PrintPotMap(itCount, PHI_MAP_INT, expPrefix, myTime,
                charge, MMAX, L, aspectRatio, yBound, phi, NMAX);

/*
 *  Calculate Faradaic Current Distribution on boundary
 */


        for(i=0, avgCurrent = ZERO; i<=MMAX; i++)
        {   current[i] = kinGrp*(phi[i][L+1] - phi[i][L]);
            if (i> 0)
            {   avgCurrent += .5*(current[i]+current[i-1])
                        *sqrt(ONE + sq(aspectRatio*dYBdu[i]))*du;
            }
        }
```

```
/*
 *    Output Current Distribution
 */
      PrintCurrentDistr(itCount, I_DISTR_INT, expPrefix,
                        myTime, charge, avgCurrent, yBound, current, MMAX);

/*
 *    Increment Boundary: Create new parametric boundary curve.
 */
      dTime = DELTA_CHARGE/avgCurrent;
      for(i=0; i<=MMAX; i++)
      {     x = (double)i /MMAX;
            temp = -aspectRatio*dYBdu[i];
            newX[i] = x + current[i]*dTime*temp/sqrt(ONE + sq(temp));
            newY[i] = yBound[i] + current[i]*dTime/sqrt(ONE + sq(temp));
      }
/*
 *    Resample Boundary into even absissa intervals
 *          using Polynomial Interpolation.
 */
      for (i=0, yBmax=0., yBmin=1.; i<=MMAX; i++)
            {     x = (double)i/MMAX;
                  PolInt( &(newX[-1]), &(newY[-1]), MPTS, x, &(yBound[i]), &dy);
                  yBmax = max( yBound[i],yBmax);
                  yBmin = min( yBound[i],yBmin);
            }

      if ( yBmin <=0.)
      {     printf("Error: Boundary out of range: yB [%6.4f, %6.4f] \n",
                        yBmax, yBmin);
            fprintf(TransientFile,
                        "Error: Boundary out of range: yB [%6.4f, %6.4f] \n",
                        yBmax, yBmin);
            fclose(TransientFile);
            exit(0);
      }
/*    Determine new Fourier Coeff. for Boundary
 */
      for(i=0; i<=MMAX; i++)
      {
            oldYBC[i] = yBCoef[i];
            yBCoef[i] = yBound[i];
      }
      CosFT(&(yBCoef[-1]), MMAX, TIME_TO_FREQ);
      for(i=MMAX-3; i<=MMAX; i++)
      {
            yBCoef[i] = 0.;
      }
```

```
/*
*    Filter Coefficients to suppress differencing noise.
*/

     for(i=0; i<=MMAX; i++)
     {
          u = ((double) i)/MMAX;
          yBCoef[i] = yBCoef[i]*exp(-sq(u/.5));
          yBound[i] = yBCoef[i];
     }
     CosFT(&(yBound[-1]), MMAX, FREQ_TO_TIME);
/*
*         The last point is determined from symmetry to avoid complicating
*              FFT.
*/
     yBound[MMAX] = 2.*yBound[MMAX/2] - yBound[0];


/*
*    Output Spectral Growth Map
*/
     PrintSpectralGrowth(itCount, SP_GROWTH_INT, expPrefix, myTime,
               charge, yBCoef, oldYBC, MMAX, dTime);

/*
*         Increment myTime and charge
*/
          myTime += dTime;
          charge += DELTA_CHARGE;


     }    /* End of Charge Loop */
/*
*         Report Final iteration, time, charge,
*              avgCurrent, peak position, solution steps.
*/
          fprintf(TransientFile,
                    "%4i \t %6.3f \t %6.3f \t %6.4f \t %6.4f\t %6i \n",
               itCount, myTime, charge,avgCurrent, yBmax, countSOR);
          fprintf(TransientFile, "** End of Report ** \n");

          printf( "%4i \t %6.3f \t %6.3f \t %6.4f \t %6.4f \t %6i \n",
               itCount, myTime, charge,avgCurrent, yBmax, countSOR);
          printf( "** End of Report ** \n");
```

```
/*
 *    Close Transient File
 */
          fclose (TransientFile);
/*
 *    Free Memory from Coefficient Matrices
 */
     for(i=0; i<=MMAX; i++)
          {    free(phi[i]);
               free(a[i]);
               free(b[i]);
               free(c[i]);
               free(d[i]);
               free(e[i]);
               free(f[i]);
          }
          printf("Say Good-night Gracie...\n");
          scanf("%1c",i);
} /* end of main */
```

B-4: Auxilliary Subroutines: Nodsubs

```
/*  Subs.h      Headers for Nodsubs.c
 *
*/
void GetModelParams(double *kinGrp, double *condGrp, double *aspectRatio, char
*expPrefix);

void GetBounds(double yBCoef[], int mMAX);

void CalcBounds( double yBCoef[], double yBound[], double *yBmin,
                    double *yBmax, double aspectRatio, int mPts );

void PrintPotMap( int itCount, int PHI_MAP_INT, char *expPrefix,
                    double myTime,
                    double charge, int MMAX, int L, double aspectRatio,
                    double *yBound, double **phi, int NMAX);

void      PrintCurrentDistr(int itCount, int I_DISTR_INT,
               char *expPrefix, double myTime,
               double charge, double avgCurrent, double *yBound,
               double *current, int MMAX);

void      PrintSpectralGrowth(int itCount, int SP_GROWTH_INT,
               char *expPrefix,
               double myTime, double charge, double *yBCoef,
               double *oldYBC, int MMAX, double dTime);
```

Nodsubs.c

```
#include    <stdio.h>
#include    <stdlib.h>
#include    <stddef.h>
#include    <time.h>

#include    "FFT.h"

#define     max(A,B)        ( (A) > (B) ? (A) : (B) )
#define     min(A,B)        ( (A) < (B) ? (A) : (B) )
#define     TIME_TO_FREQ        -1
#define     FREQ_TO_TIME        1
#define     ZERO                0.
#define     ONE                     1.

void GetModelParams(double *kinGrp, double *condGrp,
                        double *aspectRatio, char *expPrefix);

void GetBounds(double yBCoef[], int mMAX);

void CalcBounds( double yBCoef[], double yBound[], double *yBmin,
                    double *yBmax, double aspectRatio, int mPts );

void PrintPotMap( int itCount, int PHI_MAP_INT, char *expPrefix,
                     double myTime,
                    double charge, int MMAX, int L, double aspectRatio,
                    double *yBound, double **phi, int NMAX);

void    PrintCurrentDistr(int itCount, int I_DISTR_INT,
            char *expPrefix, double myTime,
            double charge, double avgCurrent, double *yBound,
             double *current, int MMAX);

void    PrintSpectralGrowth(int itCount, int SP_GROWTH_INT,
             char *expPrefix,
            double myTime, double charge, double *yBCoef,
             double *oldYBC, int MMAX, double dTime);

void GetModelParams(double *kinGrp, double *condGrp,
                        double *aspectRatio, char *expPrefix)
{
    printf("Bob's 2-D NiOOH Nodule Growth Model\n\n");
    printf("Kinetic Parameter (alpha • L / kappaLower): ");
    scanf("%lf", kinGrp);
    printf("\nRelative Conductivity (kappaLower / kappaUpper): ");
    scanf("%lf", condGrp);
    printf("\nAspect Ratio (H/L): ");
    scanf("%lf", aspectRatio);
    printf("\nEnter 4 character Experiment name: ");
    scanf("%s", expPrefix);
}
```

```
void GetBounds(double yBCoef[], int mMAX)
{
        int   n, numPts, i;
        double    temp;
        char      label[255], boundaryFileName[255];
        FILE      *boundaryFile;

    do
    {   printf("\nEnter Filename of Boundary Cosine Coeff.
        (yBound[i]/L): ");
        scanf("%s",  boundaryFileName);
    }
    while( (boundaryFile = fopen( boundaryFileName, "r")) == NULL );
    if ( (fgets( label, 80, boundaryFile)) == NULL)
        {   printf("\n EOF on file read\n");
            exit(-1);
        }
    printf( "File Label: %s\n", label);
    for(i=0; i<=mMAX; i++) yBCoef[i] =0.;
        numPts = 0;
    while(fscanf( boundaryFile, "%i \t %lf", &n, &temp) != EOF)
        {   yBCoef[n] = temp;
            numPts++;
            printf("%5i \t %6.4f \n", n, temp);
        }
    fclose( boundaryFile);
    printf (" %i Pts read from Boundary File.\n", numPts);

}

void CalcBounds( double yBCoef[], double yBound[], double *yBmin,
                    double *yBmax, double aspectRatio, int mPts )
{
    int i, mMax;
    mMax = mPts - 1;
    for (i=0, yBound[mMax]=0.; i<=mMax-1; i++)
    {   yBound[i] = yBCoef[i];
        yBound[mMax] += yBCoef[i]*(1-2*(i%2));
    }
    CosFT(&(yBound[-1]), mPts-1, FREQ_TO_TIME);
    for (i=0, *yBmax =0., *yBmin = 1.; i<=mMax; i++)
    {   *yBmax = max( yBound[i],*yBmax);
        *yBmin = min( yBound[i],*yBmin);
    }
    if ( ( *yBmin <=0.) || ( *yBmax >= 1. ) )
    {   printf("Error: Boundary out of range: yB [%6.4f, %6.4f] \n",
    yBmax, yBmin);
        exit(-1);
    }

}
```

```
/*
 *    Output Potential Map
 */
void PrintPotMap( int itCount, int PHI_MAP_INT, char *expPrefix,
                  double myTime,
                  double charge, int MMAX, int L, double aspectRatio,
                  double *yBound, double **phi, int NMAX)
{
        char        filename[255];
        int         i, j;
        static int  mapFileCount;
        double      x, y;
        FILE        *PhiMapFile;
        time_t      tp;

        if (itCount == 0) mapFileCount=0;
        if( itCount%PHI_MAP_INT == 0)
        {   mapFileCount++ ;
            time(&tp);
            sprintf( filename, "Pot%s.%0i", expPrefix, mapFileCount);
            if ( (PhiMapFile = fopen( filename, "w")) == NULL)
                {   printf( "Can't open %s\n", filename);
                }
            else
            {   fprintf( PhiMapFile, "*Potential Map:  %s \t %s",
                        filename,  ctime(&tp));
                fprintf( PhiMapFile,
                    "*Step %3i, Time: %6.4f, Charge: %6.4f \n",
                    itCount, myTime, charge);
                fprintf (PhiMapFile, "*x \t\t y \t\t Potential\n");

                for (i = 0; i<=MMAX; i++)
                {   x = (double)i/MMAX;
                    fprintf( PhiMapFile, "%6.4f  %6.4f  %6.4f   \n",
                            x,   ZERO, ZERO );

                    for (j = 0; j<L; j++)
                    {   y = (double)(j+1)*yBound[i]*aspectRatio/(L+1);
                        fprintf( PhiMapFile, "%6.4f  %6.4f  %6.4f   \n",
                                    x, y, phi[i][j] );
                    }
                    y = (.98)*yBound[i]*aspectRatio;
                    fprintf( PhiMapFile, "%6.4f  %6.4f  %6.4f   \n",
                                    x, y, phi[i][j] );
                }
                fprintf (PhiMapFile, "*Upper Domain \n");
                for (i = 0; i<=MMAX; i++)
                {   x = (double)i/MMAX;
                    for (j = L+1; j<=NMAX; j++)
                    {   y =aspectRatio*(ONE - (double)(NMAX +1 - j)
                                * (ONE - yBound[i])/(NMAX-L));
                        fprintf( PhiMapFile, "%6.4f  %6.4f  %6.4f   \n",
                                    x, y, phi[i][j] );
                    }
```

```
                        fprintf( PhiMapFile, "%6.4f  %6.4f  %6.4f   \n", x,
                                aspectRatio, ONE );
                    }
                    fclose (PhiMapFile);
                }
            }
            return;
}

void    PrintCurrentDistr(int itCount, int I_DISTR_INT, char *expPrefix, double
myTime,
            double charge, double avgCurrent, double *yBound, double *current, int
MMAX)

{       static int  iDistrFileCount;
        int         i;
        char        filename[255];
        double      x;
        time_t      tp;
        FILE        *iDistrFile;

    if (itCount == 0 ) iDistrFileCount = 0;

    if( itCount%I_DISTR_INT == 0)
        {   iDistrFileCount++ ;
            time(&tp);
            sprintf( filename, "Cur%s.%0i", expPrefix, iDistrFileCount);
            if ( (iDistrFile = fopen( filename, "w")) == NULL)
                {   printf( "Can't open %s\n", filename);
                }
            else
            {   fprintf( iDistrFile,
                        "*Current Distribution \t %s \t %s ",
                        filename, ctime(&tp) );
                fprintf( iDistrFile,
    "*Step %3i, Time: %6.4f, Charge: %6.4f,Average Current %8.5f \n",
                itCount, myTime, charge, avgCurrent);
                fprintf( iDistrFile, "*x, yBound, current/avg\n");

                for (i = 0; i<=MMAX; i++)
                    {   x = (double)i/MMAX;
                        fprintf( iDistrFile,
                        "%6.4f \t %6.4f \t %6.4f \n",
                         x, yBound[i], current[i]/avgCurrent );
                    }
                fclose (iDistrFile);
            }   /* endif */
        } /* End of Output if */

        return;
}
```

```
/*
 *    Output Spectral Growth Map
 */
void        PrintSpectralGrowth(int itCount, int SP_GROWTH_INT,
                char *expPrefix,
                double myTime, double charge, double *yBCoef,
                double *oldYBC, int MMAX, double dTime)
{
        static int  spGrFileCount;
        int         i;
        char        filename[255];
        double      x;
        time_t      tp;
        FILE        *SpGrowthFile;

    if (itCount == 0) spGrFileCount = 0;

    if( itCount%SP_GROWTH_INT == 0)
        {   spGrFileCount++ ;
            time(&tp);
            sprintf( filename, "SGR%s.%0i", expPrefix, spGrFileCount);
            if ( (SpGrowthFile = fopen( filename, "w")) == NULL)
                {   printf( "Can't open %s\n", filename);
                }
            else
            {   fprintf( SpGrowthFile,
                        "*Spectral Growth Rate: %s  \t %s",
                        filename,  ctime(&tp));
                fprintf( SpGrowthFile,
                        "*Step %3i, Time: %6.4f, Charge: %6.4f \n",
                        itCount, myTime, charge);
                fprintf( SpGrowthFile, "*Mode, Amp, SGR \n");

                for (i = 0; i<=MMAX; i++)
                {   x = (double)i/MMAX;
                    fprintf( SpGrowthFile,
                        "%6.4f \t %6.4f \t %6.4f \n", x,
                        yBCoef[i], (yBCoef[i]-oldYBC[i])/dTime );
                }
                fclose (SpGrowthFile);
            }
        }
}
```

B-5: Simultaneous Over-Relaxation Algorithm: SOR.c

```
/*
 *      SIMULTANEOUS OVER-RELAXATION
 *      from Press et al, Numerical Recipes in FORTRAN
 *      Translated and adapted into C
 *          Bob Crocker  9 Jan 91
 *              Tested OK 29 Jan 91
 *          Adaptive Convergence Feb '92
 */
#include    <math.h>
#include    <stddef.h>
#include    <stdio.h>

#define     ZERO        0.
#define     HALF        .5
#define     QTR             .25
#define     ONE             1.
#define     REPORT_INT      500000L

int SOR( double **a, double **b, double **c, double **d,
            double **e, double **f, double **u, int mMax,
            int nMax, double rJac, double epsilon, int maxIt);

int SOR( double **a, double **b, double **c, double **d,
            double **e, double **f, double **u, int mMax,
            int nMax, double rJac, double epsilon, int maxIt)
{
        double  anorm, anormf, omega, resid;
        double  lastAnorm, lepsm2, lepsm1, logeps;
        double  dOmega, deriv2;
        int     i, j, n, interval;

        interval = 2*(REPORT_INT/(nMax*nMax*mMax*mMax));

        anormf = ZERO;
        for(i=0; i<=mMax; i++)
         { for( j=0; j<=nMax; j++)
            {   anormf = anormf + fabs(f[i][j]);
            }
        }
        dOmega = 1.;
        omega = ONE;
        lastAnorm = anormf;

        for(n=1; n<=maxIt; n++)
        {   anorm = ZERO;
            for(i=0; i<=mMax; i++)
             {  for(j=0; j<=nMax; j++)
                 {  if( ((i+j)%2) == (n%2) )
                     {  resid = e[i][j]*u[i][j] - f[i][j];
                        if ( j > 0)         resid += b[i][j]*u[i][j-1] ;
                        if ( j < nMax)          resid += a[i][j]*u[i][j+1] ;
                        if ( i > 0)         resid += d[i][j]*u[i-1][j] ;
```

```
                        if ( i < mMax)        resid += c[i][j]*u[i+1][j] ;

                        anorm = anorm + fabs(resid);
                        u[i][j] -= omega*resid/e[i][j];
                    } /* even - odd */
                } /* next j */
            } /* next i */
            logeps = log10(anorm/anormf);
/*
 *      Chebychef Acceleration for first 10 iterations
 */
            if ( n == 1)
             { omega = ONE/(ONE - HALF*rJac*rJac*omega);
                lepsm2 = logeps;
                lepsm1 = logeps;
            }
            else if ( n<10 )
            {   omega = ONE/(ONE - QTR*rJac*rJac*omega);
            }

/*
 *      Report Progress and adjust convergence rate omega to maximize.
 */
             if( n % interval == 0 )
             {   printf("Iteration: %6i \t Log Epsilon: %8.4f Omega:
    %6.4f\r", n, logeps, omega);
                    deriv2 = .25*(lepsm2 - 2*lepsm1 + logeps);
                    omega += .01;
                    omega = min(max(omega*(1-deriv2*dOmega),.7), 1.98);
                    lepsm2 = lepsm1;
                    lepsm1 = logeps;
                }
/*
 *      Check for paranormal behaviour.
 */
             if ( anorm > 10*lastAnorm && n%2 == 0)
             {   printf("SOR diverging after %4i calls...Log epsilon =
    %6.4f\r", n, logeps);
                    omega = max( omega -.01, .7);
                }
            if (  anorm < epsilon*anormf )
            {   printf("\n");
                return(n);
            }
            if ( anorm/anormf > 1000. )
             { printf(" SOR going ballistic after %i iterations\n", n);
                return(-1);
            }
            lastAnorm = anorm;
    } /* next n */
    printf("Returning from SOR - %4i iterations, epsilon: %8.6f
    \n",n,anorm/anormf);
         return(-1);
}
```

B-6 Numerical Utility Routines: QRomb, FFT, PolInt

```
/*   Romberg Integration Routine from Numerical Recipes
 */

#include <math.h>
#include <stdio.h>

#define      EPS          1.0E-6
#define      JMAX    20
#define      JMAXP   21
#define      K       5
#define      KM      4
#define      NMAX    100

void      PolInt( double *xa, double *ya, int n, double x,
               double *y, double *dy);

/*   PolInt  Polynomial Interpolation Routine:
 *                Given arrays xa, ya of length n, and a given value of
 *                x, the routine estimates a value of y and its error dy.
 */
void PolInt( double *xa, double *ya, int n, double x,
                double *y, double *dy)
{    double    c[NMAX+1], d[NMAX+1], dif, dift, h0, hp, w, den;
     int i, m, ns;
     ns = 1;
     dif = fabs(x -xa[1]);
     for( i=1; i<=n; i++)
          {    dift = fabs(x - xa[i]);
               if (dift < dif)
                    {    ns = i;
                         dif = dift;
                    }
               c[i] = ya[i];
               d[i] = ya[i];
          }
     *y = ya[ns];
     ns -=1;
     for (m = 1; m<=n-1; m++)
          {    for (i=1; i<=n-m; i++)
                    {    h0 = xa[i] - x;
                         hp = xa[i+m] - x;
                         w = c[i+1] - d[i];
                         den = h0 - hp;
                         if (den == 0.) perror ("Zero den. in POLINT");
                         den = w/den;
                         d[i] = hp*den;
                         c[i] = h0*den;
                    }
               if ( 2*ns < n-m)
                    {    *dy = c[ns+1];
```

```
            }
        else
            {   *dy = d[ns];
                ns = ns-1;
            }
        *y += *dy;
    }
}
```

CosFT.c

```
/*  COSFT from Numerical Recipes translated from FORTRAN
 *
 */

void CosFT(double yC[], int n, int isign);
void SinFT(double yC[], int n, int isign);
void RealFT( double dataC[], int n, int isign);
void Four1(double dataC[], int nn, int isign);

#include    <math.h>
/*  Fast Fourier Cosine Transform from Numerical Recipes in FORTRAN
 *   Transforms n real freq domain data pts into time domain isign = 1
 *       or inverse (isign = -1)  element 1 is zeroeth (i.e. constant term)
 *       Checked OK 23 Oct 90 Crocker
 */
void CosFT(double y[], int n, int isign)
{
    double wr, wi, wpr, wpi, wtemp, theta, sum;
    double y1, y2, even, odd, enfo, sumo, sume;
    int m, j, i ;
    theta = PI/n;
    wr= 1.;
    wi = 0.;
    wpi = sin( theta);
    wpr = sin( .5*theta);
    wpr *= -2. * wpr ;
    sum = y[1];
    m = n/2;

    for (j = 1; j<= m-1; j++)
        {   wtemp = wr;
            wr = wr*wpr - wi*wpi + wr;
            wi = wi*wpr + wtemp*wpi + wi;
            y1 = .5*(y[j+1] + y[n-j+1]);
            y2 = y[j+1] - y[n-j+1];
            y[j+1] = y1 - wi * y2;
            y[n-j+1] = y1 + wi*y2;
            sum += wr*y2;
        }
```

```
        RealFT(y, m, 1);
        y[2] = sum;

        for(j=4; j<=n; j += 2)
            {   sum += y[j];
                y[j] = sum;
            }

        if ( isign == -1 )
            {   even = y[1];
                odd = y[2];
                for (i = 3; i<=n-1; i += 2 )
                    {   even += y[i];
                        odd += y[i+1];
                    }
                enfo = 2. * (even-odd);
                sumo = y[1] - enfo;
                sume = (2.*odd/n) - sumo;
                y[1] = .5*enfo;
                y[2] = y[2] - sume;
                for ( i=3; i<=n-1; i=i+2)
                    {   y[i] -= sumo;
                        y[i+1] -= sume;
                    }
                for ( i=1; i<=n; i++) y[i] *= 2./n;
            }
}
```

```
/*
 *    Fast Fourier Sine Transform from Numerical Recipes in FORTRAN
 *    It is its own inverse save a factor of 2/n
 *    Multiply new freq domain data by 2/n.
 *  Checked OK 22 Oct 90
 */
void SinFT(double y[], int n, int isign)
{
      double wr, wi, wpr, wpi, wtemp, theta, sum;
      double y1, y2, even, odd, enfo, sumo, sume;
      int m, j, i ;
      theta = PI/n;
      wr= 1.;
      wi = 0.;
      wpi = sin( theta);
      wpr = sin( .5*theta);
      wpr *= -2. * wpr ;
      y[1] = 0.;
      m = n/2;

      for (j = 1; j<= m; j++)
            {     wtemp = wr;
                  wr = wr*wpr - wi*wpi + wr;
                  wi = wi*wpr + wtemp*wpi + wi;
                  y1 = wi*(y[j+1] + y[n-j+1]);
                  y2 = .5*(y[j+1] - y[n-j+1]);
                  y[j+1] = y1 + y2;
                  y[n-j+1] = y1 - y2;
            }

      RealFT(y, m, 1);
      sum = 0.;
      y[1] = .5*y[1];
      y[2] = 0.;

      for(j=1; j<=n-1; j=j+2)
            {     sum += y[j];
                  y[j] = y[j+1];
                  y[j+1] = sum;
            }
      if (isign == -1 )
      {     for(i=1; i<=n; i++) y[i] *= 2./n;
      }
}
```

```
void RealFT( double data[], int n, int isign)
{
    double wr, wi, wpr, wpi, wtemp, theta, sum;
    double h1r, h1i, h2r, h2i, c1, c2;
    int m, j, i, n2p3, i1, i2, i3, i4;
    theta = PI/n;
    c1 = .5;
    if ( isign == 1)
        {   c2 = -c1;
            Four1(data, n, +1);
        }
    else
        {   c2 = c1;
            theta = -theta;
        }

    wpr = sin( .5*theta);
    wpr *= -2. * wpr ;
    wpi = sin( theta);
    wr= 1. + wpr;
    wi = wpi;
    n2p3 = 2*n + 3;

    for ( i=2; i<=n/2; i++ )
        {   i1 = 2*i - 1;
            i2 = i1 + 1;
            i3 = n2p3 - i2;
            i4 = i3 +1;
            h1r = c1*(data[i1] + data[i3]);
            h1i = c1*(data[i2] - data[i4]);
            h2r = -c2*(data[i2] + data[i4]);
            h2i = c2*(data[i1] -data[i3]);
            data[i1] = h1r + wr*h2r - wi*h2i;
            data[i2] = h1i + wr*h2i + wi*h2r;
            data[i3] = h1r - wr*h2r + wi*h2i;
            data[i4] = -h1i + wr*h2i + wi*h2r;
            wtemp = wr;
            wr = wr*wpr - wi*wpi + wr;
            wi = wi*wpr + wtemp*wpi + wi;
        }

    if(isign == 1)
        {   h1r = data[1];
            data[1] = h1r + data[2];
            data[2] = h1r - data[2];
        }
    else
        {   h1r = data[1];
            data[1] = c1*(h1r + data[2]);
            data[2] = c1*(h1r - data[2]);
            Four1( data, n, -1);
        }
}
```

```
void Four1(double data[], int nn, int isign)
{
    double wr, wi, wpr, wpi, wtemp, theta;
    double tempr, tempi;
    int n, m, mmax, j, i, istep;

    n = 2*nn;
    j=1;
    for (i=1; i<=n; i += 2)
        {   if (j > i)
                {   tempr = data[j];
                    tempi = data[j+1];
                    data[j] = data[i];
                    data[j+1] = data[i+1];
                    data[i] = tempr;
                    data[i+1] = tempi;
                }
            m = n/2;
            while ( (m >= 2) &&( j > m) )
                {   j -= m;
                    m = m/2;
                }
            j +=m;
        }
    mmax=2;
    while ( n > mmax )
    {   istep = 2*mmax;
        theta = 2. * PI /(isign*mmax);
        wpr = sin(.5 * theta);
        wpr *= -2.* wpr;
        wpi = sin(theta);
        wr = 1.;
        wi = 0.;
        for (m=1; m<=mmax; m += 2)
            {   for( i=m; i<=n; i += istep)
                    {   j = i + mmax;
                        tempr = wr*data[j] - wi*data[j+1];
                        tempi = wr*data[j+1] + wi*data[j];
                        data[j] = data[i] - tempr;
                        data[j+1] = data[i+1] - tempi;
                        data[i] = data[i] + tempr;
                        data[i+1] = data[i+1] + tempi;
                    }
                wtemp = wr;
                wr = wr*wpr - wi*wpi + wr;
                wi = wi*wpr + wtemp*wpi + wi;
            }
        mmax = istep;
    }
}
```

APPENDIX C:
Multi-Film Ellipsometry Modelling Software

C-1 Description, purpose, numerical techniques

The FORTRAN program MFITRI was developed to determine the optical constant spectra and film thicknesses of thin film materials from spectroscopic ellipsometer measurements. The program was compiled using version 4 of the Microsoft Optimizing FORTRAN compiler for IBM-PC compatible computers. The program also relies on the NAg Mark IV, numerical library for the downhill simplex optimization routine, E04CCF.

To determine the optical property spectrum and the thickness of a thin film, one must make measurements of more than one film of the material of interest. The unknown parameters are the real and imaginary components of the complex refractive index at each spectral point, and the thickness of each film. The ellipsometer measures two parameters, the relative phase shift, delta, and amplitude, psi, between the components of the polarized light, parallel and normal

to the plane of incidence. For the single film problem with N spectral points, there are 2N+1 unknowns and only 2N measurements. However, if one has M films, where M is greater than one, of the same material with unknown, but different thicknesses, then there are 2NM measurements and only 2N+M unknowns. The problem is then well over-determined and error estimates can be obtained for the fitted parameters.

The optical property spectra of the pure film materials are determined numerically using the principle summarized in the preceding paragraph using the downhill simplex optimization algorithm of Nelder and Meade[1]. To circumvent the difficulty of fitting a large number of unknown spectral refractive index values, however, the numerical algorithm uses a cubic spline approximation to the full optical property spectra. Since the optical property spectra of the film materials are relatively smooth and slowly varying, it was well fit by a small number of spline knots. Judicial positioning of the spline knots ensured that all of the broad spectral features were included.

C-2 Sample input/output

The inputs to this program are the ellipsometer spectrum files, a spectrum file of the substrate complex refractive index, the monochromator calibration file for the spectral files, a table of the initial guesses for the complex refractive index spectrum of the film material, and several prompts for values for the fitting process. The user is prompted for values for the range and number of spectral data to use in the fitting process, the tolerance and maximum number of iterations of the fitting routine, and initial guesses for the film thicknesses of the measured films.

The complex spectrum files for the ellipsometer measurements and the substrate refractive index are read from formatted binary files. This format is specific to the

---

1 J.A. Nelder, R. Meade, Computer Journal, **7**, 308, (1965)

spectroscopic ellipsometer developed the Muller research group at Lawrence Berkeley Laboratory. This binary format is defined in the subroutines that read and write the files, INPUTF and OUTPTF, respectively. These files rely on monochromator calibration data contained in the file WLCALC.DAT, read by the subroutine WLCALC.FOR.

The data files for the initial guess for the film complex refractive index spectrum and the fitting summary are ASCII text files. The format for the data in the initial guess table is given in the example below.

first comment line	index of ref for Ni(OH)2<CR>
second comment line	<CR>
number of spline points	7<CR>
first spline pt: wavelength, n, k	3500., 1.460, .0<CR>
	4500., 1.462, .0<CR>
	5000., 1.463, .0<CR>
	5500., 1.462, .0<CR>
	6000., 1.462, .0<CR>
	6500., 1.462, .0<CR>
last point:	7500., 1.463, .0<CR>
end of file	<EOF>

The program reports the progress of the fitting process on the computer screen. When the specified tolerance is achieved or the maximum number of iterations is exceeded, the program prompts for a filename to write the fitting summary. An example of the summary follows:

```
 "NN_OX.OT1          12:22  02/24/1990"
"                              "
 "Nambient: " 1.340
"Substrate RI spectra:" "B:RINICK.DAT    "
"Fit Range:""["3900.,7100.]"  "Encoder Step:" 4

"WL"   "Nfilm"   "Kfilm"
 3500., 1.087,  .509
 4500., 1.273, 1.086
 5000., 1.580,  .709
 5500., 1.724,  .507
 6000., 1.756,  .445
 6500., 1.797,  .368
 7500., 1.838,  .375
"Film RI stored-->""RINNOX.PR1      "
```

```
"D:CNN030.AVG   "
"T film : "    65.667
"ERRORS RMSDEL:"   .31 "AVGDEL:"   .08 "RMSPSI:"   .54 "AVGPSI:"  -.38
"D:CNN070.AVG   "
"T film : "    120.896
"ERRORS RMSDEL:"  5.57 "AVGDEL:" -2.07 "RMSPSI:"   .31 "AVGPSI:"   .14
"D:CNN180.AVG   "
"T film : "    64.261
"ERRORS RMSDEL:"   .32 "AVGDEL:"   .09 "RMSPSI:"   .52 "AVGPSI:"   .44
```

The summary includes a listing of the fitting conditions, (range, number of spectral points, date, etc.) the table of fitted spline points for the film optical constant spectrum, and the fitted film thicknesses, and a summary of the errors between the measured and predicted ellipsometer data spectra. The program also generates binary spectrum files for the refractive index of the film interpolated from the spline table and predicted ellipsometer data spectra. The predicted spectra have the same name as the measured spectra, but the file extensions are changed to PR1.

C-3 Main Program Code: MFITRI

```
      PROGRAM MFITRI

C ***************************************************************************
C       THIS PROGRAM FITS MODEL PARAMETERS TO EXPERIMENTAL OPTICAL
C       MEASUREMENTS OF DELTA AND PSI USING A SIMPLEX ROUTINE.  THE
C       ERROR FUNCTION IS GENERATED BY A SUBROUTINE FUNCT(VAR(I),SIGMA)
C       WHICH CALLS ON THE OPTICAL MODEL.
C       BOB CROCKER      6 JUN 89

C       Multifile version 29 Jun 89
C***************************************************************************
      COMMON/FLMDAT/TNA,TNKA,TNF,TNKF,TNS,TNKS,WL,PHI1,T,DELC,PSIC
      COMMON/INPUT/ DEL, PSI, WLMIN, WLMAX, ANS, ANKS, NSTEP
      COMMON/METFLM/ANF,ANKF
      COMMON/A/NAVG(400),POL(400),ANA(400)
      COMMON/M/IWAVE(400)
      COMMON/OP/NAME
      COMMON/RITAB/NVALS,RIX,RIN, RIK, RIN2, RIK2

      COMMON/MULTI/NFILES,NLOC,NGLOB
      COMMON/NAMES/NAMPAR,NVAR, FNAME
      COMMON/MONCOM/MAXCAL,LPRCAL

      COMMON/SCALE/B(50),NSC,TSC

      REAL ANS(400), ANKS(400), ANF(400), ANKF(400)
```

```
      REAL TNF,T
      REAL  DEL(400,8), PSI(400,8)
      REAL RIX(20), RIN(20), RIN2(20), RIK(20), RIK2(20)
C     DECLARATIONS FOR E04... ROUTINES
      REAL X(50)
      REAL*8 DELC, PSIC, DCHNG

      REAL W1(30), W2(30), W3(30), W4(30), W5(31)
      REAL W6(30,30), TOL, F
      CHARACTER*8 NAMPAR(5)
      CHARACTER*16 NAME, FNAME(10)
      INTEGER NVAR,NSTEP,POW, NVALS
      LOGICAL IYN
      EXTERNAL FUNCT1, ACHNG, ICHNG, DCHNG, IYN, MONIT
      DATA LIW, LW, TOL, POW /60, 400, .01, 1000/
C-----------------------------------------------MODEL SPECIFIC DATA
C  To Customize this Program:
C     To use another film model in this routine, you must change
C     the following data statements and parameter names and alter
C     subroutines FUNCT and MCOMF.  In those routines, the only
C     statements to change are the CALL MODELx(J,V) to call
C     your film model.  Finally link the program with your model
C     and libraries containing utilities ACHNG,ICHNG,IYN,SIMPLX and
C     spectral I/O subs WLCALC, INPUT, and OUTPUT.
C
      WRITE(*,*)'SIMPLX TOLERANCE: '
      TOL=ACHNG(TOL)
      WRITE(*,*)'MAXIMUM NO. OF ITERATIONS: '
      POW=ICHNG(POW)

      MAXCAL=POW
C-------------------------------------------------------------------
      WRITE(*,*) 'NUMBER OF FILES: '

      NFILES=ICHNG(NFILES)
      WRITE(*,*) 'LOWEST WAVELENGTH (A): '
      WLMIN=ACHNG(WLMIN)
      WRITE(*,*) 'HIGHEST WAVELENGTH (A): '
      WLMAX=ACHNG(WLMAX)
      WRITE(*,*) 'ENCODER INCREMENT: '
      NSTEP=ICHNG(NSTEP)
      PHI1=PHI1*3.1416/180.
C-----------------------------------------------WAVELENGTH DATA INPUT
    CALL WLCALC
C-------------------------------INPUT SUBSTRATE REFRACTIVE INDEX DATA
      WRITE(*,*) ' '
    WRITE(*,*)'ENTER REFRACTIVE INDEX FILE(A12): '
      READ(*,303)NAME
303   FORMAT(A16)

      FNAME(1)=NAME
      CALL INPUTF
      DO 4 I=1,400
       ANS(I)=ABS(POL(I)/1000.)
```

```
        ANKS(I)=ABS(ANA(I)/1000.)
   4  CONTINUE
C-----------------------------------Input Experimental Delta/Psi

        DO 10 J=1,NFILES
              WRITE(*,5)J
5             FORMAT(1X,'Delta/Psi Data File',I2,'-->',$)
              READ(*,303)NAME

              FNAME(J+1)=NAME
              CALL INPUTF
         DO 6 I=1,400
              DEL(I,J)=POL(I)/100.
              PSI(I,J)=ANA(I)/100.
6        CONTINUE

C--------------------------------Get initial guesses for parameters
C                                                specific to each file.

          WRITE(*,*)'Enter Local Parameter Guess: '
         DO 8 K=1,NLOC
              WRITE(*,7)NAMPAR(K)
7             FORMAT(1H$,A8,'->',$)
              READ(*,*) XTMP

              B( (J-1)*NLOC+K )=XTMP-TSC

              X( (J-1)*NLOC+K )=1.
8        CONTINUE
C

10       CONTINUE
C---------------------------------------Get N+iK Table
29       WRITE(*,30)
30       FORMAT(1X,'Global Film Refractive Index Guess Table-->',$)
         READ(*,31)NAME
31       FORMAT(A16)
         OPEN(UNIT=3, FILE=NAME, STATUS='OLD', ERR=29)
         READ(3,32)NGLOB
32       FORMAT(//,I2)
         WRITE(*,*)'These are the starting values: '

         DO 35 I=1,NGLOB
          J=(NFILES*NLOC) + (2*I-1)
C-------------------------WL, Nmin, Nmax, Kmin, Kmax
          READ(3,33)RIX(I), XTMP, XTMP2

          B(J)=XTMP-NSC

          B(J+1)=XTMP2-NSC

          X(J)=1

          X(J+1)=1.
```

```
33        FORMAT(3F15.0)

          WRITE(*,34)RIX(I), XTMP, XTMP2

34        FORMAT(1X, F10.0, T15, F10.3, T30, F10.3)
35       CONTINUE
         CLOSE(UNIT=3)
         NVAR=NLOC*NFILES+2*NGLOB
         N=NVAR
C-----------------------------------------------------Find best fit

C                                                          using NAg Simplex.
               IFAIL=0
               IW=N+1
          CALL E04CCF(N,X,F,TOL,IW,W1,W2,W3,W4,W5,W6,FUNCT1,
     &              MONIT, POW, IFAIL)
          WRITE(*,41) IFAIL

41        FORMAT(/,1X,'IFAIL: ',I2)
C-------------------------------------------------------------------
          DO 54 J=1,NFILES

           WRITE(*,49)FNAME(J+1)

49          FORMAT(/,' File: ',A20)
           DO 50 I=1,NLOC
                XTMP=X((J-1)*NLOC+I)*TSC+B((J-1)*NLOC+I)

                WRITE (*,51)NAMPAR(I),XTMP
51           FORMAT(1X,A8,2X,F8.3)
50         CONTINUE

54       CONTINUE
         WRITE(*,52)
52       FORMAT('0','Wavelength  n film   k film')
         DO 55 I=1,NGLOB
          J=(NFILES*NLOC) + (2*I-1)

          XTMP=NSC*X(J)+B(J)

          XTMP2=NSC*X(J+1)+B(J+1)

          WRITE(*,53)RIX(I),XTMP,XTMP2
53        FORMAT(1X,F6.0,4X, 2(2X,F5.3) )
55       CONTINUE
         WRITE(*,*)'CHI SQ. ERROR: ',F
C-----------------------------CREATE MODEL RESULT FILE
     CALL MCOMF(X)
     STOP
     END
```

C-4 Common Block Initialization Data

```
      BLOCK DATA STUFF
      COMMON/FLMDAT/TNA,TNKA,TNF,TNKF,TNS,TNKS,WL,PHI1,T,DELC,PSIC
      COMMON/INPUT/ DEL, PSI, WLMIN, WLMAX, ANS, ANKS, NSTEP
      COMMON/MULTI/NFILES,NLOC,NGLOB
      COMMON/NAMES/NAMPAR,NVAR,FNAME
      COMMON/SCALE/B(50),NSC,TSC

      COMMON/FUN/KOUNT

      REAL ANS(400), ANKS(400)
      REAL TNF,T
      REAL*8 DELC, PSIC

      REAL  DEL(400,8), PSI(400,8)
      CHARACTER*8 NAMPAR(5)

      CHARACTER*16 fname(10)
      INTEGER NVAR,NSTEP,POW
C-----------------------------------------------MODEL SPECIFIC DATA
C  To Customize this Program:
C       To use another film model in this routine, you must change
C       the following data statements and parameter names and alter
C       subroutines FUNCT and MCOMF.  In those routines, the only
C       statements to change are the CALL MODELx(J,V) to call
C       your film model.  Finally link the program with your model
C       and libraries containing utilities ACHNG,ICHNG,IYN,SIMPLX and
C       spectral I/O subs WLCALC, INPUT, and OUTPUT.
C
C-----------------------------------------------MODEL PARAMETERS
      DATA TNA, TNKA, TNKF, NSC, TSC/ 1.34, 0., 0., 1., 5./
      DATA PHI1,TNF,WLMIN,WLMAX,NSTEP /75.,1.55, 3800., 7400.,3/
      DATA NAMPAR/'T film',' ',' ',' ',' '/
      DATA NFILES, NLOC, KOUNT / 1, 1, 1 /

C-------------------------------------------------------------
      END
```

C-5 Fitting Progress Report Code: MONIT

```
      SUBROUTINE MONIT(FMIN, FMAX,SIM, N, IS, NCALL)
      COMMON/MONCOM/MAXCAL,LPRCAL

      COMMON/MULTI/NFILES,NLOC,NGLOB
      COMMON/SCALE/B(50),NSC,TSC

      COMMON/NAMES/NAMPAR,NVAR, FNAME
      COMMON/RITAB/NVALS,RIX,RIN, RIK, RIN2, RIK2

      REAL RIX(20), RIN(20), RIN2(20), RIK(20), RIK2(20)
```

```
      CHARACTER*16 NAME, FNAME(10)
      REAL FMIN, FMAX, SIM(IS,N), DIF, F
      INTEGER NCALL, LPCAL, MAXCAL, NMIN

      CHARACTER*8 NAMPAR(5)
C

      DIF=FMAX-FMIN
      WRITE(*,10)NCALL,FMIN,DIF
10    FORMAT(1X, 'Call: ',I4,4X,'Fmin: ',F10.5,4X,'Dif: ',F10.5)

C

       IF(NCALL .GT. LPCAL+50) THEN

            LPCAL=NCALL

            OPEN(UNIT=3,FILE='MONIT.PRN')

            WRITE(3,20)NCALL, FMAX, DIF

20          FORMAT(1X, 'CALL: ',I5, 1X, 'FMAX: ', F10.5, 5X,

     &              'DIF: ', F10.5 )

      DO 15 J=1,NFILES

       WRITE(3,11)FNAME(J+1)

11      FORMAT(/,' File: ',A20)
       DO 14 I=1,NLOC
            IND=(J-1)*NLOC+I

            XTMP=SIM(1,IND)*TSC+B(IND)

            WRITE (3,12)NAMPAR(I),XTMP
12        FORMAT(1X,A8,2X,F8.3)
14     CONTINUE

15    CONTINUE
      WRITE(3,16)
16    FORMAT('0','Wavelength  n film  k film')
      DO 19 I=1,NGLOB
       J=(NFILES*NLOC) + (2*I-1)

       XTMP=NSC*SIM(1,J)+B(J)

       XTMP2=NSC*SIM(1,J+1)+B(J+1)

       WRITE(3,18)RIX(I),XTMP,XTMP2
18     FORMAT(1X,F6.0,4X, 2(2X,F5.3) )
19    CONTINUE
            CLOSE(UNIT=3, STATUS='KEEP')
```

```
      ENDIF
    RETURN
    END
```

C-6 Film model code: FUNCT1, MODEL0M

```
      SUBROUTINE FUNCT1(NVRBS, V, SSQ)
C-----------------------------------------------------------------
C     This routine computes reflection coefficients for a
C     simple homogenous film.
C                                    Medium 1 - Ambient
C                                  _____r12_____ r12
C              Film                      Medium 2
C                                 ---------- r23 ---------- r23
C                                      Substrate
C-----------------------------------------------------------------
      COMMON/FLMDAT/TNA,TNKA,TNF,TNKF,TNS,TNKS,WL,PHI1,T,DELC,PSIC
      COMMON/INPUT/ DEL, PSI, WLMIN, WLMAX, ANS, ANKS,NSTEP
      COMMON/M/IWAVE(400)
      COMMON/RITAB/NVALS,RIX,RIN, RIK, RIN2, RIK2
      COMMON/MULTI/NFILES,NLOC,NGLOB
      COMMON/NAMES/NAMPAR,NVAR,FNAME
      COMMON/SCALE/B(50),NSC,TSC

      COMMON/FUN/KOUNT

      CHARACTER*8 NAMPAR(5)

      CHARACTER*16 fname(10)
      REAL DEL(400,8), PSI(400,8), ANS(400), ANKS(400)
      REAL*8 DELC, PSIC, X(5)
      REAL V(50), SSQ, T, TNF, RIX(20)
      REAL RIK2(20), RIK(20), RIN(20), RIN2(20)
C

      SSQ=0.
      IPTS=0
      UNDEL=.2
      UNPSI=.1

      KOUNT=KOUNT+1
C
      DO 5 I=1,NGLOB
       J=NLOC*NFILES + 2*I-1
       RIN(I)=V(J)*NSC+B(J)
       RIK(I)=V(J+1)*NSC+B(J+1)
5     CONTINUE
C
      CALL SPLINE(RIX,RIN,NGLOB,1.E31,1.E31,RIN2)
      CALL SPLINE(RIX,RIK,NGLOB,1.E31,1.E31,RIK2)
C
```

```
        DO 40 I=1,NFILES

         INDEX=(I-1)*NLOC+1
          X(1)=V(INDEX)*TSC+B(INDEX)
        DO 30 J= 1,400, NSTEP
              WL=IWAVE(J)
    IF (WL .GE. WLMIN .OR. WL .LE. WLMAX) THEN
C
          CALL SPLINT(RIX,RIN,RIN2,NGLOB,WL,TNF)
          CALL SPLINT(RIX,RIK,RIK2,NGLOB,WL,TNKF)
C
          X(2)=TNF
          X(3)=TNKF
C
         CALL MODEL0(J,X)
          SSQ=SSQ + DABS(DEL(J,I)-DELC)/UNDEL
          SSQ=SSQ + DABS(PSI(J,I)-PSIC)/UNPSI

          IPTS=IPTS+1

         ENDIF
30      CONTINUE

40      CONTINUE
         SSQ=(SSQ/IPTS)

C        WRITE(*,*)'CALL #',KOUNT,'    XSQ: ',SSQ
    RETURN
    END

        SUBROUTINE MODEL0(INDEX,V)
C
C   THIS ROUTINE IS A SIMPLE HOMOGENEOUS FILM
C   MODEL FOR REFRACTIVE INDEX
C-------------------------------------------------------------
C                                  Ambient(1)
C                               ------------ r12 -------------
C              Film                Medium 2
C                               ------------------------------r23
C                                  Substrate (3)
C-------------------------------------------------------------
    COMMON/FLMDAT/TNA,TNKA,TNF,TNKF,TNS,TNKS,WL,PHI1,T,DELC,PSIC
    COMMON/INPUT/DEL, PSI, WLMIN, WLMAX, ANS, ANKS,NSTEP
C
        REAL ANF(400), ANKF(400), LOCECOR
        REAL DEL(400,8), PSI(400,8), ANS(400), ANKS(400)
        REAL T, TNF, TNKF
        REAL*8 DELC, PSIC, V(50)
        COMPLEX*16 RP12, RS12, RP23, RS23, RHO
        COMPLEX*16 TN1, TN2, RS, RP
C---------------------------------------variable assignment
        T  = V(1)
        TNF = V(2)
        TNKF= V(3)
```

```
C-------------------------amb/Oxide interface reflection coeff.
        TN1=DCMPLX(TNA,-TNKA)
        TN2=DCMPLX(TNF,-TNKF)
        CALL REFL(TN1,TN2,RS12,RP12)
C-------------------------Oxide/Ni film interface reflection coeff.
        TN1=DCMPLX(TNF,-TNKF)
        TN2=DCMPLX(ANS(INDEX),-ANKS(INDEX))
D       TYPE *,'TN1: 1', TN1
        CALL REFL(TN1,TN2,RS23,RP23)
D       TYPE *,'TN1: 2', TN1
C-----------------------------------------AMB/OX/NI
        CALL DRUDE( RP12, RP23, TN1, RP, T)
D       TYPE *,'TN1: 3', TN1
        CALL DRUDE( RS12, RS23, TN1, RS, T)
C---------------------------ellipsometric parameters
        RHO= RP/RS
    PSIC= DATAN(CDABS(RHO))/0.01745329252
    DELC= DATAN2( DIMAG(RHO), DREAL(RHO))/0.01745329252
    IF (DABS(DELC) .GE. 180.) DELC = DELC - DSIGN(DBLE(360.),DELC)
D       TYPE *,'MODEL: RP,RS RHO,PSIC,DELC',RP,RS,RHO,PSIC,DELC
        RETURN
        END
```

C-7 Summary report code: MCOMF

```
    SUBROUTINE MCOMF(V)
C
C    THIS ROUTINE CREATES A DATA FILE FROM THE MODEL FIT.
C
    COMMON/FLMDAT/TNA,TNKA,TNF,TNKF,TNS,TNKS,WL,PHI1,T,DELC,PSIC
    COMMON/INPUT/ DEL, PSI,WLMIN,WLMAX,ANS, ANKS, NSTEP
    COMMON/M/IWAVE(400)
    COMMON/A/NAVG(400),POL(400),ANA(400)
        COMMON/MULTI/NFILES,NLOC,NGLOB
    COMMON/RITAB/NVALS,RIX,RIN, RIK, RIN2, RIK2
    COMMON/NAMES/NAMPAR,NVAR,FNAME
        COMMON/SCALE/B(50),NSC,TSC

    COMMON/OP/FILENM

        REAL DEL(400,8),PSI(400,8), ANS(400), ANKS(400)
        REAL*8  DELC, PSIC, X(5)
        REAL V(50), TNF, T, ANF(400), ANKF(400)
        REAL RIX(20), RIN(20), RIN2(20), RIK(20), RIK2(20)
        CHARACTER*1 LSTLET

        CHARACTER*8 NAMPAR(5)
        CHARACTER*16 FILENM, fname(10), CDUMMY
        CHARACTER*40 NAME
        LOGICAL IFLAG, JFLAG, IYN
        EXTERNAL IYN
C
```

```
C-----------------------------------------Start summary file.

      WRITE(*,*) 'Enter filename(A14) of model fit summary:'
      READ(*,1) NAME
1     FORMAT(A20)
   OPEN (UNIT=2, FILE=NAME, STATUS='UNKNOWN')
C-----------------------------------------Get last letter of extension.

      I=INDEX(NAME,' ')-1

      LSTLET(1:1)=NAME(I:I)

C-------------------------------------Write header with date and note.
            CALL GETTIM(IHR,IMIN,ISEC,IHUN)

            CALL GETDAT(IYR,IMON,IDAY)

      WRITE(2,2)NAME, IHR,IMIN, IMON,IDAY,IYR

2     FORMAT(2X,"",A20,2X,I2.2,':',I2.2,2X,I2.2,'/',I2.2,'/',I4,"")

      WRITE(*,*) 'Enter experiment note(a40): '
      READ(*,3) NAME
3     FORMAT(A40)

      WRITE(2,4)NAME

4      FORMAT("",A40,"")

      WRITE(2,5) TNA
5     FORMAT(2X, '"Nambient: " ', F5.3)

      WRITE(2,6)FNAME(1)

6      FORMAT(1X,'"Substrate RI spectra:" ', "", A16, "")

      WRITE(2,8)WLMIN,WLMAX, NSTEP

8      FORMAT('"Fit Range:"','"[", F5.0, ',', F5.0,']"',

   &   2x,'"Encoder Step:"',I2)

      WRITE(2,7)

      WRITE(*,7)

7      FORMAT(/,'"WL"',4X, '"Nfilm"', 4x, '"Kfilm"' )
C-----------------------------------Calculate Refractive Index Spectrum

      DO 10 I=1,NGLOB
       J=(NLOC*NFILES)+(2*I-1)
       RIN(I)=V(J)*NSC+B(J)
       RIK(I)=V(J+1)*NSC+B(J+1)
       WRITE(2,9)RIX(I),RIN(I),RIK(I)
```

```
          WRITE(*,9)RIX(I),RIN(I),RIK(I)

9         FORMAT(1X,F6.0,',' , F6.3,',',  F6.3)

10        CONTINUE

          CALL SPLINE(RIX,RIN,NGLOB,1.E31,1.E31,RIN2)
          CALL SPLINE(RIX,RIK,NGLOB,1.E31,1.E31,RIK2)
C
C---------------------------------Output Film Optical Constants
          DO 15 I=1,400
           WL=IWAVE(I)
           IF (WL .GE. WLMIN .OR. WL .LE. WLMAX) THEN

           CALL SPLINT(RIX,RIN,RIN2,NGLOB,WL,ANF(I))
           CALL SPLINT(RIX,RIK,RIK2,NGLOB,WL,ANKF(I))

           ELSE
           ANF(I)=0.
           ANKF(I)=0.
           ENDIF
           POL(I)=ANF(I)*1000.
           ANA(I)=ANKF(I)*1000.
15        CONTINUE

C-------------------------------------Save refractive index

C                                                  in spectral file.
C
          WRITE(*,*) 'Do you want a film refractive index file'
          IF ( IYN(I) ) THEN
            WRITE(*,17)

17          FORMAT(1X, 'Refractive index filenmame-->',$)
            READ (*,18) FILENM
18          FORMAT(A16)

            WRITE(2,19)FILENM

19          FORMAT(1X,"'Film RI stored-->'",'"',A16,'"')
           CALL OUTPTF
          ENDIF

C
C---------------------------------For each file, report local parameters

C                                          and error summary.
          WRITE(*,99)
99        FORMAT('$Generate Delta/Psi Prediction Files?',$)
           IFLAG=IYN(I)
          DO 100 I=1,NFILES
```

```
            WRITE(2,20)FNAME(I+1)
            WRITE(*,20)FNAME(I+1)
20          FORMAT(1X,"",A16,"")
           DO 30 J=1,NLOC

            IND=(I-1)*NLOC + J
           WRITE (2,29)NAMPAR(J), V(IND)*TSC+B(IND)
           WRITE (*,29)NAMPAR(J), V(IND)*TSC+B(IND)
29         FORMAT(2X, "",A8,': "  ',F10.3)

30         CONTINUE
C

          IPTS=0
          RMSDEL=0.
          RMSPSI=0.
          AVGDEL=0.
          AVGPSI=0.
C---------------------------------------Film Thickness is parameter #1

          X(1) = V((I-1)*NLOC+1)*TSC+B((I-1)*NLOC+1)
      DO 50 J=1,400
           WL=IWAVE(J)
           POL(J)=0.
           ANA(J)=0.
          IF((WL .GE. WLMIN .AND. WL .LE .WLMAX) ) THEN
            X(2)=ANF(J)
            X(3)=ANKF(J)
           CALL MODEL0(J,X)
            POL(J)=DELC*100.
            ANA(J)=PSIC*100.
            IPTS=IPTS+1
           RMSDEL=RMSDEL+(DEL(J,I)-DELC)**2
           RMSPSI=RMSPSI+(PSI(J,I)-PSIC)**2
           AVGDEL =AVGDEL+(DEL(J,I)-DELC)
           AVGPSI=AVGPSI+(PSI(J,I)-PSIC)
          ENDIF
50    CONTINUE
      RMSDEL = SQRT(RMSDEL/IPTS)
      RMSPSI = SQRT(RMSPSI/IPTS)
      AVGDEL = AVGDEL/IPTS
      AVGPSI = AVGPSI/IPTS
      WRITE(*,98) RMSDEL, AVGDEL, RMSPSI, AVGPSI
      WRITE(2,98) RMSDEL, AVGDEL, RMSPSI, AVGPSI
98     FORMAT(2X,"'ERRORS RMSDEL:" ',F6.2,' "AVGDEL:" ',F6.2,
     & ' "RMSPSI:" ',F6.2, ' "AVGPSI:" ',F6.2)
C

C-----------------------------------------Write Delta/Psi prediction

C                                                          file.
          IF( IFLAG ) THEN
C-------------------------------Encode filename with extension .PR#
```

```
          IDOT=INDEX(FNAME(I+1),'.')

          FILENM(1:IDOT+3)=FNAME(I+1)(1:IDOT)//'PR'//LSTLET(1:1)

         CALL OUTPTF

        ENDIF
100     CONTINUE

    CLOSE(UNIT=2, STATUS='KEEP')
999    RETURN
   END
```

C-8 Cubic spline interpolation code: SPLINE, SPLINT

```
      SUBROUTINE SPLINE(X,Y,N,YP1,YPN,Y2)
      PARAMETER (NMAX=100)
      DIMENSION X(N),Y(N),Y2(N),U(NMAX)
      IF (YP1.GT..99E30) THEN
       Y2(1)=0.
       U(1)=0.
      ELSE
       Y2(1)=-0.5
       U(1)=(3./(X(2)-X(1)))*((Y(2)-Y(1))/(X(2)-X(1))-YP1)
      ENDIF
      DO 11 I=2,N-1
       SIG=(X(I)-X(I-1))/(X(I+1)-X(I-1))
       P=SIG*Y2(I-1)+2.
       Y2(I)=(SIG-1.)/P
       U(I)=(6.*((Y(I+1)-Y(I))/(X(I+1)-X(I))-(Y(I)-Y(I-1))
     *  /(X(I)-X(I-1)))/(X(I+1)-X(I-1))-SIG*U(I-1))/P
11    CONTINUE
      IF (YPN.GT..99E30) THEN
       QN=0.
       UN=0.
      ELSE
       QN=0.5
       UN=(3./(X(N)-X(N-1)))*(YPN-(Y(N)-Y(N-1))/(X(N)-X(N-1)))
      ENDIF
      Y2(N)=(UN-QN*U(N-1))/(QN*Y2(N-1)+1.)
      DO 12 K=N-1,1,-1
       Y2(K)=Y2(K)*Y2(K+1)+U(K)
12  CONTINUE
      RETURN
      END

      SUBROUTINE SPLINT(XA,YA,Y2A,N,X,Y)
      DIMENSION XA(N),YA(N),Y2A(N)
      KLO=1
      KHI=N
1   IF (KHI-KLO.GT.1) THEN
```

```
        K=(KHI+KLO)/2
        IF(XA(K).GT.X)THEN
         KHI=K
        ELSE
         KLO=K
        ENDIF
       GOTO 1
       ENDIF
       H=XA(KHI)-XA(KLO)
       IF (H.EQ.0.) PAUSE 'Bad XA input.'
       A=(XA(KHI)-X)/H
       B=(X-XA(KLO))/H
       Y=A*YA(KLO)+B*YA(KHI)+
     *  ((A**3-A)*Y2A(KLO)+(B**3-B)*Y2A(KHI))*(H**2)/6.
       RETURN
       END
```

C-9 Binary spectral file I/O: INPUTF, OUTPTF, WLCALC

```
       SUBROUTINE INputf
C*************************************************************************
C    OBJECTIVE: TO READ THE SETUP INFORMATION AND SPECTRAL SCAN DATA
C                  AS FROM THE DEVICE AND OF THE NAME DICTATED BY THE
C                PROGRAM using GENERIC FORTRAN FOR PORTABILITY.
C*************************************************************************
       COMMON/A/NAVG(400),POL(400),ANA(400)
       COMMON/B/NRATE,NSCAN,IPOL,IANA
       COMMON/E/NAMEOP(20),ID(20)
       COMMON/F/LMPTYP,LMPSER(10),LMPVLT,LMPAMP
       COMMON/G/IPMTYP(10),IPMTDV
      COMMON/H/IPHASP,IPHASA,IGAINP,IGAINA,IAMPLP,IAMPLA,ITIMEP,ITIMEA
       COMMON/I/IGAGP,IGAGA,IGATP,IGATA
       COMMON/J/NWL,NPOL,NCMP,NANA
       COMMON/K/IHRS0,IMIN0,ISEC0,ITIC0,IHRSF,IMINF,ISECF,ITICF
       COMMON/L/IDAY,IMON(3),IYRS,LMPHRS
       COMMON/M/IWAVE(400)
       COMMON/OP/FILENM(4),IFLTYP
       COMMON/Z/NAME1,NAME2,IPASS,DURAT,RTIME
       CHARACTER*16 NAME
       INTEGER*2 IBUFF(256)
       EQUIVALENCE (FILENM(1),NAME)
C-------------------------------------------------------------
       DO 10 I=1,256
  10 IBUFF(I)=0
C-------------------------------------------------------
       WRITE(*,8)NAME
8      FORMAT(1X,'Reading...',A16/)
11     OPEN(FILE=NAME,ACCESS='DIRECT',STATUS='OLD',UNIT=3,
   &    RECL=512, ERR=12)
       GOTO 19
```

```
12      WRITE(*,9)NAME
9       FORMAT(1X,A16,' not found--Better name:',$)
        READ(*,13)NAME
13      FORMAT(A16)
        GOTO 11
C-------------------------------------------------
19      READ(3, REC=1)(IBUFF(I),I=1,256)
C-------------------------------------------------
        DO 20 I=1,20
        NAMEOP(I)=IBUFF(I)
 20 ID(I)=IBUFF(20+I)
        LMPTYP=IBUFF(41)
        DO 30 I=1,9
 30 LMPSER(I)=IBUFF(41+I)
        LMPVLT=IBUFF(51)
        LMPAMP=IBUFF(52)
        IPHASP=IBUFF(54)
        IGAINP=IBUFF(55)
        IAMPLP=IBUFF(56)
        ITIMEP=IBUFF(57)
        IPHASA=IBUFF(58)
        IGAINA=IBUFF(59)
        IAMPLA=IBUFF(60)
        ITIMEA=IBUFF(61)
        IGAGP =IBUFF(62)
        IGATP =IBUFF(63)
        IGAGA =IBUFF(64)
        IGATA =IBUFF(65)
        NRATE =IBUFF(66)
        NSCAN =IBUFF(67)
        IPOL  =IBUFF(68)
        IANA  =IBUFF(69)
        NWL   =IBUFF(70)
        NPOL  =IBUFF(71)
        NCMP  =IBUFF(72)
        NANA  =IBUFF(73)
        IHRS0 =IBUFF(74)
        IHRSF =IBUFF(75)
        IMIN0 =IBUFF(76)
        IMINF =IBUFF(77)
        ISEC0 =IBUFF(78)
        ISECF =IBUFF(79)
        ITIC0 =IBUFF(80)
        ITICF =IBUFF(81)
        IDAY  =IBUFF(82)
        IYRS  =IBUFF(83)
        LMPHRS=IBUFF(84)
        IMON(1)=IBUFF(85)
        IMON(2)=IBUFF(86)
        IMON(3)=IBUFF(87)
        DO 35 I=1,10
 35 IPMTYP(I)=IBUFF(87+I)
        IPMTDV=IBUFF(98)
C-------------------------------------------------
```

```
      READ(3, REC=2)(IBUFF(I),I=1,256)
C-----------------------------------------------
      DO 40 I=1,200
 40 POL(I)=IBUFF(I)
C-----------------------------------------------
      READ(3, REC=3)(IBUFF(I),I=1,256)
C-----------------------------------------------
      DO 50 I=1,200
 50 ANA(I)=IBUFF(I)
C-----------------------------------------------
      READ(3, REC=4)(IBUFF(I),I=1,256)
C-----------------------------------------------
      DO 60 I=1,200
 60 POL(I+200)=IBUFF(I)
C-----------------------------------------------
      READ(3, REC=5)(IBUFF(I),I=1,256)
C-----------------------------------------------
      DO 70 I=1,200
 70 ANA(I+200)=IBUFF(I)
      CLOSE(UNIT=3,STATUS='KEEP')
      RETURN
      END


      SUBROUTINE OUTPTF
C*********************************************************************
C   OBJECTIVE: TO WRITE SETUP INFORMATION AND DATA FROM THE
C              SPECTRAL SCAN INTO BINARY FILES.  THE NAME OF THE
C              FILE IS PASSED FROM THE CALLING PROGRAM THROUGH
C              COMMON BLOCKS.
C      A SLIGHTLY MODIFIED VERSION OF S. MAYER OUT.FOR WHICH
C       IS A VERSION OF A J. FARMER ROUTINE OUTPUT.
C      BOB CROCKER  7 JUL 87
C      MODIFIED TO GENERIC FORTRAN FOR PORTABILITY JUL 88
C*********************************************************************
      COMMON/A/NAVG(400),POL(400),ANA(400)
      COMMON/B/NRATE,NSCAN,IPOL,IANA
      COMMON/E/NAMEOP(20),ID(20)
      COMMON/F/LMPTYP,LMPSER(10),LMPVLT,LMPAMP
      COMMON/G/IPMTYP(10),IPMTDV
      COMMON/H/IPHASP,IPHASA,IGAINP,IGAINA,IAMPLP,IAMPLA,ITIMEP,ITIME
A
      COMMON/I/IGAGP,IGAGA,IGATP,IGATA
      COMMON/J/NWL,NPOL,NCMP,NANA
      COMMON/K/IHRS0,IMIN0,ISEC0,ITIC0,IHRSF,IMINF,ISECF,ITICF
      COMMON/L/IDAY,IMON(3),IYRS,LMPHRS
      COMMON/M/IWAVE(400)
      COMMON/Z/NAME1,NAME2,IPASS,DURAT,RTIME
      COMMON/OP/FILENM(4),IFLTYP
      CHARACTER*16 NAME
c-------------------------Integers for ibuff *must* be 2 bytes
      INTEGER*2 IBUFF(256)
      EQUIVALENCE (FILENM(1),NAME)
C-----------------------------------------------
```

```
5       OPEN(FILE=NAME,ACCESS='DIRECT',STATUS='UNKNOWN',UNIT=3,
   &     RECL=512, ERR=6)
        GOTO 9
6        WRITE(*,8)NAME
8        FORMAT(1X,'Error writing ',A16, ' Better name: ',$)
         READ(*,7)NAME
7        FORMAT(A16)
         GOTO 5
C-------------------------------------------------
9       DO 10 I=1,256
 10 IBUFF(I)=0
C-------------------------------------------------
        DO 20 I=1,20
        IBUFF(I)=NAMEOP(I)
                J=I+20
 20 IBUFF(J)=ID(I)
        IBUFF(41)=LMPTYP
        DO 30 I=1,9
        J=41+I
 30 IBUFF(J)=LMPSER(I)
        IBUFF(51)=LMPVLT
        IBUFF(52)=LMPAMP
        IBUFF(54)=IPHASP
        IBUFF(55)=IGAINP
        IBUFF(56)=IAMPLP
        IBUFF(57)=ITIMEP
        IBUFF(58)=IPHASA
        IBUFF(59)=IGAINA
        IBUFF(60)=IAMPLA
        IBUFF(61)=ITIMEA
        IBUFF(62)=IGAGP
        IBUFF(63)=IGATP
        IBUFF(64)=IGAGA
        IBUFF(65)=IGATA
        IBUFF(66)=NRATE
        IBUFF(67)=NSCAN
        IBUFF(68)=IPOL
        IBUFF(69)=IANA
        IBUFF(70)=NWL
        IBUFF(71)=NPOL
        IBUFF(72)=NCMP
        IBUFF(73)=NANA
        IBUFF(74)=IHRS0
        IBUFF(75)=IHRSF
        IBUFF(76)=IMIN0
        IBUFF(77)=IMINF
        IBUFF(78)=ISEC0
        IBUFF(79)=ISECF
        IBUFF(80)=ITIC0
        IBUFF(81)=ITICF
        IBUFF(82)=IDAY
        IBUFF(83)=IYRS
        IBUFF(84)=LMPHRS
        IBUFF(85)=IMON(1)
```

```
        IBUFF(86)=IMON(2)
        IBUFF(87)=IMON(3)
        DO 35 I=1,10
         J=I+87
  35 IBUFF(J)=IPMTYP(I)
        IBUFF(98)=IPMTDV
C-------------------------------------------------
        WRITE(3, REC=1)(IBUFF(I),I=1,256)
C-------------------------------------------------
        DO 40 I=1,200
         If(abs(pol(i)).gt.32767)pol(i)=0.0
         IBUFF(I)=POL(I)
40   CONTINUE
C-------------------------------------------------
        WRITE(3, REC=2)(IBUFF(I),I=1,256)
C-------------------------------------------------
        DO 50 I=1,200
         if(abs(ana(i)).gt.32767)ana(i)=0.0
         IBUFF(I)=ANA(I)
50   CONTINUE
C-------------------------------------------------
        WRITE(3, REC=3)(IBUFF(I),I=1,256)
C-------------------------------------------------
        DO 60 I=1,200
         if(abs(pol(i+200)).gt.32767)pol(i+200)=0.0
         IBUFF(I)=POL(I+200)
60   CONTINUE
C-------------------------------------------------
        WRITE(3, REC=4)(IBUFF(I),I=1,256)
C-------------------------------------------------
        DO 70 I=1,200
         if(abs(ana(i+200)).gt.32767)ana(i+200)=0.0
         IBUFF(I)=ANA(I+200)
70   CONTINUE
C-------------------------------------------------
        WRITE(3, REC=5)(IBUFF(I),I=1,256)
C-------------------------------------------------
        CLOSE(UNIT=3,STATUS='KEEP')
        RETURN
        END


        SUBROUTINE WLCALC
C**********************************************************************
C    OBJECTIVE: TO CONVERT ENCODER COUNTS INTO WAVELENGTH USING
C                  PREDETERMINED CALIBRATION CURVE PARAMETERS.
C**********************************************************************
        COMMON/M/IWAVE(400)
        COMMON/WLC/IL,IU, A1, B1, A2,B2
        OPEN(UNIT=2,FILE='WLCALC.DAT',STATUS='OLD')
        READ(2,996)IL,IU,A1,B1,R1,A2,B2,R2
 996 FORMAT(2(1X,I3),2(1X,F8.4,1X,F8.2,1X,F6.4))
        CLOSE(UNIT=2,STATUS='KEEP')
        DO 40 I=1,400
```

```
      WL=A1*I+B1
      IF(I.GE.IL .AND. I.LE.IU) WL=A2*I+B2
      IF(I.GT.IU) WL=A1*(I-400)+B1
      IWAVE(I)=WL
 40 CONTINUE
      RETURN
      END
```

C-10 Utility Subroutines for Optical Models: REFL, DRUDE

```
      SUBROUTINE REFL(TN1, TN2, RS, RP)

C-------------------------------------------------------------------
C     THis routine computes fresnel reflection coefficients for a
C      single interface. Snell's law used to determine incidences.
C
C                                                    Media 1
C                                                  ----------
C                                                    Media 2
C      Robert Crocker 16 april 87
C-------------------------------------------------------------------
      COMMON/FLMDAT/TNA,TNKA,TNF,TNKF,TNS,TNKS,WL,PHI,T,DELC,PSIC
      COMPLEX*16 TN1, TN2, CPHI1, CPHI2, RS, RP
      REAL PHI, TNA
C-----------------------------------------------Snell's law:
      CPHI1=CDSQRT(1.0 - (TNA*DSIN(DBLE(PHI))/TN1 )**2 )
      CPHI2=CDSQRT(1.0 - (TNA*DSIN(DBLE(PHI))/TN2 )**2 )
C-------------------------------------reflection coeff. film/substr.
      RS=(TN1*CPHI1-TN2*CPHI2)/(TN1*CPHI1 + TN2*CPHI2)
      RP= - (TN1*CPHI2-TN2*CPHI1)/(TN1*CPHI2 + TN2*CPHI1)
D   TYPE *,'REFL',TN1,TN2,CPHI1,RS,RP
      RETURN
      END


      SUBROUTINE DRUDE( R1, R2, TN2, REFF, T1)
C-------------------------------------------------------------
C              This routine computes the drude reflection coefficients
C
C                Ambient
C              ! ---------- interface 1 (r1)
C              ! Film
C              ! ---------- interface 2 (r2)
C              ! Substrate
C   Robert Crocker 16 april 87
C-------------------------------------------------------------
      COMMON/FLMDAT/TNA,TNKA,TNF,TNKF,TNS,TNKS,WL,PHI,T,DELC,PSIC
      COMPLEX*16 R1, R2, TN2, REFF, CPHI2, Z
      REAL TNA, PHI, T1, WL
C-------------------------------------correct Fresnel eq. for n-ik
      CPHI2=CDSQRT(1.0 - (TNA*DSIN(DBLE(PHI))/TN2 )**2 )
      Z=(0.0 , 1.0)* DCMPLX(4.0 * 3.1415927 * T1/WL , 0.) * TN2*CPHI2
```

```
      REFF=(R1+R2*CDEXP(-Z))/(1.0+R1*R2*CDEXP(-Z))
D     TYPE *,'DRUDE',R1,R2,TN2,TNA,REFF,WL,T
      RETURN
      END
```

END

DATE
FILMED
8/12/92